OFDM Passive Radar Employing Compressive Processing in MIMO Configurations

Watcharapong Ketpan

Submitted for the degree of Doctor of Philosophy

Heriot-Watt University

School of Engineering and Physical Sciences

December 2018

Abstract

A key advantage of passive radar is that it provides a means of performing position detection and tracking without the need for transmission of energy pulses. In this respect, passive radar systems utilising (receiving) orthogonal frequency division multiplexing (OFDM) communications signals from transmitters using OFDM standards such as long-term evolution (LTE), WiMax or WiFi, are considered. Receiving a stronger reference signal for the matched filtering, detecting a lower target signature is one of the challenges in the passive radar.

Impinging at the receiver, the OFDM waveforms supply two-dimensional virtual uniform rectangular array with the first and second dimensions refer to time delays and Doppler frequencies respectively. A subspace method, multiple signals classification (MUSIC) algorithm, demonstrated the signal extraction using multiple time samples. Apply normal measurements, this problem requires high computational resources regarding the number of OFDM subcarriers. For sub-Nyquist sampling, compressive sensing (CS) becomes attractive. A single snapshot measurement can be applied with Basis Pursuit (BP), whereas l_1-singular value decomposition (l_1-SVD) is applied for the multiple snapshots. Employing multiple transmitters, the diversity in the detection process can be achieved. While a passive means of attaining three-dimensional large-set measurements is provided by co-located receivers, there is a significant computational burden in terms of the on-line analysis of such data sets. In this thesis, the passive radar problem is presented as a mathematically sparse problem and interesting solutions, BP and l_1-SVD as well as Bayesian compressive sensing, fast-Besselk, are considered. To increase the possibility of target signal detection, beamforming in the compressive domain is also introduced with the application of convex optimization and subspace orthogonality. An interference study is also another problem when reconstructing the target signal. The networks of passive radars are employed using stochastic geometry in order to understand the characteristics of interference, and the effect of signal to interference plus noise ratio (SINR). The results demonstrate the outstanding performance of l_1-SVD over MUSIC when employing multiple snapshots. The single snapshot problem along with fast-BesselK multiple-input multiple-output configuration can be solved using fast-BesselK and this allows the compressive beamforming for detection capability.

Acknowledgments

First of all, I would like to thank the warmest support from my family which includes my wife, Chutima, my son, Chanapratch, and my mom. Without their encouragement during my study, all difficulties would not be easy to overcome.

And I would like to acknowledge my supervisor, Professor Mathini Sellathurai, with the valuable advice for the whole period of study. Her suggestions directed me to the better solutions regarding my research. Members of the Signal Processing for Intelligent Systems and Communications Research Group also deserves my thanks for a good collaboration, such as code sharing, paper proofreading and technical advice. This includes Dr. Qian, Dr. Chambers, Dr. Payami and Ms. Shoukry.

This study would not be able to occur if there is no financial support from the Royal Thai Air Force. Specifically, I always receive a good help from my commanders and colleagues from the Navaminda Kasatriyadhiraj Royal Air Force Academy. Furthermore, priceless suggestions for a PhD study, from Dr. Thammavichai, Dr. Kanjanasit and Mr. Phonsri, lead some proper solutions whenever I was struggling in work, as well as living in the UK.

Furthermore, in order to live in the best city like Edinburgh, I also received some assistance from staffs at a Thai restaurant, who provided some food and made my life less troublesome. Consequently, Edinburgh is an enjoyable place to study, including its scenarios and exciting weather.

ACADEMIC REGISTRY
Research Thesis Submission

Name*:*	Watcharapong Ketpan		
School:	Engineering and Physical Sciences		
Version: *(i.e. First, Resubmission, Final)*	Final	Degree Sought:	Doctor of Philosophy

Declaration

In accordance with the appropriate regulations I hereby submit my thesis and I declare that:

1) the thesis embodies the results of my own work and has been composed by myself
2) where appropriate, I have made acknowledgement of the work of others and have made reference to work carried out in collaboration with other persons
3) the thesis is the correct version of the thesis for submission and is the same version as any electronic versions submitted*.
4) my thesis for the award referred to, deposited in the Heriot-Watt University Library, should be made available for loan or photocopying and be available via the Institutional Repository, subject to such conditions as the Librarian may require
5) I understand that as a student of the University I am required to abide by the Regulations of the University and to conform to its discipline.
6) I confirm that the thesis has been verified against plagiarism via an approved plagiarism detection application e.g. Turnitin.

* *Please note that it is the responsibility of the candidate to ensure that the correct version of the thesis is submitted.*

Signature of Candidate*:*		Date:	

Submission

Submitted By *(name in capitals):*	
Signature of Individual Submitting:	
Date Submitted:	

For Completion in the Student Service Centre (SSC)

Received in the SSC by *(name in capitals):*			
Method of Submission *(Handed in to SSC; posted through internal/external mail):*			
*E-thesis Submitted (**mandatory for final theses)***			
Signature:		Date:	

Please note this form should be bound into the submitted thesis.

Contents

List of Figures

List of Tables

Abbreviations

l_1-SVD L1-Singular Value Decomposition.

1-D One-dimensional.

2D Two-dimensional.

3D Three-dimensional.

AoA Angle-of-Arrival.

AWGN Additive white Gaussian noise.

BCRB Bayesian Cramer-Rao Bound.

BCS Bayesian Compressive Sensing.

BER Bit Error Rate.

BP Basis Pursuit.

BS Base Station.

CAF Cross Ambiguity Function.

CDF Cumulative Density Function.

CF Characteristic Function.

CFAR Constant False Alarm Rate.

COFDM Coherent Orthogonal Frequency Division Multiplexed.

CRLB Cramer-Rao Lower Bounds.

CS Compressive Sensing.

CSMA Carrier-Sense Multiple Access.

DAB Digital Audio Broadcasting.

dB decibels.

DFT Discrete Fourier Transform.

DOA Direction of Arrivals.

DVB-T Digital Video Broadcasting - Terrestrial.

DVB/DAB Digital Video/Audio Broadcasting.

Eb/No Energy per bit to Noise Power Density ratio.

EIRP Effective Isotropic Radiated Power.

EKF Extended Kalman Filter.

EM Expectation-Maximization.

FDA Frequency Diverse Array.

FFT Fast Fourier Transform.

FM Frequency Modulation.

GPR Ground Penetrating Radar.

GSM Global System for Mobile communications.

i.i.d. independent and identically distributed.

IMM Interacting Multiple Model.

ISI Intersymbol Interference.

LCMV Linearly Constrained Minimum Variance.

LTE Long-Term Evolution.

MAC Media Access Control.

MAP Maximum-a-Posteriori.

MIMO Multiple-Input Multiple-Output.

MISO Multiple-Input Single-Output.

mmWave Millimetre Wave.

MRC Maximum Ratio Combining.

ms milliseconds.

MUSIC Multiple Signal Classification.

MVDR Minimum Variance Distortionless Response.

NMSE Normalised Mean Square Error.

NSP Null-Space Property.

OC Optimum Combining.

OFDM Orthogonal Frequency Division Multiplexing.

OMP Orthogonal Matching Pursuit.

PBR Passive Bistatic Radar.

PDFs Probability Density Functions.

PGFL Probability Generating Functional.

PPP Poisson Point Process.

PSK Phase-Shift Keying.

QAM Quadrature Amplitude Modulation.

RCS Radar Cross Section.

RF Radio Frequency.

RIP Restricted Isometry Properte.

RVM Relevance Vector Machin.

SAR Synthetic Aperture Radar.

SFN Single Frequency Network.

SINR Signal-to-Interference plus Noise Ratio.

SIR Signal-to-Interference Ratio.

SNR Signal-to-Noise Ratio.

SOCP Second-Order Cone Program.

SVD Singular Value Decomposition.

UAVs Unmanned Aerial Vehicles.

ULA Uniform Linear Array.

URAs Uniform Rectangular Arrays.

WiMAX Worldwide Interoperability for Microwave Access.

WLAN Wireless Local Area Network.

Nomenclature

A_p An attenuation of each incoming path.

A_{ki} QAM In-phase components.

A_{kq} QAM Quadrature-phase components.

C_k A channel impulse response of k-th sample.

D_{km} The distance between the k-th base station and the m-th receive antenna.

G_k The gain of the k-th station antenna.

L The number of blocks in one OFDM frame transmitted by the OFDM base station.

M The number of snapshots.

N (1) The number of signal samples in one OFDM block in the theory (2) The number of OFDM subcarriers used in the simulation.

$N'L'$ The number of measurements regarding the subcarrier domain and the OFDM blocks domain respectively.

N_a The number of elements in a vector $\mathbf{a}$.

N_f The number of bits in an OFDM frame.

N_p The total number of paths impinging at the receiver in the multipath scenario.

N_θ A number of possible steering vectors in $\mathbf{B}$.

P_k The power of transmitted signal from the base station k.

Q The number of distributed reflectors.

R_c A radius of a multistatic passive radar cell.

R_g the length of a guard region of a multistatic passive radar cell.

S_x The narrowband snapshot in the frequency-domain before applying subspace algorithm.

T Period of one OFDM symbol before applying cyclic prefix.

T' The length of an OFDM block in time.

T_{cp} The length of a cyclic prefix in time.

T_{max} The time at which maximum SNR occurs after applying the matched filter.

X_k The complex-valued signal points of the k-th subcarrier information symbols.

Δ_i An eigenvector of the index i.

Δf Frequency of the intervals between each OFDM subcarriers.

Φ A sensing basis in compressive sensing or an instantaneous PPP in stochastic geometry.

Ψ A sparsity basis.

α A path-loss exponent.

α_m An arbitraty real positive constant of the matched filter.

$\hat{Q}(\psi)$ A null spectrum function in subspace algorithm.

$\hat{U}_S$ The signal subspace using subspace algorithm.

$\hat{U}_W$ The noise subspace using subspace algorithm.

λ A regularisation parameter in compressive sensing or a density of point process in stochastic geometry.

$\lambda^{(x)}$ A density of unit x regarding its corresponding point process $\Phi^{(x)}$.

$\mathbf{B}$ An overcomplete matrix constructed by all possible steering vectors as its column.

$\mathbf{I}(\theta)$ The fisher information matrix.

$\mathbf{R}$ A correlation matrix of received signals.

$\mathbf{R}$ A data correlation matrix.

$\alpha_{N_p}^{k(m)}$ A vector of all path attenuations from transmitter k to receiver antenna m.

$\mathbf{a}$ An original sparse vector whose non-zero elements correspond to attenuation values.

$\mathbf{b}$ A steering vector.

$\mathbf{h}(\hat{\tau})$ Channel estimates at time $\hat{\tau}$.

$\mathbf{r}_{ti}$ The OMP residual at iteration ti.

$\mathbf{w}$ A vector of additive noise.

$\mathscr{A}$ A physical cross-sectional area of a target.

$\mathscr{H}$ A Hessian function used in a Newton search method.

$\mathscr{K}$ the number of tiers in heterogeneous multistatic passive radar networks.

$\mathscr{L}$ the log-normal shadowing of the channel.

$\mu(\cdot)$ A coherence between a sparsity basis and a sensing basis.

ϕ_k An angle of arrivals of the received signal.

σ_w^2 Variance of the additive noise.

τ_p^{km} The time delay of the signal path p originated from the station k and impinging on the receiver m.

θ_g a scale parameter for the Gamma distribution of the fading component.

$\tilde{N}$ The number of groups in an OFDM fram when applying FFT algorithm.

ζ_q The reflectivity of the reflector q.

a^{km} The ratio between a target (or a transmitter)'s range-rate and speed of light of the signal originated from the station k and impinging on the receiver m.

d The space between each receive antenna in the array.

f_D^{km} The Doppler frequency of the signal originated from the station k and impinging on the receiver m.

f_c The carrier frequency.

f_k The frequency of the k-th subcarrier.

f_{MUSIC} Two-dimensional MUSIC spectrum.

k_g a shape parameter for the Gamma distribution of the fading component.

n_r The number of receive antennas.

n_t The number of transmit base stations.

v The number of cyclic prefix samples in one OFDM block.

x The transmitted OFDM signal.

$y(t)$ The OFDM signal received at the radar receiver.

Publications

1. W. Ketpan, S. Phonsri, R. Qian, and M. Sellathurai, "On the Target Detection in OFDM Passive Radar Using MUSIC and Compressive Sensing," in *2015 Sensor Signal Processing for Defence (SSPD)*. IEEE, Sep 2015, pp. 15.

2. W. Ketpan and M. Sellathurai, "Compressive sensing-based 3D signal extraction for MIMO passive radar using OFDM waveforms," in *2016 IEEE International Conference on Communications (ICC)*, May 2016, pp. 16.

3. W. Ketpan, R. Qian, M. Sellathurai, and P. Chambers, "OFDM passive radar and compressive domain processing," *IEEE Systems Journal*, p. Submitted, May 2018.

4. W. Ketpan and M. Sellathurai, "A study of OFDM passive radar networks using stochastic geometry," *IEEE Access*, p. Submitted, July 2018.

Chapter 1

Introduction

1.1 Background

Previously, surveillance and reconnaissance were military operations which provided the required information during wartime only. These operations presently play notable roles in both military and non-military applications. There are many kinds of sensors used for many different purposes, such as camera, laser guidance or radar. Camera-type sensors can produce impressive surveillance pictures, but they require a suitable amount of light and fine weather. Laser has lately become more interesting due to its very high data rate transmission; however, the distance applied is relatively short as the wave cannot penetrate obstacles. Many missions, either in the commercial sector or government-led, continue to use radar. The range of frequencies employed ranges from radio to microwave. Without the demand for good conditions, radars can be operated efficiently. Additionally, there is considerable ongoing research and development.

What drives this research is the increasing determination to degrade radar detection ability. Regarding military activities, there is currently an increase in deployment of stealth platforms. Many areas of research (e.g. aircraft design, aerodynamics, composite materials or signal scattering) are being combined to improve the capability of detection avoidance. Another activity to decrease the ability of radar is jamming. Jamming is a cheap and easy algorithm compared to other warfare devices. Many communication systems utilise a frequency-hopping technique which can effectively eliminate jamming issues. Another similar successful concept alongside stealth and jamming is to know the characteristics of radar signals. In this case, it is impossible to prevent this as radar normally transmits a beam of waveform to sense its targets. Moreover, some light aircrafts, e.g. Unmanned Aerial Vehicles (UAVs), keep flying at a low altitude and at a very low

speed, which can cause many problems for the radar due to the reflections of surrounding clutters.

This is interesting because there is a possibility of communication signals exploitation by the radar systems. Due to the fact that there are a large number of communication signals being applied throughout the world, radar should be able to understand the available signals and employ the techniques to distinguish the target signature from the original version. The available and proper commercial signals are Frequency Modulation (FM) radio, Digital Video/Audio Broadcasting (DVB/DAB), the Global System for Mobile communications (GSM), and even wireless internet communication signals. The name of the radar which does not transmit a signal is *passive radar*. As the transmitter and receiver are at different locations, passive radar works in bistatic or multistatic scenarios [5]. It is obvious that passive radar requires only half of the monostatic hardware configurations, and the burdens of a transmitter, as well as a transmitted signal, are not necessary. Contrast to a standard active radar, the radar jammer may struggle to interfere with the overall frequency bands used in the communication systems, and this frequency diversity leads to the probability of detecting very slow-moving targets. Passive radar can cope with the problem of the sensors searching for the radar signals or locations. This is a contribution not only regarding military usage, but also commercial applications. In regular radar scanning, the passive radar does not send an electromagnetic signal out into the atmosphere, and can be regarded as a *green radar*. The number of communication channels utilised in the area is consistent due to the fact that there is no need for its frequency allocation. For the illustration, Fig. 1.1 shows the configurations of active radars with monostatic and bistatic, in contrast to the passive radar with bistatic configuration.

1.2 Problems and Motivations

Classically, passive radars have separate transmitters and receivers, namely Passive Bistatic Radar (PBR) [6]. A bistatic configuration can be handled more economically than its monostatic counterparts, provided that the concept can be combined with the passive paradigm. Recently, there has been a move to a multistatic configuration, where multiple differently-located transmitters are seen to illuminate a target and enhance the spatial diversity of the target's cross section, as well as provide greater resolution [7]. This idea may then be extended to that of the Multiple-Input Multiple-Output (MIMO) passive radar, where differently located transmitters illuminate a target whereas receive signals are

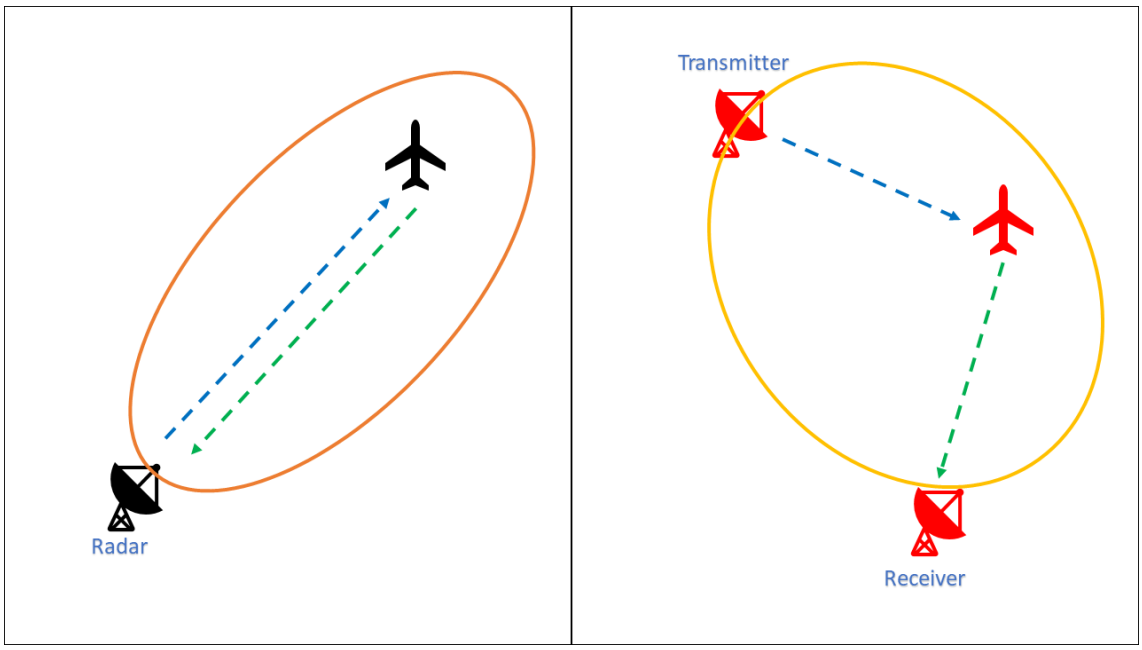

(a)

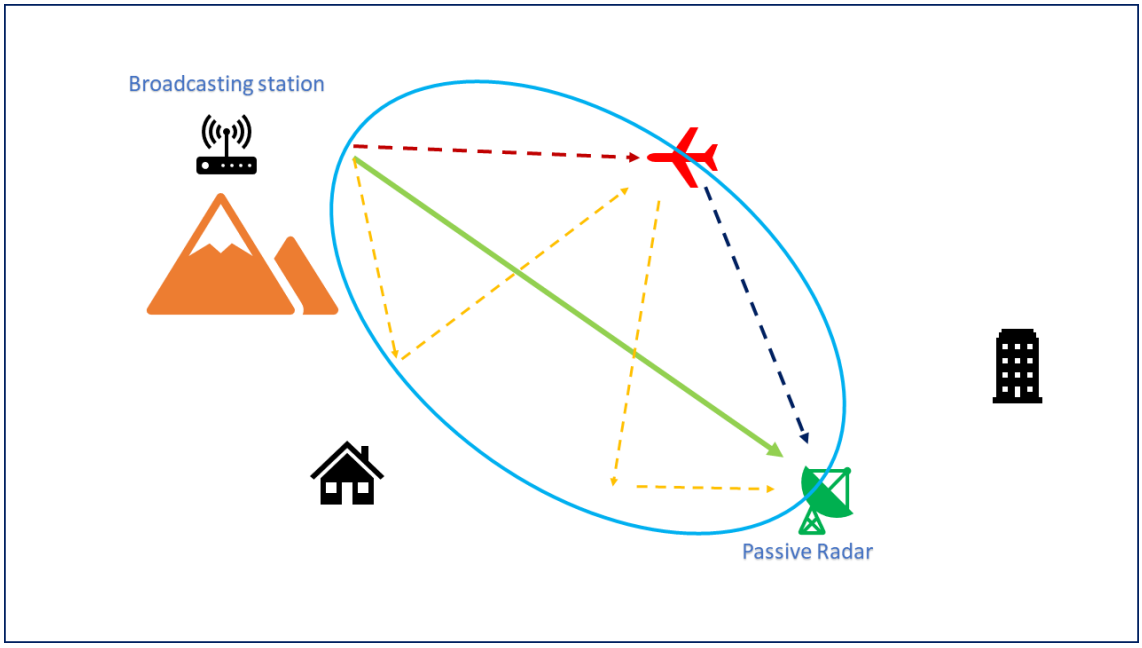

(b)

Figure 1.1: Configuration of (a) active radars with monostatic and bistatic; and (b) a bistatic passive radar.

detected using multiple receivers. One of the major obstacles in the passive radar signal processing is the cancellation of the direct signal. Hack et al. [8], [9] proposed the passive MIMO radar network, comparing the idea of centralised and decentralised Cross Ambiguity Function (CAF) processing. In [8], multichannel receivers are utilised, along with a generalized likelihood ratio and test statistic distributions. It has been shown that the measurement data affords more correlations and concludes that the quality of passive

radar depends on the direct-path signal. The author also dedicates one antenna for a reference (direct) signal, whereas the reference signal is declared as interference in [9]. It is accepted that state-of-the-art passive radar should use Orthogonal Frequency Division Multiplexing (OFDM) waveforms, which have been recently used in Digital Audio/Video Broadcasting (DAB/DVB), Wi-Fi and Worldwide Interoperability for Microwave Access (WiMAX) standards for local area wireless computer networking or Long-Term Evolution (LTE) for mobile communications as mentioned in [10]. The methods for data association in MIMO-OFDM passive radars have been discussed in [11], as it is possible that the transmitters send a nonorthogonal signal when they are operated in a single frequency network [12], [13]. A similar discussion is also displayed in [14] when a Multiple-Input Single-Output (MISO) system is mentioned inclusively.

This research aims to explore target detection in the OFDM passive radar. The problem of detecting targets is based on a Two-dimensional (2D) array of time delays and Doppler frequencies. In order to facilitate 2D parameter extraction in terms of time delay and Doppler frequency, the addition of closely-spaced receivers in the case of MIMO passive radar would, in fact, allow for Three-dimensional (3D) parameter extraction [15], because theAngle-of-Arrival (AoA) information also becomes evident. A key challenge here is how to make this 3D parameter extraction tractable from an algorithmic point-of-view. Another challenge with MIMO passive radar is that the device itself must listen to a clean copy of what is being transmitted, and this naturally means that the passive radar device must be placed near to a Base Station (BS). This creates the problematic effect that the clean BS signal copy is at high power, and could overwhelm the reception of the much weaker target-reflected signal copy. Thus, as an additional feature, some form of null steering/beamforming is required.

1.3 List of contributions

The details of contributions in this thesis can be explained as follows:

1. The results from the literature where compressive sensing is used to detect the target parameters of a two-dimensional channel estimates are extended by applying a multiple time samples algorithm and then deriving for MIMO-OFDM passive radars. The comparisons are performed through multiple samples Compressive Sensing (CS) and non-CS algorithms, as well as CS algorithms with a different number of snapshots.

2. The three dimensional matched filter is derived for the OFDM passive radars with MIMO using co-located antennas. This allows an increment of degree of freedom, and the angle of arrivals can be extracted to discriminate each path of the received signal, especially in a situation called single frequency network. The matched filter output is then related to the channel estimates, which can be expressed in CS representation. A spatial smoothing method is employed, and the sensing matrix for the CS algorithms is designed.

3. The 2D and 3D Cramer-Rao bounds presented in this work are specifically for the parameters of channel estimates which are also referred to the matched filter in the passive radar using OFDM waveforms only.

4. A Bayesian Compressive Sensing (BCS) method, based on an approach known as the Fast-BesselK method, can provide the exact degree of sparse sensing matrix performance as in the previous approaches, e.g. Basis Pursuit (BP) and L1-Singular Value Decomposition (l_1-SVD), but with greater computational efficiency. This thus renders the approach suitable for 3D parameter extraction. The results after applying the algorithm in this thesis demonstrate satisfaction.

5. With regard to the second key challenge of the null steering/beamforming compensation for the high power BS signal, it has been found that traditional techniques, such as Minimum Variance Distortionless Response (MVDR), do not work well with the proposed Fast-BesselK BCS method due to issues regarding the formation of the correlation matrix that would, in turn, perform the beam steering. As a result, this work proposes a novel BCS domain beamforming method to alleviate this problem. Throughout, the novel Fast-BesselK BCS based parameter extraction method and the novel BCS domain beamforming method are compared with previous approaches.

6. This thesis studies and presents the possibility of passive radar networks, using stochastic geometry to model and analyse the interference of the systems. The networks are modelled employing both bistatic and multistatic configurations which are similar to ad-hoc and cellular networks in communications. Stochastic geometry theory provides the derivation of interference statistical characteristics and the results are compared with simulations.

1.4 Outline of the thesis

The remainder of this thesis is organized as follows.

Chapter 2 begins with the discussion of passive radar block diagrams followed by OFDM signal characteristics in order to demonstrate the capability of radar signal application. In this chapter, Multiple Signal Classification (MUSIC) algorithm and compressive sensing techniques are compared. One time sample (Basis Pursuit) and multiple samples (l_1-SVD) are discussed as the candidates for a signal extraction scheme. Review of beamforming concept and stochastic geometry foundations are also discussed in this chapter.

Chapter 3 covers a modelling of the OFDM passive radar using widely spread antennas. System and signal models are examined, along with an explanation of target characteristics. The matched filter for multiple 2D channel estimates is derived. Basis Pursuit and l_1-SVD for multiple antennas are presented. Cramer-Rao lower bounds, which indicate the efficiency of the signal extraction module via the estimation errors of each parameter in the channel estimates, are derived for 2D version. The numerical simulations display an extension of [16] regarding the multiple time samples and multiple receivers.

Chapter 4 introduces the OFDM passive radar using co-located antennas, along with its system and signal model. The 3D matched filter is proposed. The problem in this thesis is formulated into compressive sensing representations using the formerly mentioned algorithms, along with the proposal of the Bayesian CS-based method. Three-dimension Cramer-Rao lower bounds are then derived. The application of beamforming to enhance the ability of target detection for compressive sensing measurements are discussed, and the proposed technique is compared with the Orthogonal Matching Pursuit (OMP) beamformer. The complexity of the relevent CS method is analysed in this chapter. This chapter concludes with the numerical simulations illustrating the comparison of methods discussed in this thesis, using different scenarios.

Chapter 5 studies the demonstration of interference using stochastic geometry. It starts by constructing the scenario of Ad-Hoc bistatic radar networks. Then, multistatic passive radars using cellular and heterogeneous networks are shown. Interference statistics are derived for all configurations mentioned in this chapter. The statistical behaviours of interference regarding their corresponding networks are displayed in the simulation results.

Chapter 6 summarises the most important conclusions drawn from the thesis, and proposes several research paths for future work.

Chapter 2

Literature review

In this chapter, the literature review is presented to provide some essential backgrounds regarding OFDM passive radar and related techniques. To address the possibility of the research area in passive radar, the first section displays its block diagram where all of the components show many interesting research aspects. Then, the OFDM signal is discussed, followed by an introduction to compressive sensing. In OFDM section, crucial information regarding the advantages of OFDM application is exhibited along with a discussion of MUSIC algorithm. In the CS section, basis pursuit and l_1-SVD, signal extraction methods which are demonstrated to make a comparison with MUSIC are then presented. This chapter also reviews the beamforming concept and stochastic geometry which are the necessary tools mentioned in chapter 4 and 5, respectively.

2.1 Components of the passive radar

This section reviews the concepts utilised by passive radar. The PBR system [6] typically applies at least two antennas with one antenna reserved for the direct (reference) signal. The system components, displayed in Fig. 2.1, can be described as follows.

1. *Data Collection Process*: In order to gather the required information, the PBR might encounter the problem of the direct signal. The ability of target detection decreases as the direct path maybe more than 50 decibels (dB) stronger than the reflections from the targets. It leads to the requirement of efficient cancellation methods. To reduce the strength of the direct component, the antennas may need steering away and then the analogue canceller can be implemented prior to the sampling step. Moreover, cancellation can be achieved by analogue beamforming or even applying terrain features. Recent research claims that the fast block least

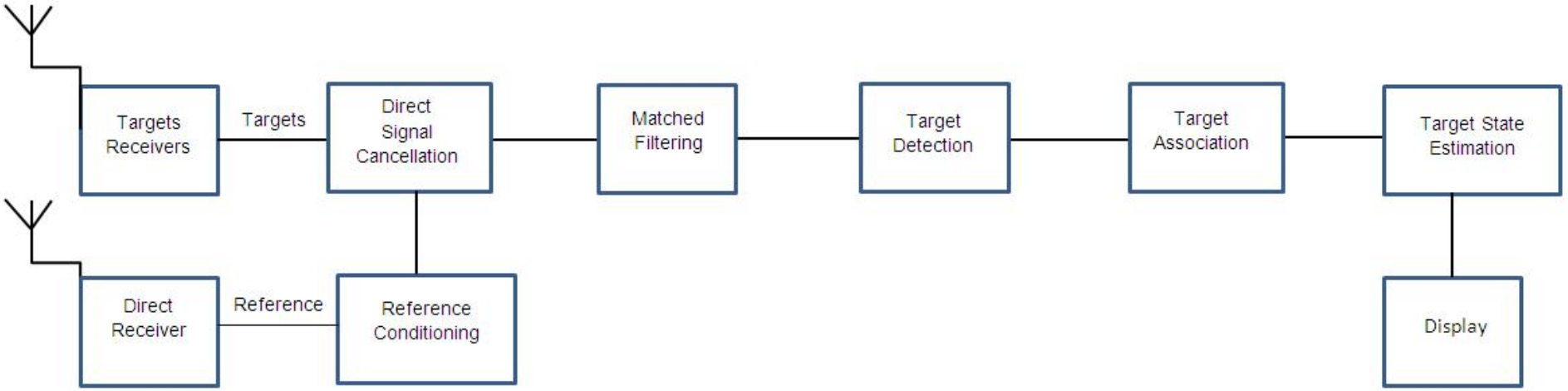

Figure 2.1: Block diagram of the passive radar.

mean squares filter is able to display good reference signal mitigation [17].

2. *Condition on the reference signal*: The matched filtering is performed by correlating the reference and the target signal. In consequence, the reference signal may be needed to be processed. This processing is crucial in a Single Frequency Network (SFN). Berger et al. [16] mentioned that the SFN, a network of broadcast stations transmits the signal in the same frequency band, can solve the problem of target localisation and tracking but it can result in multiple detections from a single target after correlating the signals. Then, the reference signal processing should exploit the multipath-resistant features of the Coherent Orthogonal Frequency Division Multiplexed (COFDM) waveform in order to regenerate it.

3. *Cancellation algorithms for direct signal and clutter*: After decreasing the effect of the direct signal, there is still the requirement of adaptive filtering in the time domain. Cherniakov [6] (cited in [18] for passive radar using the FM radio signal) referred to an adaptive noise canceller which utilise the reference signal to approximate the noise in the target signal and eliminate it. Another example, Berger et al. [16] suggested that significant leakage into the nonzero Doppler bins, which is caused by the clutter as the shape of the ambiguity function is similar to a *sinc* function, can be limited by the removal of the direct signals using adaptive signal processing on the digital data. The received signal employs least-squares fitting to a template assuming no time variation of an insufficient degree of change.

4. *The matched and mismatched filter*: The Doppler-shifted version of the reference signal is correlated with the target signal for every probable Doppler frequency. There are two objectives of the matched filter. Firstly, in order that target can be detected, adequate signal processing gain needs to be above the noise floor. Secondly, the bistatic range and bistatic Doppler shift of the target signal needs evaluating. The derivation of the matched filter used in the OFDM passive radar is displayed in Section 3.2.4 for a 2D version and 4.2.2 regarding a 3D version. For the competent approach, the assumptions that the targets will not exist at every possible Doppler shift or will only be seen at delays of the order of 2 milliseconds (ms) can be applied.

   The matched filter is the optimal choice of receiver filter for maximization of the received Signal-to-Noise Ratio (SNR). Conventionally, the matched filtering pro-

cess is based on correlating all the possible transmit waveforms with the received waveform. In the case of MIMO passive radar, the transmitted waveform is ascertained by listening to a nearby BS, thus by time-reversing and conjugating the transmitted waveform, $h(\hat{\tau}) = \alpha_m x^*(T_{max} - \hat{\tau})$, the matched filtering process may be written as:

$$z(\hat{\tau}) = \int_{-\infty}^{\infty} y(t)h(\hat{\tau} - t)dt$$

$$= \alpha_m \int_{-\infty}^{\infty} y(t)x^*(t + T_{max} - \hat{\tau})dt. \tag{2.1}$$

where α_m is an arbitrary real positive constant, T_{max} denotes the time at which maximum SNR occurs and the conjugation of the transmitted signal is represented by x^*. Contrast to the matched filter, [19] presented the mismatched processing with the reference signal alteration. The cross-correlation output was interested in order to diminish the pilots influence. Demodulation and remodulation of the reference signal were cautiously formed in consideration of clutter suppression and noise reduction. Briefly, a standards-based Digital Video Broadcasting - Terrestrial (DVB-T) demodulator was applied in the first demodulation to acquire an error-free copy. Next, the copy was remodulated and compared with unprocessed reference signal to calculate the subtle phase offset. Two remodulation mechanisms were employed with the error-free digital data. For adaptive clutter cancellation in the surveillance signal, full-power pilots were applied to produce a clutter-free and noise-free reference signal while pilot attenuation was used in a mismatched reference. Mismatched reference signal was built up by remodulating the error-free data and also adjusting the amplitude of the pilot symbols. This weakened the amplitude of the pilots in the mismatched signal. This method decrease ambiguity peaks as well as the main zero-delay, zero-Doppler peak.

5. *Detection of the target*: Providing that the adaptive signal processing be achieved and the direct signal leakages are discarded, target detection can be accomplished by determining the peak signal in the correlation surface over the threshold along with a Constant False Alarm Rate (CFAR) algorithm [20].

6. *Association of the target*: In this stage, a standard Kalman filter can be employed to analyse the range, Doppler shift and Doppler rate as well as bearing angle and bearing rate, recently shown in [21] . For better capability in detecting target motion, the Interacting Multiple Model (IMM) technique [22] can be used.

7. *Estimation of the target state*: The process is similar to the Extended Kalman Filter (EKF) [23]. However, more accurate estimation can be provided if the stage of the target association and the target state estimation can be combined. The challenge in this stage is when multiple transmitters are used, and the system needs to associate the target signals from different senders especially where false alarms and missed detections exist. One solution is to distinctively associate the targets from each transmitter and affiliate the tracks from each respective transmitter.

It can be concluded that each part of passive radar demands a challenging research, which involves modern signal processing concepts. For instance, MIMO radar [24] can be applied for the improvement of targets recognition. Compressive sensing in the target detection can be used if sparse signal representation is achieved. In addition, [25] [26] suggest a promising filter to associate and estimate the targets. Before developing the performance of passive radar system, it is important to understand the passive radar transmit signals. It is discussed in the next section.

2.2 OFDM waveforms in radar

Due to the fact that the operated signals are not distinct from the commercial signals, the activity of passive radar may not need additional transmit power. Currently, wireless internet and mobile communications are functioned with the OFDM signals, whose orthogonal characteristic between subcarriers is used to reduce the intersymbol interference and increase the bandwidth efficiency. Further, the OFDM signals can be generated efficiently with the Fast Fourier Transform (FFT). As a result, passive radar equipped with OFDM signal has become an area of significant interest within the target detection research.

2.2.1 Characteristics of OFDM waveforms

There are many arising trends for modern communication technology which employ the OFDM [27]. Inevitably, passive radar needs to be concerned with this new architecture in order to successfully exploits its signal. In OFDM, the applicable channel bandwidth is isolated into subbands. The Intersymbol Interference (ISI) in OFDM system could be imperceptible as the channel frequency response is necessarily consistent across each subband with sufficiently narrow interval (Δf). Orthogonality over the symbol interval accomplishes by marking the symbol rate in each of the subchannels to be equal to the

frequency disengagement of the neighbouring subcarriers. OFDM subcarriers may employ M-ary Quadrature Amplitude Modulation (QAM) and the signal can be declared as:

$$u_k(t) = \sqrt{\frac{2}{T}} A_{ki} \cos 2\pi f_k t - \sqrt{\frac{2}{T}} A_{kq} \sin 2\pi f_k t, \tag{2.2}$$

where A_{ki} and A_{kq} are in-phase and quadrature-phase components of the signal point QAM respectively. Given T is the OFDM symbol interval as well as f_k is the frequency at the kth subcarrier, the received signal can be:

$$y_k(t) = \sqrt{\frac{2}{T}} |C_k| A_{kc} \cos(2\pi f_k t + \phi_k) - \sqrt{\frac{2}{T}} |C_k| A_{ks} \sin(2\pi f_k t + \phi_k) + n_k(t). \tag{2.3}$$

There are two channel parameters, $|C_k|$ and ϕ_k, which are normally assumed to be known at the receiver. Relying on awareness of the carrier phase at the receiver, the demodulation will be achieved by cross-correlation between $y_k(t)$ and the two basis functions. As a result, a parallel bank of 2N cross-correlators is expected. This leads to the use of the more effective FFT algorithm due to the fact that the calculation of the DFT and its inverse is comparable to the operation of the modulator and the demodulator. Regarding an FFT algorithm implementation, the data flow is divided into frames of N_f bits by a serial-to-parallel buffer and then are decomposed into $\tilde{N}$ groups. The complex-valued signal points corresponding to the information symbols on the subcarriers can be denoted by X_k. A time series collected after reckoning the $\tilde{N}$ -point IDFT of X_k may not be identical to $\tilde{N}$ QAM-modulated subcarriers. Proakis [1] suggests devising $N = 2\tilde{N}$ information symbols by explaining that:

$$X_{N-k} = X_k^*, \qquad k = 1, \ldots, \tilde{N} - 1. \tag{2.4}$$

To avert ISI, each block of N signal samples can apply a cyclic prefix (CP). CP is attached to the inception of each block. The inclusion of the cyclic prefix to the block of data broadens the length of the block to N+v samples, which may be indexed from $n = -v, \ldots, N-1$.Then if the sampled channel impulse response can be designated by $\{C_n, 0 \leq n \leq v\}$, its convolution with $\{X_n, -v \leq n \geq N-1\}$ delivers the received sequence $\{y_n\}$ which are interesting in the samples for $0 \leq n \leq N-1$, from which the N-point DFT modulation can reclaim the transmitted sequence. The diagram of OFDM symbols generation employing the DFT is shown in Fig. 2.2.

However, the OFDM signal along with multipath channel estimates produces high complexity at the receiver. In this context, Palmer et al. [19] has proposed the ambiguity function analysis for the passive radar employing DVB signals to estimate the channels

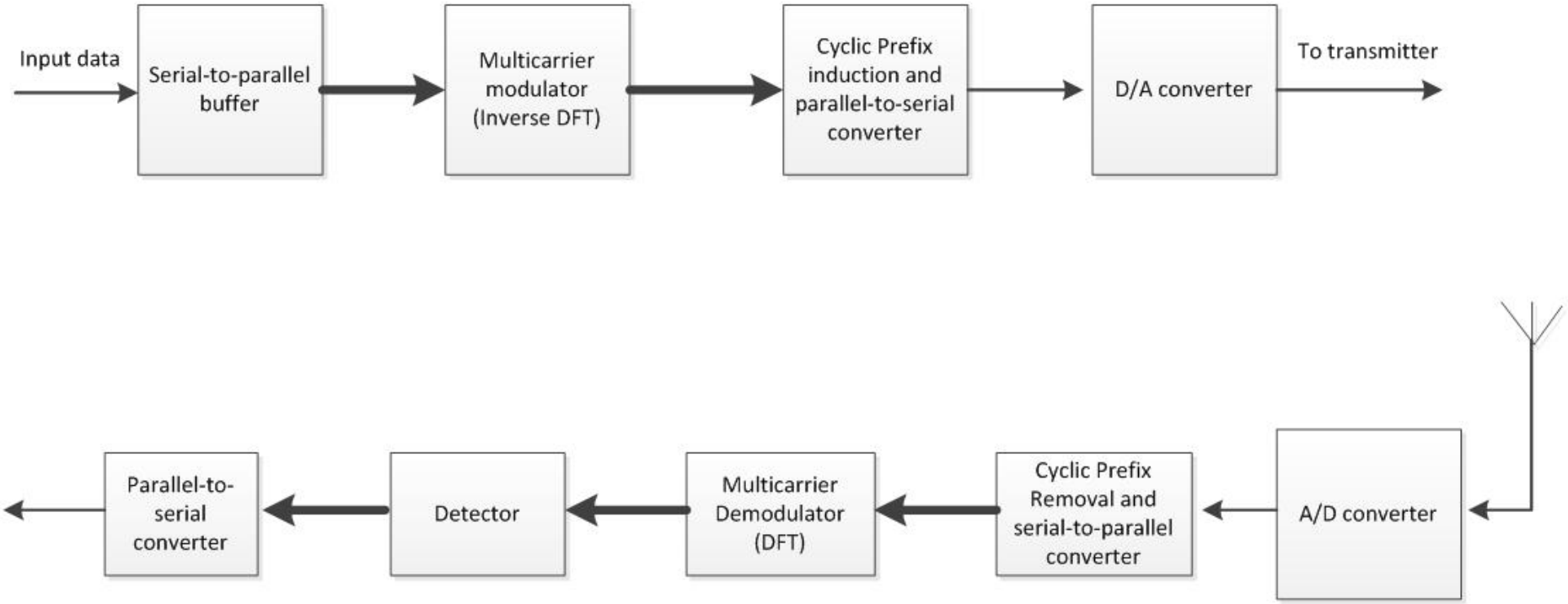

Figure 2.2: An FFT algorithm Implementation of an OFDM system. [1]

and reduce the effect of the clutters. Moving-target detection via moving platform can be found in [28] using Space Time Adaptive Processing. There are also some interesting applications of the OFDM passive radar demonstrated on a passive Synthetic Aperture Radar (SAR) [29] and the employment of Probability Hypothesis Density filter in the OFDM passive radar for multi-target tracking is demonstrated in [25]. To emphasise the target detection problem, this work reviews the OFDM passive radar developed by Berger et al. [16], where the channel estimates are efficiently implemented as fast Fourier transform and can be used directly for target detection. Berger et al. claimed a novel matched filter which is generally employed in radar systems by correlating the transmitted and received signal to determine the peak of delay-matched power. The first proposed signal extraction method is the MUSIC algorithm, which is normally used to identify the Direction of Arrivals (DOA). Chan et al. [30] has employed the MUSIC for DOA detection of ground moving objects. The other recently proposed detection method is compressive sensing which can achieve recovery of sparse signals along with a slower sampling rate than Nyquist's sampling theorem.

Table 2.1: DAB OFDM signal parameters [4]

Carrier frequency f_c	227.36 MHz
Bandwidth	32 or 128 kHz
Number of subcarriers N	32 or 128
OFDM data symbol length T	1 ms
Cyclic prefix length T_{cp}	0.25 ms
OFDM block length T'	1.25 ms
OFDM blocks/frame L	16 or 64
Subcarriers spacing Δf	1 kHz
No. Tx antennas n_t	2
No. Rx antennas n_r	9
Antenna Array Spacing d	$\lambda/2$

2.2.2 An example of OFDM signals

As this thesis discusses about passive radar employing OFDM signals as its source, the first simulation works on how to simulate the OFDM waveforms. Regarding the characteristic of the OFDM mentioned in Section 2.2.1, the algorithm can be presented as the following:

1. Generate a binary data vector;
2. Reshape the binary data into a symbol of k bits (where $k = \log_2 M$);
3. Proceed M-ary QAM modulation;
4. Separate the modulated data into OFDM blocks;
5. Operate inverse FFT over each block;
6. Attach cyclic prefix to every block.

The algorithm is performed in MATLAB environment [31] using the specifications in Table 2.1 which is modified from the DAB specifications displayed in [16]. The results of generation is shown in Fig. 2.3. In Fig. 2.3a, it can be observed that the signals on the right hand side (after 1 ms) are identical to the signal at the starting point on the left. This is the example of how the cyclic prefix is appended. In order to verify the creation of the OFDM, the demodulator is also implemented. The generated signals are passed through the Additive white Gaussian noise (AWGN) channel (built-in function in MATLAB). Then, the OFDM demodulator is operated to retrieve the symbols sent by the transmitter followed by the calculation of Bit Error Rate (BER). The result is displayed in the plot in Fig. 2.4 which is the illustration of the BER and the Energy per bit to Noise Power Density ratio (Eb/No). The simulations have been altered in the number of bits per symbol used in the QAM modulation. Passive radar is an important technology for facilitating covert surveillance. Signals from DVB/DAB base stations, which employ OFDM, are collected and analysed using a correlation process. This allows for the extraction of a moving target's parameters as a result of the fact that there is a signal making a direct path from a BS to the passive radar device along with other signals that are reflections from the target itself to the passive radar device. As well as offering covert surveillance, due to the fact that the signals used can not be distinguished as traditional radar monitoring activities,

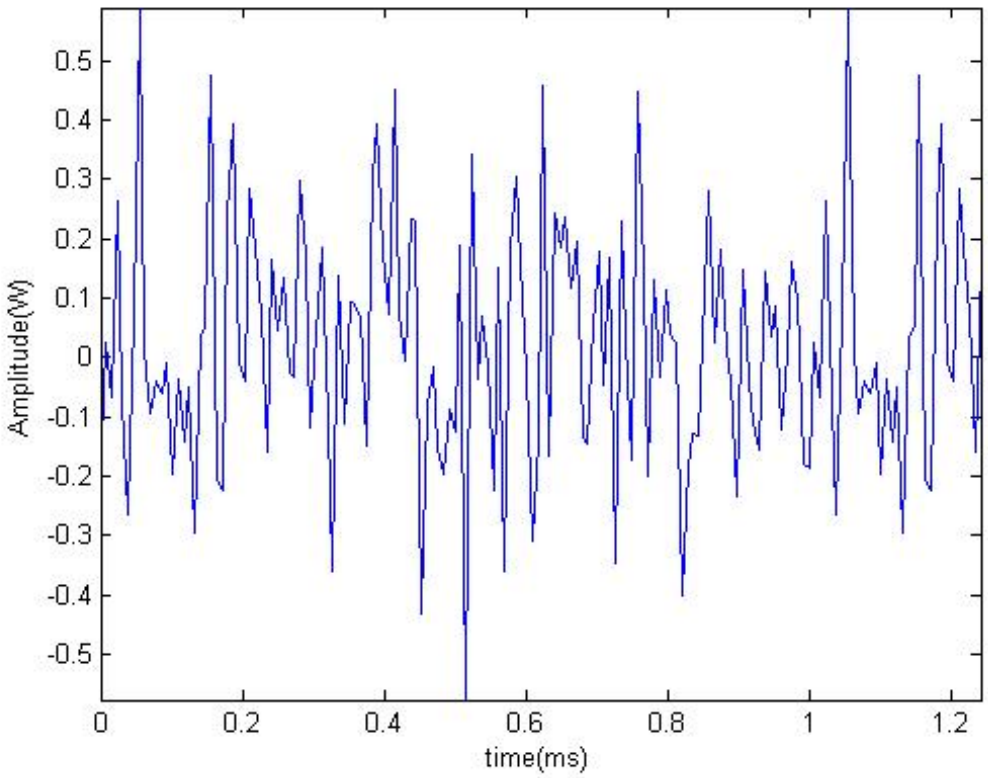

(a)

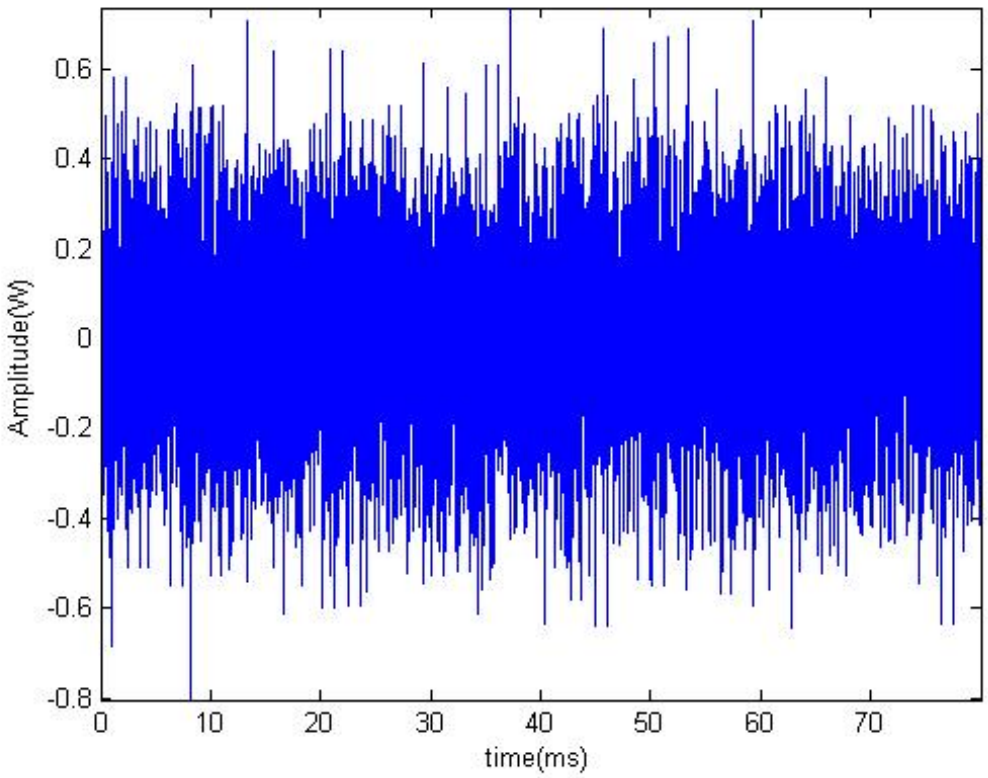

(b)

Figure 2.3: Simulation of the OFDM signals generation in: (a) one block; and (b) 64 blocks.

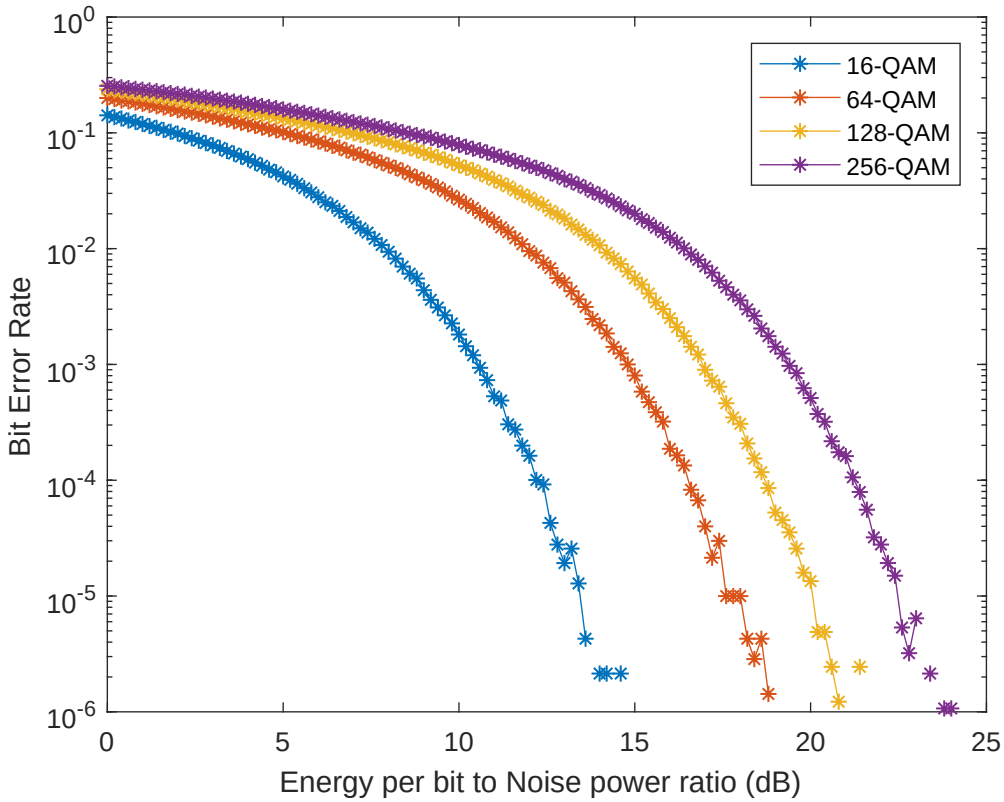

Figure 2.4: The plot of Bit Error Rate versus the energy per bit to noise power ratio for the OFDM demodulation process.

this technology also inherently does not demand spectrum allowance. Furthermore, there is also no requirement for transmitter design. However, these advantages must be traded off against high complexity receiver design.

The information in this section signifies that the OFDM signals can be effectively implemented and utilised in communication systems. With the radar applications; however, this multicarrier transmission can cause more complexity for the multipath channel. As the derivation of the OFDM channel estimates is challenging, it affects the ability of targets detection. There are a number of detection algorithms and this research has tried to find the optimum solution for the passive radar. Regarding the detection methods applying MUSIC algorithm, it is explained in general concepts in the next subsection.

2.2.3 Introduction to MUSIC algorithm

Subspace Algorithm

Due to the fact that whenever the received waveform incorporates N_p plane-wave signals plus uncorrelated noise, the problem could be lessened directly from an N-dimensional problem to a N_p-dimensional problem. The signal subspace is able to be completely

provoked because the angles of arrival of the N_p signals are known. An analogous result detained for correlated noise, assuming that the spectral matrix of the noise is known. The narrowband snapshot in the frequency-domain model can be utilised as:

$$S_x = V(\psi)S_f V^H(\psi) + \sigma_w^2 I, \tag{2.5}$$

where

$$V(\psi) = [v(\psi_1)|v(\psi_2)|\ldots|v(\psi_{N_p})]. \tag{2.6}$$

The matrix can be addressed in terms of its eigenvalues and eigenvectors which are assumed to be in order of declining size. As there are N_p signals, the first N_p eigenvalues are assigned to the signal-subspace $(\hat{U}_S)$ along with their eigenvectors. The remaining eigenvectors characterize a noise subspace $(\hat{U}_W)$. In practice, the eigenvalues and eigenvectors may be not known and might be deduced from the data. There are two prevalent steps in diverse subspace algorithms. First, signal and noise subspace need working out. Note that N_p should have already assessed. Second, a null spectrum function $\hat{Q}(\psi)$ will be ciphered and cast the N_p minima of $\hat{Q}(\psi)$. The reciprocal values of ψ are the $\hat{\psi}_i$, $i = 1,2,\ldots,N_p$. Obviously, $\hat{Q}(\psi)$ is a one-dimensional function so that exploring over a N_p-dimensional space to find ψ is no longer needed [32].

MUSIC Algorithm

The MUSIC is the technique employed to estimate the parameters of multiple signals arriving at an antenna array, exploiting the measurements of the received waveforms. Assuming that the number of incident signals is not larger than the number of array elements, the subspace algorithm can be used. Involving signal and noise eigenvectors subspace, the One-dimensional (1-D) MUSIC algorithm is developed by Schmidt in [33]. In the case of spectral MUSIC, $\hat{Q}(\psi)$ is asserted in terms of the eigenvectors of the noise subspace as:

$$\hat{Q}_{MU}(\psi) = v^H(\psi)\hat{U}_W\hat{U}_W^H v(\psi), \tag{2.7}$$

equivalently, in terms of the eigenvectors of the signal subspace as:

$$\hat{Q}_{MU}(\psi) = v^H(\psi)[I - \hat{U}_S\hat{U}_S^H]v(\psi). \tag{2.8}$$

The advances in the algorithm are (i) either signal or noise subspace is enumerated using the singular value decomposition (SVD) procedure. (ii) $\hat{Q}_{MU}(\psi)$ will be plotted over $-\pi \leq \psi \leq \pi$ and the N_p minima are elected. There are some asymptotically unbiased estimations which can be supplied by MUSIC, i.e. the number of incident wavefronts, the direction of arrival, the strengths and cross correlations among the occurrence

waveforms and the noise/interference strength. Schmidt [33] also suggested the special properties apart from general and wide application techniques which include the conventional interferometry, the monopulse direction finding using multiple colocated antennas and the multiple frequency estimation. Since S_x as well as $\hat{U}_W$ is asymptotically entirely determined, it is clear that MUSIC is asymptotically unbiased and $v(\psi)$ does not rely on the data. Shan et al. [34] introduced the eigenstructure technique which applies the overlapping subarrays. It was proved that if the number of subarrays is larger than or equal to the number of signals impinging on the antenna array, the modified covariance matrix of the signals will be nonsingular and this literature showed that the favourable means to this application is the nonsingularity of the covariance matrix of signals. In addition, if the covariance matrix of the sources is block diagonal, i.e. there are definite uncorrelated groups of coherent signals, the number of subarrays can be scaled down to the size of the largest group of coherent signals. The robustness of profitably handling the eigenstructure method, however, could diminish effective aperture as this application required the number of sensors to be at least double of the number of signals.

The above expressions are for the 1-D MUSIC algorithm. On the other hand, the target detection problem for the passive radar is a 2D problem, which involves the Doppler frequency and time delay. Berger et al. [16] have illustrated the derivation of the 2D MUSIC as:

$$f_{MUSIC}(\hat{\tau},\hat{a}) = \left(|\mathbf{b}^H(\hat{\tau},\hat{a})\mathbf{U}_W|^2\right)^{-1} \tag{2.9}$$

$$= \left(N'L' - |\mathbf{b}^H(\hat{\tau},\hat{a})\mathbf{U}_S|^2\right)^{-1}. \tag{2.10}$$

Implementations exploiting noise subspace and signal subspace are shown in (2.9) and (2.10) respectively. Berger et al. claimed that the interpretation of either (2.9) or (2.10) can be achieved with 2D FFT. This fundamental concept has also been applied in this research including the pseudo-code mentioned in Berger's paper. To implement the 2D MUSIC algorithm, first, the direct signal should be eliminated from the observation matrix by using high-pass filter or least-squares fitting the received data to a template assuming no time variation of a very limited degree of change. This work assumes that this step has been completed rather perfectly as the cancellation algorithm is beyond the scope of this thesis. Secondly, there is an observation matrix $\mathbf{R} = [\mathbf{h}_1, \ldots, \mathbf{h}_M]$ where $\mathbf{h}$ is from and M is the number of snapshots. An eigen-decomposition is calculated as shown:

$$\mathbf{R}^H\mathbf{R} = \mathbf{U}\Sigma\mathbf{U}^H. \tag{2.11}$$

The matrix of eigenvectors $\mathbf{U}$ has been sorted according to the eigenvalue in Σ. The number of eigenvectors and eigenvalues are then selected as the number of impinging signal paths N_p and $\mathbf{U}_p$ can be generated as $\mathbf{U}_p = [\mathbf{R}\mathbf{U}(:,1:N_p)\Sigma(1:N_p)]^{\frac{-1}{2}}$. Next, the channel estimates $\mathbf{h}$ is projected on the space orthogonal to the stationary components as the following:

$$\mathbf{h}_m = (\mathbf{I} - \mathbf{U}_p\mathbf{U}_p^H)\mathbf{h}. \tag{2.12}$$

The steering vector $\mathbf{b}$ is created from the resulted $\mathbf{h}_m$ and then formulate another observation matrix $\mathbf{R}_s = [\mathbf{b}^{(1)},\ldots,\mathbf{b}^{(K)}]$. The eigen-decomposition is applied to the subarray-version matrix before finding the matrix $\mathbf{B}_s = [\mathbf{U}_s(:,1:N_p)\Sigma_s(1:N_p)]^{\frac{-1}{2}}$. The MUSIC spectrum is finally computed by applying 2D-FFT on the multiplication between $\mathbf{R}_s$ and each column of $\mathbf{B}_s$ and then calculate the summation over all transformed results.

Next, the thesis focuses on one of the recent research topics, namely *Compressive Sensing*. This concept is applicable when the interested signal can be represented as a sparse signal and there is a proposal of this method to be used in the radar applications.

2.3 Passive radar in compressive sensing (CS) domain

With regard to the first challenge of algorithmic tractability, the emergence of sparse representation and CS concepts are influential in this work. The received passive radar signals are used to construct a sensing matrix provided that the matrix properties known as the Null-Space Property (NSP) and the Restricted Isometry Properte (RIP) of the sensing matrix can be ascertained, it then becomes possible to develop a sparse representation of the sensing matrix hence leading to more efficient parameter extraction algorithms. CS in corporate with OFDM has been employed in some intriguing researches such as [35], where CS along with OFDM waveforms application consistently matches a frequency agility approach. OFDM waveforms are accessible in an agile paradigm where the arrangement of OFDM is applied to each pulse. This work then provides common matched filter observation along with 1-D range profile and compares the proposed idea with the chirp signal where pulse compression is used. A compressive OFDM also authorises an operating adeptness of a Ground Penetrating Radar (GPR) [36], [37]. The fact that the synthesized pulse signal duty cycle is very low, introduces time sparsity. Additionally, the scatters of interests in GPR sensing are spatially sparse in the scanning area. In that work, CS with OFDM signal permits a reduced set of frequency tones regardless conceding precision and cross interferences between tones are underrated. The author also employs

L1-optimisation to reorganise a full spectrum characterisation. Sparse reconstruction along with convex optimisation is also utilised in Frequency Diverse Array (FDA) antenna [38], where a multi-carrier FDA practice creates a dot-shaped transmit to solve a defective target localisation in the range-angle dimension.

2.3.1 Emergence of compressive sensing

Due to the increasing requirement of high frequency communication, the sampling process may confront the resources constraint. The idea of compressive sensing (CS) is to sample the required signal slower than Nyquist's sampling theorem. Donoho [39] claimed that the signal reconstruction of $x \in \mathbf{R}^n$ can be accomplished via compressive sensing using only m number of measurements where $m \ll n$, given that x is compressible or sparse. There are three crucial features showing the dissimilarity between compressive sensing and classical sampling as follows [40]

1. infinite-length, continuous-time signals are likely to be commonly recognised by sampling theory while finite-dimensional vectors in $\mathbf{R}^n$ measurement is attracted by a mathematical theory of CS,

2. measurements in the form of inner products between the signal and more general test functions are consistently achieved by CS systems instead of sampling the signal at particular points of time and

3. in order to rescue the initial signal from the compressive measurements, *sinc interpolation*, a linear process that demands slight calculation and has a straightforward clarification, is employed in the Nyquist-Shannon framework. In contrast, highly non-linear methods are necessary for CS.

One of two important prospects of CS is sparse representation. This is to mathematically convey a signal $\mathbf{u}^0$ as:

$$\mathbf{u}^0 = \sum_{i=1}^{p} \psi_i x_i^0 \tag{2.13}$$

where all but a small number of entries x_i^0 are zero. $\Psi = [\psi_1 \psi_2 \dots \psi_p]$ is called a dictionary. Han et al. [41] mentioned that p is generally chosen as 1 and 2, and $\|y\|_p$ is illustrated as $(\sum_i |y_i|^p)^{\frac{1}{p}}$. The other aspect is CS encoding and decoding. The signal $\mathbf{u}^0 = \Psi \mathbf{x}^0$ is encoded to $\mathbf{b} = \mathbf{A}\mathbf{u}^0$ where $\mathbf{A}$ is a sensing matrix with an orthogonal basis Φ. There is a concept of *coherence* determining the kind of matrix $\mathbf{A}$ that allows the recovery of $\mathbf{u}^0$

from $\mathbf{b} = \mathbf{Au}$ given that $\mathbf{x}^0$ is sparse or nearly sparse. The coherence between the basis Φ and the basis Ψ ,which quantifies how small the closest angle between any two elements of Φ and Ψ, can be displayed as:

$$\mu(\Phi,\Psi) = \sqrt{n} \max_{1\leq i,j\leq n} \frac{|\langle \phi_i, \psi_j \rangle|}{\|\phi_i\|_2 \|\psi_j\|_2}. \tag{2.14}$$

It can be shown that, for low coherence, $\mu(\Phi,\Psi)$ is much closer to 1 than $\sqrt{n}$, every measurement is able to offer a fruitful amount of information of all the non-zeros of $\mathbf{x}^0$ regardless their positions whereas the quality of measurements relies on the locations of the non-zeros of $\mathbf{x}^0$ if the coherence is high. As CS expects a sensing matrix $\mathbf{A}$ to be independent of any particular signal or its existing measurements, it is surprising to find that several kinds of random matrices satisfy the NSP and the RIP, with at least high probability up to proper scaling. This includes sensing matrices whose entries are independent and identically distributed (i.i.d.) samples from the standard normal distribution, symmetric Bernoulli distribution, as well as other sub-Gaussian distributions. Manifold structured random matrices also assure the RIP such as those formed by random rows collection of a discrete Fourier matrix, as well as random circulant or Toeplitz matrices.

2.3.2 Compressive sensing with a single time sample: Basis Pursuit (BP)

A compressive sensing method using a single time sample, *basis pursuit*, has been used in the scenario with one transmitter and multistatic receivers [42]. When the single time sample is studied and the parameter estimation problem is nonlinear, the aim of this is to approximate θ in the matrix $\mathbf{B}(\theta)$ which is unknown. An overcomplete exhibition $\mathbf{B}$ in terms of all possible parameter values is presented. The number of promising values N_θ is commonly higher than the total number of paths N_p or the number of receivers n_r where a sampling grid of all values can be denoted as $\{\tilde{\theta}_1,\ldots,\tilde{\theta}_{N_\theta}\}$. Matrix $\mathbf{B} = [\mathbf{b}(\tilde{\theta}_1),\mathbf{b}(\tilde{\theta}_2),\ldots,\mathbf{b}(\tilde{\theta}_{N_\theta})]$ consists of steering vectors reciprocal to each value as its columns. Regardless the true parameter values θ, $\mathbf{B}$ is known. Let $N_\theta \times 1$ vector $\mathbf{a}(t)$ describe the signal field. If the value of $\tilde{\theta}_n$ is corresponded to the parameter of the incoming signal path p, the n-th element, $a_n(t)$ becomes nonzero, and equal to the attenuation caused by that path A_p, and zero any other elements. The problem of parameter estimation of θ can be alternated with the problem of sparse spectrum estimation of $\mathbf{a}$ as a consequence of the overcomplete exhibition. For instance, the resolution produces an approximate of the signal energy by discovering superior peaks at the exact source locations included in a function of hypothesized source location as in numerous nonparametric source locali-

sation techniques [2]. With the assumption that the number of sources is small and they can be explored as point sources, the inverse problem of this sparse spatial spectrum can be clarified employing l_1 methodology. The evaluations of parameter values complement to the positions of the peaks in $\mathbf{a}$ after the algorithm achieves.

In order to detect the targets, the channel model according to the target problem, is modified as a sparse representation problem. Given $\mathbf{B}_{N_p}(\tilde{\theta}) = [\mathbf{b}(\tilde{\theta}_1)\dots\mathbf{b}_{N_p}(\tilde{\theta}_{N_p})]$ and $\mathbf{a}_{N_p} = [A_1\dots A_{N_p}]$, the basic narrowband observation model can be expressed as [2]:

$$\mathbf{h}(t) = \mathbf{B}_{N_p}(\tilde{\theta})\mathbf{a}_{N_p}(t) + \mathbf{w}(t), \tag{2.15}$$

where M snapshots are assumed, and $t \in \{t_1,\dots,t_M\}$. In order to focus on a single sample, the number of snapshots M is equal to 1. Being aware that $\mathbf{a} = \mathbf{a}_{N_p}(t)$ is a sparse vector, the problem can be evolved into:

$$\min_{\mathbf{a}} \|\mathbf{h} - \mathbf{B}\mathbf{a}\|_2^2 + \lambda\|\mathbf{a}\|_1, \tag{2.16}$$

where λ denotes the regularisation parameter. In this case, however, $\mathbf{a}$ is a complex vector where its l_1-norm can be calculated by $\|\mathbf{a}\|_1 = \sum_{i=1}^{N_a}\left(\mathbf{Re}\{\mathbf{a}_i\}^2 + \mathbf{Im}\{\mathbf{a}_i\}^2\right)^{\frac{1}{2}}$ where the number of elements in $\mathbf{a}$ is denoted by N_a. Therefore, the problem cannot be computed employing an l_1-regularised least-squares program. The objective function in (2.16) is devised as:

$$\begin{aligned} &\min_{\mathbf{a}} \quad \left\| \tilde{\mathbf{h}} - \tilde{\mathbf{B}} \begin{bmatrix} \mathbf{Re}\{\mathbf{a}\} \\ \mathbf{Im}\{\mathbf{a}\} \end{bmatrix} \right\|_2^2 + \lambda \mathbf{1}^T \mathbf{u} \\ &\text{subject to} \quad \sqrt{\mathbf{Re}\{\mathbf{a}_i\}^2 + \mathbf{Im}\{\mathbf{a}_i\}^2} \le u_i, \quad i = 1,\dots,N_a \end{aligned} \tag{2.17}$$

where the function data are

$$\tilde{\mathbf{B}} = \begin{bmatrix} \mathbf{Re}\{\mathbf{B}\} & -\mathbf{Im}\{\mathbf{B}\} \\ \mathbf{Im}\{\mathbf{B}\} & \mathbf{Re}\{\mathbf{B}\} \end{bmatrix} \in \mathbb{R}^{2N_h \times 2N_a},$$

$$\tilde{\mathbf{h}} = \begin{bmatrix} \mathbf{Re}\{\mathbf{h}\} \\ \mathbf{Im}\{\mathbf{h}\} \end{bmatrix}. \tag{2.18}$$

which is a Second-Order Cone Program (SOCP) problem. The algorithm applied to this problem is found on an interior point method using approximate Newton search directions [43]. The l_1-regularised least-squares programs with complex variables is utilised in this thesis as the elements of the sensing matrix Φ and the sparsity basis Ψ are complex and

the real and imaginary parts of the matrices are not spread. The dictionary matrix $\mathbf{B}$ is a matrix with complex elements, where $\mathbf{B} = \Phi\Psi^{-1}$. The optimal result using this method conduces more simultaneous zero real and imaginary elements in the output than the complex-extended algorithm since its institution jointly buckles the real and imaginary parts of the expected matrix. The logarithmic barrier applied in the interior-point method for the enclosed constraints $-u_i \leq x_i \leq u_i$ can be characterised as:

$$\Delta(x,u) = -\sum_{i=1}^{n} \log(u_i + x_i) - \sum_{i=1}^{n} \log(u_i - x_i) \tag{2.19}$$

within the domain of Δ, that is $\{(x,u) \in \mathbb{R}^n \times \mathbb{R}^n | |x_i| < u_i, i = 1,\ldots,n\}$. Let $\Delta(\mathbf{Re}\{\mathbf{a}\}, \mathbf{Im}\{\mathbf{a}\}, \mathbf{u})$ be the barrier function for the constraint of (2.17) as shown:

$$\Delta\left(\mathbf{Re}\{\mathbf{a}\}, \mathbf{Im}\{\mathbf{a}\}, \mathbf{u}\right) = -\sum_{i=1}^{N_a} \log\left(u_i^2 - (\mathbf{Re}\{\mathbf{a}_i\})^2 - (\mathbf{Im}\{\mathbf{a}_i\})^2\right). \tag{2.20}$$

The associated centering problem applying the standard barrier function for second-order cone constraints can be expressed as:

$$\min_{\mathbf{a}} \mathscr{T} \left\| \tilde{\mathbf{h}} - \tilde{\mathbf{B}} \begin{bmatrix} \mathbf{Re}\{\mathbf{a}\} \\ \mathbf{Im}\{\mathbf{a}\} \end{bmatrix} \right\|_2^2 + \mathscr{T}\lambda \mathbf{1}^T \mathbf{u} + \Delta\left(\mathbf{Re}\{\mathbf{a}\}, \mathbf{Im}\{\mathbf{a}\}, \mathbf{u}\right). \tag{2.21}$$

The preconditioner that estimates the Hessian of the first term in the objective of the centering problem (2.21) with its diagonal items can be shown as:

$$\mathscr{P} = \mathscr{T} diag(\tilde{\mathbf{B}}^T \tilde{\mathbf{B}}) + \nabla^2 \Delta\left(\mathbf{Re}\{\mathbf{a}\}, \mathbf{Im}\{\mathbf{a}\}, \mathbf{u}\right), \tag{2.22}$$

while the Hessian of the logarithmic barrier is preserved. The preconditioner becomes a block diagonal matrix where N_a 3×3 matrices are contained after the suitable interchanging. The Hessian of the problem mentioned above is as follows:

$$\mathscr{H} = \mathscr{T}\tilde{\mathbf{B}}^T \tilde{\mathbf{B}} + \nabla^2 \Delta\left(\mathbf{Re}\{\mathbf{a}\}, \mathbf{Im}\{\mathbf{a}\}, \mathbf{u}\right). \tag{2.23}$$

Regarding the determination of the centering problem (2.21), the proconditioner shown above performs rather productively. Equation (2.16) shows the compressive sensing for a single snapshot using basis pursuit. For some applications, multiple snapshots can provide correlation between sources. To enable target detection, this problem is a bit more difficult than a single snapshot case. One promising solution employs the SVD to achieve correlation between snapshots and reduce computation complexity, namely l_1-SVD [2].

2.3.3 *Compressive sensing with multiple time samples: l_1-SVD*

To determine each problem ordered by t individually is the first choice when converting to multiple time samples. The number of outcomes, $\hat{\mathbf{a}}(t)$, is M. This method is proper when considering the fast-moving sources. However, integrating the liberated estimates $\hat{\mathbf{a}}(t)$ to get one ideal estimate of the values is preferred if the sources are immobile over time samples. Although its directness is its principal interest as it is noncoherent processing, to accomplish better precision and vitality to noise, the sufficiently coherent integrated processing is required.

An understandable proposal that applies dissimilar time samples in collaboration is considered in joint-time inverse problem. Define $\mathbf{H} = [\mathbf{h}(t_1), \ldots, \mathbf{h}(t_M)]$, and identical to $\mathbf{A}$ and $\mathbf{W}$, it can be shown that:

$$\mathbf{H} = \mathbf{BA} + \mathbf{W}. \tag{2.24}$$

As the signal $\mathbf{a}(t)$ is not ordinarily sparse in time, sparsity is only implemented in space although matrix $\mathbf{A}$ is parameterised temporally and spatially. A distinctive prior is appointed to serve this problem. First, sparsity in the spatial dimension is desired but sparsity in time is not needed. The algorithm is as follows: the l_2-norm of all time-samples of an appropriate spatial index of $\mathbf{a}$ is first computed as $a_i^{(l_2)} = \|[a_i(t_1), a_i(t_2), \ldots, a_i(t_M)]\|_2$. After the l_1-norm of $\mathbf{a}^{(l_2)} = [a_1^{(l_2)}, \ldots, a_{N_\theta}^{(l_2)}]$ is penalized, the cost function can be displayed as:

$$\min \|\mathbf{H} - \mathbf{BA}\|_f^2 + \lambda \|\mathbf{a}^{(l_2)}\|_1, \tag{2.25}$$

where $\|\mathbf{H} - \mathbf{BA}\|_f^2 = \|\mathrm{vec}(\mathbf{H} - \mathbf{BA})\|_2^2$. As $\mathbf{a}^{(l_2)}$ is a function of $\mathbf{A}$, the optimisation is executed over $\mathbf{A}$. There is no sparsifying consequences on the 2-norm of the time-samples aggregation. Sparsity is invoked on the composition of the spatial samples. Due to the fact that the greater penalty is caused by the fact that supports of $\mathbf{a}(t)$ for particular t do not accurately organise, the diverse time-indices of $\mathbf{a}$ strengthen each other. Calculation cost is the major disadvantage of this algorithm. Whereas the size of the inverse problem advances linearly with M, The enhancement in the demanded computational exertion is much greater. The solution of the real-time system is not practicable when the number of time samples is extensive.

In order to compare with the MUSIC, the expression introduced in Section 2.3.2 may not be enough due to only one time sample. To realise the real system, multiple time samples technique is required. The application of sparse signal representation for practical problems is broadened due to a utilisation of a large number of coherent time samples.

The concept is retaining the signal subspace after disintegrating the data matrix, and the multiple-sample sparse spectrum estimation problem reviewed above is employed along with a curtailed-dimensions problem. On the other hand, the MUSIC algorithm usually preserves the noise subspace. The singular value decomposition (SVD) of the $N_h \times M$ data matrix at the receiver $\mathbf{R} = [\mathbf{h}(t_1) \cdots \mathbf{h}(t_M)]$ is applied for a degradation of the computational complexity and the sensitivity to noise. Recall that N_p is the number of path whose parameter values are expected. The set of vectors $\{\mathbf{h}(t_i)\}_{i=1}^{M}$ would stretch into a N_p-dimensional subspace provided that the noise on the receivers is eliminated. Sparse connections of columns of $\mathbf{B}$ are approximated by maintaining N_p basis vectors for the subspace instead of M. In order that the M-dimension data matrix is reduced to N_p-dimension as the signal and noises subspaces are separated by the SVD and a basis for the signal subspace is deposited; that is:

$$\mathbf{R} = \mathbf{ULV}'. \tag{2.26}$$

It results in the reduced dimensional matrix $\mathbf{R}_{SV} = \mathbf{ULD}_{N_p} = \mathbf{RVD}_{N_p}$, which remarkable signal power is included and $\mathbf{D}_{N_p} = [\mathbf{I}_{N_p}\mathbf{0}']$. $\mathbf{I}_{N_p}$ is an identity matrix with the dimension $N_p \times N_p$ and $\mathbf{0}$ is a matrix of zeros with the dimension $N_p \times (M - N_p)$. Define $\mathbf{A}_{SV} = \mathbf{AVD}_{N_p}$ and $\mathbf{W}_{SV} = \mathbf{WVD}_{N_p}$, it can be shown that:

$$\mathbf{R}_{SV} = \mathbf{BA}_{SV} + \mathbf{W}_{SV}. \tag{2.27}$$

The column conforms to a signal subspace singular vector is determined as follows:

$$\mathbf{h}_{SV}(p) = \mathbf{Ba}^{SV}(p) + \mathbf{w}^{SV}(p), \quad p = 1, \ldots, N_p. \tag{2.28}$$

Apart from the singular vector number indexing instead of time, the equation above resembles (2.15). The main difference of this method from the one mentioned above is the decline of the size of the problem. If the number of time samples is in the order of hundreds while the number of incoming paths is small, this complication decline is considerable. In order to enforce sparsity in the matrix $\mathbf{A}_{SV}$ only in the spatial dimension but not in the singular vector index p, l_2-norm of all time-samples ($\tilde{\mathbf{a}}^{(l_2)}$) is set, where each element is the l_2-norm of the column vector of A_{SV}, i.e. $\tilde{\mathbf{a}}^{(l_2)} = \sqrt{\sum_{p=1}^{N_p}(a_i^{SV}(p))^2}, \forall i$. The sparse spectrum, which is expressed by the derived $N_a \times 1$ vector of $\tilde{\mathbf{a}}^{(l_2)}$, can be determined by:

$$\text{minimize} \|\mathbf{R}_{SV} - \mathbf{BA}_{SV}\|_f^2 + \lambda \|\tilde{\mathbf{a}}^{(l_2)}\|_1, \tag{2.29}$$

and then the minimization is performed by Second-Order Cone (SOC) programming displayed in [2] for the details.

As seen in this section, compressive sensing provides a reduced dimension problem. Start by designing the overcomplete matrix where all possible parameter values are illustrated. Both basis pursuit and l_1-SVD decrease the size of the measurement matrix by sub-Nyquist sampling. The performances of these algorithms are displayed in the next chapter to confirm the ability of signal extraction without sensing all of the data existed in the scenario.

2.4 Beamforming methods

In communication systems, the beamforming algorithm is also one of the interesting area of research. The famous adaptive beamformer is shown in [44], where cyclostationary characteristic of the communication signals was used for the accretion of the channel capacity and co-channel interference abolition. In the literature, a method, namely, blind cyclic adaptive beamforming displayed impressive results in spatial reuse of frequency spectrum. In the scenario of satellite and terrestrial networks coincidence [45], transmit beamforming is also applied. To magnify the Signal-to-Interference plus Noise Ratio (SINR) favouring the desired terrestrial downlink signal and lighten the interference against the satellite terminals, Linearly Constrained Minimum Variance (LCMV) is presented. This beamformer does not require the prior information about the precise positions and the number of satellite terminals. Transmit beamforming is also discussed in [46], where the transmitters send the identical data with various amplitudes and phases to achieve high signal power. The transmitted signal components are designed to be summed destructively at the unexpected users. Expected users acquire large inner products while unexpected users acquire small inner products of the beamforming and the channel vectors. In order to provide conditions for interference aligning in a subspace orthogonal to the desired signals, beamforming technique is also presented in [47] to maximise degrees of freedom in compounded MIMO broadcast channel with mixed classes of users. Another example of recent beamforming application is shown in [48], where the uncertainty model in the channel state information is included. This literature presents low-complexity power loading algorithm to enhance the beamforming ability.

Bayesian Cramer-Rao bound (BCRB) is another metric used as the optimisation criterion for beampattern design [49]. In this literature, previous measurements are pro-

gressively regulated by the transmitters and the beamforming algorithm is utilised for the target tracking problem in a shallow underwater environment. Another type of array beamforming mentioned in the literature is the superdirective beamformers [50], where joint diagonalization method is proposed to improve the beamforming performance. Subspace superdirective beamforming algorithm is discussed in this literature and applied in the microphone arrays problem.

Convex optimisation in conjunction with beamforming was shown in [51] where interior-point methods were applied to synthesise the pattern of antenna array. This is appealing as the problems of convex synthesis and robustness can inclusively be conducted. In Millimetre Wave (mmWave) communications [52], alternate optimisation of transmit and receive beamforming vectors is used for the large-scale antenna system in the congested wireless communication. The product of the assertive singular values of the divided channel matrices is escalated to achieve capacity gain. In [53], a novel spatial diversity scheme for mmWave Radio Frequency (RF) beamforming is discussed where incomplete information of the channel to the receiver is supposedly known. The geometric mean of the projections of the RF precoder on the transmit steering vectors and of the RF combiner on the receive steering vectors are enlarged in the spatial diversity composition. Semidefinite relaxation and gradient ascent algorithm are utilised in this literature. Regarding the passive radar, optimisation with the beampattern is also employed in as in [54], where the circular-array antennas are equipped with digital beamforming, whereas the space-time beamformer relied on constrained least mean squares algorithm is displayed applying the recursively adaptive algorithm with multiple constraints [55]. The angle mismatch problem can also be coped with the method presented in this literature.

Capon beamforming is discussed in [56], where diagonal loading is involved to develop the beamformer performance, specially when the desired steering vector is unknown. It is claimed that the uncertainty set of the steering vector can provide an accurate amount of diagonal loading. In this thesis, a modified convex constrained optimisation and compressive sensing beamforming model is presented based on Capon beamformer. The passive radar received signal, which is sparse according to spatial smoothing technique, which will be introduced in Section 4.3.1, is reconstructed employing the BCS-based Fast-BesselK method. The purpose of using a beamforming algorithm is to reduce the power in the clean signal component, to which the passive radar device is listening, and which is being emitted from a nearby BS. It should be noted that throughout, the term 'beamforming' is used as a generic description of the technique that is being employed

but in actual fact, the process effectively steers a null to this clean BS signal course. Such techniques [57], [58], are able to demonstrate some impressive outcomes however they require a complete measurement of the received signal to create the correlation matrix upon which ultimately the beamsteering technique is based. Since the estimation relies on sparse (incomplete) data, a novel modified beamforming technique has been developed here in order to incorporate into the CS domain applying MUSIC algorithm where, in [59], the capability of MUSIC-based beamforming is compared with Bucci algorithm.

2.4.1 Compressive beamforming with Orthogonal Matching Pursuit

As the system considered can be operated under the dynamic scenario, the number of snapshots captured might be insufficient. This matches the concept of applying CS algorithm mentioned throughout this thesis since CS allows the reconstruction of the original signal using a sub-Nyquist sampling. Oppose to what is included in this work, the OMP algorithm is discussed here for the purpose of beamforming only. The reason that OMP is opted out from the OFDM passive radar is shown in [60] where it cannot resolve the problem of the direct signal leakages. Consequently, basis pursuit and Bayesian CS are covered due to their superior in accuracy. In this work, the Fast-Besselk method is also utilised for beamforming in the compressive domain. For comparison, OMP is discussed in the following regarding its advantage of low complexity [61].

Refer to the parameters in the OFDM passive radar, given a discretionary N_p-sparse signal, $\alpha \in \mathbb{R}^{N_\alpha}$, and a group of N_h measurement vectors, $\{\mathbf{x}_1, \ldots, \mathbf{x}_{N_h}\}$. A matrix $\mathbf{B}$ is assembled with a dimension of $N_h \times N_\alpha$ with the measurement vectors as its rows. An N_h-dimensional data vector after accumulation is shown as $\mathbf{h} = \mathbf{B}\alpha$. The columns of the measurement matrix $\mathbf{B}$ is designated by $\mathbf{b}_1, \ldots, \mathbf{b}_{N_\alpha}$. Recall that this thesis has not mentioned the measurement vectors but worked with the columns of the measurement matrix which is called *steering vectors*. The number of perfect data is $N_\alpha = N \times L \times N_\theta$, where N is the number of OFDM subcarriers, L is the number of OFDM blocks and N_θ is the number of possible angle of arrivals, whereas, the number of measurement vectors is $N_h = N' \times L' \times n_r$ where N', L' refer to the number of reduced subarrays in delay and frequency domain respectively, as well as the number of antenna arrays is n_r.

It can be considered that the data vector $\mathbf{h}$ is a linear combination of N_p columns from $\mathbf{B}$ and displays an N_p-term representation over the dictionary $\mathbf{B}$. OMP aims to resolve which columns of $\mathbf{B}$ engage in the measurement vectors $\mathbf{h}$ using a greedy manner. The

column of **B** which is most greatly connected to the remaining elements of **h** is selected at each iteration. The subtraction of its augmentation to **h** is performed followed by emphasising on the residual. The algorithm is expected to discover the precise set of columns within N_p steps.

From Algorithm. 1, Steps 5, and 6 can be more competently achieved. The columns of $\mathbf{B}_{t_i}$ are consistently orthogonal to the residual $\mathbf{r}_{t_i}$. The matrix $\mathbf{B}_{t_i}$ has full column rank and the algorithm chooses a new atom at iteration t_i if $\mathbf{r}_{t_i-1}$ is nonzero. It is worth marking that, in Step 6, the estimate and residual as well as $\mathbf{x}_{t_i}$ considered in Step 5 are distinctively concluded. There is a concern arose from the algorithm requirements above. The system needs to determine the sparsity in the perfect data, i.e. the number of nonzero values should be known. This is similar to the prior information of basis pursuit. In most scenarios, however, it is not easy to come across the sparsity as the number of base stations and targets might not explicitly display. To the contrary, l_1-SVD demonstrates that the small error in sparsity approximation does not affect the efficiency of the algorithm. The method which does not require the number of sparsity as a prior is the Fast-BesselK.

2.5 Introduction to stochastic geometry

2.5.1 Motivations

Apart from the diversity of multiple OFDM stations that will be determined in this thesis, the receiver diversity can accommodate a better target point of view as long as the interference that a system takes into account is accurately modelled. Regarding modern wireless communications, when interference is included in the system, the SINR is able to determine the network performance rather than the SNR. Furthermore, the path loss and the fading components are involved in the interference function and large wireless networks engage a high magnitude of uncertainty. Therefore, the previous analysis of the system-level performance and interference model for the communication networks was mathematically intractable.

However, this has been solved by an approach called *Stochastic Geometry*, where the network performance can be explicitly manipulated using the randomisation of transceiver locations. The objective of stochastic geometry in passive radar is to determine the effect of radar positions on the received target signal-to-noise ratio and whether or not clutter exists. The locations of OFDM stations are also significant and then the inclusion of reference signal might influence the efficiency of the radar receivers.

Algorithm 1 Orthogonal Matching Pursuit [61]

Require:

An $N_h \times N_\alpha$ measurement matrix $\mathbf{B}$

An N_h-dimensional data vector $\mathbf{h}$

The sparsity level N_p

Ensure:

$\hat{\alpha}$ is an approximate of the expected signal

A set Λ_{N_p} consisting of N_p elements of $1,\ldots,N_\alpha$

An N_h-dimensional estimate of $\mathbf{h}$, i.e. $\hat{\mathbf{h}}_{N_p}$

An N_h-dimensional residual $\mathbf{r}_{N_p} = \mathbf{h} - \hat{\mathbf{h}}_{N_p}$

1: Initialise $\mathbf{r}_0 = \mathbf{h}$, $\Lambda_0 = \emptyset$, and iteration counter $t_i = 1$.

2: **repeat**

3: Figure out the optimisation problem

$$\lambda_{t_i} = \underset{j=1,\ldots,N_\alpha}{\arg\max} \, |\langle \mathbf{r}_{t_i-1}, \mathbf{b}_j \rangle|.$$

Split the link of the results if various indices take place.

4: Given that $\mathbf{B}_0$ is an empty matrix, expand $\Lambda_{t_i} = \Lambda_{t_i-1} \cup \{\lambda_{t_i}\}$ and $\mathbf{B} = [\mathbf{B}_{t_i-1} \quad \mathbf{b}_{\lambda_{t_i}}]$.

5: Answer a least squares problem

$$\mathbf{x}_{t_i} = \underset{\mathbf{x}}{\arg\min} \, \|\mathbf{h} - \mathbf{B}_{t_i}\mathbf{x}\|_2.$$

6: Compute the new estimate of the residual and data

$$\mathbf{r}_{t_i} = \mathbf{h} - \hat{\mathbf{h}}_{t_i}$$

$$\hat{\mathbf{h}}_{t_i} = \mathbf{B}_{t_i}\mathbf{x}_{t_i}.$$

7: $t_i = t_i + 1$.

8: **until** $t_i > N_p$

9: The approximation of the perfect signal, $\hat{\alpha}$, carries nonzero indices at the elements of Λ_{N_p} and its content in the index λ_j corresponds to the jth element of $\mathbf{x}_{t_i}$.

In recent researches, random wireless networks of interest employ the Poisson Point Process (PPP). In order to achieve the above configuration, the uplink communication may be considered, whereby the regular base stations will be substituted by the passive radars. In the regular uplink scenario, mobile users send the data to a base station and then the latter estimates their channel for downlink transmission. From recent works, it is rational to suggest that the radar receiver locations within the network can refer to a homogeneous PPP. This idea is motivated by the fact that base stations and mobile terminals in the most recent works are also modelled using a PPP to enable understandable mathematical expressions; this makes the scenario practical by facilitating different received signal-to-noise ratios from the OFDM stations, clutter and targets regarding the locations of the radar receivers. The next motivation is related to the number of investigations and challenges in radar works. Although [3] provides an interesting research, the insights of which are outlined in the following sections, the applications of stochastic geometry in the radar area are highly limited. Individually, in the passive radar where the OFDM base stations are the transmitters of opportunity, the challenge of manipulating the interferences needs to be recognising and the strong transmitter signals cannot be neglected. To accept the motivations outlined above, the following subsection explains the literature review in relation to stochastic geometry. This will fill the gap between communication and radar exercises.

2.5.2 Applications of stochastic geometry

Modelling of passive radar networks can be categorised in three types when applying stochastic geometry. The first is the incorporation of ad-hoc networks with a bistatic passive radar. In large multihop-mobile wireless networks using an ALOHA-type access control [62], Poisson arrangements for the position of interferences were averaged in order to optimise the production of the number of concurrently fruitful transmissions per unit of space based on the average range of each transmission. Significantly, stochastic geometry provided mathematical gadgets for their spatial reuse ALOHA; that is, the locations of the stations followed a mark PPP, the medium access indicators of stations were independent random variables, and an assumed general distribution was imposed on the random transmitted powers. Specifically, with the PPP, the intensity of the transmitters regarding the distance only can be formulated for general power distribution. Since stochastic geometry displays an impact on interference studies, interference properties of ad-hoc networks

were developed in [63], where a singularity of the path loss function was included. The work also demonstrated upper and lower bounds on the Cumulative Density Function (CDF) of the interference. The characterisation of CDF was evaluated given that there is a sender at the origin. Their simulations compared PPP with the Thomus cluster and hard core (minimum distance) point processes and it was shown that the Gaussian distribution assumption for interference distribution provided worse outcomes than inverse Gamma and inverse Gaussian distribution. Apart from its properties, spatial and temporal correlation of the interference could decrease the performance of communication systems, such as transmission capacity. Given that a PPP is assigned to the units in ad-hoc networks, [64] assessed the consequence of this correlation in which ALOHA multiple-access was applied. It was shown that spatial and temporal correlation incurred link outages of the system and should be included when examining the networks.

When considering multistatic passive radar systems, cellular networks can be exploited. A comprehensive comparison of the PPP and the hexagonal grid models was proposed in [65]. From the results, the PPP model offered upper bounds of the coverage probabilities and higher accuracy. Another cellular-related research is in [66], where the author presented a stochastic geometry-based unified three-dimensional channel model for land mobile radio cellular systems with an assumption of uniformly distributed scattering objects. The work presented closed-form joint and marginal Probability Density Functions (PDFs) of azimuth and elevation AoA. The performance bounds of partial fading and Rayleigh fading wireless cellular networks were derived in [67]. In this work, the Laplace transform of the inverted SINR was employed. The bounds for average Shannon and outage rates were also found in closed-form. Regarding the more complex interference environment in the passive radar networks, heterogeneous networks are presented. [68] considered downlink performance in a fixed-size cell, which is imprinted in a weighted Voronoi cell in a Poisson field of interferers; this was done by adopting stochastic geometry. The work contained a nearest out-of-cell interferer, out-of-cell interferers outside a guard region, and cross-tier interferers; it discussed whether the total interference could be defined by its Laplace transform. The Gamma distribution was exploited to estimate the interference distribution. The results demonstrated that the sum interference in the cellular systems could be succeeded by an equivalent interference random variable. An application with uplink heterogeneous cellular networks was also shown in [69], where all tiers of multiple-antenna base stations were distributed following homogeneous and independent PPP. Stochastic geometry assisted in the formulation of mathematically

tractable coverage probability and average rate. This work also discussed the dependencies of coverage and rate and compared the gain of Maximum Ratio Combining (MRC) and Optimum Combining (OC). Stochastic geometry also supplies solutions for the performance analysis of dense cellular networks [70]. The most energy-efficient method indicated in the paper for the forthcoming dense urban environments is a homogeneous pico deployment for the data plane with a separate layer of signalling macro-cells.

One research has also considered massive MIMO, a modern technology that can be equipped with passive radar receivers. It was then performed in the following two works. In the first paper [71], beamforming was operated in the cellular system under stochastic geometry. The author developed an outage probability for three different reuse factors for the case of orthogonal pilots. Handling Gauss hypergeometric function, the complementary CDF for Signal-to-Interference Ratio (SIR) was subsequently acquired. Secondly, stochastic geometry was also operated to characterise the spatially distributed users in an uplink large-scale MIMO system [72]. The author practised large dimensional random matrix theory to obtain deterministic approximations of the sum rate, and generated close-form approximations for deterministic rates at low and high SNR regimes in this work. Stochastic geometry is famous in spectrum sensing and cognitive radio. In [73], the author found the result for large wireless networks by working out the Euclidean distances whose distribution is PPP, while the spatial throughput of a multi-antenna Poisson cognitive radio network was measured in [74] with the presence of optimal medium access probability. The author of [75] employed stochastic geometry to confront the various signal-to-noise ratios based on the generalised likelihood ratio test detector. Another challenging spectrum scenario was spectrum sharing between a drone small cells network and cellular networks [76]. The network was formed by the three-dimensional PPP. The optimal density of drone aerial base stations was discovered, and the author examined its scaling behaviour with respect to the outage probability constraint under different heights of drones. The particular primary regions were also considered as the cellular networks needed protection.

One of the most significant researches in the area of radar is [3], discussing the statistics of radar interference in automotive radar. Two spatial distributions, a Poisson Point Process and a Bernoulli Lattice Process, were mentioned and the interference statistics and systematic expressions for the probability of favourable range estimation were acquired. According to the review in [77], executions of the connectivity, the capacity, the outage probability, and other fundamental limits of wireless networks are

achieved by stochastic geometry and random geometric graph theory. The author also claimed that stochastic geometry is one of the mathematical techniques able to represent a communication-theoretic conclusion to justify the network's geometrical configuration. Stochastic geometry can also be employed to calculate the mean cost of route and its fluctuation in routing protocols. The joint modelling of point processes and fading, which is practical for networks with uncertain distance, can be regarded as other applications of stochastic geometry.

2.5.3 Related mathematical foundations

There are some theoretical foundations that should be addressed. These backgrounds are crucial and they will frequently be discussed in the chapter 5. This subsection begins with a point process, along with its properties. The point process is applied when the locations of base stations and passive radars are discussed. Its properties assist tractable mathematics in computation. Then, the Gamma random variable is demonstrated. Specifically in a cellular network configuration, some statistical matrices can be represented by the Gamma distribution. This is also helpful when the interference function is formulated.

A point process

This section begins by discussing a point process (also known as a spatial point process). Denoting the sequence $\phi \subset \mathbb{R}^2$, the set of all sequences can be signified as $\mathbb{N}$, which should comply with the following conditions: (a) the number of points in any bounded set $A \subset \mathbb{R}^2$ should also be bounded (finite condition); (b) if there are two variables i and j where $i \neq j$, it should be shown that $x_i \neq x_j$ (simple condition). According to [78] and [79], a point process in $\mathbb{R}^2$ can be briefly explained as a random variable whose values are collected from the space $\mathbb{N}$. A point process can be symbolised as $\Phi = \sum_i \delta_{x_i}$, where

$$\delta_{x_i}(A) = \begin{cases} 1 & \text{if } x \in A, \\ 0 & \text{otherwise,} \end{cases} \tag{2.30}$$

is the Dirac measure at x. ϕ designates an instance of the point process, and $\Phi(A)$ refers to the number of points of the point process in a set A. A point process characterisation will be discussed in the following paragraph.

Two point processes are equivalent if they have the same void probability distribution, which can be shown as $\mathbb{P}(\Phi(K) = 0)$ for $K \subset \mathbb{R}^2$. If the distribution of a point process is invariant concerning translation, it is called a stationary point process, whereby it provides a statistically analogous display to any point in space and cannot be interpreted based on a

subset of $\mathbb{R}^2$. The density of a stationary point process can be illustrated as $\frac{\mathbb{E}[\Phi(B)]}{|B|}$, where $B \subset \mathbb{R}^2$ and its selection does not need to be specific. In this work, the point process of interest is the stationary PPP, which is the most extensively applied model for spatial locations of nodes. Node positions in PPP are not conditioned among one another. PPP can also be outlined in the complete space. The characterisation of PPP will be mentioned in the following paragraph.

With a Poisson random number of points in a set $A \subset \mathbb{R}^2$ where its mean is equal to $\lambda|A|$, the distribution can be shown as

$$\mathbb{P}(\Phi(A) = n) = \exp(-\lambda|A|)\frac{(\lambda|A|)^n}{n!}, \tag{2.31}$$

where λ refers to the intensity of PPP and does not depend on the set A. Note that unconnected sets produce an independent number of points. The points are independently and uniformly distributed in the set A. The next property is related to the PPP transformation, which is called as the independent thinning. Assuming there are two point processes, that are, the yellow point process, Φ_y, and blue point process, Φ_b. With probability p, a node $x \in \Phi$ becomes yellow and will be blue with probability $1-p$. It can therefore be concluded that $\Phi = \Phi_y \cup \Phi_b$; hence, a yellow PPP is of density λp, whilst a blue PPP is of density $\lambda(1-p)$ and Φ_y and Φ_b are independent. This follows the void probabilities of two PPP. In case of modelling Carrier-Sense Multiple Access (CSMA) in media access control (MAC), dependent thinning or Matern's hard-core process is used in a minimum distance mechanism. Dissimilar to independent thinning, each node will independently receive a mark m_x, which is uniformly distributed. To denote a ball centralised at point x with a radius R, $B(x,R)$, a node is chosen regarding the following:

$$\Psi = \{y : y \in \Phi, m_y \leq m_x, \forall x \in B(y,R) \cap \Phi\}. \tag{2.32}$$

Thus, the lowest mark among all the points in the ball will be elected. The dependent thinning eventually has a density of:

$$\lambda_m = \frac{1-\exp(-\lambda\pi R^2)}{\pi R^2}, \tag{2.33}$$

provided that Φ has an intensity of λ.

In many researches, there is a point denoted as a *typical* point to allow for tractable calculation. The reason for this is a reduced Palm probability that is conditional to the presence of a node at a specific location. Regarding the Slivnyak theorem, reduced Palm distribution of a PPP equals the initial distribution. As a result, an introduction of a new

point does not upset other locations of the PPP. The following paragraph discusses some critical theories related to the mathematical operation of PPP.

To perform the summation over a PPP, Campbell's theorem provides assistance. Given a PPP, Φ, of intensity λ and assuming a function $f(x) : \mathbb{R}^2 \to \mathbb{R}^+$, Campbell's theorem states that [80]

$$\mathbb{E}\left[\sum_{x\in\Phi} f(x)\right] = \lambda \int_{\mathbb{R}^2} f(x)dx. \tag{2.34}$$

Another tool, Probability Generating Functional (PGFL), is a method that aids the product operation over PPP. Given a PPP, Φ, of intensity λ and assuming a function $f(x) : \mathbb{R}^2 \to [0,1]$ to be a real valued function, the PGFL of the homogeneous PPP can be shown as [81]

$$\mathbb{E}\left[\prod_{\Phi} f(x)\right] = \exp\left(-\int_{\mathbb{R}} [1-f(x)]\lambda(dx)\right), \tag{2.35}$$

where $\lambda(dx)$ is the intensity measured on the infinitesimal volume dx. The integration is performed over the region of interest $\mathbb{R}$.

Voronoi tessellation

A tessellation refers to a collection of open, pairwise disarrange polyhedra, the union of whose closures blanket the space, and which is locally finite [82]. Subject to $\mathbb{R}^2$ is considered, polygons are commonly used. Given a simple point measure μ on $\mathbb{R}^d$ and a point $x \in \mathbb{R}^d$, an open set Voronoi cell, $\mathscr{C}_x(\mu)$, of the point $x \in \mathbb{R}^d$ with respect to μ can be described as the closure of the last set of the following

$$\mathscr{C}_x(\mu) = \{y \in \mathbb{R}^d : |y-x| < \inf_{x_i\in\mu_i, x_i\neq x} |y-x_i|\}. \tag{2.36}$$

Given a simple point process $\Phi = \sum_i \varepsilon_i$ on $\mathbb{R}^d$, the Voronoi tessellation or mosaic instituted by Φ is defined to be the marked point process

$$\mathscr{V} = \sum_i \varepsilon_{(x_i, \mathscr{C}_{x_i}(\Phi)-x_i)}. \tag{2.37}$$

In other words, $\mathscr{C}_{x_i}(\Phi)$ of x_i is the set of all those points of $\mathbb{R}^d$ that are more adjoining to this x_i than to any other point of Φ. Frequently, the Voronoi cell might be determined as the closure of the set. It can also be shown that not every section in $\mathbb{R}^d$ is enclosed by some Voronoi cell. Providing a Voronoi tessellation is founded by a homogeneous PPP and the typical cell $\mathscr{C}_0(\mu)$ under the palm distribution is recognised, it is shown that all cells are bounded with a probability of 1.

Another important definition related to the Voronoi tessellation is about its neighbours. Let $\mathscr{C}_x(\mu)$ be the Voronoi cell of $x \in \mathbb{R}^d$ achieved by a point pattern μ, for simplicity,

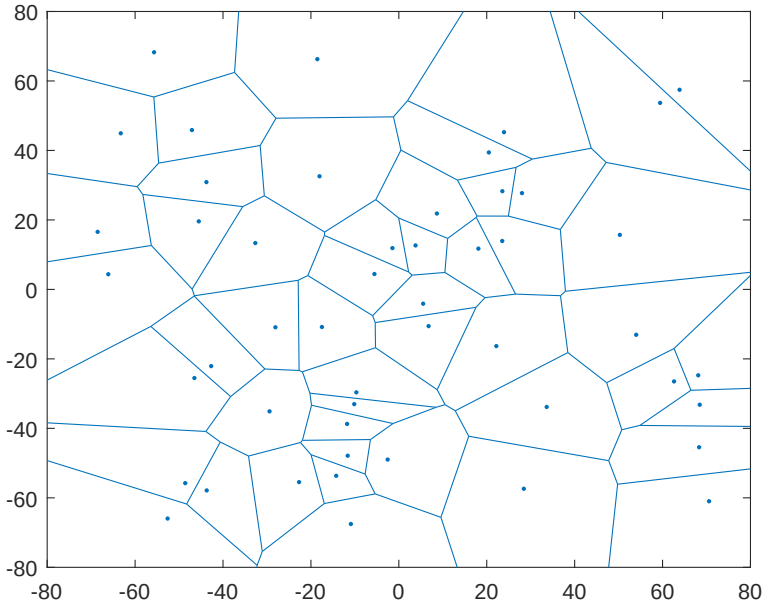

Figure 2.5: An example of Voronoi tessellation using Poisson Distribution with mean = 50

assume that $\mu(\{z\}) = 0$ or 1, any point $y \in \mu$ such that $y \neq x$ and $|a-x| = |a-y|$ for some $a \in \mathscr{C}_x(\mu)$, where $\mathscr{C}_x(\mu)$ is defined to be the closure, is called a Voronoi neighbour of x. Moreover, a graph with a set of vertices μ and edges linking $y \in \mu$ to any of its Voronoi neighbours is called the Delauney triangulation where μ is a simple point measure. The example of Voronoi tessellation created using Matlab function is illustrated in Fig. 2.5.

Gamma random variables

One of the objectives of stochastic geometry is to understand the characteristic of the interference. The design of the system usually includes shadowing and fading corresponding to the source signal. There is a tool that allows for the modelling of fading distribution, estimation of the product of shadowing and fading, as well as interference power. This application was introduced in [68], referred to as Gamma random variables utilisation. Useful descriptions and theorem are discussed below.

Definition: the PDF of a Gamma random variable, $X = \Gamma[k, \theta]$, where $k > 0$ and $\theta > 0$ are finite shape and scale parameters respectively, can be shown as

$$f_X(x) = x^{k-1} \frac{\exp[-x/\theta]}{\theta^k \Gamma(k)}. \tag{2.38}$$

The cumulative distribution function is

$$F_X(x) = \frac{\gamma(k, x\theta)}{\Gamma(k)}, \tag{2.39}$$

where $x \geq 0$ and $\gamma(a,b) = \int_0^b t^{a-1}\exp(-t)dt$ is the lower incomplete Gamma function. The first two moments and the variance can be shown as

$$\mathbb{E}[X] = k\theta \quad \mathbb{E}[X^2] = k(1+k)\theta^2 \quad \text{var}[X] = k\theta^2. \tag{2.40}$$

Regarding the scaling property, with scalar $a > 0$, if X is $\Gamma[k,\theta]$, then aX is $\Gamma[k,a\theta]$.

Gamma 2nd Order Moment Match: two distributions are acknowledged. Denoting $\mu = \mathbb{E}X, \mu^{(2)} = \mathbb{E}X^2$, and variance $\sigma^2 = \mu^{(2)} - \mu^2$, the distribution $\Gamma[k,\theta]$ with the same first- and second-order moments has the parameters:

$$k = \frac{\mu^2}{\sigma^2} \qquad \theta = \frac{\sigma^2}{\mu}. \tag{2.41}$$

Given the random variable for the fading $\Gamma[k_g,\theta_g]$ and log-normal shadowing with parameter σ, the product distribution can be rationally approximated using a Gamma distribution over a sensible bound of σ_{dB} by matching the first and second central moments; this leads to the next Lemma.

Gamma Approximation of Product Distribution: let G be $\Gamma[k_g,\theta_g]$, L is log-normal with variance σ and P_t as a constant, parameters of the Gamma random variable, $\Gamma[k_p,\theta_p]$, the same first-order and second-order moments can be calculated by:

$$k_p = \frac{1}{(1/k_g+1)\exp[\sigma^2]-1} \tag{2.42}$$

$$\theta_p = (1+k_g)\theta_g \exp[3\sigma^2/2] - k_g\theta_g \exp[\sigma^2/2]. \tag{2.43}$$

In this thesis, the techniques above are essentially utilised in the discussion of some statistical channel characteristics, specifically in cellular networks.

2.6 Summary

This chapter has presented the literature review, regarding OFDM waveforms, compressive sensing, beamforming, and stochastic geometry. A passive radar system consists of the components where there are a lot of current research relavant. In this thesis, matched filtering is selected to deal with a problem of target detection. Since the OFDM technology is available throughout communication areas, the passive radar can exploit its multiple subcarriers and extract the target signatures. The example of OFDM waveforms generation using MATLAB has also been shown in this chapter. Subspace algorithm is one of extraction methods to understand the parameters of incoming signals. Multiple snapshots MUSIC algorithm has been presented in both one and two dimensions. A

sub-Nyquist method, compressive sensing, has been discussed to displayed fundamental concepts of signal reconstruction. In order to increase the target received power, beamforming equipped with OMP has also been presented. The final section in this chapter has concerned about the literature review of stochastic geometry and some useful mathematical resources.

Beginning in the next chapter, the concept of OFDM passive radar is provided. The results of OFDM application, along with the extraction methods, are illustrated. Compressive sensing has displayed some impressive results with lower dimension of a measurement matrix. Beamingforming with compressive domain is discussed in chapter 4 and passive radar networks with stochastic geometry are determined in chapter 5.

Chapter 3

OFDM passive radar using MIMO with widely-separated antennas

3.1 Introduction

One of the major issues with passive radar occurs when the receiver simultaneously acquires a reference signal with high power and a relatively low power target signal. This results in a difficulty in the target detection. Two groups of receivers: one for the reference signal and the other for surveillance signals, can be dedicated to reduce the effect of the direct channel. This solution requires the cancellation method to be of a high quality [6]. Nowadays, MIMO concept is proposed in the radar area to overcome this difficulty by employing spatial diversity. Spatial distribution of transmitters and receivers is credited with major advancements in wireless communications, as well as in the conventional radar domain. The hereditary location ambiguity can be waived by extra pairs of tranceivers. This involves an additional location dimension and errors in term of variance or bias regarding shadowed links can also be decreased [83].

MIMO radar can be categorised into two configurations: widely separated antennas and co-located antennas. In widely-spread antennas, the OFDM base stations are continuously emitting their signals, the transmit signals impinging on the target in various angles are synchronously gathered at separate receiver locations. The accomplishment of localisation patterns can be promoted by the effective alliance of MIMO and passive radars, providing spatial diversity of the transmit and receive elements. MIMO passive radars are able to take the advantage of spatial diversity in order to lower the missed detection rate [11]. A Radar Cross Section (RCS) aspect is also key to MIMO passive radars with separated antennas. In [24], the author discusses noncoherent and coherent

processing. To identify the target and measure the parameters, noncoherent processing is manipulated to acquire a diversity gain of RCS spatial fluctuations. On the other hand, a better resolution can be supplied by coherent processing. The passive radars, which apply the signals of opportunity and demand for high performance in target detection, are likely to exploit this profit. The MIMO concept utilised in the passive radar also facilitates the ability to locate the transmitters and targets in Cartesian space by joining the detection across the receivers [8]. Many works discuss multistatic receiver [12][84][85], which is similar to MIMO in its widely spread antennas, but it has centralised processing.

MIMO-OFDM radar supplies data with regard to the number of subcarriers. In order to process the incoming signals, all of the information should be perceived by the receivers. Moreover, the summation of all transmit signals requires high computational cost, whereas most of the values represent noise effects. Incorporated with compressive sensing, sparse signal and image can be completely recovered without the effort of Nyquist-rate sampling. Regardless of the reduced efficiency of the sensor network, group sparsity has been engaged in the passive radar using a Wireless Local Area Network (WLAN) for the decline of required data rate [86]. This chapter begins by discussing the MIMO-OFDM passive radar model, employing both widely-separated antennas, and multiple 2D matched filters. The problem is then formulated into CS representations, followed by the application of the multiple snapshots CS algorithm. The two-dimensional Cramer-Rao Lower Bounds (CRLB) for OFDM passive radar is derived and the simulation results conclude this chapter.

3.2 System and signal model for widely separated receivers

The configuration in this chapter consists of multiple base stations, which are normally spread throughout the area. The passive radar receivers are also located separately from one another in order to achieve spatial diversity. The example regarding one receiver is shown in Fig. 3.1 in a MISO scheme. The figure displays an instance of MISO transmission of one receiver; the others can be operated in the same way. This section begins by illustrating the OFDM waveforms transmitted by the broadcast stations. Then, the distributed target review is displayed in the following.

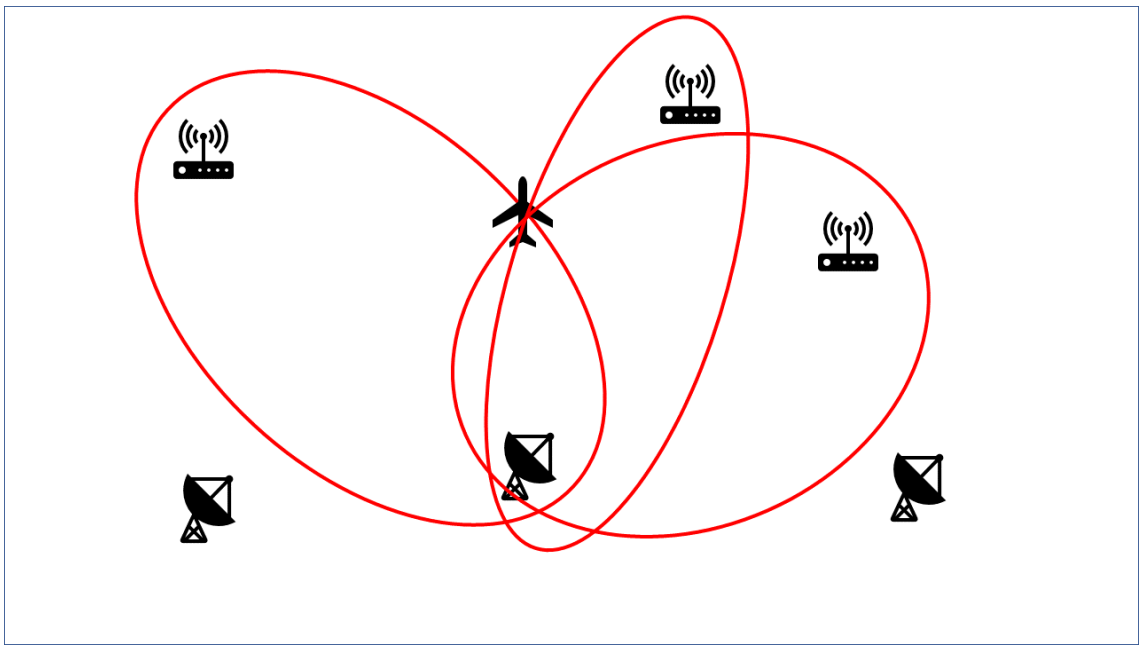

Figure 3.1: The example scenario of MIMO passive radar with widely spread antennas as discussed in this thesis. In this figure, red ellipses show the operation of the passive radar applying Multiple-Input Single-Output.

3.2.1 Transmitter signal model

Suppose that, in the MIMO-OFDM passive radar system, there are n_t transmitters highlighting a target situated at positions (x_k, y_k, z_k), $k = 1, \ldots, n_t$. Passive radar receivers, which are deposited at arbitrary locations (x_m, y_m, z_m), $m = 1, \ldots, n_r$, listen to the target reflections. The bistatic pair between the k-th transmitter and the m-th receiver is denoted as the (k,m)-th pair. The passive radars acquire the OFDM signal, which is a multicarrier modulation scheme with N subchannels. Suppose that M-ary QAM is used, then on the n-th subcarrier, the signal is:

$$\begin{aligned} u_{i,n}^{(k)}(t) &= s_{ni} \cos 2\pi f_n t - s_{nq} \sin 2\pi f_n t \\ &= S_n^{(k)} e^{j\theta_n} e^{j2\pi f_n t} \\ &= s_i^{(k)}[n] e^{j2\pi f_n t}, \end{aligned} \tag{3.1}$$

where $S_n^{(k)} = \sqrt{s_{ni}^2 + s_{nq}^2}$ and $\theta_n = \tan^{-1}\left(\frac{s_{nq}}{s_{ni}}\right)$ are the amplitude and the phase of a complex data symbol $s_i^{(k)}[n]$ respectively. Note that other types of modulation, such as Phase-Shift Keying (PSK), are also possible without affecting the OFDM characteristic. Each n-th subcarrier frequency is denoted f_n and the subcarrier frequencies are assumed to be orthogonal with a separation of Δf. Each data segment period of OFDM block is

$T = 1/\Delta f$ long. In order to avoid inter-carrier interference, a cyclic prefix, which consists of a copy of the time domain signal samples at the end of the block, is placed at the beginning. The entire OFDM block length is therefore $T' = T + T_{cp}$ long where T_{cp} denotes the cyclic prefix length in time. Given the rectangular window $q(t)$ defined as:

$$q(t) = rect\left(\frac{t}{T+T_{cp}}\right), \tag{3.2}$$

$$= \begin{cases} 1, & t \in [-T_{cp}, T], \\ 0, & \text{otherwise.} \end{cases} \tag{3.3}$$

One block of the OFDM signal transmitted from the k-th transmitter can be written as:

$$x_i^k(t) = \sum_{n=-N/2}^{N/2-1} s_i^k[n] e^{j2\pi n\Delta f t} q(t), \tag{3.4}$$

The signal from each k-th transmitter can now be written as [16]:

$$x^k(t) = \sum_{i=-\infty}^{\infty} x_i^k(t - iT'). \tag{3.5}$$

3.2.2 Two-dimensional receiver signal model

Similar to MIMO communication, the signals received at n_r receivers can be expressed as the matrix multiplication between the channel estimates $\mathbf{H} \in \mathbb{C}^{n_r \times n_t}$ and the transmitted signal $\mathbf{x} \in \mathbb{C}^{n_t}$. The received signal in a matrix notation can be derived as:

$$\mathbf{y} = \mathbf{H}\mathbf{x} + \mathbf{w}, \tag{3.6}$$

where $\mathbf{y} = [y^1(t) \cdots y^{n_r}(t)]^T$, $\mathbf{x} = [x^1(t) \cdots x^{n_t}(t)]^T$ and $\mathbf{w} = [w^1(t) \cdots w^{n_r}(t)]^T$ represents the noise experienced by the receivers, where $w^m(t) = \sum_k w^{km}(t)$. The channel estimates for all transceiver pairs are given as:

$$\mathbf{H} = \begin{bmatrix} H(t)^{11} & \cdots & H(t)^{n_t 1} \\ \vdots & \ddots & \vdots \\ H(t)^{1 n_r} & \cdots & H(t)^{n_t n_r} \end{bmatrix}. \tag{3.7}$$

The channel matrix above performs an important role in this work and it will be derived in detail using the matched filter below. Considering that the signal impinges upon the m-th distributed receiver, $m \in 1, \ldots, n_r$, $y^{(m)}$ is the combination of the reference (direct) signal $x_r^k(t)$, the target signal $x_s^k(t)$ and the clutter (unwanted strong scatterers) signal $x_c^k(t)$. This can be expressed as [87]:

$$y^{(m)}(t) = \sum_{k=1}^{n_t} x_r^{k(m)}(t) + \sum_{k=1}^{n_t} x_s^{k(m)}(t) + \sum_{k=1}^{n_t} x_c^{k(m)}(t) + w^{k(m)}(t). \tag{3.8}$$

Throughout this thesis, time delays or phase shifts of the impinging signals are only considered in relation to the sense of the transceivers/target sites. Therefore, the system ignores path loss issues. The signals impinging on the receiver consist of both the direct signal and target reflections. The echo, either from a clutter or a target, is described by a delay and a Doppler shift. Given the centre frequency of the k-th transmitted signal f_c^k, the existing Doppler shift of the target signal illuminated by the k-th transmitter and then received by the m-th receiver can be given as $f_D^{km} = a^{km} f_c^k$, where a^{km} denotes a quotient of range-rate divided by the speed of light, c, along the (k,m)-th transceiver pair. τ_p^{km} is the delay for the p-th path of the (k,m)-th bistatic pair, where $p \in \{1,\ldots,N_p^{km}\}$ and N_p^{km} identifies the total number of multiple paths for this pair. Let A_p^{km} and $w^{km}(t)$ respectively refer to the attenuation and additive white Gaussian noise in the (k,m)-th bistatic pair. The signal received at the m-th receiver is expressed as:

$$y^m(t) = \sum_k \sum_p A_p^{km} e^{j2\pi a_p^{km} f_c^k t} x^k(t - \tau_p^{km}) + w^{km}(t). \tag{3.9}$$

From (3.9), the path index p corresponds to the path of the reference signal if $\tau_p^{km} = \sqrt{(x_k - x_m)^2 + (y_k - y_m)^2 + (z_k - z_m)^2}/c$ and it belongs to the path of the surveillance signal if $\tau_p^{km} = \tau_p^{kq} + \tau_p^{qm}$ where $\tau_p^{kq} = \sqrt{(x_k - x_q)^2 + (y_k - y_q)^2 + (z_k - z_q)^2}/c$ and $\tau_p^{qm} = \sqrt{(x_q - x_m)^2 + (y_q - y_m)^2 + (z_q - z_m)^2}/c$ where the target characteristic is discussed in Section 3.2.3. As seen from the discussion above, at each receiver, the received signal reflects a multipath scenario where the paths that correspond to the reference signals provide stronger power. The rest of the impinging signals correspond to the target reflections and clutter signals. At the processing stage, the system aims to reconstruct the noise-free signal in order to extract the parameters of interest. Regarding multiple OFDM transmitters, this results in a large amount of data as the waveforms consist of numerous subcarriers and their corresponding blocks. CS becomes attractive in this case since the measurement size should be reduced.

3.2.3 Discussion of the distributed target model

One of the advantages of MIMO passive radar with widely-spread antennas is the RCS spatial diversity, which means that a distributed target identification can be employed. Suppose there is a scene illuminated by multiple OFDM base stations and there are multiple radar receivers in different locations, a target resides in that space and provides Q, independent, isotropic distributed reflectors. The coordinates where a target appears can be denoted as (x_q, y_q, z_q). A complex random variable ζ_q that is zero-mean, independent

and identically distributed (i.i.d) can be employed to create the reflectivity of a reflector with variance $\frac{1}{Q}$. A $Q \times Q$ diagonal matrix, $\Sigma = diag(\zeta_1, \ldots, \zeta_q)$, can be used to contain target reflectivity values. According to [24], the target average RCS is equal to 1 regardless of the number of reflectors in the design. The model of the target can be applicable to a Swerling case I providing that the RCS fluctuations are stabilised amid a scan and they alternate freely from scan to scan [88]. The bandwidth of the transmitted signals is supposed to be incapable of undertaking particular target reflections. Let an RCS centre of gravity of the target locate at (x_0, y_0, z_0), then the time delay components corresponding to the surveillance path can be displayed as:

$$\tau_p^{kq} = \sqrt{(x_k - x_0)^2 + (y_k - y_0)^2 + (z_k - z_0)^2}/c$$

$$\tau_p^{qm} = \sqrt{(x_0 - x_m)^2 + (y_0 - y_m)^2 + (z_0 - z_m)^2}/c. \tag{3.10}$$

From the conclusion in [24], the MIMO radar antennas need to be adequately isolated. Spatial decorrelation upholds a diversity of path gains as each element of the channel matrix **H** serves as the path gain of a transceiver pair. This means that the elements of the channel matrix decorrelate if the target's beamwidth cannot concurrently irradiate two sensors, provided that the distributed target is judged as an antenna. Individual reflectivity and position lead to a different fading signal at the receivers. Unlike a single spherical reflector with uniform RCS, the elements of the channel matrix ultimately correlate as no fading signals are constituted. Thus it can be concluded that distributed targets can be detected more precisely by applying the MIMO concept. The usefulness of the MIMO passive radar system is confirmed, and in the following part, the matched filter regarding the signal received at the radar is discussed.

3.2.4 Two-dimensional matched filter

The passive radar system applies the matched filter in order to search for peaks of output where the parameters of the signals are equal. This subsection reviews the two-dimensional (2D) matched filter from [16] utilising the MIMO radar. Similar to [16], the mf-th correlator in (2.1), which is considered at every $\hat{\tau}$ with selected integration time T_i interval, along with a fixed value of Doppler frequency $\hat{a}_{mf} f_c^k$, can be displayed in the following (let $T_{max} = 0$):

$$z_{mf}^{(m)}(\hat{\tau}) = \sum_{k=1}^{n_t} \int_0^{T_i} e^{-j2\pi \hat{a}_{mf} f_c^k t} x_k^*(t - \hat{\tau}) y^{k(m)}(t) dt. \tag{3.11}$$

With the derivation in Section A.1 in the Appendix, the output of the overall 2D matched filter can be shown as:

$$z_{mf}^{(m)}(\hat{\tau}) = \sum_{k=1}^{n_t} \sum_{i=1}^{L} \sum_{n=\frac{-N}{2}}^{\frac{N}{2}-1} e^{-j2\pi(i\hat{a}_{mf} f_c^k T' - n\Delta f \hat{\tau})} H_{n(i)}^{k(m)}. \tag{3.12}$$

The above equation shows that the matched filter output can be effectively generated using a 2D discrete Fourier transform of the channel estimates. The result of this implementation will be displayed in Section 3.5.1. If the base stations ensure their orthogonality, the matched filter output provides simple extraction as the signal from different transmitters cannot deliver the correlation outcomes and the transmitter signal association is not too complicated. However, in the SFN, the OFDM stations transmit a nonorthogonal signal. Without the proper association methods, the receiver cannot understand which transmitter the signals belong to.

3.2.5 Problem formulation

The channel has been demonstrated to be equivalent to the signal model where N_p wavefronts impinge on a URA sensors. Let $\mathbf{b}^{km}$ denote the steering vectors of the URA corresponding to the (k,m)-th bistatic pair. This is expressed as $\mathbf{b}^{km}(\hat{\tau}_p, \hat{a}_p) = vec\{\mathbf{G}^{km}(\hat{\tau}_p, \hat{a}_p)\}$, where $\mathbf{G}^{km} \in \mathbb{C}^{N' \times L'}$ is a subarray matrix resulting from the spatial smoothing technique, a method used for generating a full-rank set of observation vectors while applying a smaller equivalent aperture, N' and L', with the entries $g_{n,i} = e^{j2\pi(i\hat{a}f_c T' - n\Delta f \hat{\tau})}$. The channel for the (k,m)-th bistatic pair represented by the steering vector is thus given as:

$$\mathbf{h}^{km} = \sum_{p} A_p^{km} \mathbf{b}^{km}(\hat{\tau}_p, \hat{a}_p), \tag{3.13}$$

where A_p^{km} is the amplitude of the p-th path in the bistatic pair. In this context, target detection is equivalent to signal processing with 2D uniform rectangular arrays (URA), where each array element's position is defined by the delay $\hat{\tau}_p$ and Doppler shift $\hat{a}_p$.

3.3 Signal extraction using the multiple snapshots CS-based method

The objective of this problem is determining the delay($\hat{\tau}$) and the Doppler frequency ($\hat{a}f_c$) of the impinging signals. The sparse representation problem begins with creating an overcomplete representation $\mathbf{B}$ in terms of all possible delays and Doppler frequencies which are $\hat{\tau} = 0, \frac{T}{N'}, \ldots, (N'-1)\frac{T}{N'}$ and $\hat{a} = 0, \frac{1}{f_c T' L'}, \ldots, \frac{(L'-1)}{f_c T' L'}$. In this case, the matrix $\mathbf{B}^m$ is known. $\mathbf{a}(t)$ can be described as an $(N' \cdot L') \times 1$ vector, where there are N_p nonzero

elements. Without the knowledge of the N_p pairs of $(\hat{\tau}_p, \hat{a}_p)$, this problem can be realised as l_1-norm requlariza tion in BP. In contrast to Section 2.3, this subsection discusses the basis pursuit and l_1-SVD with some modifications for multiple antennas. For a single time sample ($M = 1$), the sparse signal can be recovered by l_1-norm regularisation. With the assumption that $\alpha^m =$
$[A^{1m}(t) \cdots A^{n_t m}(t)]^T$ is a sparse vector in a single snapshot case and a sparse matrix ($\mathbf{A}^m$) applying multiple snapshots, a suitable choice of an optimisation benchmark is $\min \|\alpha^m\|_1$ subject to $\|\mathbf{h}^m - \mathbf{B}^m \alpha^m\|_2^2 \leq \gamma^2$, where γ is a parameter designating how much noise is granted. This problem can be developed into:

$$\text{minimize} \|\mathbf{h}^m - \mathbf{B}^m \alpha^m\|_2^2 + \beta \|\alpha^m\|_1, \tag{3.14}$$

where $\mathbf{B}^m = [\mathbf{B}^{1m}(\hat{\tau}, \hat{a}, \hat{\theta}) \cdots \mathbf{B}^{n_t m}(\hat{\tau}, \hat{a}, \hat{\theta})]$ is the matrix of the overcomplete representations in terms of all possible delays, Doppler frequencies and angle of arrivals for each bistatic pair. β denotes the regularisation parameter, which regulates the tradeoff between the sparsity of the spectrum and the residual norm. The l_2-term causes the residual $\mathbf{h}^m - \mathbf{B}^m \alpha^m$ to be small, whereas the l_1-term imposes sparsity of representation.

When only a single snapshot is used, the objective equation (3.14) can be solved by the basis pursuit. There is a promising solution available that involves employing Singular Value Decomposition (SVD) to achieve correlation between snapshots and reduce computation complexity. The l_1-SVD process starts with the data matrix for the m-th receiver $\mathbf{R}^m = [\mathbf{h}^m(t_1) \cdots \mathbf{h}^m(t_M)]$. The M-dimensional problem is reduced to an N_p-dimensional one ($N_p = \sum_k N_p^{km}$) by the SVD of the data matrix, that is:

$$\mathbf{R}^m = \mathbf{U}\mathbf{L}\mathbf{V}'. \tag{3.15}$$

This results in a reduced dimensional matrix $\mathbf{R}_{SV}^m = \mathbf{U}\mathbf{L}\mathbf{D}_{N_p} = \mathbf{R}^m \mathbf{V}\mathbf{D}_{N_p}$, where $\mathbf{D}_{N_p} = [\mathbf{I}_{N_p} \mathbf{0}']$. $\mathbf{I}_{N_p}$ is an $N_p \times N_p$ identity matrix and $\mathbf{0}$ is a matrix of zeros with a dimension of $N_p \times (M - N_p)$. Defining $\mathbf{A}_{SV} = \mathbf{A}\mathbf{V}\mathbf{D}_{N_p}$ and $\mathbf{W}_{SV} = \mathbf{W}\mathbf{V}\mathbf{D}_{N_p}$, it can be shown that:

$$\mathbf{R}_{SV}^m = \mathbf{B}^m \mathbf{A}_{SV} + \mathbf{W}_{SV}. \tag{3.16}$$

In order to enforce sparsity in the matrix $\mathbf{A}_{SV}$, l_2-norm of all time-samples ($\tilde{\mathbf{a}}^{(l_2)}$) is set, where each element is the l_2-norm of the column vector of A_{SV}. The sparse spectrum of $\tilde{\mathbf{a}}^{(l_2)}$ can be determined by:

$$\text{minimize} \|\mathbf{R}_{SV}^m - \mathbf{B}^m \mathbf{A}_{SV}\|_f^2 + \beta \|\tilde{\mathbf{a}}^{(l_2)}\|_1. \tag{3.17}$$

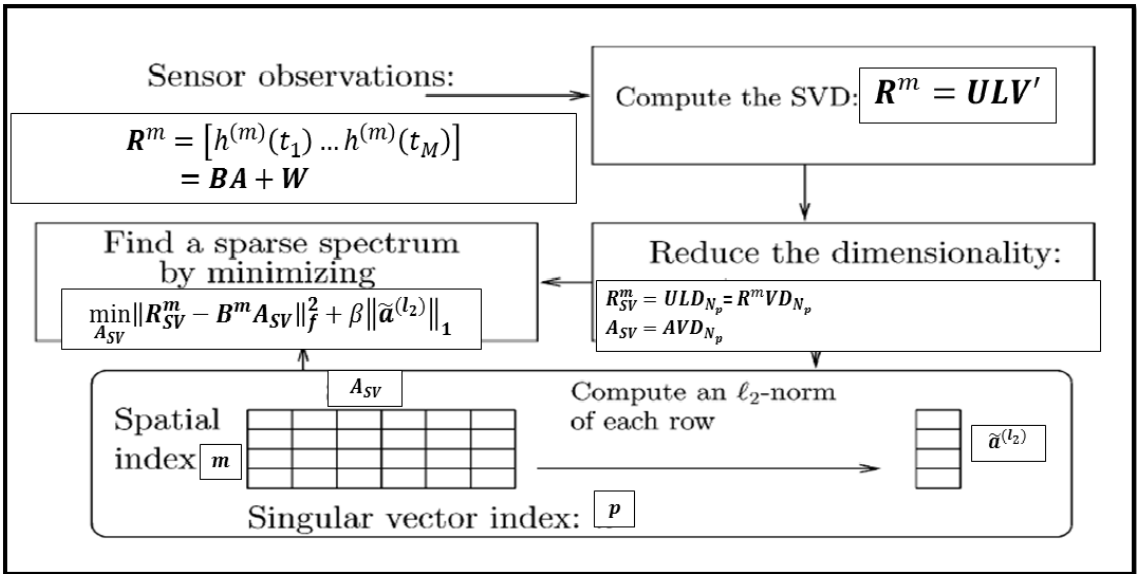

Figure 3.2: Diagram of the l_1-singular value decomposition method adapted from [2].

The diagram concluding the l_1-SVD algorithm is illustrated in Fig.3.2. The regularisation parameter (β) is determined by analysing the constrained version of (2.29), which is identical to Lagrange Multipliers for some parameter γ. The γ is accordingly selected assuming that the noise distribution is known.

3.4 Two-dimensional Cramer-Rao lower bounds

In many applications, CRLB is used to place a lower bound on the variance of any unbiased estimator; therefore, it is valuable for determining local estimation efficiency. This thesis applies this bound to the area of OFDM passive radar. The reason for this is to provide an indicator for detection algorithms as well as the effect of each variable in system and signal model. The CRLB of any estimator can be determined by [89]:

$$\text{var}(\hat{\theta}) \geq \frac{1}{\mathbf{I}(\theta)}, \tag{3.18}$$

where $\mathbf{I}(\theta)$ is the Fisher information matrix. In the case of the distributed OFDM passive radar, θ is a vector parameter and it is equal to $[\tau \;\; a]^T$. In this section, the 2×2 Fisher information matrix is first derived and can be declared as:

$$\mathbf{I}(\theta) = \begin{bmatrix} -E[\frac{\partial^2 \ln p(\mathbf{h};\theta)}{\partial \tau^2}] & -E[\frac{\partial^2 \ln p(\mathbf{h};\theta)}{\partial \tau \partial a}] \\ \\ -E[\frac{\partial^2 \ln p(\mathbf{h};\theta)}{\partial a \partial \tau}] & -E[\frac{\partial^2 \ln p(\mathbf{h};\theta)}{\partial a^2}] \end{bmatrix}. \tag{3.19}$$

In this work, the channel estimates (A.12) discussed in Section 3.2.4 are applied as the measurement signals according to the bandlimited signal representation [16]. Using a

model similar to (2.15), the measurements referring to *km*-bistatic pair can be shown as:

$$\hat{H}_{n(i)}^{k(m)} = \sum_{p=1}^{N_p} A_p^{k(m)} e^{j2\pi(i\hat{a}_p^{k(m)} f_c^k T' - n\Delta f \hat{\tau}_p^{k(m)})} + w_{n(i)}^{k(m)}, \tag{3.20}$$

which has been formerly interpreted as a 2D channel estimates with a dimension of $N \times L$. Since the antennas are widely separated, $H_{n(i)}^{k(m)}$ are statistically independent for dissimilar transceiver pairs, which is caused by free looks of the target. The additive zero-mean white Gaussian noise with variance σ_w^2 is represented by $w_{n(i)}^{k(m)}$ and the path attenuations $A_p^{k(m)}$ can be declared as zero-mean Gaussian distributed variables with variance σ_A^2. In order to calculate each element of $\mathbf{I}(\theta)$, the log-likelihood function [7] can be shown as:

$$\ln p(\mathbf{h};\theta) = \sum_m \sum_k \ln p(\mathbf{h}^{k(m)};\theta), \tag{3.21}$$

and

$$\ln p(\mathbf{h}^{k(m)};\theta) = \sum_i \sum_n \ln p(H_{(n,i)}^{k(m)};\theta), \tag{3.22}$$

where

$$p(\mathbf{h};\theta) = \sum_m \sum_k \sum_i \sum_n p(\hat{H}_{n(i)}^{k(m)};\theta),$$

$$= \frac{1}{(2\pi\sigma_w^2)^{\frac{NLn_t n_r}{2}}} \exp\left[-\frac{1}{2\sigma_w^2} \sum_m \sum_k \sum_i \sum_n \left(\hat{H}_{n(i)}^{k(m)} - \sum_p A_p^{k(m)} e^{j2\pi[i a_p^{k(m)} f_c^k T' - n\Delta f \tau_p^{k(m)}]} \right)^2 \right]. \tag{3.23}$$

is the likelihood function of the estimated channel parameters. According to the calculation in Appendix B.1, the final derivations can be:

$$[\mathbf{I}(\theta)]_{11} = -\frac{2\pi^2 \Delta f^2 N(N+1)(2N+1)Ln_r}{3\sigma_w^2} \sum_k (A^k)^2, \tag{3.24}$$

$$[\mathbf{I}(\theta)]_{12} = [\mathbf{I}(\theta)]_{21} = \frac{\pi^2 \Delta f T' N(N+1)L(L+1)n_r}{\sigma_w^2} \sum_k f^k (A^k)^2, \tag{3.25}$$

$$[\mathbf{I}(\theta)]_{22} = -\frac{2\pi^2 T'^2 NL(L+1)(2L+1)n_r}{3\sigma_w^2} \sum_k (f^k)^2 (A^k)^2, \tag{3.26}$$

Finally, matrix inversion is performed and the CRLB for each parameter can be determined as:

$$\mathrm{var}(\hat{\tau}) \geq [\mathbf{I}^{-1}(\theta)]_{00},$$

$$\mathrm{var}(\hat{a}) \geq [\mathbf{I}^{-1}(\theta)]_{11}.$$

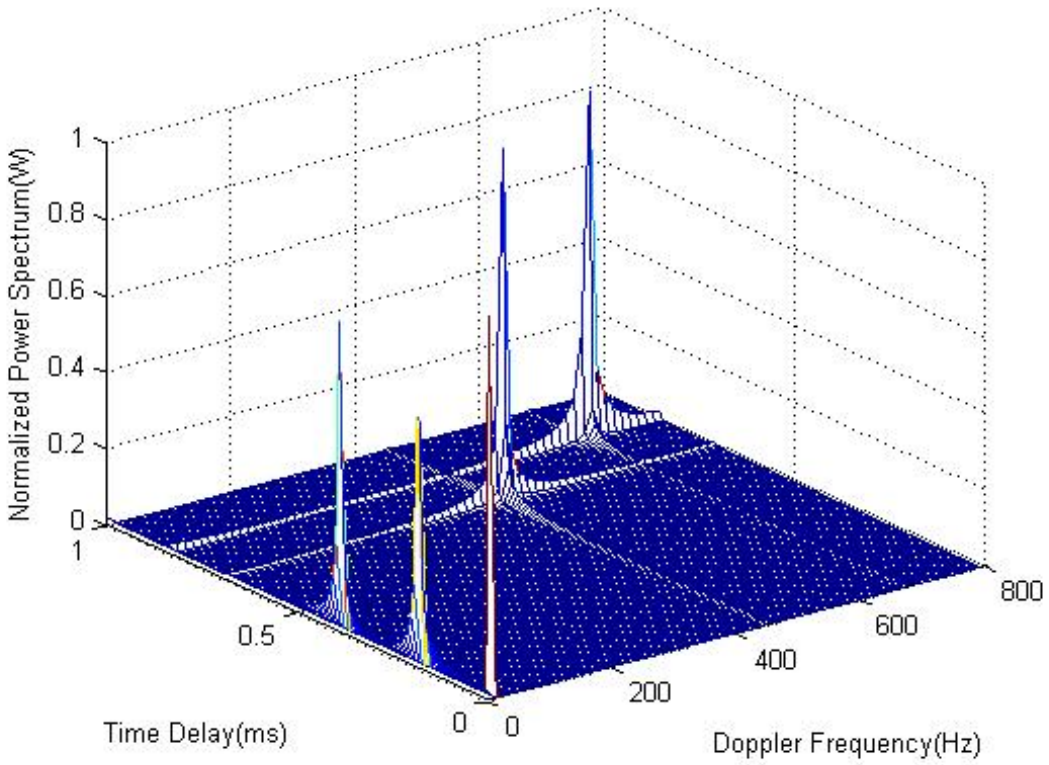

Figure 3.3: The result of the matched filter in two dimensions.

3.5 Performance analysis

Current research on passive radar aims to provide similar functionalities to active radar, for example, target detection, tracking and imaging. This thesis will also display some techniques that can increase the capabilities of passive radar. Before considering the main contributions in the following chapter, this work begins with one of the configurations of the passive radar and the application of compressive sensing algorithms. The section discusses the combination with compressed domain, along with some crucial results that lead to the proposal in the following chapter.

In order to compare the target detection performance of the MUSIC and compressive sensing methods, this research simulates the scenario of a static OFDM passive radar capturing the reflections from the moving targets and stationary clutters, along with the direct signals, so as to be able to test various detection algorithms proposed in the recent literature, including 2D MUSIC and compressive sensing. The MUSIC algorithm, which is implemented by modifying the pseudo-code presented in [16], is able to identify the target parameters; however, many snapshots of the incoming signals should have been applied. On the other hand, the basis pursuit presented in [16] with a single snapshot may

not be sufficient to recover signals in noise. This thesis also proposes a method employing multiple time samples compressive sensing called l_1-SVD and compares its performance with the MUSIC algorithm as well as with its single sample counterpart. This thesis also displays a comparison between MUSIC and compressive sensing for very close targets in order to understand the resolution provided by these methods.

In this section, the ability of compressive sensing is first illustrated when an individual pair of transceivers is analysed. The MUSIC algorithm with multiple time samples is applied in comparison with a single time sample basis pursuit and l_1-SVD. As the passive radar system in this section does not require central processing, noncoherent examination of the receiver is presented. This section then discusses the effect of multiple transmitters and receivers. The simulations here demonstrate how each extraction algorithm functions and leads to the possible approach suggested in the last chapter of this thesis.

3.5.1 The matched filter for the OFDM passive radar

Regarding the realisation of the system, standard Digital Audio Broadcasting (DAB) specifications are applied with some modifications, as seen in Table 2.1. The carrier frequency used in this simulation is 227.36 MHz, along with 1 kHz spacing between the subcarriers. This makes the symbol length 1 ms. In contrast to Table I in [16], this simulation uses 128 subchannels, along with 64 blocks per frame due to the computational constraints. Hence, the amount of bandwidth is reduced, along with the size of the cyclic prefix, which is normally equal to a quarter of symbol time. From the two-dimensional matched filter derivation discussed in Section 3.2.4, it can be understood that the matched filter of the OFDM passive radar can be generated using two-dimensional FFT function. Applying the OFDM parameters discussed above, the channel estimates can be created using (A.12) and then employed with 2D-FFT function in MATLAB [31], as shown in (A.13). Fig. 3.3 displays the two-dimensional results of the matched filter employing five multipath components, which are: 1) a direct signal; 2) two clutter reflection signals; and 3) two moving-target reflection signals with equal received signal power.

Fig. 3.4, however, illustrates the scenario when the direct signal is approximately 50-dB higher than the targets. The direct signal path possesses the shortest delay, while the targets' path delays are longer. The first target velocity is about 591 m/s, whereas the second travels around 887 m/s. The results illustrates one dimension of the output signal, where time domain is shown in Fig. 3.4a and frequency domain is shown in Fig. 3.4b.

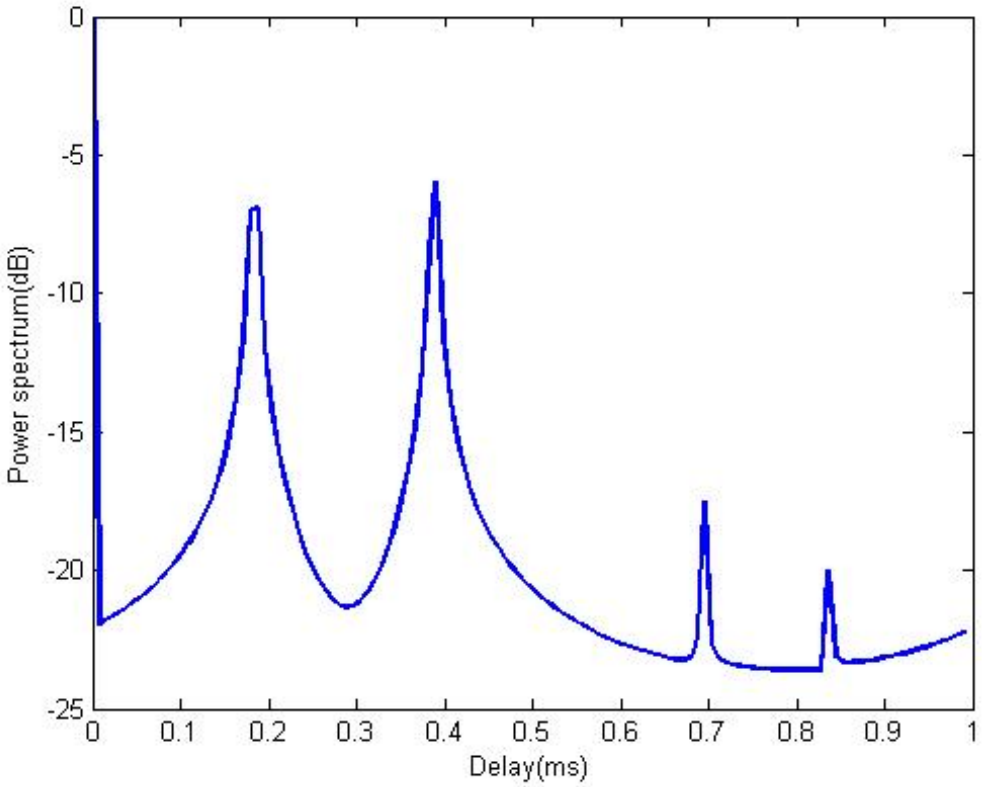

(a)

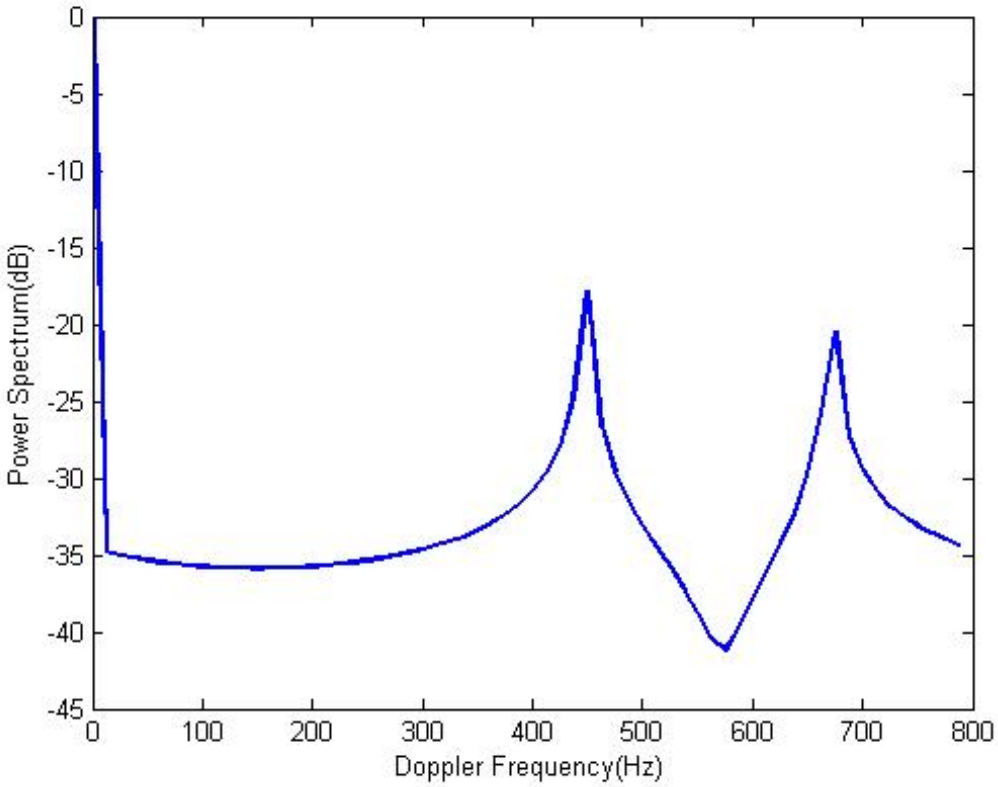

(b)

Figure 3.4: Simulation results from the output of the matched filter in: (a) time delay domain; (b) Doppler frequency domain.

The peaks of all impinging signals can easily be determined from the figures. In addition, it can be predicted that the target signals may be hard to identify if the strength of the direct signal becomes larger. The results in this subsection are also presented in [90].

3.5.2 Comparison between the MUSIC algorithm and compressive sensing

In order to implement the MUSIC algorithm, 500 snapshots (M = 500) have been included. The number of subarrays applied here is equal to 3200. The first result comes after applying the MUSIC algorithm to the observation matrix (mentioned in Section 2.2.3). There are five multipath components and each component is composed of the same level of power, as shown in Fig. 3.5. The number of multipath signals can be determined by the number of significant peaks in the delay domain in Fig. 3.5a. From the Doppler domain in Fig. 3.5b, however, two targets are only captured as one of the three peaks with zero value. Utilising the MUSIC algorithm, if the power of the direct component is much higher, the results are not sufficiently apparent, as shown in Fig. 3.6. The leakages from the reference signal can cause false peaks in both Fig. 3.6a and Fig. 3.6b. In order to overcome this issue, direct signal cancellation must be applied before trying to detect targets. It might be possible therefore to conclude that the MUSIC algorithm can produce satisfying results as the direct signal can be weaker, due to the number of snapshots used by the algorithm. In addition to this, a significant level of noise and interference are still demonstrated.

In the following simulation results, the direct signal power is set to be lower, but still greater than zero, as the cancellation method might not be good enough to completely cancel the direct signal. For comparison, the same observation matrix has also been applied with single time sample compressive sensing and the results are displayed in the same figure. The compressive sensing in this work utilises CVX programming in order to compute the SOCP problem [91]. The regularisation parameter (λ) employed in this experiment is calculated by the formula in [43], which is $\lambda \geq \lambda_{max} = \|2B^T h\|_\infty$. There is no simulation result from l_1-SVD compressive sensing for the five-component multipath scenario because of the constraint of memory size in the PC workstation. For clarity of the comparison, and to address the problem of computational size, the number of wavefronts is decreased to three: a single direct transmission and two moving-target illuminations, as displayed in the 2D mesh in Fig. 3.7.

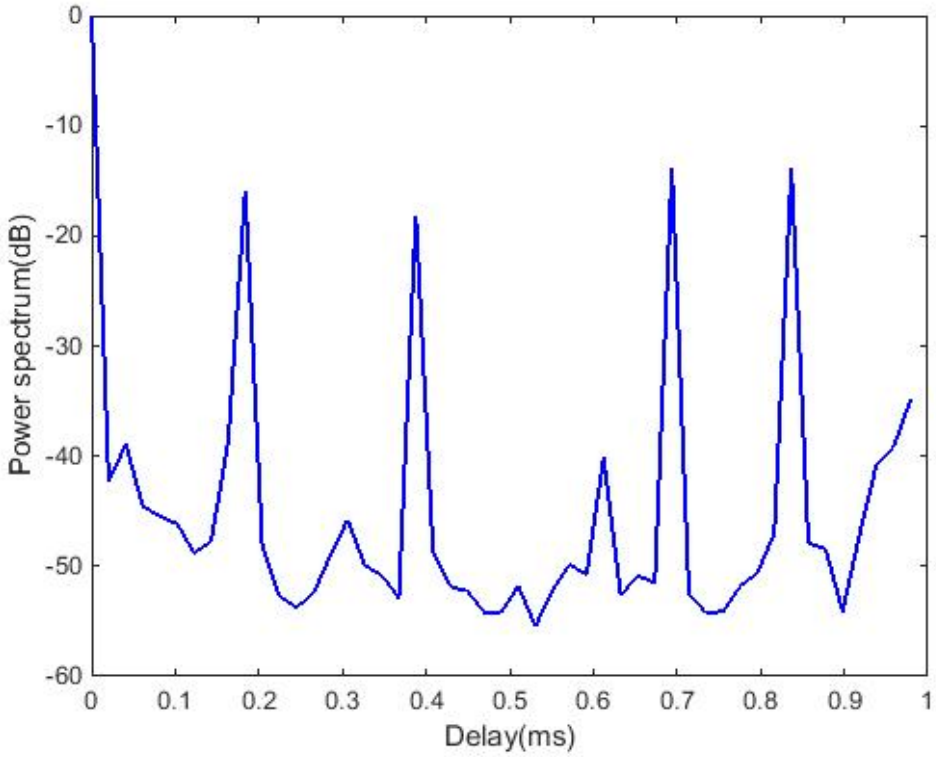

(a)

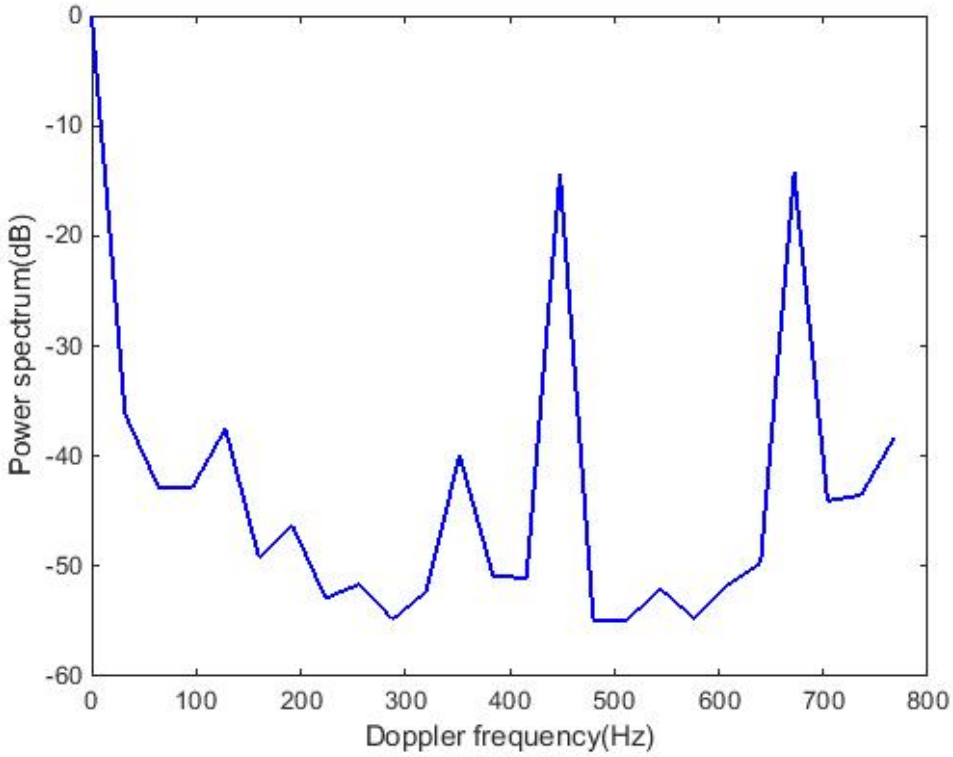

(b)

Figure 3.5: The results from the MUSIC algorithm with the same level of power among the paths in: (a) time delay domain; (b) Doppler frequency. The number of snapshots is equal to 500.

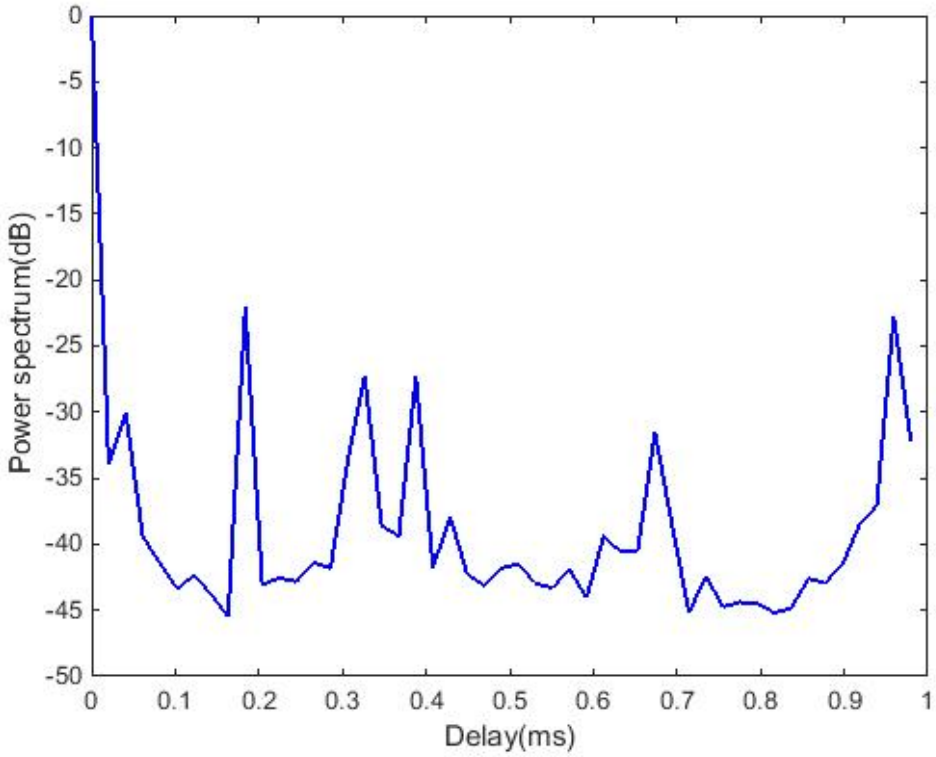

(a)

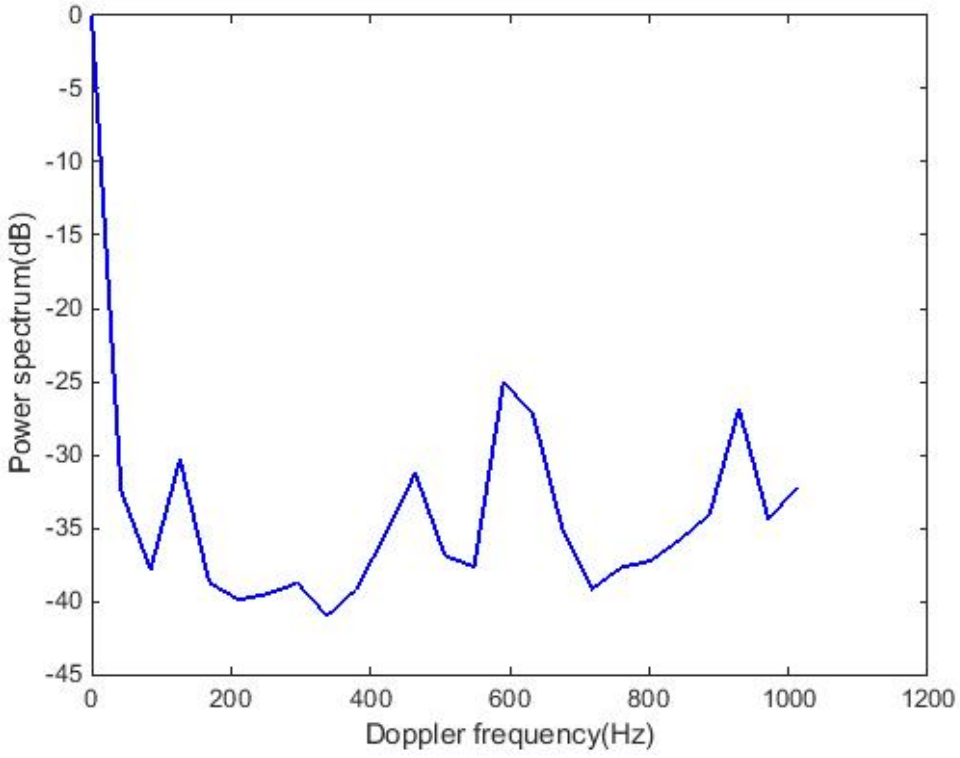

(b)

Figure 3.6: The MUSIC algorithm results with 50-dB stronger direct path in: (a) time delay domain; and (b) Doppler frequency domain. The number of snapshots is equal to 500.

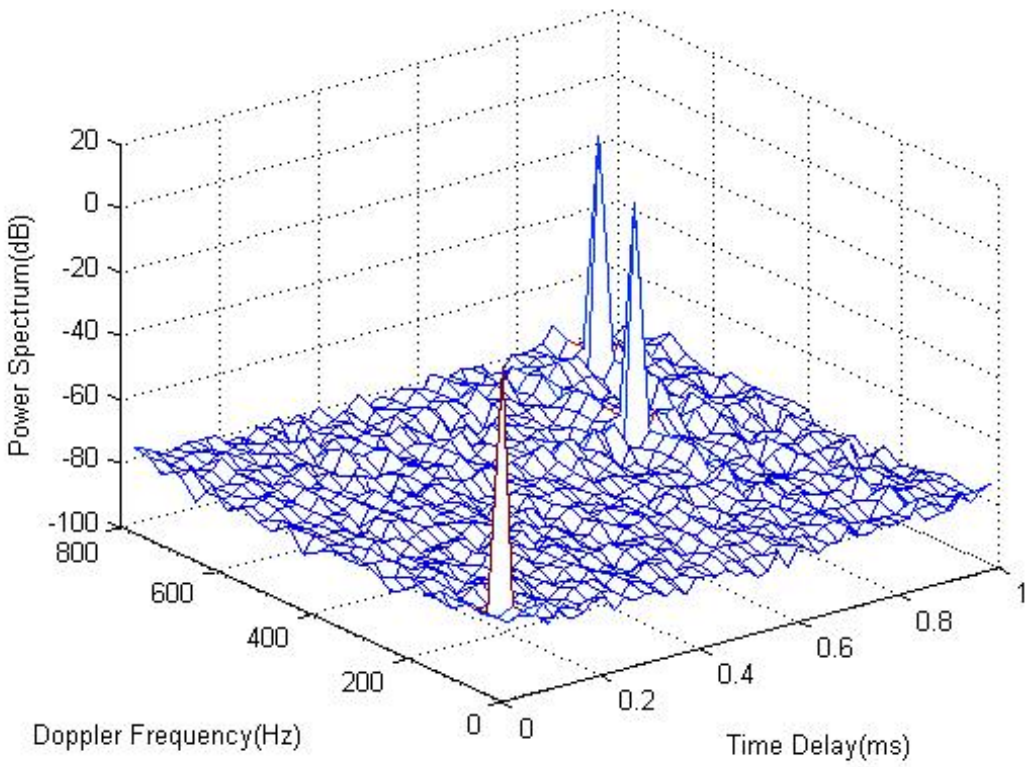

Figure 3.7: The result of the l_1-SVD compressive sensing in two dimensions applying 500 snapshots

A comparison between this l_1-SVD and the MUSIC over each dimension is demonstrated Fig. 3.8a and Fig. 3.8b, where the targets with their parameters consistent with the former simulations are determined. The pictures show that these two methods can achieve comparable outcomes, but l_1-SVD produces the lower level of noise. In order to clarify the efficiency of the algorithms, the experiments have been conducted for very closed target parameters. Firstly, the target parameters have been set to be 0.0204 ms apart in time domain and 32 Hz apart in frequency domain (the smallest virtual Uniform Rectangular Arrays (URAs) grid). Fig. 3.9a and Fig. 3.9b display a comparison between different numbers of snapshots, l_1-SVD, and basis pursuit in delay and Doppler domain respectively, while Fig. 3.10a and Fig. 3.10b show a comparison between outputs from the same number of snapshots, the MUSIC algorithm and l_1-SVD. Both figures determine that all methods lack the ability to distinguish these two targets. The other simulations in Fig. 3.11 illustrate that the two targets are able to be separated at 0.0408 ms (12.24 km) in delay in Fig. 3.11a and 64 Hz (84.45 m/s) in Doppler frequency in Fig. 3.11b. In this case, the simulations show that both algorithms can unambiguously detect the targets. This means that the intervals between adjacent possible steering vectors in the overcomplete

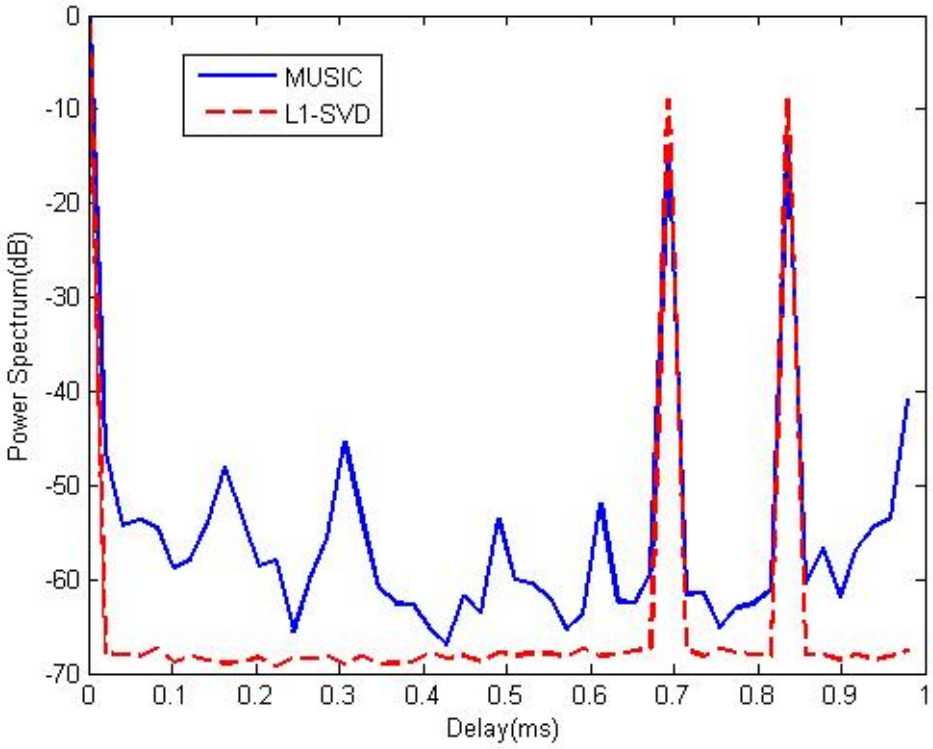

(a)

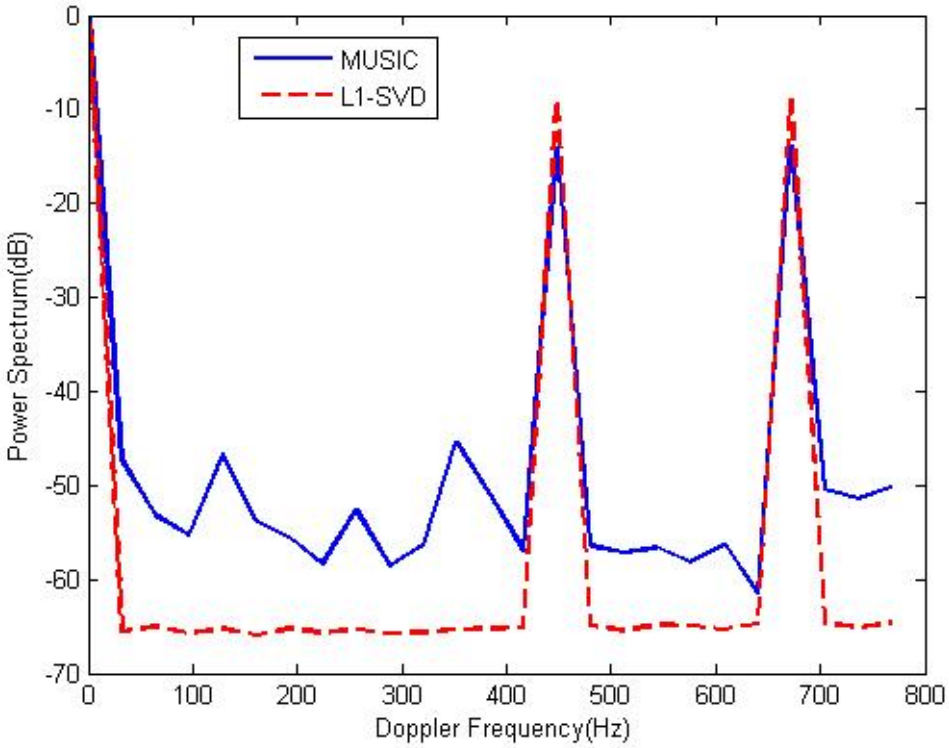

(b)

Figure 3.8: Comparison between the results from the MUSIC algorithm and l_1-SVD with multiple time samples: (a) time delay domain; (b) Doppler frequency domain. The number of snapshots for both algorithms is 500.

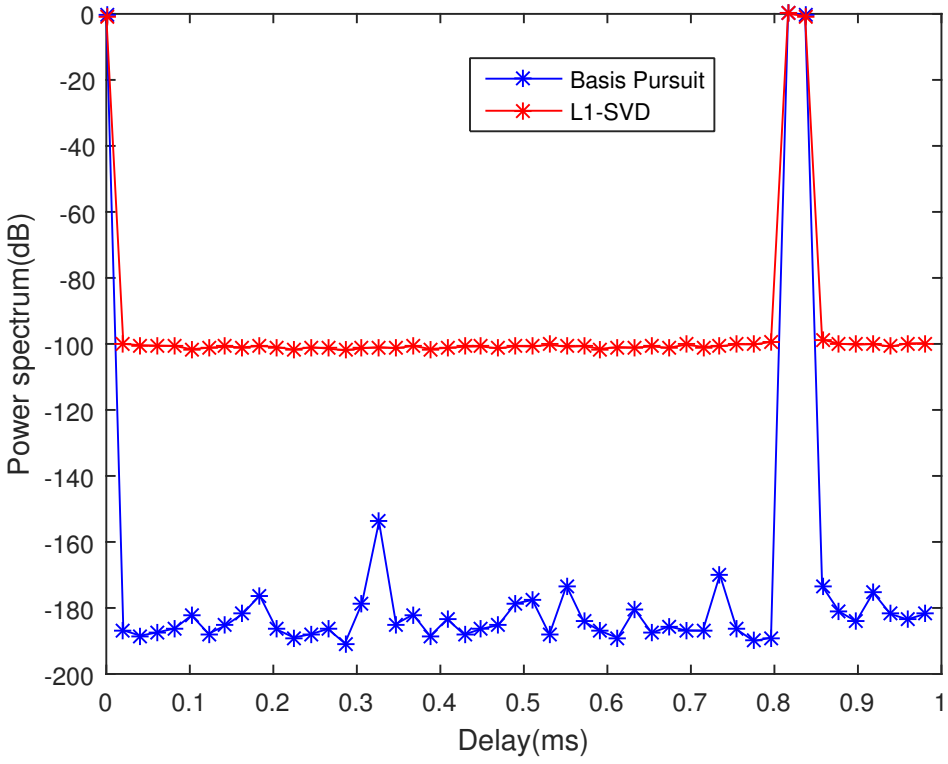

(a)

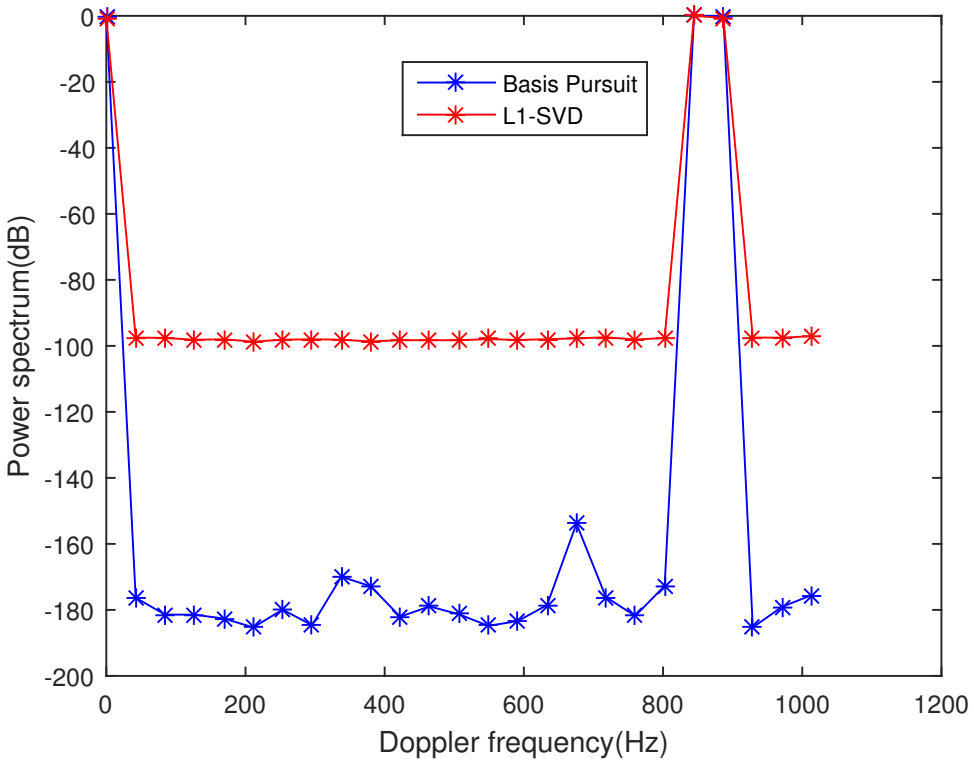

(b)

Figure 3.9: Compressive sensing with single time sample experiments on two close targets with five multipath components detected: (a) time delay domain; (b) Doppler frequency domain. The number of snapshots for l_1-SVD is 500.

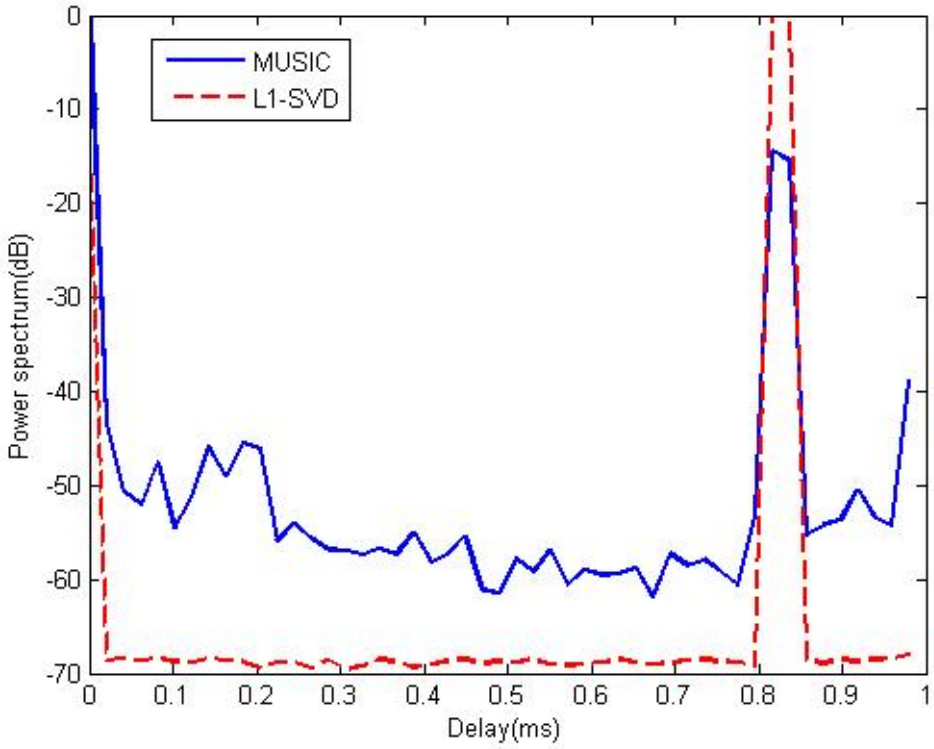

(a)

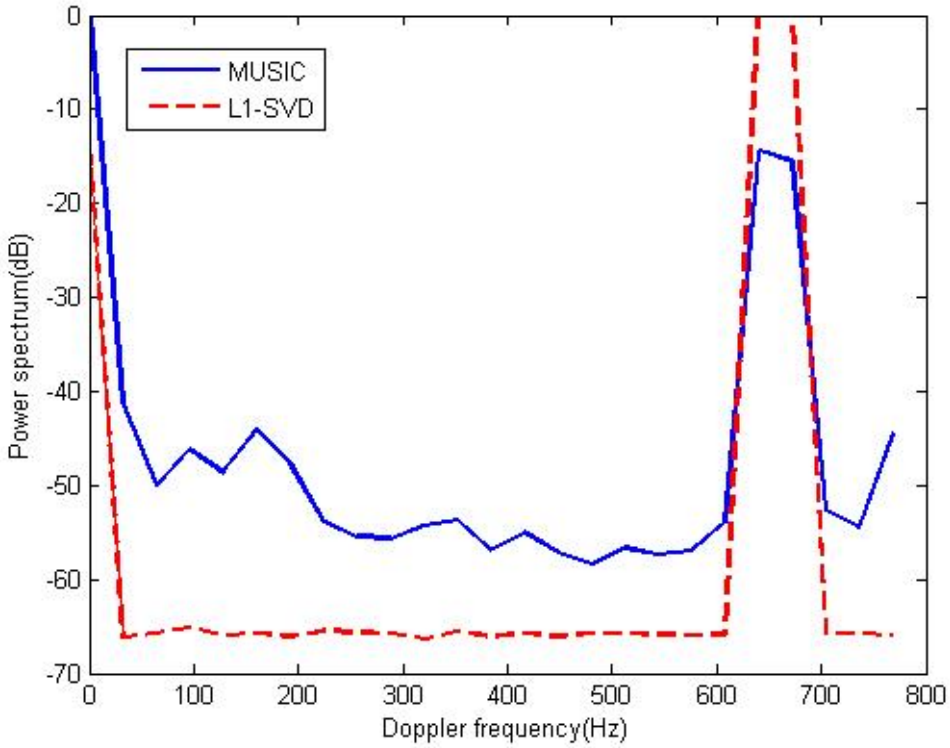

(b)

Figure 3.10: Comparison between the results from the MUSIC algorithm and l_1-SVD on the non-distinguishable targets with multiple time samples: (a) time delay domain; (b) Doppler frequency domain. The number of snapshots for both algorithms is 500.

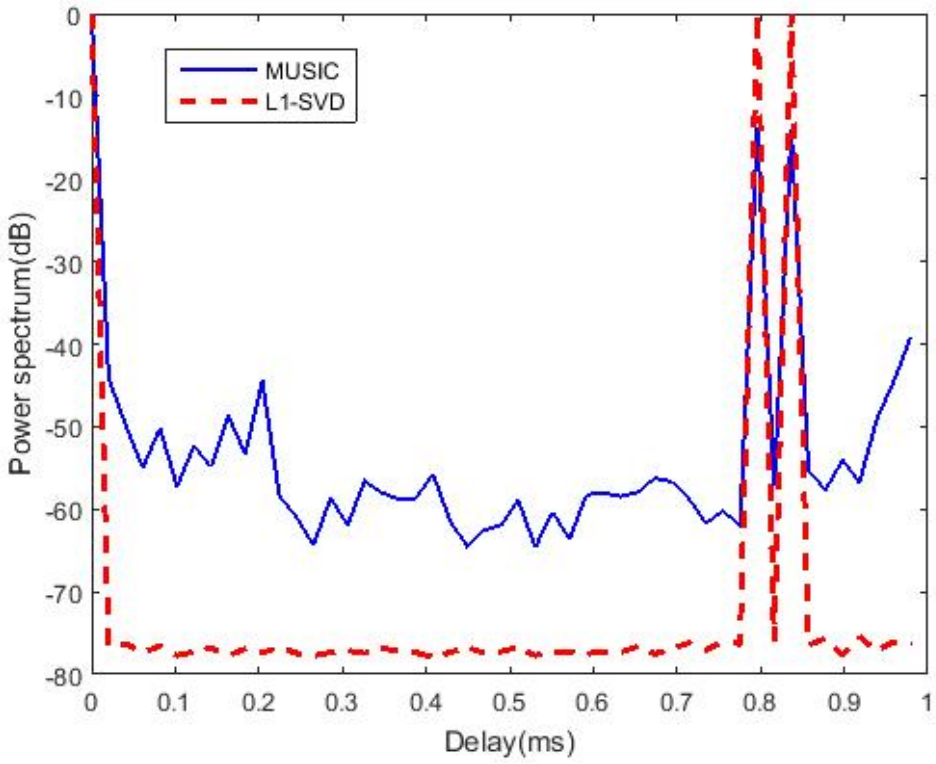

(a)

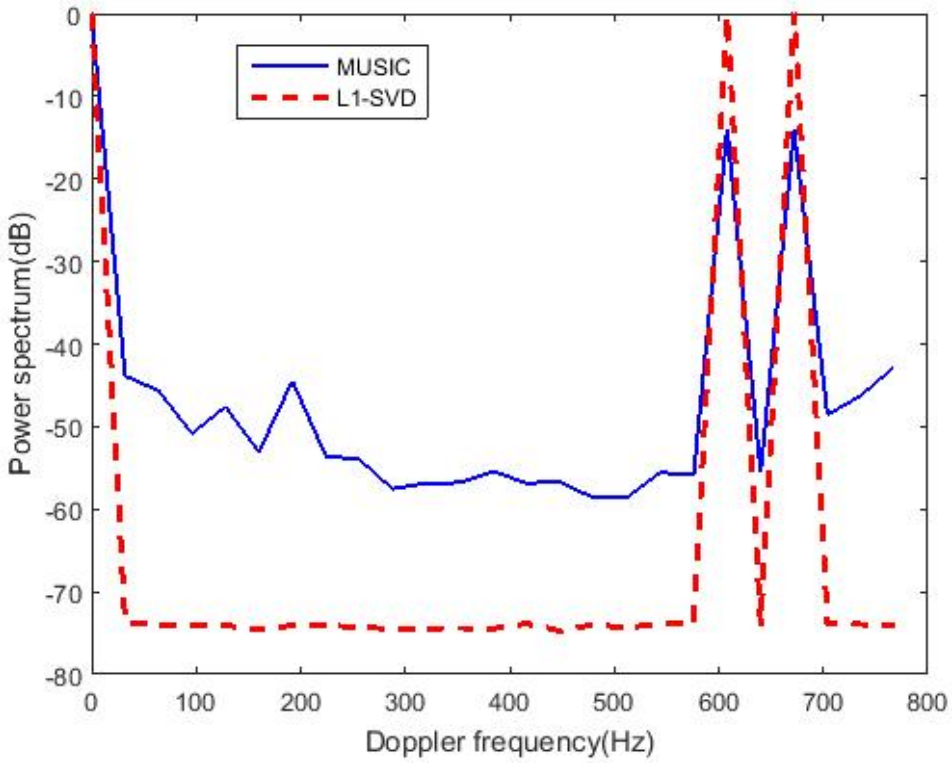

(b)

Figure 3.11: Comparison between the results from the MUSIC algorithm and l_1-SVD on the very close target parameters with multiple time samples: (a) time delay domain; (b) Doppler frequency domain. The number of snapshots for both algorithms is 500.

Table 3.1: CPU time for an iteration of target detection algorithms

Methods	**Elapsed time (sec)**
MUSIC	96.81
One-time sample CS (BP)	15488.94
Multiple-time samples (l_1-SVD)	9367.13

matrix, which is determined by OFDM parameters, could be able to affect the capacity for detection. Fig. 3.12a displays the sparse signal of the multipath components ($\mathbf{A}_{SV}$ in (2.29)), where the two closed targets are included, and Fig. 3.12b shows the result after applying the l_1-SVD algorithm over the observation matrix alone. As mentioned above, the resolutions in the system displayed in the previous figures are unacceptable owing to the fact that the size of the channel estimates (the number of subchannels N and symbols L) is limited by the computational cost of compressive sensing and matrix multiplication for the MUSIC algorithm. This size is less than the standard DAB configuration. Therefore the smaller dimensions of the subarray matrix are produced, the wider separation between the receiver grid arrays is supplied.

Nevertheless, no evidence of the maximum subarray size could be computed, which might be determined in future work. Fig. 3.13a and Fig. 3.13b show the simulation when applying a single time sample compressive sensing onto five paths of signals (with additional cluster signals) involving two close targets. It is able to detect the targets, but the simulation results display a greater level of noise. From the figures, it can be predicted that l_1-SVD is able to work with a higher power of direct signal, whilst this is not likely for its counterpart. The computational time for each algorithm when applying a three-multipath scenario (as in Fig. 3.8 and Fig. 3.11) is shown in Table 3.1.

In conclusion, the new compressive sensing algorithms extend favours in target resolution and clutter suppression by eliminating sidelobes, but they are more complex. OMP, a low intricacy compressive sensing algorithm, has been actualised in [60]. It was found that OMP cannot control direct arrivals in the experimental data and it had to be reinstated by more expensive computation basis pursuit for a single time sample and l_1-SVD for multiple time samples.

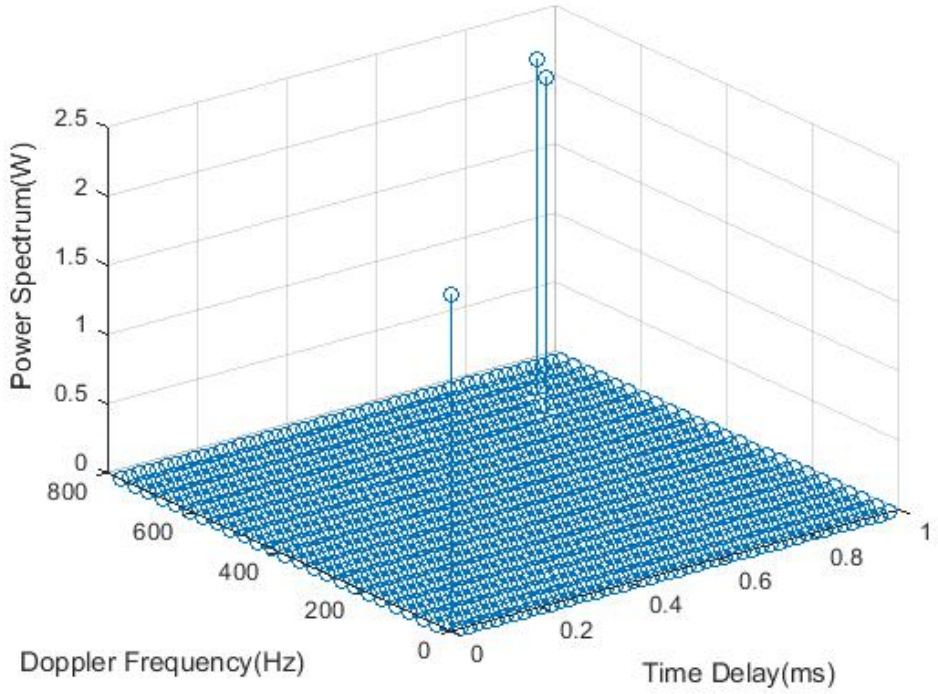

(a)

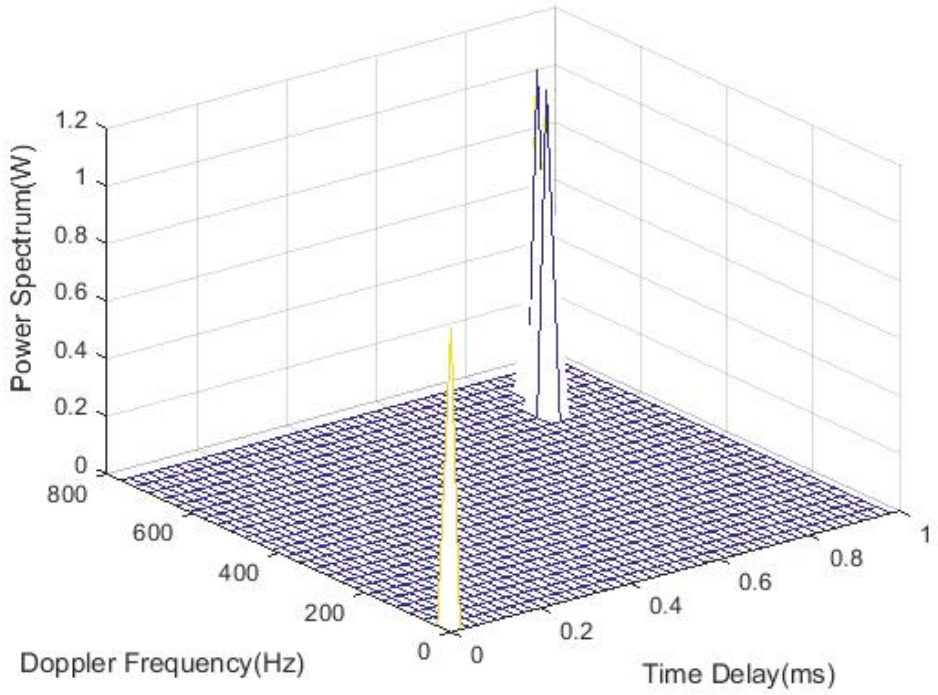

(b)

Figure 3.12: The simulation result from l_1-SVD for two closed target parameters, compared with the signal representation where: (a) sparse signal representation ($\mathbf{A}_{SV}$) is displayed; and (b) the extraction result from l_1-SVD in two dimensions is shown. The number of snapshots is equal to 500.

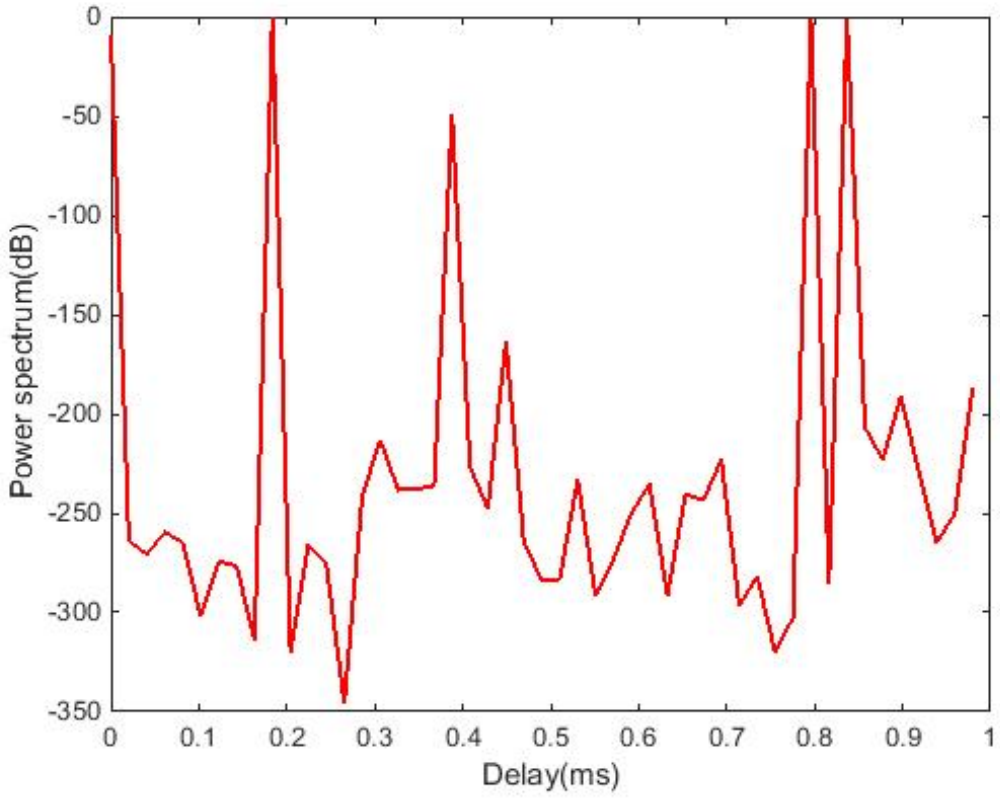

(a)

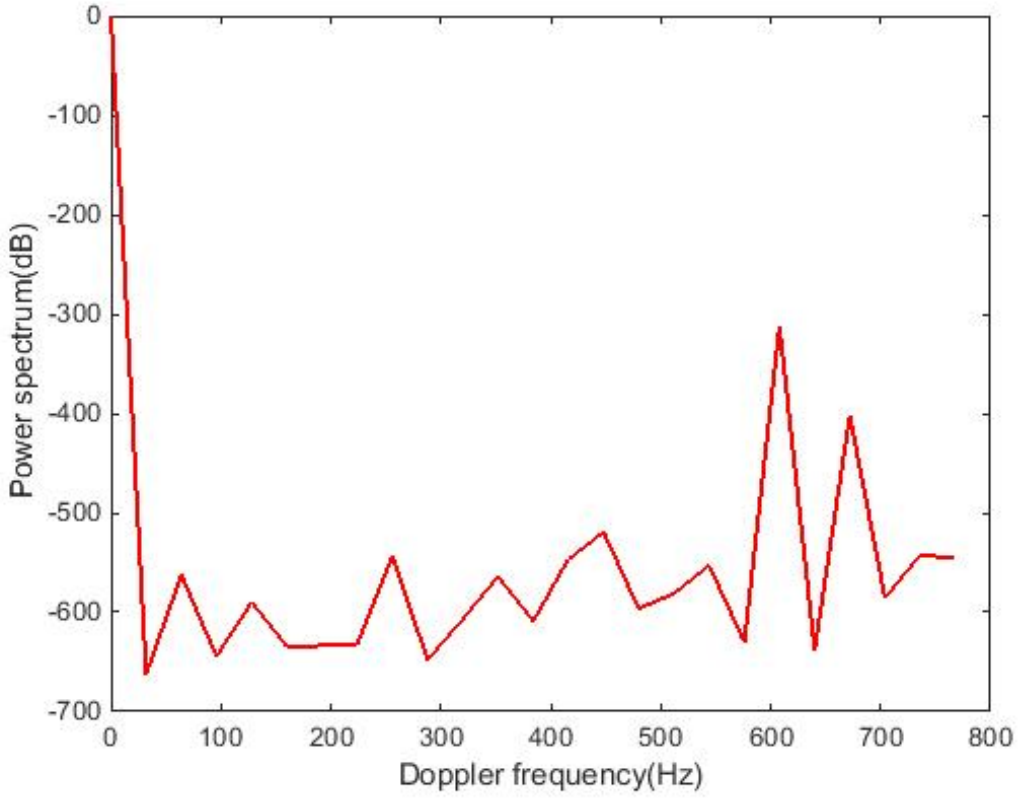

(b)

Figure 3.13: Compressive sensing with single time sample (BP) experiments on two close targets in: (a) time delay domain; and (b) Doppler frequency domain.

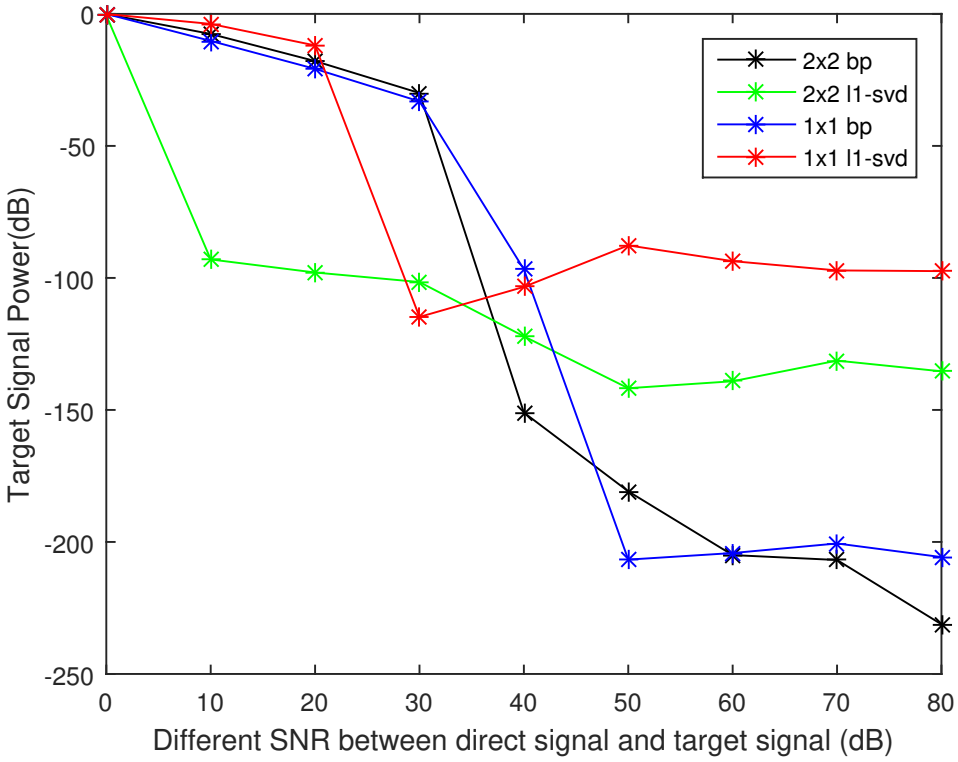

(a)

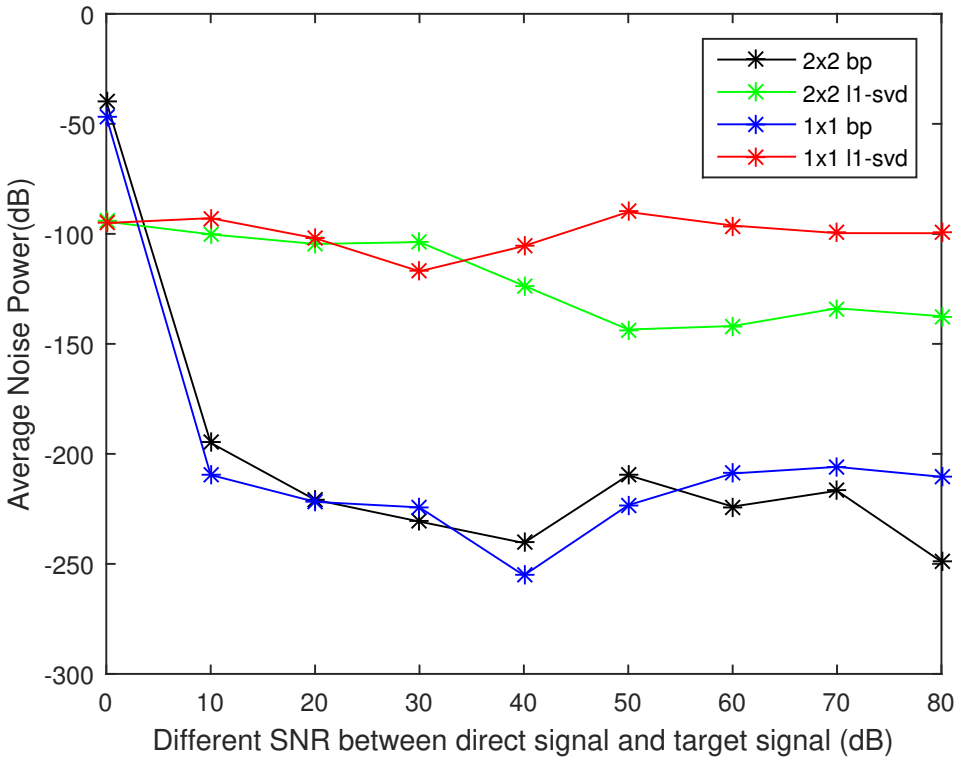

(b)

Figure 3.14: Comparison between the MIMO and SISO system using instantaneous compressive sensing algorithms (BP vs l_1-SVD) where: (a) power of received target signals are shown; and (b) average power of noise leakages are shown.

3.5.3 Signal extractions using widely-separated radar receivers

This work considers two transmitters and two receivers in MIMO-OFDM radar. In this case, all the antennas are separately located. Each transmitter uses 227.36 MHz in carrier frequency, along with 1 kHz spacing between the subcarriers. The number of subchannels is 64, whereas 32 blocks per frame are sent. The difference between the two transmitters lies in the complex data symbols. For comparison, there is also a simulation model for one transmitter and one receiver, where the same configurations are assumed. The delay time from the first transmitter (the same transmitter in the SISO system) is 0.1818 ms received by the first receiver, and the time of signal reflected by the target is 0.4242 ms from the first sender to the first receiver. The target Doppler frequency is assumed to be constant in a period of sampling that is equal to 423.5294 Hz. In the simulations, the difference between the attenuations in power (dB) of the direct and the target paths are varied. It is assumed that the smallest direct signal power received at the receiver is equal to the target signal power.

Fig. 3.14a and Fig. 3.14b display the results of target power and noise power using compressive sensing methods respectively. These figures demonstrate the characteristics of extracted received signal while contrasting the direct signal power and the target power. It is not surprising that basis pursuits for both MIMO and SISO systems produce the smallest amount of noise leakages as they use only one single time sample. It is worth emphasising that basis pursuit for both MIMO and SISO systems provides similar results for both target and noise signal. Regarding the target power, the MIMO and SISO basis pursuit, as well as its counterpart SISO l_1-SVD, performs better than MIMO l_1-SVD if the difference between the reference signal and the surveillance signal is lower than 40 dB. In the higher difference, however, the target signatures from all algorithms are below -100 dB, where the signal strength from l_1-SVD are higher. These simulation outcomes do not infer the disadvantage of MIMO but they show the worthwhile consideration which lead to presentations in the following chapters. It is also shown by referring to the simulations that diversity from l_1-SVD might not be achieved. The following presents a discussion of the numerical results comparing between MIMO and SISO are followed. The comparisons are shown in both the delay time and Doppler frequency domain. It is shown that all the methods have the capability to detect the target if the direct signal power is not higher than 10 dB corresponding to the target.

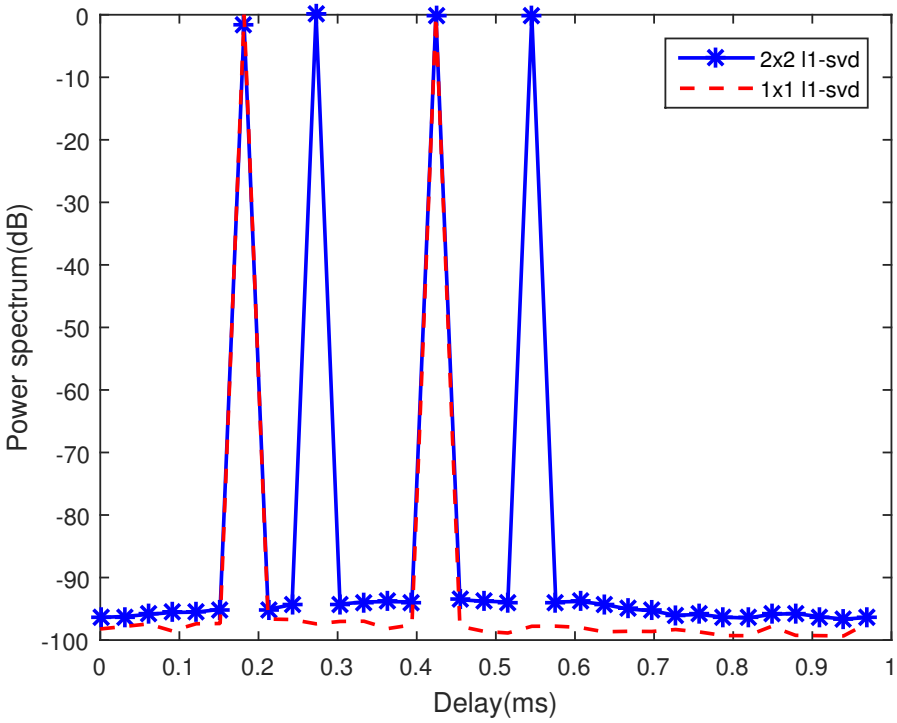

(a)

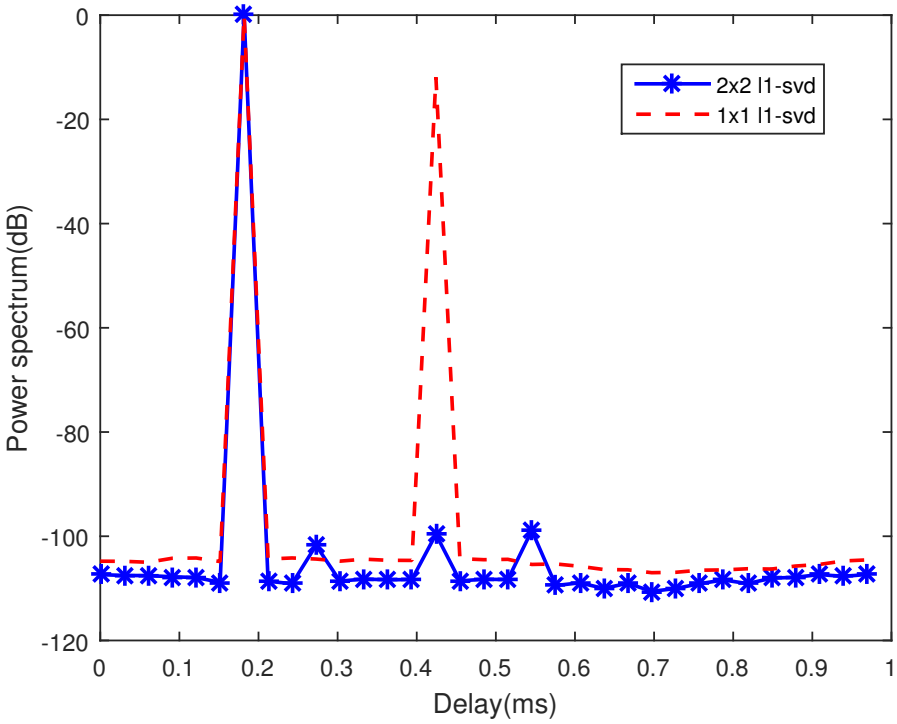

(b)

Figure 3.15: Instantaneous numerical results when applying centralised l_1-SVD over the MIMO and SISO systems in delay time domain where: (a) the power of direct path and target path is equal; and (b) direct path power is 20 dB higher. The number of snapshots is 200.

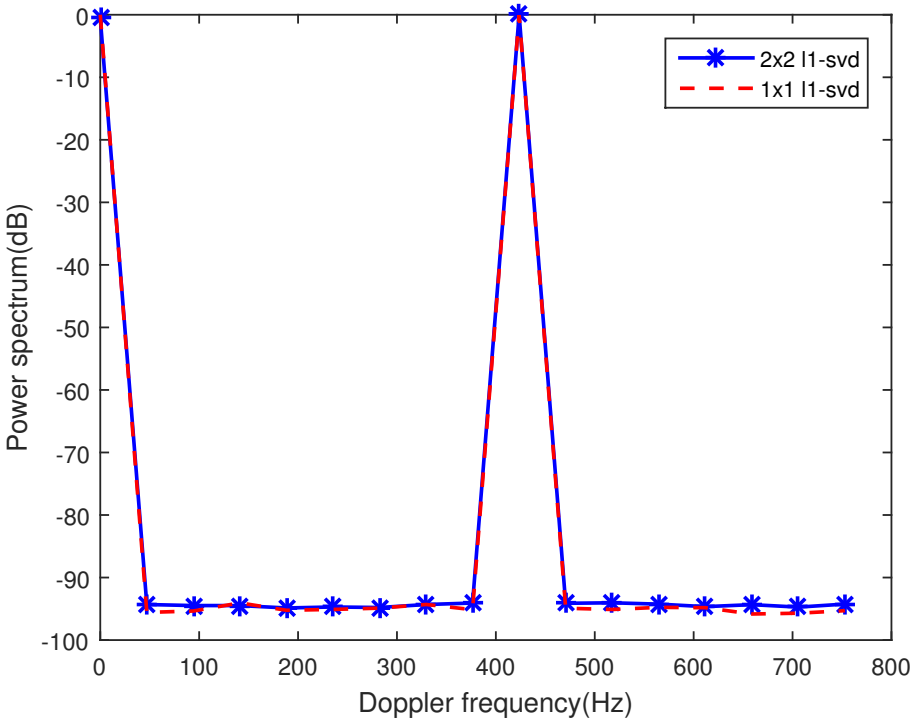

(a)

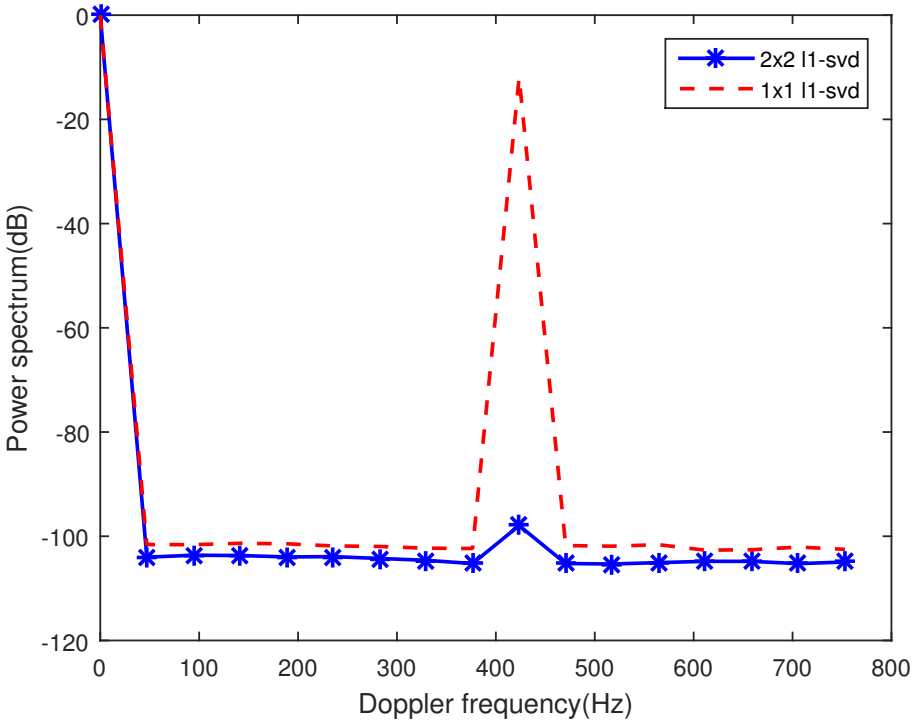

(b)

Figure 3.16: Instantaneous numerical results when applying centralised l_1-SVD over the MIMO and SISO systems in Doppler frequency domain where: (a) the power of direct path and target path are equal; and (b) the direct path power is 20 dB higher. The number of snapshots is 200.

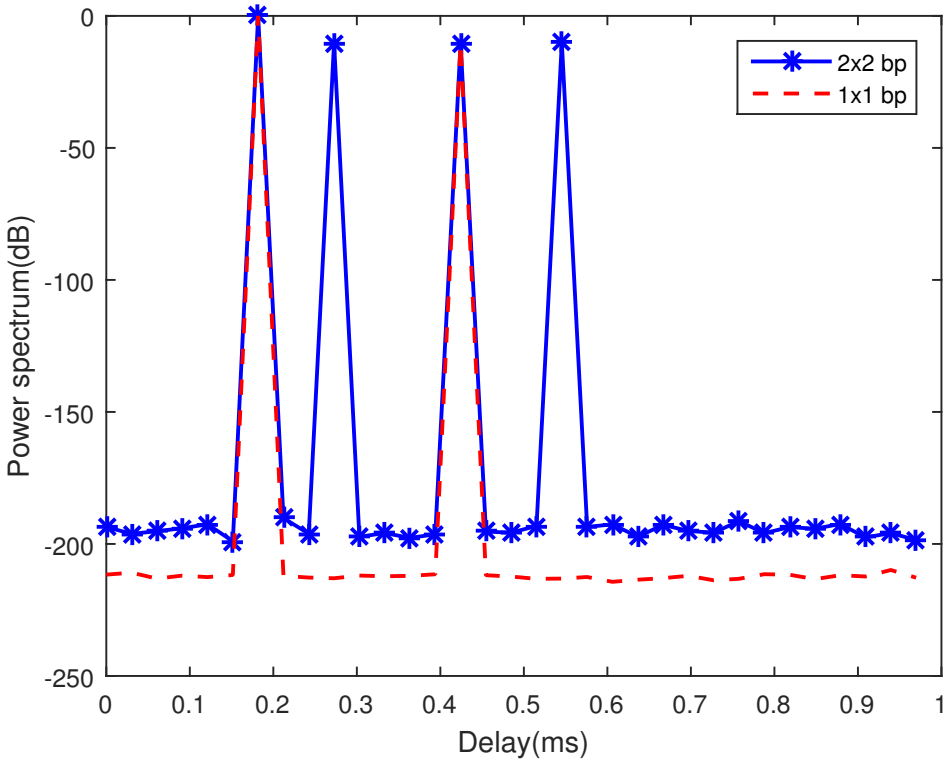

(a)

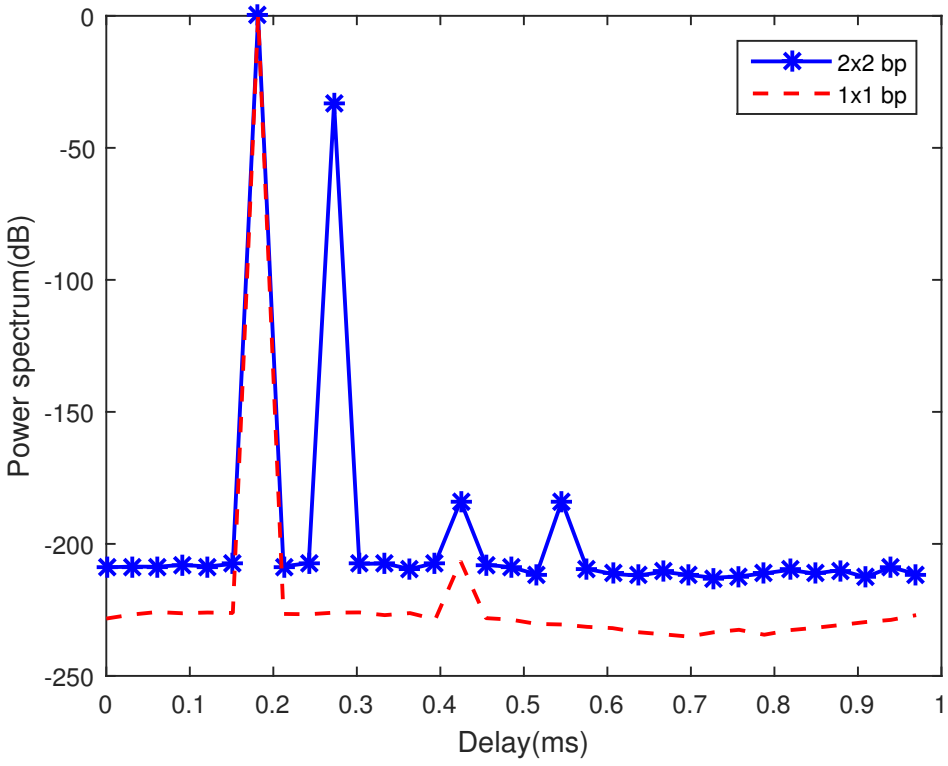

(b)

Figure 3.17: Instantaneous numerical results when applying centralised basis pursuit over the MIMO and SISO systems in delay time domain where: (a) the power of the direct path is 10 dB higher; and (b) the power of the direct path is 50 dB higher.

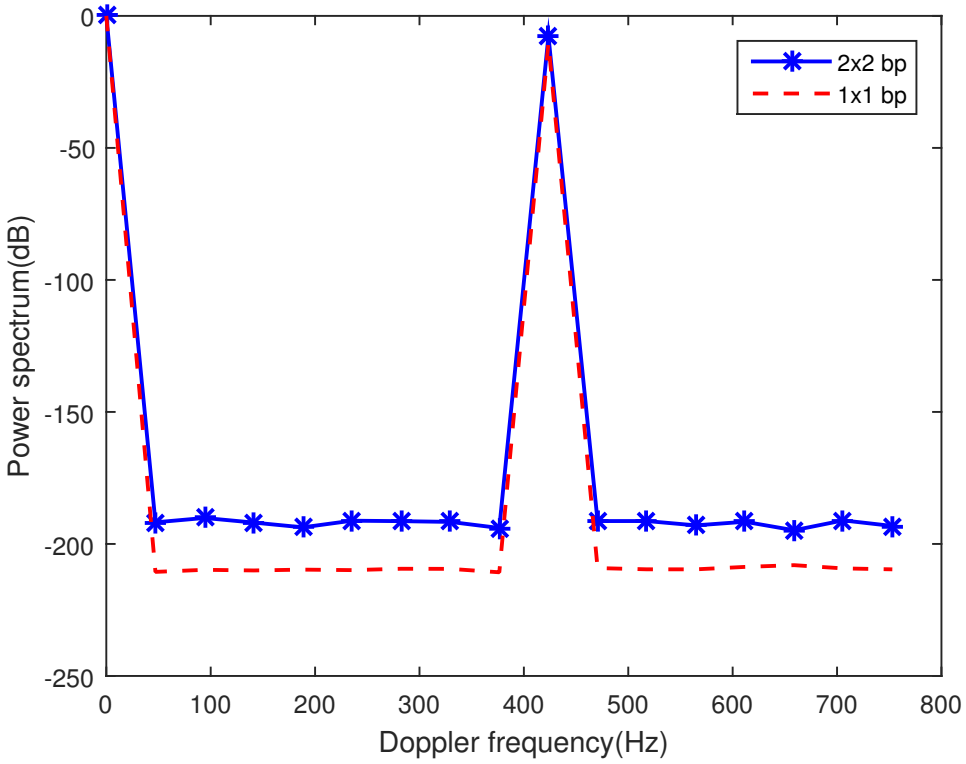

(a)

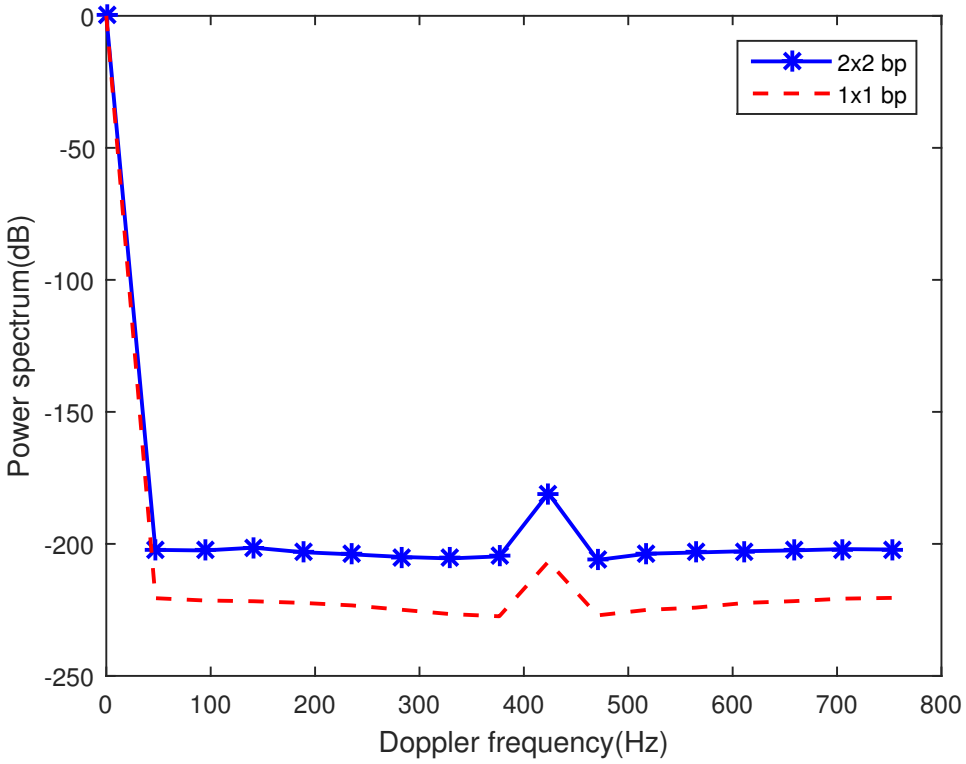

(b)

Figure 3.18: Instantaneous numerical results when applying centralised basis pursuit over the MIMO and SISO systems in the Doppler frequency domain where: (a) the power of the direct path is 10 dB higher; and (b) the power of the direct path is 50 dB higher.

In the MIMO scenario, the results display more peaks in the delay domain due to two illuminations from another transmitter. This is an advantage of using MIMO transceivers when the extracted parameters can determine the locations of the transmitters, and the target in the xy-plane by applying the available association techniques. In order to avoid data associations, this thesis performs centralised compressive sensing by stacking the received signals from each receive antenna together. The overcomplete matrix **B** is enlarged and the signals are reconstructed with the larger dimensions. In Fig. 3.15b, the target reflections from the MIMO scenario are decreased when the direct signal is stronger compared to the SISO version, whereas this impact is not displayed in Fig. 3.15a if the multipath powers are equal. This is similar to the simulation in Fig. 3.16a and Fig. 3.16b, l_1-SVD, with MIMO still exhibiting a problem. The Doppler signature of the detected signal for multiple antennas is much lower in power in Fig. 3.16b. This means that the target signature can be obviously captured if the power difference between the direct and target path is less than 20 dB. On the other hand, basis pursuit provides some promising results, as shown in Fig. 3.17a and Fig. 3.17b although the signal power difference reaches 50 dB as in Fig. 3.17b. In Fig. 3.18a and Fig 3.18b, the simulation results confirm the detection of the target at the same power difference. With a 50 dB difference in Fig. 3.18b, the system allows for the receiving of the reference signal without concerning the performance of the cancellation ability. The inferior l_1-SVD is caused by the correlation between noise in the channel as the number of transceivers increases. This also demonstrates that the centralised processing for widely separated antennas needs the association between the received signal.

Finally, the last set of figures concerns the extraction ability in a comparison between the MUSIC algorithm and l_1-SVD. Contour plots are utilised where the plots show the parameter values, such as time delays and Doppler frequencies. The greater the contour intensity, the stronger the power received. To demonstrate the exact scenario, Fig. 3.19a and Fig. 3.19b show that the expected sparse signal should be received at the first and the second radar receivers respectively. Fig. 3.20a and Fig. 3.20b display the extraction ability as seen from the first antenna, using l_1-SVD and MUSIC respectively, while the second antenna numerical simulation is shown in Fig. 3.21a and Fig. 3.21b. It is evident that l_1-SVD performs better than MUSIC as the correct location of path parameters are determined. On the other hand, in the Doppler domain, the contours extracted by the MUSIC algorithm are not solid and the flaws occur similarly for both antennas. The reason for the contour plot is to demonstrate how difficult it is for the received parameters

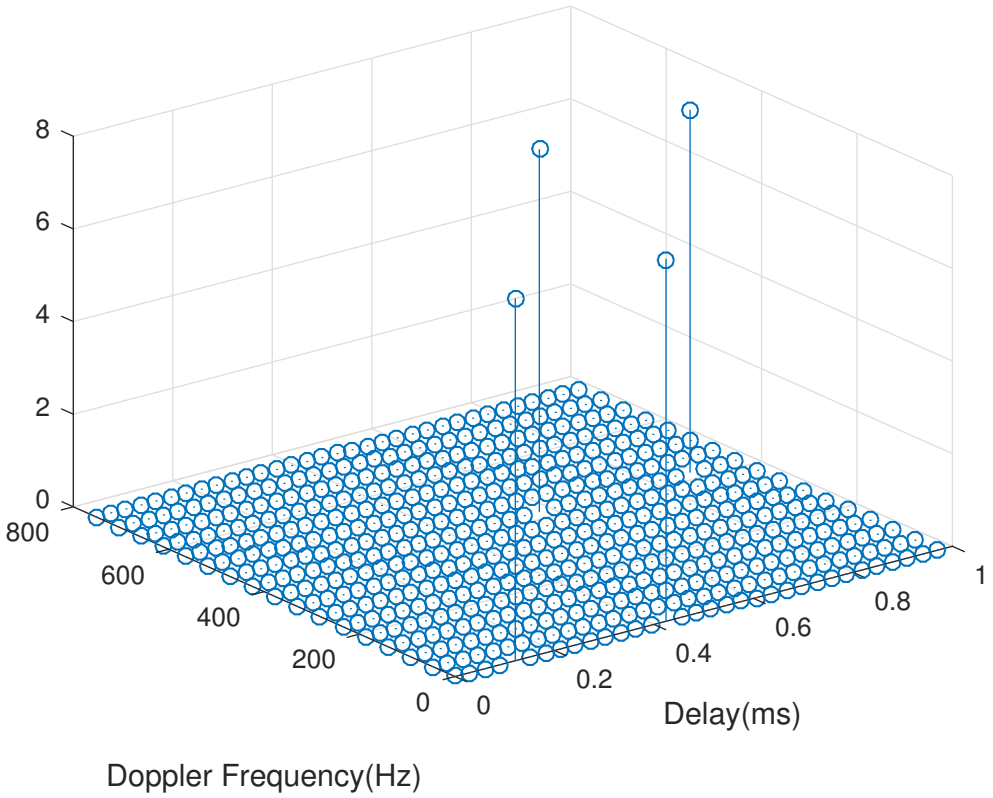

(a)

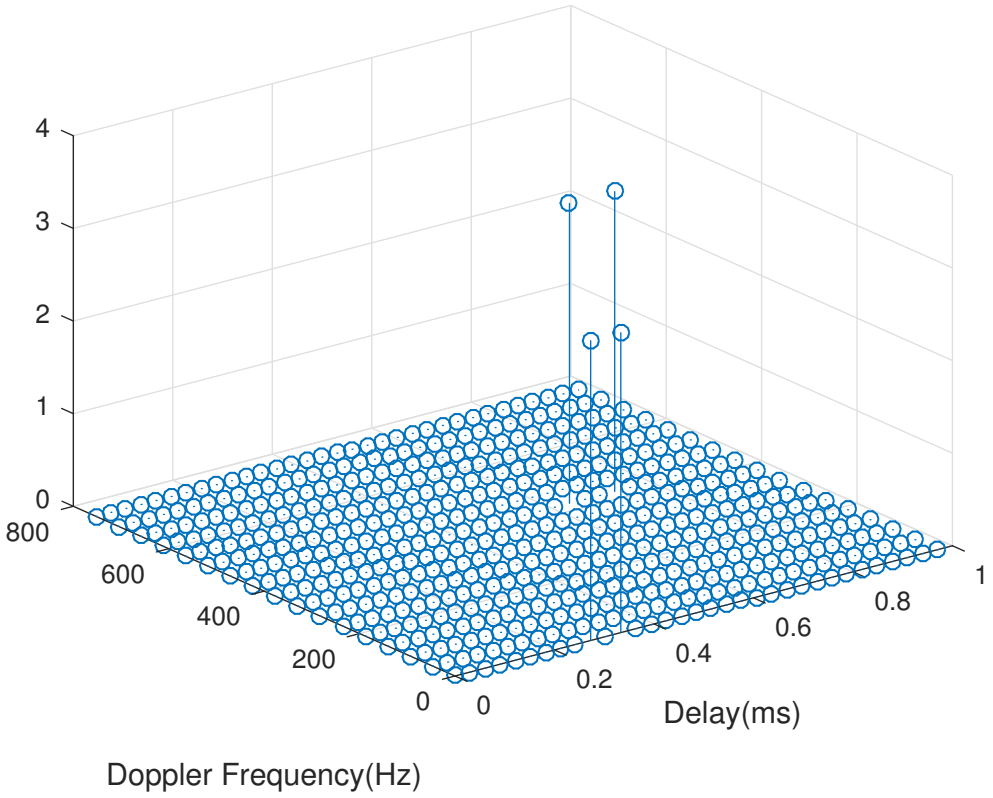

(b)

Figure 3.19: Original sparse signals for: (a) the first receiver; (b) the second receiver

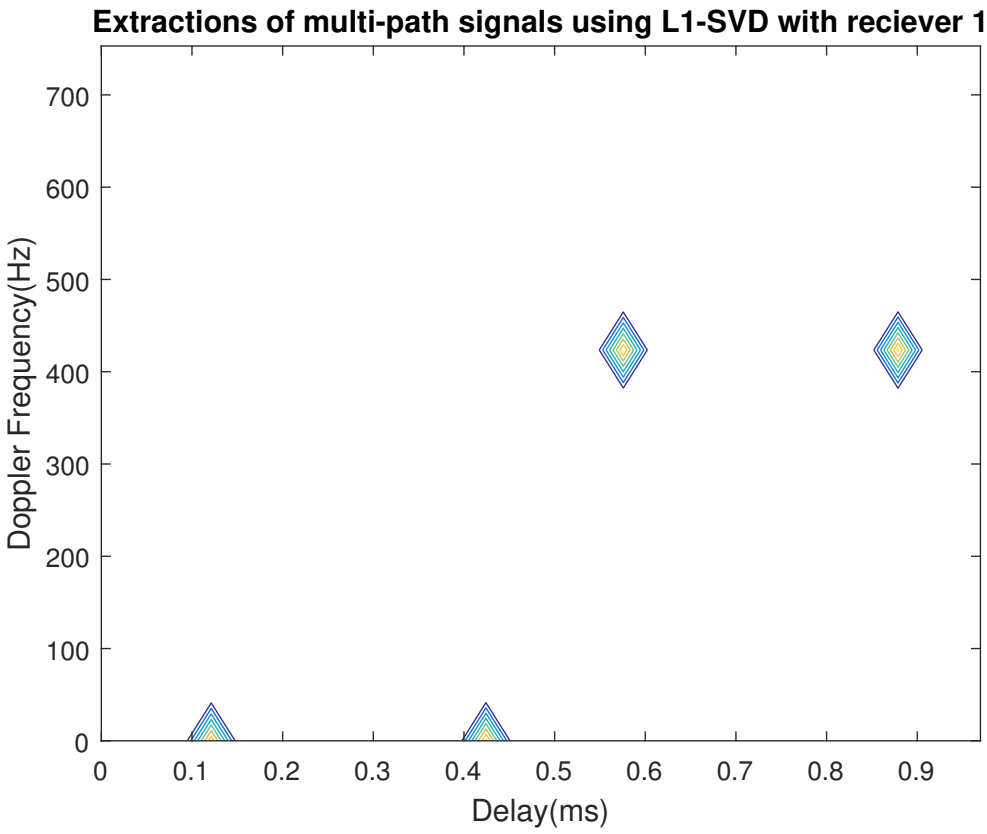

(a)

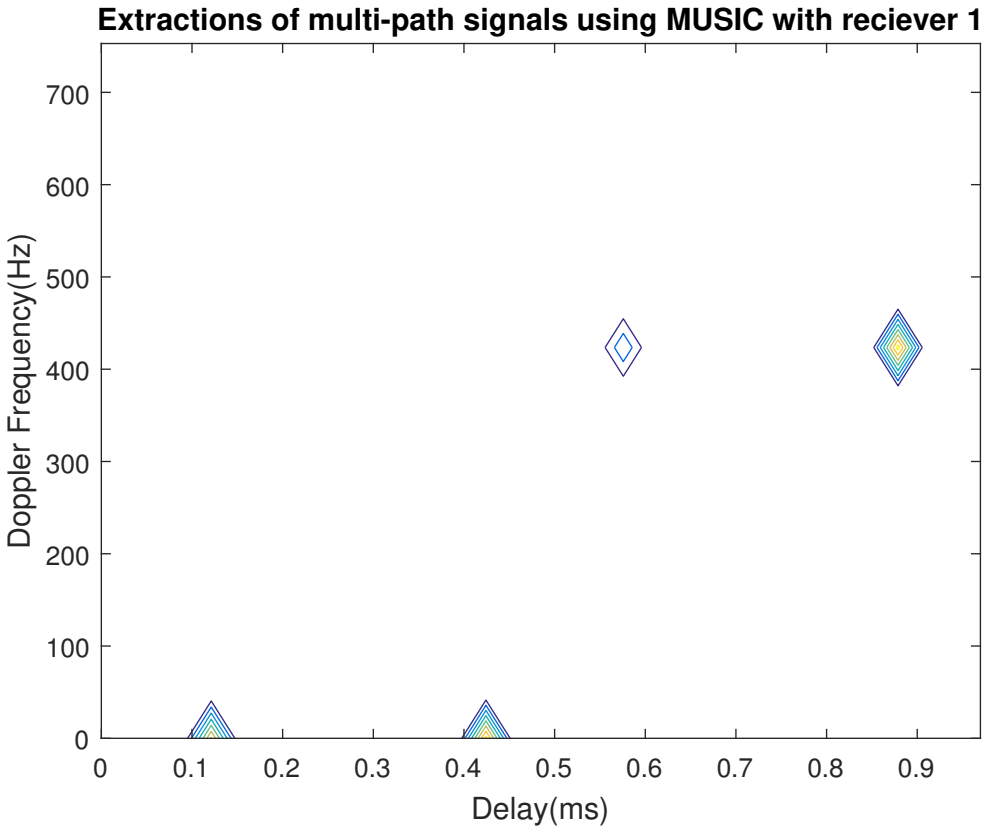

(b)

Figure 3.20: Contour plots for the first receiver applying: (a) l_1-SVD; (b) MUSIC

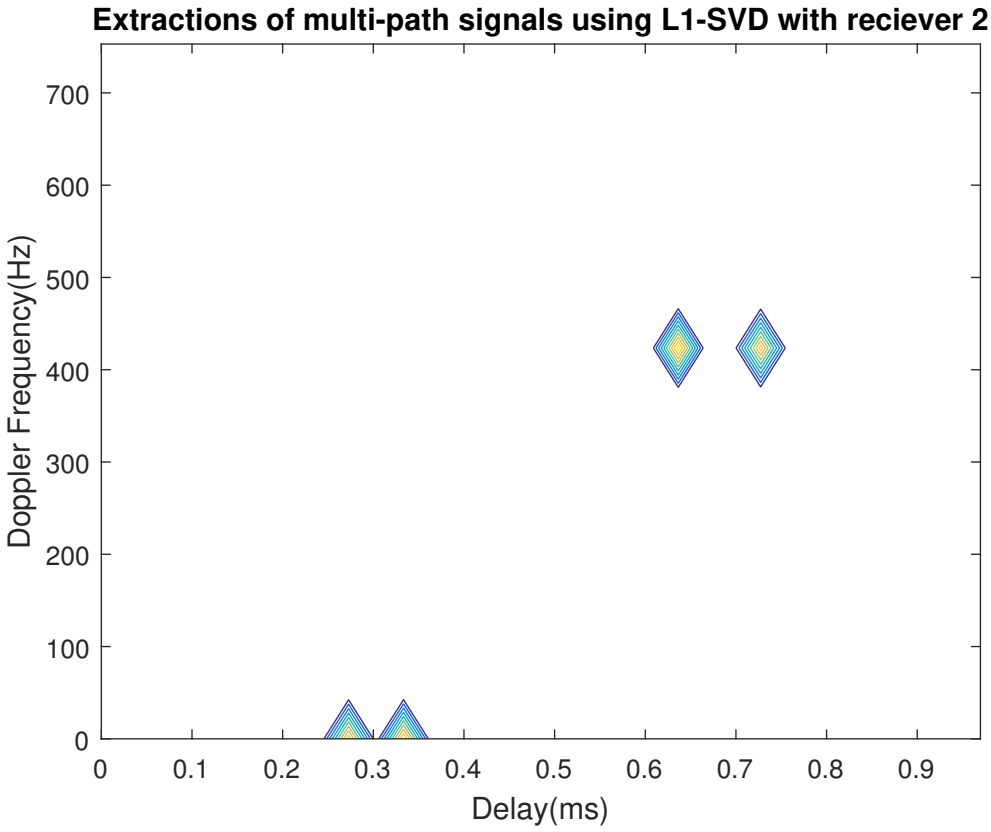

(a)

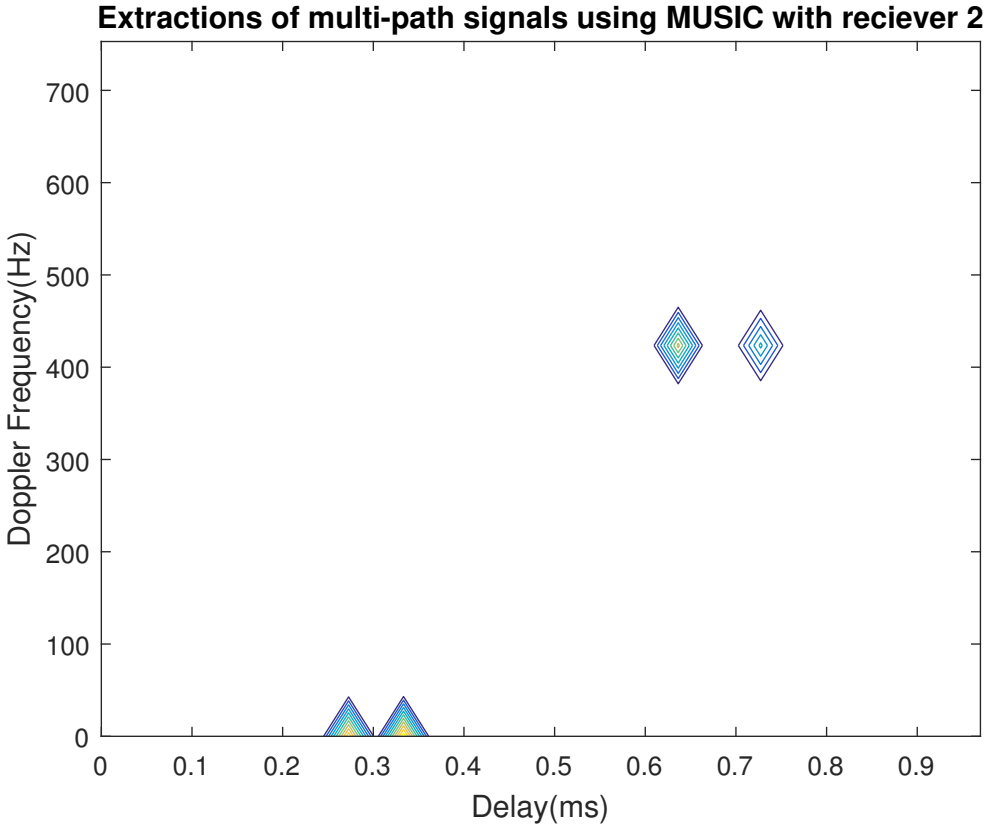

(b)

Figure 3.21: Contour plots for the second receiver applying: (a) l_1-SVD; (b) MUSIC

from different antennas to be combined without an impressive associated techniques. As this is beyond the scope of this thesis, however, the details of receiver association and localisation techniques will be discussed in future works.

3.6 Summary

In this chapter, the MIMO-OFDM passive radar setup is focused, in terms of widely-spread transceiver pairs. This thesis adapts the 2D signal model presented in the literature to derive MIMO passive radar equation. This chapter also provides basic concept of OFDM passive radar signal and channel model. With widely-separated antennas, the radars are suitable for distributed target detection, unlike the next chapter. 2D matched filter is also discussed and manipulated in MIMO configuration. Regarding signal extraction algorithms, compressive sensing methods with different number of snapshots are proposed in both SISO and MIMO scenarios. l_1-SVD has been applied to the multiple snapshots measurement signal and supplies impressive results compared to the MUSIC algorithm. However, the multiple samples CS did not provide satisfaction when multiple antennas were equipped and processor performs the algorithm centrally. As mentioned in [11], dealing with signals of multiple transmitters where it is not ensure which transmitters are belong to is not a trivial issue. In order to receive the expected diversity gain and accurate estimation, suitable association techniques are required. The idea of one-time sample CS become interesting and other algorithm should be discussed as Basis Pursuit requires much resources. The extracted parameters from this chapter are also not sufficient in target localisation, as the data from each receiver need to be associated. In [92], MIMO radars with co-located antennas increase the capability of parameter identification and allow the arrays to be applied with some adaptive techniques. Due to lacking of the joint parameters or the fact that beamformer is not feasible in widely-spread receivers, the next chapter presents co-located receivers, along with a new algorithm which is more efficient than the previous methods.

Chapter 4

OFDM passive radar using MIMO with co-located antennas

4.1 Introduction

In co-operating with the SFN, the 2D channel estimates of OFDM signals increase complexity in extracting and associating the signals with their source, because the same frequency is transmitted. The possibility of utilising 3D channel model becomes tempting, which was studied in [93] using MIMO co-located antennas. The co-located receiver requires less space than the separate platforms. Furthermore, in some applications, especially military operations, it is difficult to associate the data with each widely separated antennas. System security can be monitored centrally as the receivers are located in the same place.

Without the algorithm of data fusion between each widely-separated antenna, this research employs the antenna array receiver to improve parameter identifiability [92]. The 2D channel model for the OFDM waveforms is extended to 3D for extracting the angle of arrivals. Here, the signal extraction methods employ compressive sensing which was already presented in the passive radar signal processing [16]. Employing the CS theory, the 3D sparse signal can be analysed. A method which can be applied to increase the SINR should also be discussed. Array beamforming is an algorithm that has been utilised in many areas of research. The significant impact of beamforming starts from [57], where the MVDR technique is proposed. As the robustness of the system can be quantified by a gain against white noise caused by the uncorrelated errors, a quadratic inequality constraint on the array gain against the uncorrelated noise was also proposed in [57], where the output power condition on multiple linear equality constraints is diminished.

The projection of undecided weights in the subspace orthogonal to the linear constraints can be exploited. MVDR is also used in the direct position determination concept in the electromagnetic energy emitting source localisation [94]. This technique is an alternative to the maximum likelihood in case that the number of sources is unknown and their powers are fragile.

This chapter begins with the modelling of the system and signal employed in co-located receivers. In contrast to the 2D matched filter in widely-spread receivers, this chapter proposes 3D matched filter followed by a discussion of sensing matrix used for CS algorithm. Then, a statistical-based compressive sensing algorithm for signal extraction, namely, Fast-BesselK is presented. It is a method relied on the Bayesian Compressive Sensing, which is impressive in a modern area of research [95]. The Cramer-Rao Lower Bound for this 3D channel estimates is also derived. This chapter also presents the application of compressive beamforming. The simulations at the end of this chapter starts by comparing the extraction output using multiple time samples CS, l_1-*SVD*, between 2D and 3D channel estimates models. For the 2D problem, it is shown in the previous chapter that the CS-based method is suited for an application with the passive radar. Applying to 3D problem, however, the CS-based algorithms do not provide satisfactory results. Fast-BesselK results are illustrated and demonstrate the 3D signal reconstruction with the analysis. Beamforming results and the illustrations of CRLB conclude this chapter.

4.2 System model for co-located receivers

A MIMO-OFDM passive radar system is shown in Fig. 4.1. The omnidirectional MIMO transmitter is comprised of n_t distributed BSs while the MIMO receiver is equipped with an array of n_r collocated antennas. The OFDM signal being transmitted has parameters according to the DAB standard (see Table 2.1).

4.2.1 Three-dimensional receiver signal model

Using the transmitter signal discussed in Section 3.2.1, each of the components in (3.8) will now be discussed individually. First assume that at the transmitter, the transmit power is P_k and any transmit antenna gain is $G_{k(\cdot)}$, hence the (linear) Effective Isotropic Radiated Power (EIRP) of k-th communication transmitter is: $P_k G_{k(\cdot)}$. Next, $\tau_{km} = D_{km}/c$ is the time delay as the signals travel the distance, D_{km}, from the k-th BS to the m-th Uniform Linear Array (ULA) receiver element. ϕ_k is the angle of arrival of each k-th transmitter's

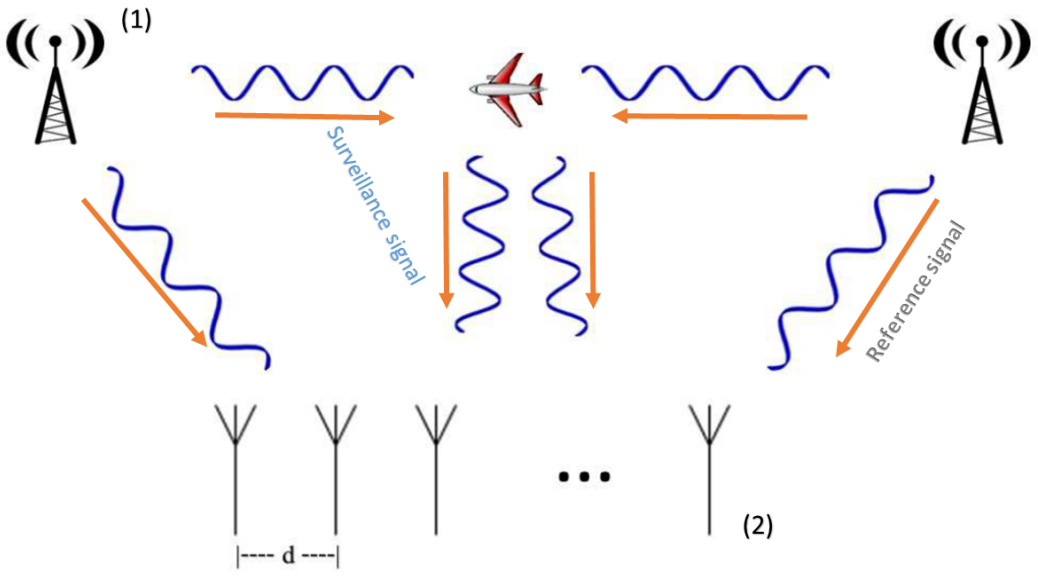

Figure 4.1: MIMO passive radar system model. (1) is the OFDM base station and (2) is a co-located receive antenna

ray. v_{rel} refers to the relative velocity of the target and c is the speed of light.

Reference Signal: The expected reference signal observed at the m-th receive antenna can be written:

$$x_r^{(m)}(t) = \sum_{k=1}^{n_t} x_r^{k(m)}(t)$$

$$= \sum_{k=1}^{n_t} \frac{\sqrt{P_k} G_{km}}{D_{km}(t)} x^{k(m)}(t - \tau_{km}(t)) e^{j2\pi[a_{km} f^k t + (m-1)\frac{d}{\lambda_k}\sin(\phi_k)]}, \tag{4.1}$$

where a_{km} means the ratio between relative velocity and speed of light ($= v_{rel}^{k(m)}/c$). The Doppler shift with respect to the (k,m)-th transmitter/receiver pair is defined: $f_d^{k(m)} = a_{km} f^k$, where f^k denotes the narrowband carrier frequency of k-th transmitting BS.

Surveillance (Target) signal: The target is thought of as being composed of a series of Q unresolvable moving scatterers. As a result, the expected signal received at the m-th antenna is expressed as:

$$x_s^{(m)}(t) = \sum_{k=1}^{n_t} x_s^{k(m)}(t)$$

$$= \sum_{k=1}^{n_t} \sum_{q=1}^{Q} \frac{\sqrt{P_k} G_{kq} \sigma_{kq}}{D_{kq}(t) D_{qm}(t)} x^{k(m)}(t - \tau_{kq}(t) - \tau_{qm}(t)) e^{j2\pi([a_{kq}+a_{qm}] f^k t + (m-1)\frac{d}{\lambda_k}\sin(\phi_q))},$$

(4.2)

where D_{kq} is the distance between the k^{th} BS and q^{th} target scatterer and D_{qm} is distance between the q^{th} target scatterer and the m^{th} receiver. The parameters of time delays (τ_{kq}

and τ_{qm}), along with the range-rate ratios (a_{kq} and a_{qm}), are declared in the same way as the reference signal parameters above. Taking a distributed targets approach similar to [96], the fading contributions of each target scatterer are modelled using the term, σ_{kq}, which is defined as a function of RCS, $\sigma(x_0, y_0, z_0)$, with respect to the source of transmitted signal k, where:

$$\sigma(x_0, y_0, z_0) = \sum_{q=1}^{Q} \alpha_q \delta(x_0 - x_q)\delta(y_0 - y_q)\delta(z_0 - z_q), \tag{4.3}$$

where a centre of mass of the target locates at the point (x_0, y_0, z_0) and a random variable $\alpha_q \sim \mathcal{N}_c(0,1)$ is denoted and $\delta(\cdot)$ denotes the Dirac delta function. For less complexity, the simulation in this thesis assumes the point target and also have an assumption that the power scattered by the target is much lower than the reference and clutter signal.

In passive radar [5], the spatially dependent bistatic RCS, target dynamics and the radar design parameters can be combined into the target detection and location. Using processing approaches, targets can be detected in range, Doppler and angle. The target bistatic RCS, σ_{kq} may differ from the monostatic version, especially for stealth targets. The forward scatter region is determined as the bistatic angle can be expanded to 180° and the target cross-sections can be significantly raised. Refer to Babinet's principle, the forward scatter from a perferctly-absorbing target is comparable to a target-shaped aperture in a perfectly-conducting sheet. If $\mathscr{A}$ designates a physical cross-sectional area of a target, a radar cross-section can be $\sigma_{kq} = 4\pi\mathscr{A}^2/\lambda^2$ whereas $\phi_{kq} = \lambda/d_t$ denotes the angular width of the scattered signal in the horizontal or vertical plane, where the target linear dimension in the corresponding plane is denoted by d_t. In [5], it is also shown that the forward scatter is more suitable if low frequencies are operated. This sufficiently wide angular range leads to an accomplishment in target detection. The range approximation, however, is not straightforwardly calculated employing forward scatter.

Clutter signal: The clutter signal arises from reflections from non-target related scatterers. Assuming P_c of these statistically independent scatterers, the clutter signal can be written as:

$$x_c^{(m)}(t) = \sum_{k=1}^{n_t} x_c^{k(m)}(t)$$

$$= \sum_{k=1}^{n_t} \sum_{c=1}^{P_c} \frac{\sqrt{P_k} G_{kc} \sigma_{kc}}{D_{kc} D_{pm}(t)} x^{k(m)}(t - \tau_{kc}(t) - \tau_{cm}(t)) e^{j2\pi([a_{kc}+a_{cm}]f^k t + (m-1)\frac{d}{\lambda_k}\sin(\phi_c))}. \tag{4.4}$$

As seen from (4.1), (4.2) and (4.4), the terms: $\frac{\sqrt{P_k}G_{km}}{D_{km}(t)}$, $\frac{\sqrt{P_k}G_{kq}\sigma_{kq}}{D_{kq}(t)D_{qm}(t)}$, $\frac{\sqrt{P_k}G_{kc}\sigma_{kc}}{D_{kc}D_{pm}(t)}$ quantify a different attenuation depending on each category of received signal components between a transmitter k and an antenna element m, denoted as $A_{ref}^{k(m)}$, $A_q^{k(m)}$ and $A_c^{k(m)}$ respectively. Obviously, these signal components perform a multipath scenario within each transceiver pair. Therefore, the attenuation at the received element can be derived as $A_p^{k(m)}$. Now, substituting (4.1), (4.2) and (4.4) into (3.8), a complete expression for received signal may now be written:

$$y^{(m)}(t) = \sum_{k=1}^{n_t} \sum_{p}^{N_p} A_p^{k(m)}(t) e^{j2\pi(a_p^{k(m)} f^k t + (m-1)\frac{d}{\lambda_k}\sin(\phi_p^{k(m)}))} x^{k(m)}(t - \tau_p^{k(m)}(t)) + w^{k(m)}(t). \tag{4.5}$$

Regarding (4.5), apart from the attenuation mentioned above, three substantial parameters are also replaced. Their subscripts are altered to p instead of each individual category. This representation displays multipath scenario which is caused by the direct signal, the reflected signals from the clutters and the target where the total number of path is denoted by N_p.

4.2.2 Three-dimensional channel estimation using matched filter

The idea of matched filter in Section 2.1 leads to the following proposition.

Proposition 1. *Given the idea of matched filtering with respect to a known transmitted waveform, the matched filter output may be written in terms of a 3D Discrete Fourier Transform of:*

$$H_{n,i}^{k(m)} = A_0^{k(m)}[s_{k(i)}[n]]^2 T e^{j2\pi[a_0^{k(m)} f^k i T' + (m-1)\frac{d}{\lambda_k}\sin\phi_0^{k(m)} - n\Delta f \tau_0^{k(m)}]}, \tag{4.6}$$

where $H_{n,i}^{k(m)}$ is the channel estimates of MIMO-OFDM passive radar using co-located antennas.

The proof of the above proposition is in Section A.2. In simulation, a multidimensional Fourier transform can be performed using a function *fftn(x)* in MATLAB. In reality, however, to examine the matched filter output might require all of the incoming OFDM subcarriers and blocks. Therefore, a sensing method which employs sub-Nyquist sampling is of interest.

4.3 Application of compressive sensing

As mentioned, one of the key aims of this work is to extract the 3D target parameters in a computationally tractable and efficient manner. The concept of sparse signal manipulation is first introduced followed by a discussion about the sensing matrix in compressive sensing. Furthermore, the Bayesian compressive sensing technique, known as the Fast-BesselK algorithm, is then described.

4.3.1 Sparse representation

Signals received by MIMO passive radar receiver can be represented as a Fourier transform comprising 3D channel target parameters (4.6). Within this Fourier transform, the received signal is composed of a few of non-zero elements while all the other values are close to zero. This kind of sparsity initiates the idea of using compressive sensing methods for signal reconstruction. With the CS, sub-Nyquist sampling rates are permitted. This means the number of measurements at the receiver will be reduced. Assume $\mathbf{x}$ is sensed linearly through projections on the rows of a sensing matrix $\Phi^{\dagger} \in \mathbb{C}^{N'L' \times NL}$, for each antenna m, consider the measurement $\mathbf{y}^{(m)} \in \mathbb{C}^{N'L'}$ which can be written as:

$$\mathbf{y}^{(m)} = \Phi^{\dagger}\mathbf{x} + w^{(m)}, \tag{4.7}$$

where $\mathbf{x} \in \mathbb{C}^{NL}$ corresponds to the matched filter output of the OFDM signal whose dimensions relate to the number of subcarriers(N) and the number of blocks(L). The sensing matrix which is designed in this work is discussed as follows. Taking a similar approach to the spatial smoothing method in [32], a subarray matrix, $\mathbf{G}^{k(m)}$, is now initialised:

$$\mathbf{G}^{k(m)}(\hat{\tau}, \hat{a}, \hat{\phi}) = \begin{bmatrix} g_{1,1}^{k(m)} & \cdots & g_{1,L'}^{k(m)} \\ \vdots & & \vdots \\ g_{N',1}^{k(m)} & \cdots & g_{N',L'}^{k(m)} \end{bmatrix} \tag{4.8}$$

The notation N' and L' stand for the sensing dimensions where: $N' \ll N$, $L' \ll L$. It should be noted that the number of antennas n_r is less than the possible values of angle of

arrivals ϕ. Regarding the elements of the subarray matrix, these terms are defined:

$$g_{n,i}^{k(m)}(\hat{\tau},\hat{a},\hat{\phi}) = e^{j2\pi[\hat{a}f^k iT' + (m-1)\frac{d}{\lambda_k}\sin\hat{\phi} - n\Delta f\hat{\tau}]}, \tag{4.9}$$

where $(\hat{\tau},\hat{a},\hat{\phi})$ corresponds to the expected estimated target parameter. Next, a vectorization operation is applied that a vector is generated from the subarray matrix in a column-wise manner in order to acquire a steering vector $\mathbf{b}^{k(m)}(\hat{\tau},\hat{a},\hat{\phi}) = \text{vec}\{\mathbf{G}^{k(m)}(\hat{\tau},\hat{a},\hat{\phi})\}$. By stacking the steering vectors over each other, the channel estimates in (4.6) may be rewritten as:

$$\mathbf{h}^{(m)} = \sum_{k=1}^{n_t}\sum_{p} A_p^{k(m)}\mathbf{b}^{k(m)}(\hat{\tau}_p,\hat{a}_p,\hat{\phi}_p). \tag{4.10}$$

By performing the following manipulations, $\mathbf{h}^{(m)}$ can be rewritten in the same form as the well-known CS equation in (4.7), where the channel estimates are applied as the measurements $\mathbf{y}^{(m)}$ according to [16], thus re-arrange $\mathbf{B}_{N_p}^{k(m)}$ and define $\alpha_{N_p}^{k(m)}$ as:

$$\mathbf{B}_{N_p}^{k(m)} = [\mathbf{b}^{k(m)}(\hat{\tau}_1,\hat{a}_1,\hat{\phi}_1)\ldots\mathbf{b}^{k(m)}(\hat{\tau}_{N_p},\hat{a}_{N_p},\hat{\phi}_{N_p})] \tag{4.11}$$

$$\alpha_{N_p}^{k(m)} = [A_1^{k(m)}\ldots A_{N_p}^{k(m)}]^T, \tag{4.12}$$

where $\alpha_{N_p}^{k(m)}$ can be referred to $\mathbf{x}$ in (4.7). Thus, $\mathbf{h}^{(m)}$ can be rewritten as:

$$\mathbf{h}^{(m)} = \sum_{k=1}^{n_t}\mathbf{B}_{N_p}^{k(m)}\alpha_{N_p}^{k(m)} + \mathbf{w}^{k(m)}. \tag{4.13}$$

In theory, it may be possible to use a least-squares method to solve for $\alpha_{N_p}^{k(m)}$ however the approach taken here will be to construct a larger list of possible parameters, which will in turn make the sensing matrix $\mathbf{B}^{k(m)}$ fat. The overall process described here is depicted in Fig.4.2 and in the analysis that follows, CS algorithms will be used to extract the target parameters from $\mathbf{B}^{k(m)}\alpha^{k(m)}$. It should be clear at this point that $\mathbf{B}^{k(m)}\alpha^{k(m)}$ contains many zero elements, i.e., has a sparse structure, due to the opening comments in this subsection regarding 3D Fourier transform.

4.3.2 Discussion of sensing matrix for OFDM passive radar

Apart from the sparsity in the vector to be recovered, the numerical structure of the sensing matrix, $\mathbf{B}^{k(m)}$, also needs to be considered. For CS algorithms to be applicable, the sensing matrix needs to satisfy two important properties known as the null space property (NSP) and restricted isometry property (RIP) [97]. As mentioned in the reference (see theorem 2.12), both Gaussian and Bernoulli random matrices satisfy the NSP and

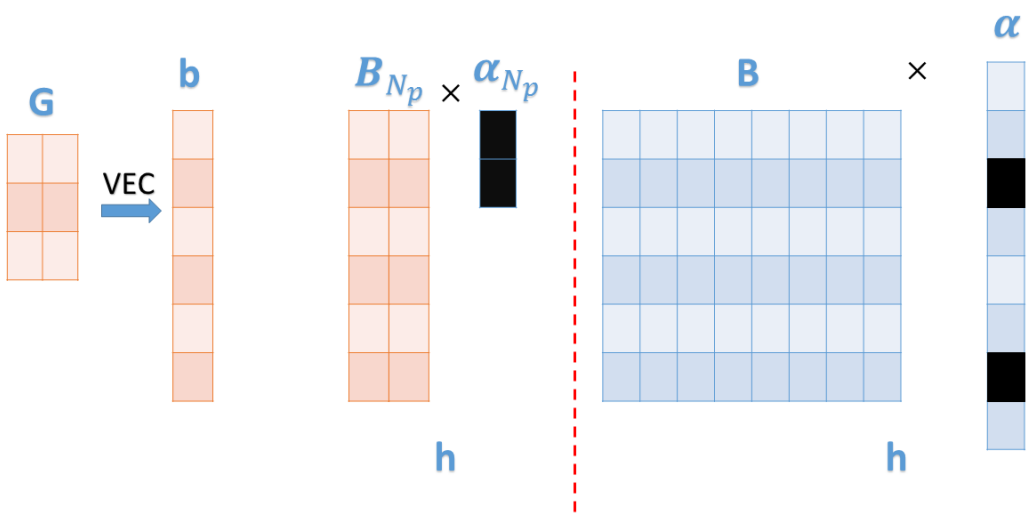

Figure 4.2: Illustration of sparse representation and manipulation for passive radar.

the RIP properties, however, it is not clear whether a MIMO passive radar will provide measurements with such a convenient structure. In order to ensure that $\mathbf{B}^{k(m)}$ will satisfy NSP and RIP properties, it should be noted firstly that it is orthonormal in structure, due to the fact that is derived from a DFT, and using this in combination with theorem 4.4 in [97] will facilitate NSP and the RIP provided that the number of measurements, N_{mes}, satisfies:

$$N_{mes} \geq C\mathbf{coh}^2 N_p \ln^4(N_\alpha), \tag{4.14}$$

N_{mes} is in fact equal to the product of N', L' and n_r. $C > 0$ is a suitable constant, N_p is the number of multipath components and determines the sparsity in the vector $\alpha^{k(m)}$ which totally consists of N_α elements. In this work, **coh** stands for the coherence between the random measurement basis and Fourier sparsity basis, which can be defined as:

$$\mathbf{coh} = \sqrt{N_\alpha} \max_{1 \leq i,j \leq N_\alpha} |\langle b_i, \mathscr{F}_j \rangle|. \tag{4.15}$$

The expression in (4.14) guarantees the sparse recovery with probability of at least $1 - N_\alpha^{-(C_1/C_2)\ln^3(N_\alpha)}$, where $C_1, C_2 > 0$ are some constants.

4.3.3 Bayesian-based compressive sensing: Fast-BesselK method

In [90] and [98], the viability of the basis pursuit (BP) algorithm, the interior point method and the l_1-SVD algorithm was examined in an attempt to produce algorithmic tractability. It was found that the results for 2D parameter extraction were acceptable, but 3D parameter extraction was not tractable. Along with this issue, problems arose in the low SNR regime. In contrast to the convex optimisation used in this work, the BP equation has also

been solved by other techniques, such as iterative shrinkage [99], where it was used in time-domain least square channel estimator for the OFDM system with IQ imbalances. Its complexity, however, is still greater than matching pursuit and other CS methods. Although, adaptive orthogonal matching pursuit is applied in the full duplex OFDM systems as well [100], it has been shown in previous passive radar works that the reconstruction signal is subject to more leakages and errors than BP. Therefore, statistical engagement is of interest.

In [98] it was seen that a common CS algorithm, known as the basis pursuit (BP) algorithm, was too computationally expensive for 3D target parameter extraction. In this subsection, Bayesian compressive sensing (BCS) [101] is introduced to solve this problem. BCS adopts a two-layer hierarchical prior model, where a conditional prior and a hyperprior probability density function (PDF) are associated. Previously, BCS has been applied to real-valued data while MIMO passive radar utilises complex data. This thesis, therefore, employs the Fast-BesselK [102] in order to reconstruct an expected signal from noisy MIMO measurements. In the following, the derivation of a model as a probabilistic expression is discussed. The objective function is then considered and finally the parameter updates are accomplished using an Expectation-Maximization (EM) [103] algorithm.

Probabilistic Model: The BesselK model for (4.13) amplified by the 2-Layer prior for α is written as:

$$p(\mathbf{h},\alpha,\gamma) = p(\mathbf{h}|\alpha)p(\alpha|\gamma)p(\gamma). \tag{4.16}$$

Given that $\mathscr{CN}(\cdot|\mathbf{x},\mathbf{Y})$ signifies a multivariate complex Gaussian PDF with mean vector $\mathbf{x}$ and covariance matrix $\mathbf{Y}$, then $p(\mathbf{h}|\alpha) = \mathscr{CN}(\mathbf{h}|\mathbf{B}\alpha,\beta^{-1}\mathbf{I})$ for the complex data system. β indicates the noise precision and the identity matrix is denoted by $\mathbf{I}$. The conditional prior pdf $p(\alpha|\gamma)$ is chosen to partition in a product of zero-mean Gaussian PDF as $p(\alpha|\gamma) = \prod_i p(\alpha_i|\gamma_i)$, where

$$p(\alpha_i|\gamma_i) = (\frac{\rho}{\pi\gamma_i})^{\rho} e^{(-\rho\frac{|\alpha_i|^2}{\gamma_i})}. \tag{4.17}$$

When α is complex, the assignment $\rho = 1$ is made. It is mentioned in [102] that a sparsity-inducing prior for real weights is not automatically sparsity-inducing for complex weights. The mixing density $p(\gamma)$ is taken by $p(\gamma) = \prod_i p(\gamma_i;\varepsilon,\eta)$ with $p(\gamma_i;\varepsilon,\eta) \triangleq Gamma(\gamma_i;\varepsilon,\eta)$. The prior PDF for α can be written as $p(\alpha;\varepsilon,\eta) = \int p(\alpha|\gamma)p(\gamma;\varepsilon,\eta)d\gamma =$

$\prod_i p(\alpha_i;\varepsilon,\eta)$, where

$$p(\alpha_i;\varepsilon,\eta) = \frac{2(\rho\eta)^{\frac{(\varepsilon+\rho)}{2}}}{\pi^{\rho}\Gamma(\varepsilon)}|\alpha_i|^{\varepsilon-\rho}K_{\varepsilon-\rho}(2\sqrt{\rho\eta}|\alpha_i|). \tag{4.18}$$

and $K_v(\cdot)$ is the modified Bessel function of the second kind and order v. By definition of the gamma PDF, $Gamma(\cdot|y,z) = \frac{z^y}{\Gamma(y)}x^{y-1}\exp(-zx)$, where y is a shaping parameter and z is a rate parameter.

Cost Function: The vector, $\mathbf{h}$, is used to establish the Maximum-a-Posteriori (MAP) estimate of γ as:

$$\begin{aligned}\hat{\gamma}(\mathbf{h}) &= \arg\max_{\gamma} p(\gamma|\mathbf{h}) \\ &= \arg\max_{\gamma} \log \int p(\mathbf{h}|\alpha)p(\alpha|\gamma)p(\gamma)d\alpha. \end{aligned}\tag{4.19}$$

Closed-form solution is not available for the MAP estimate in (4.19). The Relevance Vector Machin (RVM) [104], an iterative inference method, must be applied. Employing the framework in [105], this algorithm is considered as a fast version. Then, the minimizer of

$$\mathscr{L} \triangleq \rho\mathbf{h}^H\mathbf{C}^{-1}\mathbf{h} + \rho\log|\mathbf{C}| - \log p(\gamma), \tag{4.20}$$

is the estimator of γ, i.e., $\hat{\gamma}$, where $\mathbf{C} \triangleq \beta^{-1}\mathbf{I} + \mathbf{B}\Gamma\mathbf{B}^H$ and $\Gamma = diag(\gamma)$. Given $\hat{\Gamma} = diag(\hat{\gamma}(\mathbf{h}))$ and the expectation with respect to the pdf $p(\mathbf{a})$ is defined as: $\langle\cdot\rangle_{p(\mathbf{a})}$. The estimator of α is:

$$\hat{\alpha}(\mathbf{h}) = \langle\alpha\rangle_{p(\alpha|\mathbf{h};\hat{\gamma}(\mathbf{h}))} = (\mathbf{B}^H\mathbf{B} + \beta^{-1}\hat{\Gamma}^{-1})^{-1}\mathbf{B}^H\mathbf{h} \tag{4.21}$$

Correspondingly, by enforcing Theorem 2 in [106], $\hat{\alpha}(\mathbf{h})$ is the minimizer of

$$\mathscr{L}(\alpha) \triangleq \rho\|\mathbf{h} - \mathbf{B}\alpha\|_2^2 + \beta^{-1}r(\alpha), \tag{4.22}$$

with $r(\alpha) = \sum_i r(\alpha_i)$ is the penalty function, where:

$$r(\alpha_i;\varepsilon,\eta) = \min_{\gamma_i}\{\rho\frac{|\alpha_i|^2}{\gamma_i} + \rho\log(\beta^{-1}+\gamma_i) + (1-\varepsilon)\log\gamma_i + \eta\gamma_i\} \tag{4.23}$$

Estimation using EM-based Sparse Bayesian Inference: The EM algorithm handles $\{\alpha,\mathbf{h}\}$ as the complete data for γ. An estimate of γ, which is calculated in the M-step is the maximizer of:

$$\langle\log p(\mathbf{h}|\alpha)p(\alpha|\gamma)p(\gamma)\rangle_{p(\alpha;\hat{\gamma})} \tag{4.24}$$

with $p(\alpha|\hat{\gamma})$ already calculated in the E-step. The parameter β is encompassed in the framework since it notably affects the sparsity-inducing property on $r(\alpha)$. This means to find the MAP estimate of $\{\gamma,\beta\}$, which is the maximizer of

$$\mathscr{L}(\gamma,\beta) = \log p(\mathbf{h},\gamma,\beta) = \log(p(\mathbf{h}|\gamma,\beta)p(\gamma)p(\beta)). \tag{4.25}$$

It is necessary that $\{\alpha,\mathbf{h}\}$ be the complete data for $\{\gamma,\beta\}$. From this, the EM algorithm solves the conditional expectation

$$\langle \log p(\mathbf{h},\alpha,\gamma,\beta)\rangle_{p(\alpha|\mathbf{h},\gamma^{[t]},\beta^{[t]})} \tag{4.26}$$

where $p(\alpha|\mathbf{h},\gamma^{[t]},\beta^{[t]}) = \mathscr{CN}(\alpha|\mu^{[t]},\Sigma^{[t]})$. The notation $(\cdot)^{[t]}$ designates the estimate of the argument at iteration t. The parameters of the conditional pdf of α indicate

$$\Sigma^{[t]} = (\beta^{[t]}\mathbf{B}^H\mathbf{B} + (\Gamma^{[t]})^{-1})^{-1}, \tag{4.27}$$

$$\mu^{[t]} = \beta^{[t]}\Sigma^{[t]}\mathbf{B}^H\mathbf{h}. \tag{4.28}$$

Given that N_α refers to the total number of α elements (or columns of $\mathbf{B}$) and $i = 1,\ldots,N_\alpha$, it is possible to subsequently update the estimate of $\{\gamma,\beta\}$ from eqn (4.26) to acquire:

$$\gamma_i^{[t+1]} = \frac{\varepsilon-\rho-1+\sqrt{(\varepsilon-\rho-1)^2+4\rho\eta\langle|\alpha_i|^2\rangle^{[t]}}}{2\eta}, \tag{4.29}$$

$$\beta^{[t+1]} = \frac{N'L'n_r}{\|\mathbf{h}-\mathbf{B}\mu^{[t]}\|_2^2 + \mathrm{tr}(\mathbf{B}^H\mathbf{B}\Sigma^{[t]})}, \tag{4.30}$$

where $\mathrm{tr}(\cdot)$ is the trace operator and $\langle|\alpha_i|^2\rangle^{[t]}$ is the ith diagonal component of $\Sigma^{[t]} + \mu^{[t]}(\mu^{[t]})^H$.

As in the Appendix of [102] with the function $\varphi_i^{[t]}$ parametrised by ε, η, $a_i^{[t]} \triangleq \mathbf{c}_i^T\Sigma_{-i}^{[t]}\mathbf{c}_i$, and $b_i^{[t]} \triangleq \beta^{[t]}\mathbf{c}_i^T\Sigma_{-i}^{[t]}\mathbf{B}^H\mathbf{h}$, the update of an estimate of γ_i can be written:

$$\gamma_i^{\text{new}} = \varphi_i^{[t]}(\gamma_i^{\text{old}}), \tag{4.31}$$

where $\Sigma_{-i}^{[t]} \triangleq (\beta^{[t]}\mathbf{B}^H\mathbf{B} + \sum_{j\neq i}(\gamma_j^{[t]})^{-1}\mathbf{c}_j\mathbf{c}_j^T)^{-1}$ and $\mathbf{c}_i$ signifies an $N_\alpha \times 1$ vector of all zeros but 1 at the ith position. γ_i is updated as follows. The fixed points of the function $\varphi_i^{[t]}$ are calculated by determining the fourth order equation:

$$0 = \gamma_i\Big(\eta\gamma_i^3 + \gamma_i^2\big[2\eta a_i - (\varepsilon-\rho-1)\big] + \gamma_i\big[\eta a_i^2 - 2(\varepsilon-\rho-1)a_i - \rho(a_i+|b_i|^2)\big]$$

$$-(\varepsilon-1)a_i^2\Big) \tag{4.32}$$

$\gamma_i^{[t+1]}$ can be set $\gamma_i^{[t+1]} = 0$ provided that there are no strictly-positive fixed points of $\varphi_i^{[t]}$, i.e., the fixed point of $\varphi_i^{[t]}$ is 0. On the other hand, the fixed point $\tilde{\gamma}_i$, which corresponds to the largest value among all strictly positive fixed points, will be chosen if the solutions exist. In conclusion, the algorithm mentioned above is written in the steps with connection with the beamforming algorithm as shown in Section 4.4.4.

4.4 Compressive beamforming for MIMO-OFDM passive radar

The following starts by the modifying the signal model for applying beamforming technique and then the novel convex constrained optimisation-based beamforming algorithm procedure is described.

4.4.1 Signal formulation

Comparing the signal model in (4.5) with the corresponding channel estimates in (4.10) and recall that there is one target reflection and $N_p - 1$ unwanted reference and clutter signals and $N_p < n_r$. At time sample t, the $N'L'n_r \times 1$ receive signal model for ULA beamforming can be written as:

$$\mathbf{h}(t) = \sum_{k=1}^{n_t} \left(A_0^k(t)\mathbf{b}^k(\hat{\tau}_0, \hat{a}_0, \hat{\phi}_0) + \sum_{p=1}^{N_p-1} A_p^k(t)\mathbf{b}^k(\hat{\tau}_p, \hat{a}_p, \hat{\phi}_p) + \mathbf{w}^k(t) \right) \tag{4.33}$$

According to the above expression, the $N'L'n_r \times 1$ expected surveillance signal steering vector is denoted by $\mathbf{b}^k(\hat{\tau}_0, \hat{a}_0, \hat{\phi}_0)$. The receiver array steering vectors which belong to the other incoming signals are declared as $\mathbf{b}^k(\hat{\tau}_p, \hat{a}_p, \hat{\phi}_p)$. Similar to the previous chapter, $\hat{\tau}, \hat{a}, \hat{\phi}$ refer to the parameters that are extracted using the proposed compressive sensing algorithms, i.e., time delay, Doppler frequency and angles of arrivals, respectively. Additionally, the signal attenuation is denoted by $A_p^k(t)$ and $\mathbf{w}^k(t)$ represents $N'L'n_r \times 1$ additive noise which is statisically independent from the source waveforms. From this explanation, the first addend in the expression above determines the surveillance signal whereas the unwanted signals are shown by the other. The steering vectors are derived as in Section 4.3.1. Given that the signal and noise are uncorrelated, at a time sample t, $t \in \{t_1, \ldots, t_M\}$, the correlation matrix of the data at the n_r-array receiver is:

$$\mathbf{R} = \alpha_0^2 \mathbf{b}(\hat{\tau}_0, \hat{a}_0, \hat{\phi}_0)\mathbf{b}^H(\hat{\tau}_0, \hat{a}_0, \hat{\phi}_0) + \sum_{p=1}^{N_p-1} \alpha_p^2 \mathbf{b}(\hat{\tau}_p, \hat{a}_p, \hat{\phi}_p)\mathbf{b}^H(\hat{\tau}_p, \hat{a}_p, \hat{\phi}_p) + \mathbf{R}_\mathbf{w} \tag{4.34}$$

where $\alpha_p^2 = \mathbb{E}\{|A_p(t)|^2\}$ designates the power of each path, and $\mathbf{R}_\mathbf{w}$ embodies the system noise correlation matrix.

4.4.2 *Conventional beamformers*

An assortment of $N'L'n_r$ complex weights residing in the narrowband beamformer can be considered as a linear filter [107]. The desired signal should be approximated as the result of the beamformer as in:

$$\mathbf{y}(t) = \hat{A}_0(t) = \omega^H \mathbf{h}(t). \tag{4.35}$$

The purpose of the beamformer is to increase the target-of-interest from the expected steering vector $\mathbf{b}(\hat{\tau}_0, \hat{a}_0, \hat{\phi}_0)$ and reduce unwanted signals from other angles. The beam response can be defined as [108]

$$\mathscr{B}(\tau_p, a_p, \phi_p) \triangleq \omega^H \mathbf{b}(\tau_p, a_p, \phi_p). \tag{4.36}$$

The antenna pattern of this passive radar can be calculated from $|\mathscr{B}(\tau_p, a_p, \phi_p)|^2$ and the beamformer output power can be shown as

$$P_r(\hat{\tau}_0, \hat{a}_0, \hat{\phi}_0) \triangleq \omega^H \mathbf{R}_{hh} \omega. \tag{4.37}$$

In order to appoint the weights, the optimisation benchmarks, e.g. minimum mean square error (MMSE), minimum variance distortionless response (MVDR) and minimum power distortionless response, can be employed. Using MMSE, it can be shown that the estimator of $A_0(t)$ refers to the conditional mean of the expected signal given the measurements as shown:

$$\hat{A}_{MMSE}(t) = \mathbb{E}\{A_0(t)|\mathbf{h}(t), \mathbf{h}(t_{-1}), \mathbf{h}(t_{-2}), \cdots\} \approx \mathbb{E}\{A_0(t)|\mathbf{h}(t)\}. \tag{4.38}$$

Due to the fact that the estimator should be linear, the spatial Wiener filter weights are utilised to minimise the mean square error as follows:

$$\omega_{MS}(\hat{\tau}_0, \hat{a}_0, \hat{\phi}_0) = [\mathbb{E}\{\mathbf{h}(t)\mathbf{h}^H(t)\}]^{-1} \mathbb{E}\{\mathbf{h}(t) A_0^*(t)\} = \mathbf{R}_{hh}^{-1} \mathbf{b}(\hat{\tau}_0, \hat{a}_0, \hat{\phi}_0) \alpha_0^2. \tag{4.39}$$

Then the estimator is shown as:

$$\hat{A}_{MMSE}(t) = \omega_{MS}^H(\hat{\tau}_0, \hat{a}_0, \hat{\phi}_0) \mathbf{h}(t). \tag{4.40}$$

Also, the maximum a posteriori (MAP) can be used if the signals and noise are Gaussian. The MVDR, however, minimises the estimation error variance with respect to a distortionless constraint. Denote $\mathbf{R}_{int}$ be corresponded to a covariance matrix of the unwanted signals and noise, i.e. $\mathbf{R}_{int} = \sum_{p=1}^{N_p - 1} \alpha_p^2 \mathbf{b}(\hat{\tau}_p, \hat{a}_p, \hat{\phi}_p) \mathbf{b}^H(\hat{\tau}_p, \hat{a}_p, \hat{\phi}_p) + \mathbf{R}_{\mathbf{w}}$. The MVDR weights are calculated by:

$$\omega_{MV} = \frac{\mathbf{R}_{int}^{-1} \mathbf{b}(\hat{\tau}_0, \hat{a}_0, \hat{\phi}_0)}{\mathbf{b}^H(\hat{\tau}_0, \hat{a}_0, \hat{\phi}_0) \mathbf{R}_{int}^{-1} \mathbf{b}(\hat{\tau}_0, \hat{a}_0, \hat{\phi}_0)}. \tag{4.41}$$

The beamformer output utilising the minimum power distortionless response by substituting $\mathbf{R}_{hh}$ over $\mathbf{R}_{int}$ can equivalently provided if $\mathbf{R}_{hh}, \mathbf{R}_{int}, \alpha_0^2$, and $\mathbf{b}(\hat{\tau}_0, \hat{a}_0, \hat{\phi}_0)$ are approachable. Comparing (4.39) to (4.41), it can be shown that the formula of beamformer should be [107], $\omega_0(\hat{\tau}_0, \hat{a}_0, \hat{\phi}_0) = \upsilon \mathbf{R}_{hh}^{-1} \mathbf{b}(\hat{\tau}_0, \hat{a}_0, \hat{\phi}_0)$, where υ is a scaling factor. The spatial Wiener filter is applied if $\upsilon = \alpha_0^2$, and the MVDR weights are acquired if $\upsilon = (\mathbf{b}^H(\hat{\tau}_0, \hat{a}_0, \hat{\phi}_0)\mathbf{R}_{hh}^{-1}\mathbf{b}(\hat{\tau}_0, \hat{a}_0, \hat{\phi}_0))^{-1}$. Additionally, the beamformer can be called *optimal* if the weight vector can optimise the output SINR.

As discussed in [109], a fine covariance matrix can be invented allowing that a device is in a low dynamic scenario. In an extremely dynamic scheme, the receiver can be manoeuvred rapidly. Specifically, in the three-dimensional territory, this makes the interrelated stationary time decrease. When the receiver array is drifting at an angular velocity ω_r, one of the parameters of interest, $\hat{\phi}$, will alter from ϕ_1 to ϕ_2 and $\phi_2 - \phi_1 = \omega_r T^{int}$, providing that T^{int} corresponds to the stationary time. For a limited number of snapshots M, the actual correlation matrix can be determined. M can be related to the actual sampling time, T_s, that is $M = T_s f_s$, where f_s is the sampling rate of the system. The actual correlation matrix can be written as:

$$\hat{\mathbf{R}}_M = \frac{1}{M} \sum_{t=t_1}^{t_M} \mathbf{h}(t)\mathbf{h}^H(t) \tag{4.42}$$

Covered by stationary and ergodic assumptions, $\hat{\mathbf{R}}_M$ will converge to $\mathbf{R}_{hh}$ as $M \to \infty$. The MVDR weights evolve into:

$$\omega_{MV} = \frac{\hat{\mathbf{R}}_M^{-1}\mathbf{b}(\hat{\tau}_0, \hat{a}_0, \hat{\phi}_0)}{\mathbf{b}^H(\hat{\tau}_0, \hat{a}_0, \hat{\phi}_0)\hat{\mathbf{R}}_M^{-1}\mathbf{b}(\hat{\tau}_0, \hat{a}_0, \hat{\phi}_0)}. \tag{4.43}$$

There are two problems in this scenario. First, the computational speed for the beamforming algorithm may not be able to cope with the alternating angular velocity. Secondly, conventional beamforming might not be constructed as the number of snapshots is not adequate.

4.4.3 Convex-Constraint Optimization using MUSIC algorithm

The beamforming applied in this thesis is based on the Capon beamforming [56] where the signal to interference plus noise ratio is magnified. This method aims to diminish clutter signal and noise while conserving the target reflection. As mentioned in the former chapters, the surveillance signal is known to be very weak compared to the direct and clutter path.To achieve the beamforming goal, the classic Capon's beamformer selects the

weights ω as the minimiser of the output power (4.37) while the beam corresponding to a specific direction of the target $(\hat{\tau}_0, \hat{a}_0, \hat{\phi}_0)$ is constrained to be unity.

$$\begin{aligned} \min \quad & \omega^H \mathbf{R}_{hh} \omega \\ \text{s.t.} \quad & \omega^H \bar{\mathbf{b}}(\hat{\tau}_0, \hat{a}_0, \hat{\phi}_0) = 1, \end{aligned} \tag{4.44}$$

where $\bar{\mathbf{b}}(\hat{\tau}_0, \hat{a}_0, \hat{\phi}_0)$ is the actual target signal steering vector and ω denotes the optimal weight from the conventional beamforming method. The target SINR of the array can be written as:

$$SINR = \frac{|\omega^H \mathbf{b}(\hat{\tau}_0, \hat{a}_0, \hat{\phi}_0) A_0(t)|^2}{\omega^H \mathbf{R}_{int} \omega}, \tag{4.45}$$

where $\mathbf{b}(\hat{\tau}_0, \hat{a}_0, \hat{\phi}_0) A_0(t)$ is the expected target signal. Substitute into (4.45) with the optimisation expression of the beamforming in (4.44), the resulted equation can be shown as:

$$\begin{aligned} SINR =& n_r \alpha_0^2 \mathbf{b}^H(\hat{\tau}_0, \hat{a}_0, \hat{\phi}_0) \mathbf{R}_{int}^{-1} \mathbf{b}(\hat{\tau}_0, \hat{a}_0, \hat{\phi}_0) \\ & \times \frac{|\mathbf{b}^H(\hat{\tau}_0, \hat{a}_0, \hat{\phi}_0) \mathbf{R}_{int}^{-1} \bar{\mathbf{b}}(\hat{\tau}_0, \hat{a}_0, \hat{\phi}_0)|^2}{\left(\mathbf{b}^H(\hat{\tau}_0, \hat{a}_0, \hat{\phi}_0) \mathbf{R}_{int}^{-1} \mathbf{b}(\hat{\tau}_0, \hat{a}_0, \hat{\phi}_0)\right) \left(\bar{\mathbf{b}}^H(\hat{\tau}_0, \hat{a}_0, \hat{\phi}_0) \mathbf{R}_{int}^{-1} \bar{\mathbf{b}}(\hat{\tau}_0, \hat{a}_0, \hat{\phi}_0)\right)}, \end{aligned} \tag{4.46}$$

where

$$0 \leq \frac{|\mathbf{b}^H(\hat{\tau}_0, \hat{a}_0, \hat{\phi}_0) \mathbf{R}_{int}^{-1} \bar{\mathbf{b}}(\hat{\tau}_0, \hat{a}_0, \hat{\phi}_0)|^2}{\left(\mathbf{b}^H(\hat{\tau}_0, \hat{a}_0, \hat{\phi}_0) \mathbf{R}_{int}^{-1} \mathbf{b}(\hat{\tau}_0, \hat{a}_0, \hat{\phi}_0)\right) \left(\bar{\mathbf{b}}^H(\hat{\tau}_0, \hat{a}_0, \hat{\phi}_0) \mathbf{R}_{int}^{-1} \bar{\mathbf{b}}(\hat{\tau}_0, \hat{a}_0, \hat{\phi}_0)\right)} \leq 1. \tag{4.47}$$

In [109], it was claimed that the mismatch between the estimated target steering vector $\mathbf{b}(\hat{\tau}_0, \hat{a}_0, \hat{\phi}_0)$ and the actual target steering vector $\bar{\mathbf{b}}(\hat{\tau}_0, \hat{a}_0, \hat{\phi}_0)$ leads to the aggravation of the effectiveness of the SINR. As a result, the steering vector $\mathbf{b}(\hat{\tau}_0, \hat{a}_0, \hat{\phi}_0)$ can be calculated by applying the multiple signal classification (MUSIC) [110] principle which can be stated as:

$$\mathbf{R}_{hh} = \mathbb{E}\{\mathbf{h}(t)\mathbf{h}^H(t)\} = \mathbf{B}(\hat{\tau}_P, \hat{a}_P, \hat{\phi}_P) \mathbf{R}_{AA} \mathbf{B}^H(\hat{\tau}_P, \hat{a}_P, \hat{\phi}_P) + \beta_{\mathbf{w}}^2 \mathbf{I}, \tag{4.48}$$

where $\mathbf{B}(\hat{\tau}_P, \hat{a}_P, \hat{\phi}_P)$ demonstrates a matrix of stacked steering vectors, which can be defined as $\{\mathbf{b}(\hat{\tau}_0, \hat{a}_0, \hat{\phi}_0), \ldots, \mathbf{b}(\hat{\tau}_{N_p-1}, \hat{a}_{N_p-1}, \hat{\phi}_{N_p-1})\}$ and $\mathbf{R}_{AA}$ is a signal correlation matrix. $\mathbf{B}(\hat{\tau}_P, \hat{a}_P, \hat{\phi}_P) \mathbf{R}_{AA} \mathbf{B}^H(\hat{\tau}_P, \hat{a}_P, \hat{\phi}_P)$ is a full-rank matrix since the expected signals are independent. The noise variance is denoted by $\beta_{\mathbf{w}}^2$. Given that $\{\delta_0, \ldots, \delta_{n_r-1}\}$ refers to the eigenvalues of $\mathbf{R}_{hh}$, and the eigenvector, corresponding to the eigenvalue δ_i, is Δ_i, it can be shown that $|\mathbf{R}_{hh} - \delta_i I| = 0$. This leads to $cv_i = \delta_i - \beta_{\mathbf{w}}^2$ becomes the characteristic value of $\mathbf{B}(\hat{\tau}_P, \hat{a}_P, \hat{\phi}_P) \mathbf{R}_{AA} \mathbf{B}^H(\hat{\tau}_P, \hat{a}_P, \hat{\phi}_P)$. Furthermore, $\mathbf{B}(\hat{\tau}_P, \hat{a}_P, \hat{\phi}_P) \mathbf{R}_{AA} \mathbf{B}^H(\hat{\tau}_P, \hat{a}_P, \hat{\phi}_P)$ is a

positive semidefinite $n_r \times n_r$ matrix with rank N_p when the number of array elements n_r is higher than the number of impinging paths N_p. The number of zeros in the eigenvalues of $\mathbf{B}(\hat{\tau}_P, \hat{a}_P, \hat{\phi}_P)\mathbf{R}_{AA}\mathbf{B}^H(\hat{\tau}_P, \hat{a}_P, \hat{\phi}_P)$ is equal to $n_r - N_p$ and it can be displayed as:

$$cv_0, cv_1, \ldots, cv_{N_p-1} > cv_i = 0, \tag{4.49}$$

where the index i in the above equation refers to the range of $N_p, N_p+1, \ldots, n_r-1$. Consequently, the eigenvalues of $\mathbf{R}_{hh}$ can be demonstrated as:

$$\delta_0, \delta_1, \ldots, \delta_{N_p-1} > \delta_{N_p} = \ldots = \delta_{n_r-1} = \beta_{\mathbf{w}}^2. \tag{4.50}$$

As the eigenvector can be shown as $(\mathbf{R}_{hh} - \delta_i I)\Delta_i = 0$, for the vectors of $n_r - N_p$ smallest eigenvalues, this can be written as:

$$(\mathbf{R}_{hh} - \delta_i I)\Delta_i = \mathbf{B}(\hat{\tau}_P, \hat{a}_P, \hat{\phi}_P)\mathbf{R}_{AA}\mathbf{B}^H(\hat{\tau}_P, \hat{a}_P, \hat{\phi}_P)\Delta_i + \beta_{\mathbf{w}}^2 I\Delta_i - \beta_{\mathbf{w}}^2 I\Delta_i = 0, \tag{4.51}$$

which leads to $\mathbf{B}(\hat{\tau}_P, \hat{a}_P, \hat{\phi}_P)\mathbf{R}_{AA}\mathbf{B}^H(\hat{\tau}_P, \hat{a}_P, \hat{\phi}_P)\Delta_i = 0$. As a result, $\mathbf{B}^H(\hat{\tau}_P, \hat{a}_P, \hat{\phi}_P)\Delta_i = 0$ due to the fact that $\mathbf{R}_{AA}$ is nonsingular and $\mathbf{B}(\hat{\tau}_P, \hat{a}_P, \hat{\phi}_P)$ is full rank. This means there are $n_r - N_p$ eigenvalues whose values are $\beta_{\mathbf{w}}^2$ and they coincide with the eigenvectors which belong to a noise subspace. The conjunction between the noise and N_p signal steering vectors can be determined as:

$$\left\{\mathbf{b}(\hat{\tau}_0, \hat{a}_0, \hat{\phi}_0), \ldots, \mathbf{b}(\hat{\tau}_{N_p-1}, \hat{a}_{N_p-1}, \hat{\phi}_{N_p-1})\right\} \perp \left\{\Delta_{N_p}, \ldots, \Delta_{n_r-1}\right\}. \tag{4.52}$$

Therefore, a noise eigenvector matrix can be constructed as $\mathbf{U}_w = \{\Delta_{N_p}, \ldots, \Delta_{n_r-1}\}$. Given the orthogonality mentioned above, it can be seen that:

$$\mathbf{B}^H(\hat{\tau}_P, \hat{a}_P, \hat{\phi}_P)\mathbf{U}_w\mathbf{U}_w^H\mathbf{B}(\hat{\tau}_P, \hat{a}_P, \hat{\phi}_P) = 0. \tag{4.53}$$

Further to this, function $f(\hat{\tau}, \hat{a}, \hat{\phi})$ may be defined as:

$$f(\hat{\tau}, \hat{a}, \hat{\phi}) = \mathbf{B}^H(\hat{\tau}_P, \hat{a}_P, \hat{\phi}_P)\mathbf{U}_w\mathbf{U}_w^H\mathbf{B}(\hat{\tau}_P, \hat{a}_P, \hat{\phi}_P), \tag{4.54}$$

where $f(\hat{\tau}, \hat{a}, \hat{\phi})$ can attain the minimum output power if $\mathbf{B}(\hat{\tau}_P, \hat{a}_P, \hat{\phi}_P)$ (the signal steering vectors) is orthogonal to $\mathbf{U}_w$ (the noise subspace eigenvectors). Consequently, a convex constrained optimization beamforming (CCOB) algorithm is applied in order that the robustness is increased and the target signal protection is complimented. The optimization used in this research is written as:

$$\min_{\hat{\mathbf{B}}} \quad \hat{\mathbf{B}}^H(\hat{\tau}_P, \hat{a}_P, \hat{\phi}_P)\mathbf{U}_w\mathbf{U}_w^H\hat{\mathbf{B}}(\hat{\tau}_P, \hat{a}_P, \hat{\phi}_P)$$

$$\text{subject to} \left\| \left(\mathbf{I} - \frac{\bar{\mathbf{B}}(\hat{\tau}_P, \hat{a}_P, \hat{\phi}_P)\bar{\mathbf{B}}^H(\hat{\tau}_P, \hat{a}_P, \hat{\phi}_P)}{\bar{\mathbf{B}}^H(\hat{\tau}_P, \hat{a}_P, \hat{\phi}_P)\bar{\mathbf{B}}(\hat{\tau}_P, \hat{a}_P, \hat{\phi}_P)} \right) \hat{\mathbf{B}}(\hat{\tau}_P, \hat{a}_P, \hat{\phi}_P) \right\|^2 \leq \zeta, \tag{4.55}$$

where $\bar{\mathbf{B}}(\hat{\tau}_P, \hat{a}_P, \hat{\phi}_P)$ is the assumed steering vector matrix of the desired signal that will be erroneous with respect to the actual steering vector matrix. ζ is the small positive number. The optimal estimated value $\hat{\mathbf{B}}(\hat{\tau}_P, \hat{a}_P, \hat{\phi}_P)$ can be reached. With the assumption that the power of unwanted signal is much higher than the power of the surveillance signal ($\alpha_p^2 >> \alpha_0^2$), the total output power of the receiver array is minimised in order to maximise the SINR. Regarding the alterations in the numerator and denominator, the constrained optimization problem in (4.44) can be written as:

$$\begin{aligned} \min \quad & \omega^H \mathbf{R} \omega \\ \text{s.t.} \quad & \omega^H \hat{\mathbf{B}}(\hat{\tau}_P, \hat{a}_P, \hat{\phi}_P) = 1. \end{aligned} \tag{4.56}$$

where the optimal weight can be calculated by:

$$\omega_0 = \frac{\mathbf{R}^{-1} \hat{\mathbf{B}}(\hat{\tau}_P, \hat{a}_P, \hat{\phi}_P)}{\hat{\mathbf{B}}^H(\hat{\tau}_P, \hat{a}_P, \hat{\phi}_P) \mathbf{R}^{-1} \hat{\mathbf{B}}(\hat{\tau}_P, \hat{a}_P, \hat{\phi}_P)}. \tag{4.57}$$

The estimated desired target-reflection steering vector can be calculated from (4.55). In conclusion, this section exploits the property of MUSIC algorithm regarding the noise subspace and derive the optimisation expression using its orthogonality. This technique is performed in the passive radar systems along with the compressive sensing methods. In this thesis, the Fast-Besselk algorithm has been applied. In the literature, however, one of the low-computation method in CS, namely, the Orthogonal Matching Pursuit (OMP), is utilised. To complete the discussion in this chapter, the explanation of OMP is presented next and the outcomes from both CS algorithms are demonstrated in the last section.

4.4.4 Compressive-domain beamforming algorithm

The beamforming algorithm, as well as signal reconstruction applying Fast-BesselK, is described as in Algorithm. 2. The input parameters for Fast-BesselK algorithm are the measurement vector $\mathbf{h}$ and its variance var($\mathbf{h}$) applied for the noise variance in the algorithm. The other parameter required is the overcomplete matrix $\mathbf{B}$ which consists of the possible steering vectors as its columns. First, the value of ρ in (4.17) is selected to 1 as the algorithm deals with the complex number. The number of iteration as well as the value of stopping criterion are set. Then the method can choose one of the Bayesian CS algorithm by fixing the values of ε and η. Next, the variable of the mixing density, γ, the noise precision, β, the parameters of the conditional PDF of α, i.e. μ and Σ and the parameters $\mathbf{a}$ and $\mathbf{b}$ appear in (4.32) are initialised utilising the input parameters.

Algorithm 2 CCOB with Fast-BesselK Reconstruction

procedure FAST-BESSELK($\mathbf{h}, \mathbf{B}, \text{var}(\mathbf{h})$)
    Pick $\rho = 1$ for complex value.
    Appoint an iteration counter and a termination criterion.
    Mark ε and η for the selected method ($\varepsilon = 0.5$ and $\eta = 1$ for Fast-BesselK).
    Initialise $\gamma, \beta, \mu, \Sigma$ and $\mathbf{a}, \mathbf{b}$ appear in (4.32) $\leftarrow \mathbf{h}, \mathbf{B}, var(\mathbf{h})$;
    for $iteration\_count = 0$ to $max\_iteration$ **do**
        update a_i, b_i;
        update $\gamma \leftarrow$ (4.32);
        update $\Sigma \leftarrow$ (4.27), $\mu \leftarrow$ (4.28), $\mathbf{a}, \mathbf{b}$ and $\beta \leftarrow$ (4.30);
        if $\|\mu^{[t-1]} - \mu^{[t]}\|_2 <$ termination criterion **then**
            exit for loop.
        end if
    end for
    Conclude $\hat{\alpha} \leftarrow \mu^{[t]}$ with corresponding basis functions.
end procedure
procedure CCOB($\hat{\alpha}$)
    Calculate $\hat{\mathbf{h}} = \mathbf{B}\hat{\alpha}$;
    Find $\hat{\mathbf{R}} \leftarrow \hat{\mathbf{h}}(t)\hat{\mathbf{h}}^H(t)$;
    Institute (4.55) using $\mathbf{U}_w = \{\Delta_{N_p}, \ldots, \Delta_{n_r-1}\}$;
    Compute optimal $\hat{\mathbf{B}}(\hat{\tau}_P, \hat{a}_P, \hat{\phi}_P) \leftarrow$ (4.55);
    Determine $\omega_0 \leftarrow$ (4.57)
end procedure

In each iteration, the parameters mentioned above are updated using (4.27)-(4.32), as shown in the algorithm. The operation exits the loop when either the iteration counter reaches the maximum value or the change in the value of μ is less than the stopping criterion. At the end of the algorithm, the outputs include the approximation of the original signal α and the support vector which can be recovered. The following steps regarding the beamforming algorithm are concluded from the explanation in Section 4.4.3. The approximated result then projects on the overcomplete matrix in order to find the channel estimates. The correlation matrix is figured out and the eigenvalue decomposition is performed. Using the eigenvalues, the noise subspace can be construct according to the details described. Next, the optimisation problem in (4.55) is analysed and finally the

antenna weights can be calculated using (4.57).

4.5 CS algorithm complexity analysis

In this section, the complexity of BCS algorithms used efficiently for the less computationally demanding extraction 2D channel parameters is analysed and compared with the Fast-BesselK approach taken by this work. Each method is compared in Table 4.1. In Fast-BesselK, for each iteration, the calculation of (4.27) is the most complex operation. The computation time of the matrix inversion process for matrices the size of $N_\alpha \times N_\alpha$ might be as slow as $\mathcal{O}(N_\alpha^3)$. Fortunately, the development of the fast relevant vector machine algorithm [105], which applies the marginal likelihood maximisation, allows a useful addition and deletion of candidate basis functions (columns of $\mathbf{B}$). It should be noted that complexity of this algorithm is more dependent on N_p than N_α [101]. Utilizing the matrix inverse identity [104], the inverse operation discussed earlier can also be realized with reduced complexity. In conclusion, the complexity of the Fast-BesselK algorithm can be $\mathcal{O}(N_\alpha N_p^2)$.

Regarding the BP algorithm, the truncated Newton interior-point method [43], with extension to complex variables as used in [16], [90], and [98], is considered. The problem has been devised as the convex problem, Precisely, a second-order cone programming (SOCP) problem and the computational complexity is mainly calculated from the preconditioned conjugate gradients steps, which provide $\mathcal{O}(N_\alpha)$ of running time. However, it is also necessary to include the norm-operation loop for each bit according to the SOCP formulation. The complexity of the BP algorithm becomes $\mathcal{O}(N_\alpha^2)$. Another algorithm considered in Table 4.1 is the l_1-SVD. As mentioned in [2], to optimise the l_1-SVD objective function, the SOCP framework is also used and complexity is seen to be $\mathcal{O}\left((N_p N_\alpha)^3\right)$. Regarding the OMP algorithm discussed in Section 2.4.1, the highest calculation is demanded for Step 3. The cost of computation is $\mathcal{O}(N_p N_h N_\alpha)$ while it requires $\mathcal{O}\left((t_i)N_h\right)$ for the least squares problem at iteration t_i. Better effective utilisation of OMP can be achieved if the structured measurement matrix is used. The cost of efficient OMP is only $\mathcal{O}(N_p \log N_\alpha)$ [111]. It is clear from Table 4.1 that the complexity of the Fast-BesselK approach proposed by this work is comparable with other approaches and hence is reasonable. Graphical illustrations of CS complexity are shown in Fig. 4.3 where the number of measurement data is constant. The CS complexity where the number of signal paths is constant is shown in Fig. 4.4.

Table 4.1: Complexity of some compressive sensing reconstruction algorithm

Algorithm	Complexity
Fast-BesselK(BCS)	$\mathcal{O}(N_\alpha N_p^2)$
Basis Pursuit	$\mathcal{O}(N_\alpha^2)$
l_1-SVD	$\mathcal{O}((N_p N_\alpha)^3)$
SpaRSA[112]	$\mathcal{O}(N_\alpha \log N_\alpha)$
OMP[111]	$\mathcal{O}(N_p \log N_\alpha)$
CoSaMP[113]	$\mathcal{O}(N_p \log^2 N_\alpha)$

4.6 Three-dimensional Cramer-Rao lower bounds

In case of the MIMO passive radar with co-located antennas, θ is a vector parameter and is equal to $[\tau \;\; a \;\; \phi]^T$. Since there are three variables, this leads to 3×3 Fisher information matrix, which may be written as:

$$\mathbf{I}(\theta) = \begin{bmatrix} -E[\frac{\partial^2 \ln p(\mathbf{h};\theta)}{\partial \tau^2}] & -E[\frac{\partial^2 \ln p(\mathbf{h};\theta)}{\partial \tau \partial a}] & -E[\frac{\partial^2 \ln p(\mathbf{h};\theta)}{\partial \tau \partial \phi}] \\ -E[\frac{\partial^2 \ln p(\mathbf{h};\theta)}{\partial a \partial \tau}] & -E[\frac{\partial^2 \ln p(\mathbf{h};\theta)}{\partial a^2}] & -E[\frac{\partial^2 \ln p(\mathbf{h};\theta)}{\partial a \partial \phi}] \\ -E[\frac{\partial^2 \ln p(\mathbf{h};\theta)}{\partial \phi \partial \tau}] & -E[\frac{\partial^2 \ln p(\mathbf{h};\theta)}{\partial \phi \partial a}] & -E[\frac{\partial^2 \ln p(\mathbf{h};\theta)}{\partial \phi^2}] \end{bmatrix}. \tag{4.58}$$

From (4.6), $r^{k(m)}(\phi_{pth})$ is defined as $(m-1)\frac{d}{\lambda_k}\sin\phi_{pth}^{k(m)}$, therefore:

$$H_{(n,i)}^{k(m)} = \sum_{pth=1}^{mpth} A_{pth}^{k(m)} e^{j2\pi[i a_{pth}^{k(m)} f^k T' - n\Delta f \tau_{pth}^{k(m)} + r^{k(m)}(\phi_{pth})]} + w^{k(m)}, \tag{4.59}$$

consists of a 3-D channel signal and additive Gaussian noise with variance σ_w^2. In order to calculate each element of $\mathbf{I}(\theta)$, the log-likelihood function can be shown as:

$$p(\mathbf{h};\theta) = \frac{1}{(2\pi\sigma_w^2)^{\frac{NLn_t n_r}{2}}} \exp\Bigg[-\frac{1}{2\sigma_w^2} \sum_m \sum_k \sum_i \sum_n \big(H_{(n,i)}^{k(m)} - \sum_{pth=1}^{mpth} A_{pth}^{k(m)} e^{j2\pi[i a_{pth}^{k(m)} f^k T' - n\Delta f \tau_{pth}^{k(m)} + r^{k(m)}(\phi_{pth})]}\big)^2 \Bigg]. \tag{4.60}$$

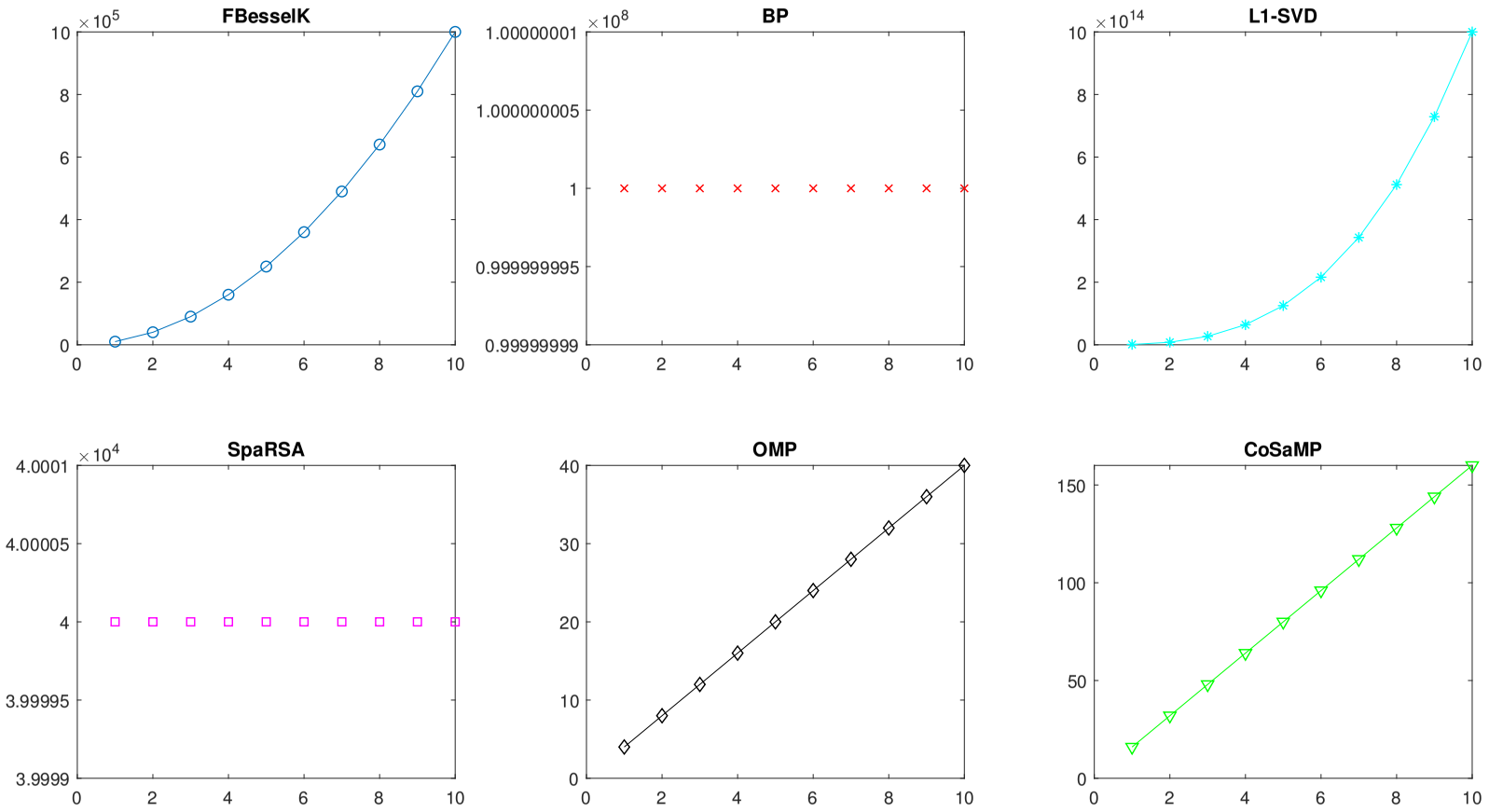

Figure 4.3: The complexity graphs for compressive sensing algorithms where the x-axis refers to the number of signal paths in the system. The higher value of the y-axis is, the more resources required by the algorithm.

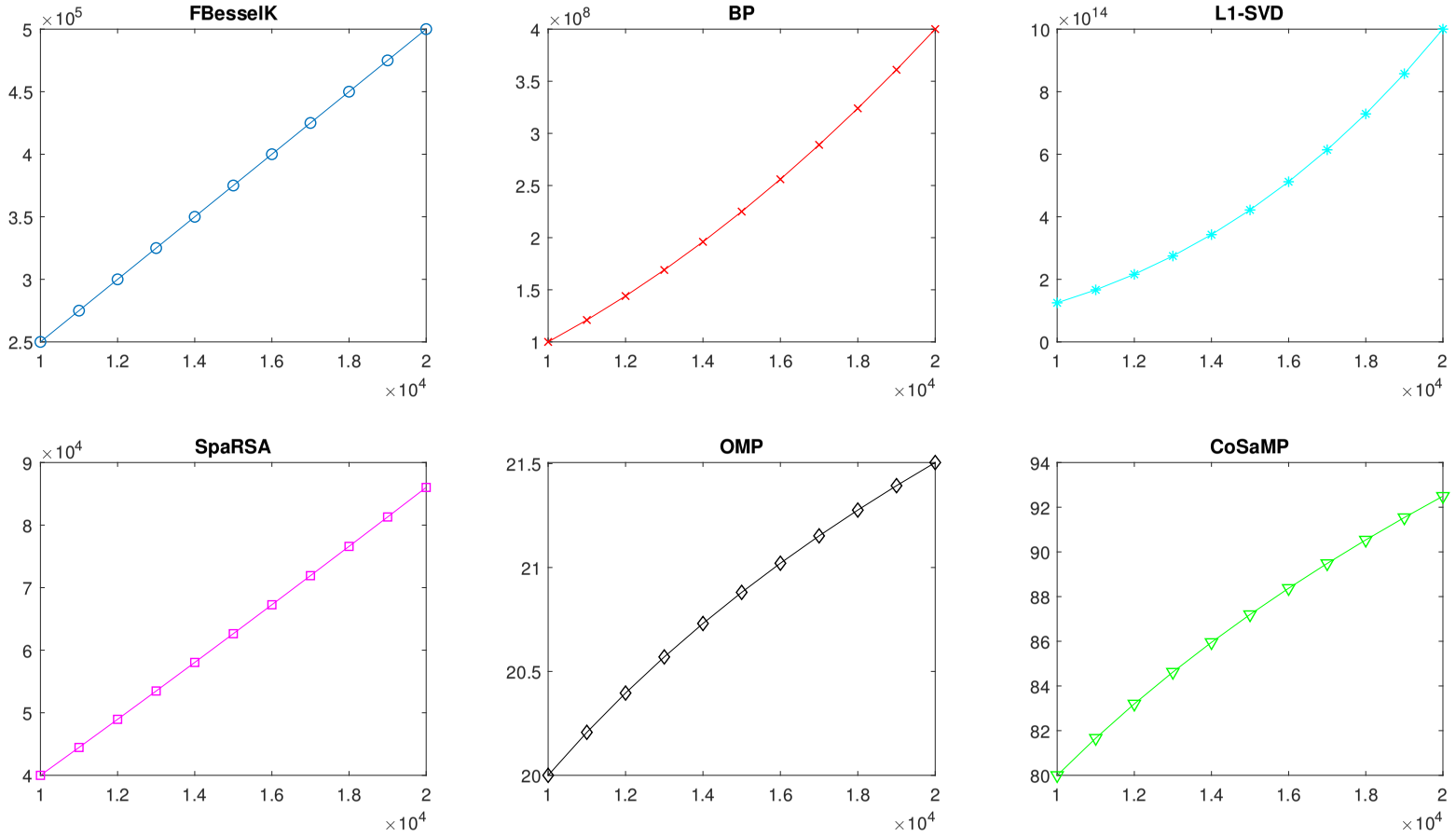

Figure 4.4: The complexity graphs for compressive sensing algorithms where the x-axis refers to the number of measurement data in the system. The higher value of the y-axis is, the more resources required by the algorithm.

$$\ln p(\mathbf{h};\theta) = -\frac{NLn_t n_r}{2}\ln 2\pi\sigma_w^2 - \frac{1}{2\sigma_w^2}\sum_m\sum_k\sum_i\sum_n\Big(H_{(n,i)}^{k(m)} - \sum_{pth=1}^{mpth} A_{pth}^{k(m)} e^{j2\pi[ia_{pth}^{k(m)} f^k T' - n\Delta f\tau_{pth}^{k(m)} + r^{k(m)}(\phi_{pth})]}\Big)^2. \tag{4.61}$$

Using the derivation in Appendix B.1, the rest of the Fisher information matrix can be shown as:

$$[\mathbf{I}(\theta)]_{13} = [\mathbf{I}(\theta)]_{31} = \frac{2\pi^2\Delta f dN(N+1)L}{\sigma_w^2}\sum_m\sum_k\frac{(m-1)(A^k)^2\cos\phi^{k(m)}}{\lambda_k}, \tag{4.62}$$

$$[\mathbf{I}(\theta)]_{23} = [\mathbf{I}(\theta)]_{32} = -\frac{2\pi^2 T' dNL(L+1)}{\sigma_w^2}\sum_m\sum_k\frac{f^k(m-1)(A^{k(m)})^2\cos\phi^{k(m)}}{\lambda_k}, \tag{4.63}$$

$$[\mathbf{I}(\theta)]_{33} = -\frac{4\pi^2 d^2 NL}{\sigma_w^2}\sum_m\sum_k(\frac{(m-1)A^{k(m)}\cos\phi^{k(m)}}{\lambda_k})^2. \tag{4.64}$$

The final part of the CRLB process involves inverting the Fisher matrix to obtain the CRLBs for each parameter as:

$$\text{CRLB}^{\hat{\tau}}(\theta) \geq [\mathbf{I}^{-1}(\theta)]_{11},$$

$$\text{CRLB}^{\hat{a}}(\theta) \geq [\mathbf{I}^{-1}(\theta)]_{22},$$

$$\text{CRLB}^{\hat{\phi}}(\theta) \geq [\mathbf{I}^{-1}(\theta)]_{33}.$$

CRLBs for the system in this thesis are crucial when it is equipped with the new extraction schemes. The bound can be seen as the baseline for the algorithm and consider how efficient it is. The derivation above can be regarded as a noncoherent CRLB and the system exploits spatial diversity of the target. In order to achieve high resolution for the passive radar, the processing should determine the phase coherence and a coherent CRLB will be used. The simulation of the bound is displayed in the Appendix B.3.

4.7 Performance analysis

4.7.1 Comparison of BP and l_1-SVD over 2D and 3D MIMO-OFDM passive radar systems

The considered MIMO passive radar system employs $n_t = 2$ OFDM transmitters and $n_r = 4$ elements of ULA receiver with $d = \frac{\lambda}{2}$ element spacing.

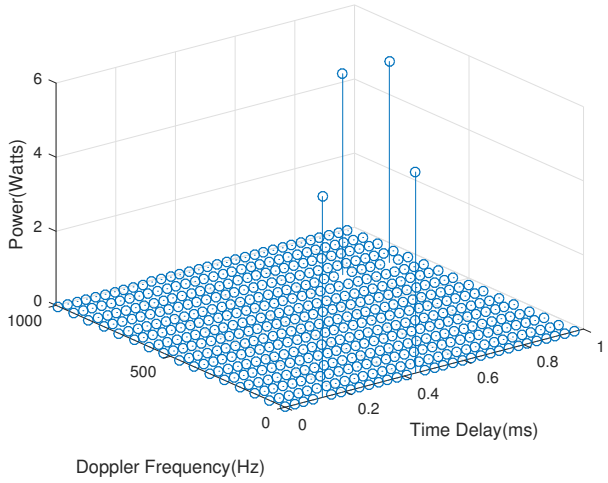

(a)

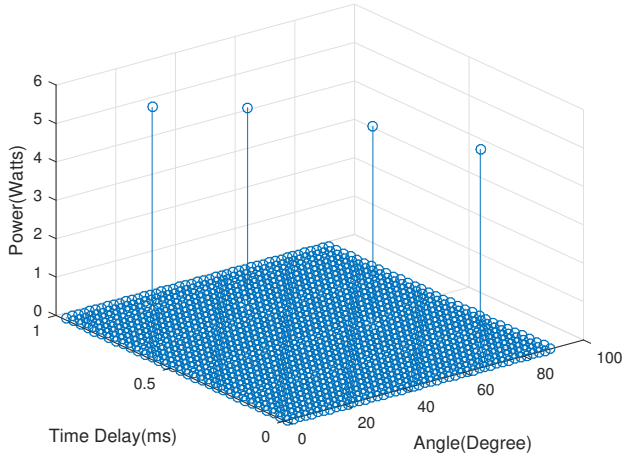

(b)

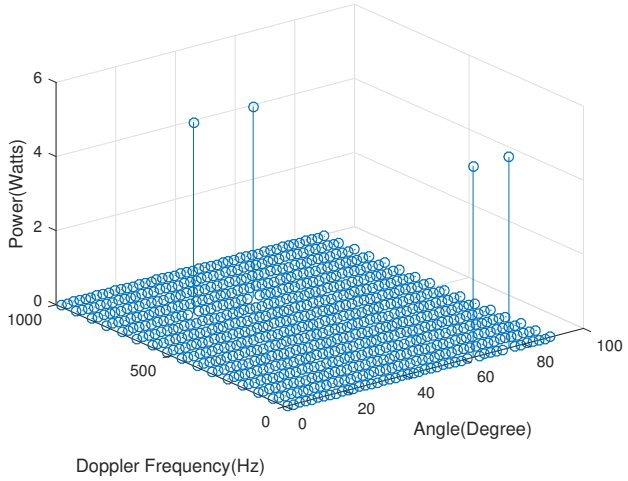

(c)

Figure 4.5: The sparse representation of the multipath signal in: (a) time delay and Doppler domain; (b) time delay and angular domain; and (c) Doppler and angular domain.

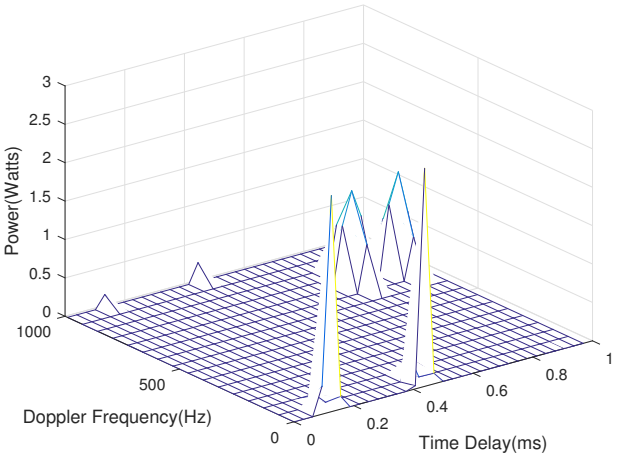

(a)

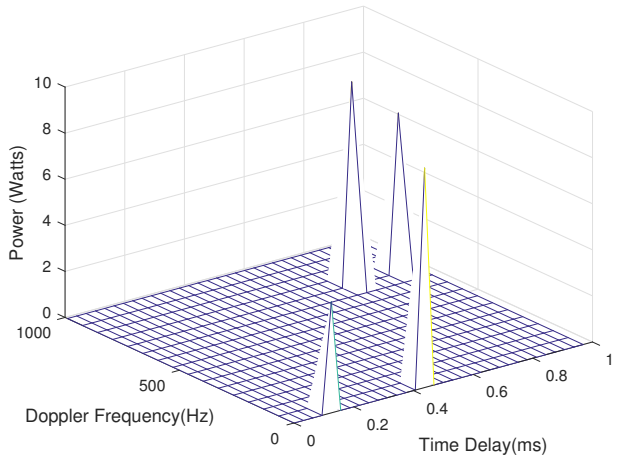

(b)

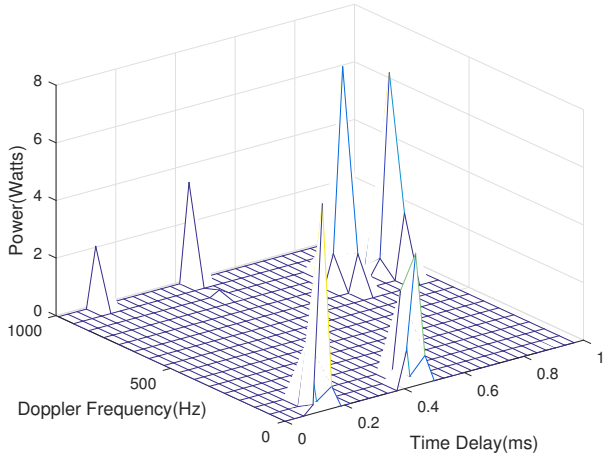

(c)

Figure 4.6: The signal extraction in Doppler frequency and time delay domain with the same level of power in the multipath scenario using: (a) l_1-SVD; (b) Basis Pursuit; and (c) 2D l_1-SVD.

The OFDM parameters are listed in Table 2.1. In this simulation scenario, it is assumed that there is only one target. The analysis of many targets is going to conduct in the future work as the Matlab programming displays the memory problem while increasing the number of multipath fading. The CPU time when running CVX programming for the basis pursuit is roughly 3500 seconds when it consumes about 2000 seconds for the l_1-SVD. These results are simulated on Intel Core i3 Windows workstation. After applying the proposed method, two multipath which corresponds to the target have to demonstrate the same non-zero Doppler frequencies. Time delay from the first transmitter is 0.125 ms, while from the second transmitter is 0.4375 ms. The time delay for the signal reflected from the target illuminated by the first transmitter is 0.75 ms, whereas the signal illuminated by the second transmitter causes the time delay of 0.9062 ms. The target is moving and provides the Doppler frequency of 725.72 Hz. The angle of arrivals for the reference signals from transmitter 1, transmitter 2, surveillance signals as seen from transmitter 1 and transmitter 2 are 75, 63, 45 and 25 degrees respectively. Both of the sources are stationary.

In order to display the extraction capability of the proposed method, there are the original sparse representations shown in Fig. 4.5. Each figure presents the 2D version manipulated from the original 3D signals in the delay-Doppler domain, delay-angular domain and Doppler-angular domain respectively. The parameters value is set as described above. With regard to clear presentation, all of the multipath power are set to be equal. Although this assumption is unrealistic, it is arguable that the reasonable reference-signal cancellation method in the surveillance channel is supposed to be used.

Fig. 4.6a displays the signal extraction in 3D channel estimates when using l_1-SVD with 200 time samples. Due to the CS theory, the dimension of the observation matrix is only 15×7 in time delay and Doppler frequency domain. It is shown that the target parameters can be determined correctly while there are some small leakages around the expected values. Basis pursuit result (Fig. 4.6b) shows a very good signal extraction.

From the literature [2] and [90], however, a single time sample may not be suitable for source localisation application and is not likely to work when the reference signal power is too high. The other figure (Fig. 4.6c), shows the result from l_1-SVD when applied to the 2D channel estimates. It can display the peaks with higher power. This is expected as the size of noise subspace is relatively small compared to the 3D case. These figures also demonstrate the ability of the l_1-SVD in terms of noise and leakages reduction. The angular domain only exists when using 3D model. Fig. 4.7 and Fig. 4.8

show the results from the l_1-SVD signal extraction in comparison with the basis pursuit. The l_1-SVD results display a number of unwanted peaks; nevertheless, the peaks are very close to the expected parameter values. With some errors, the results may be used for target detection applications but there is a requirement for an adaptive approximation between each estimated domain. Both figures are still able to determine the angle of arrivals for each source signals.

While the target detection may be achieved by both 2D and 3D channel extraction, the mean square error signifies the interesting information. After applying the Mean Square Error for both channel models, it is shown that the extraction signals from 3D channel estimates provide fewer errors. In this case, the amount of power received from the reference signal is varied. This means that the correlation between each dimension contributes a successful extraction from noisy measurements. The results can predict that the system can let the reference signal power be much higher than the target signal but the optimised power will be evaluated in the future work.

4.7.2 Scenario for the simulation applying Fast-BesselK

In this section, the performance of the novel Fast-BesselK compressive sensing algorithm for 3D parameter extraction in MIMO passive radar along with the appropriately developed beamforming algorithm is compared with other more conventional approaches. The results discussed in the following are also displayed in [114]. Firstly, the normalised mean square error of the estimated signals with respect to the actual signals is calculated as means of determining how well the algorithm is performing by comparison with the BP and l_1-SVD algorithms introduced in [90], [98]. Further to this, the reconstructed signal and the original signals are compared visually among three domains.

In order to further strengthen the case for the Fast-BesselK approach proposed by this work, a similar normalised mean square error comparison is performed with respect to two more algorithms, namely a 'Fast Relevance Vector Machine (Fast-RVM)' method [105], and a 'Fast-Laplace' method [115]. The former discusses the highly accelerated algorithm for maximizing the marginal likelihood function while the latter utilised a hierarchical form of the Laplace prior to model the sparsity of the unknown signal. Finally, in this section the performance of the proposed CS domain beamforming technique is examined in terms of the target SINR. For this, it is assumed there are two 10 dB-higher reference (direct) signals impinging on the receiver array coming from two single-antenna

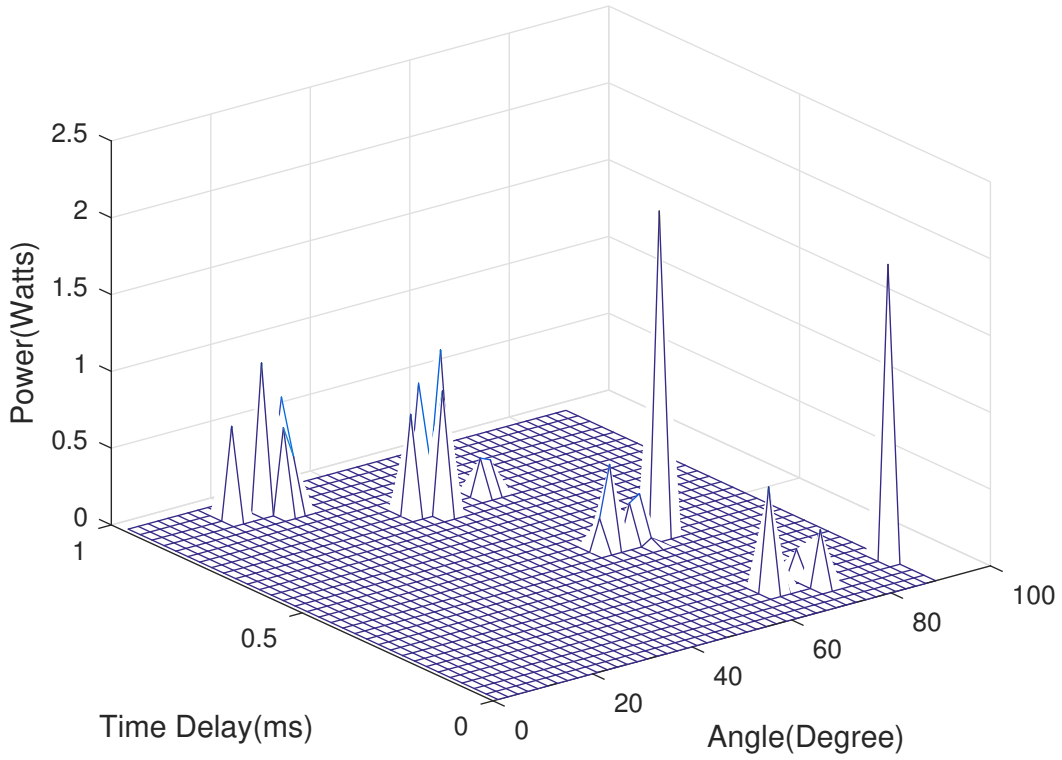

(a)

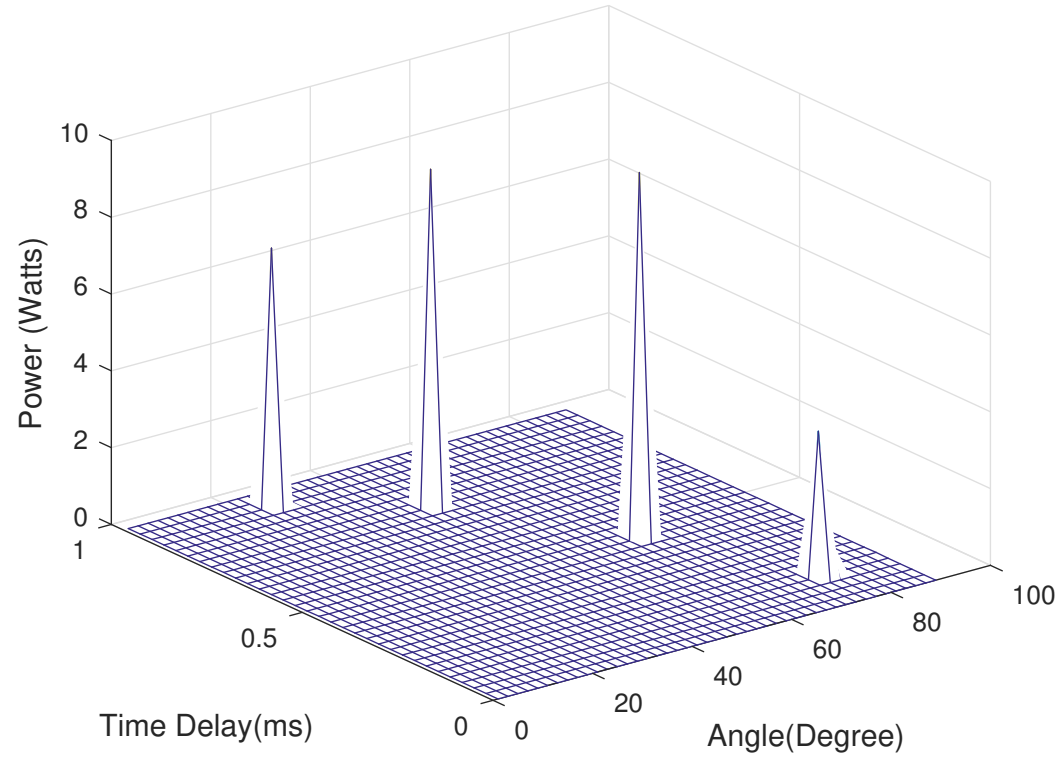

(b)

Figure 4.7: The comparison between signal extraction of the multipath signal in time delay and angular domain using: (a) l_1-SVD; and (b) Basis Pursuit.

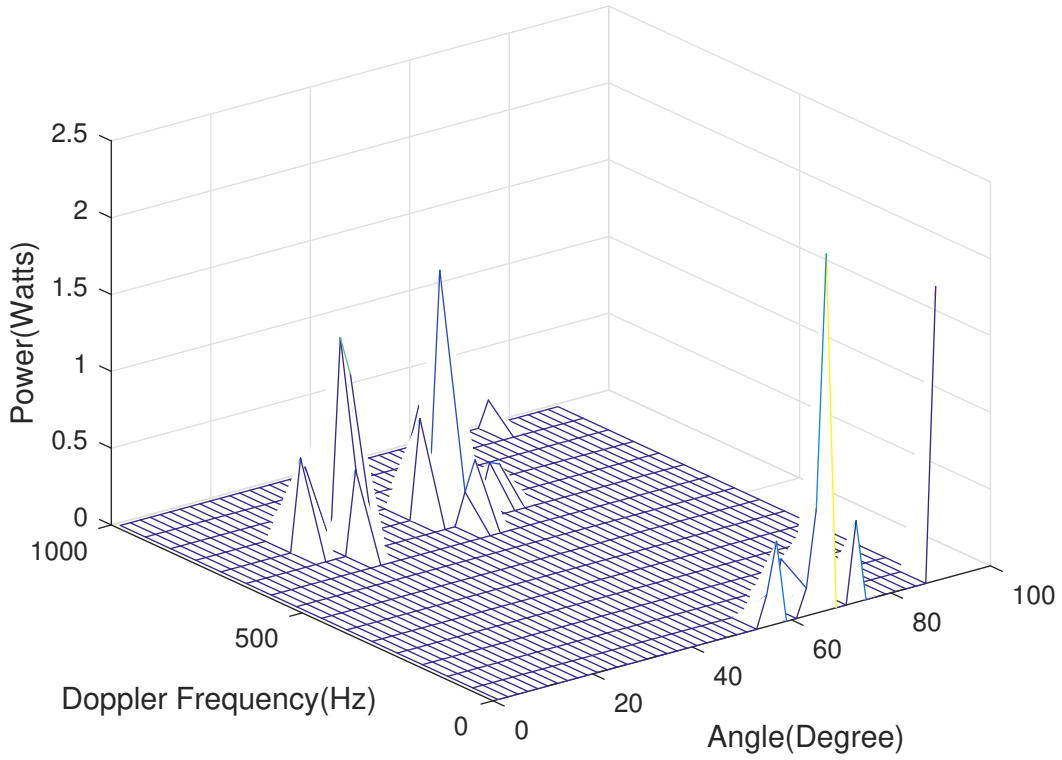

(a)

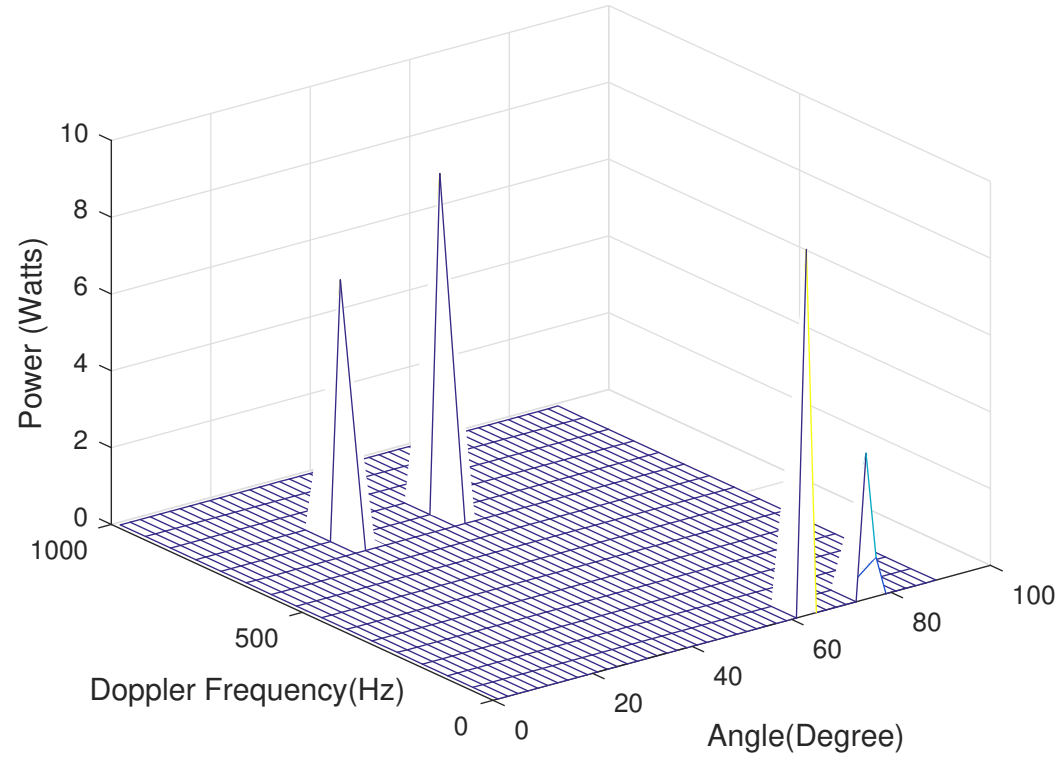

(b)

Figure 4.8: The comparison between signal extraction of the multipath signal in Doppler frequency and angular domain using: (a) l_1-SVD; and (b) Basis Pursuit.

OFDM BSs. Throughout, the analysis that follows, the OFDM signal parameters are described in Table 2.1 and are based on the DAB standard in [4], and is assumed that there is only one target and no clutterers. This scenario is a sufficient comparison regarding the performance of extracting the direct and target signal from the noise background and increasing the number of paths in the scenario decelerate the computation of BP. Moreover, the clutter suppression method is not mentioned in the current work. Signal parameters that are being estimated are chosen randomly according to a suitable uniform distribution with the time delays(τ) being chosen from $0-1$ ms, a, the ratio between range-rate and speed of light, being chosen from $0-3.3\times10^{-6}$ and the angles of arrivals being chosen from $1-179$ degrees.

4.7.3 Comparison of proposed Fast-BesselK method with BP and l_1-SVD methods

Here, the actual signal and the reconstructed signal in the delay-Doppler domain (Fig. 4.9), the delay-AoA domain (Fig. 4.10) and the Doppler-AoA domain (Fig. 4.11) are compared using the proposed Fast-BesselK approach as well as the BP approach and l_1-SVD approach from previous works. As can be seen from the actual signals, the algorithm's task in each case is to ascertain: four time delay values (two values from the transmitter and two scatterers), two Doppler frequencies, of which one element is close to zero, and three (or four) AoA values. Next the true values determined in each figure are described for the purpose of comparison. In a Bayesian scenario, Fig. 4.9a, Fig. 4.10a and Fig. 4.11a, two strong signals form the sources which hold 0 ms and 0.4063 in time delay are expected. This means the farther base station is 121.89 km away from the closer one. Both base stations provide zero Doppler frequencies. Two target signals carry 0.5 ms and 0.8438 ms in delay which can be interpreted as the signal travel 150 km and 253.14 km in bistatic distances from the transmitters. Doppler frequency of the target displays 700 Hz or equally 923.64 m/s in range-rate. Actual angular point for the reference source is 37 degree whereas the other source provides 169 degree. The target signal's AoA in this case is 105 degree. Regarding an l_1-SVD scenario, Fig. 4.9b, Fig. 4.10b and Fig. 4.11b, the values of 0.0938 ms and 0.3125 ms are required. This shows that the closer transmitter is 28.14 km away and 93.75 km belongs to the second transmitter. The reflected signal from the target which is emitted from the closer station should travel 178.125 km (0.5938 ms) in a bistatic distance and the longer path should travel 215.625 km (0.7188 ms). The target in this scenario travels at 197.925 m/s or 150 Hz in Doppler frequency.

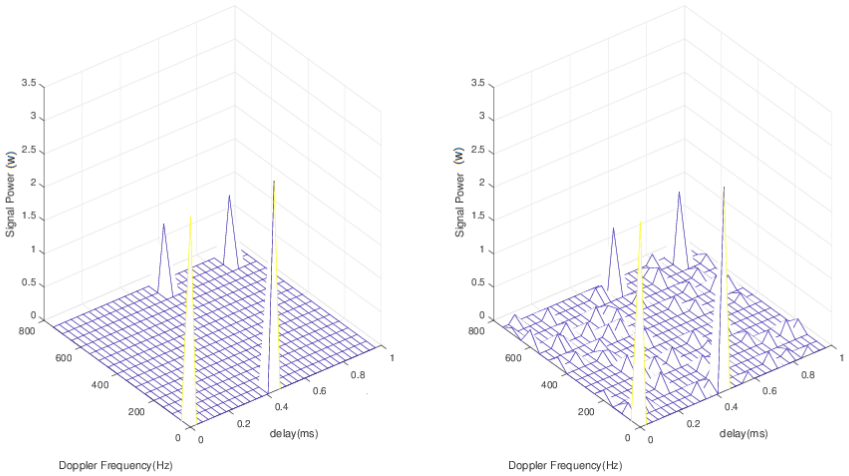

(a) Left:Original Right:Reconstructed

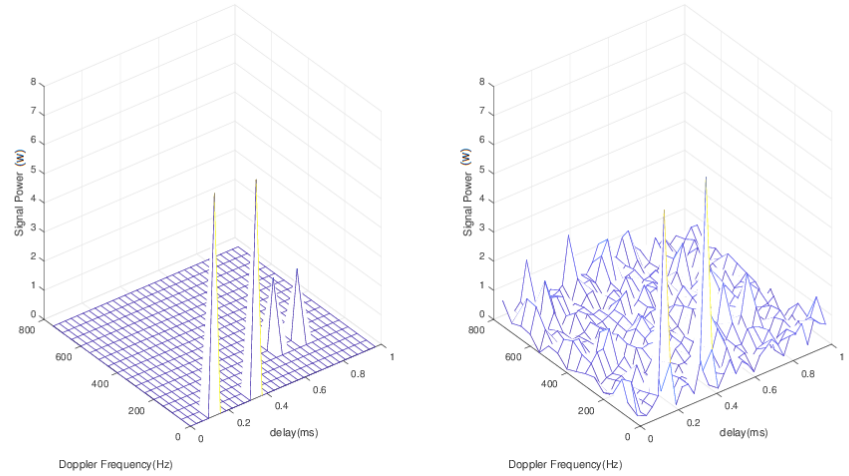

(b) Left:Original Right:Reconstructed

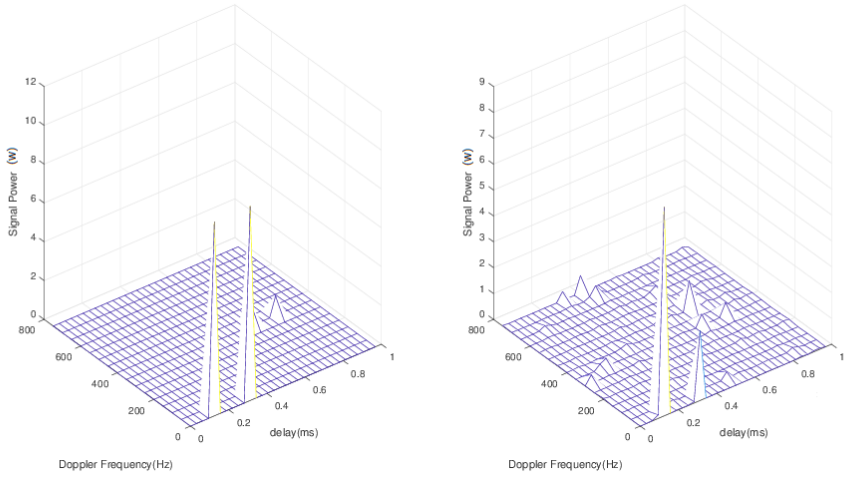

(c) Left:Original Right:Reconstructed

Figure 4.9: Reconstruction signal comparison in Delay-Doppler domain for target signal SNR = -10dB using: (a) Fast-BesselK; (b) l_1-SVD; and (c) Basis Pursuit.

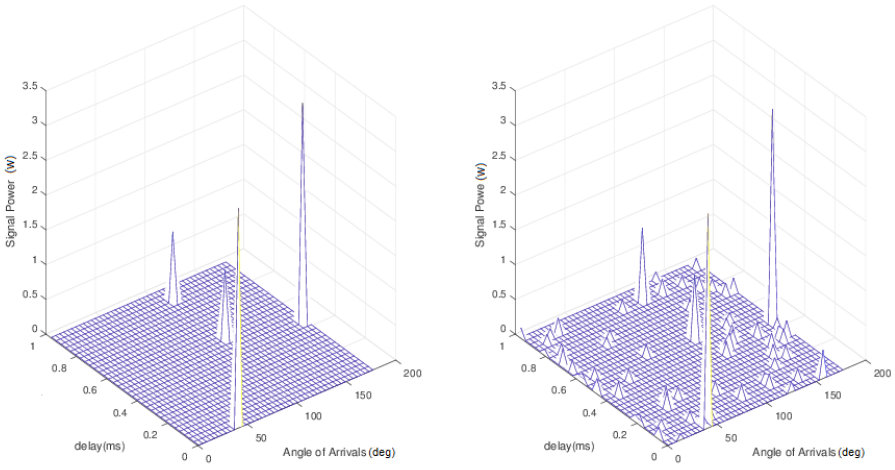

(a) Left:Original Right:Reconstructed

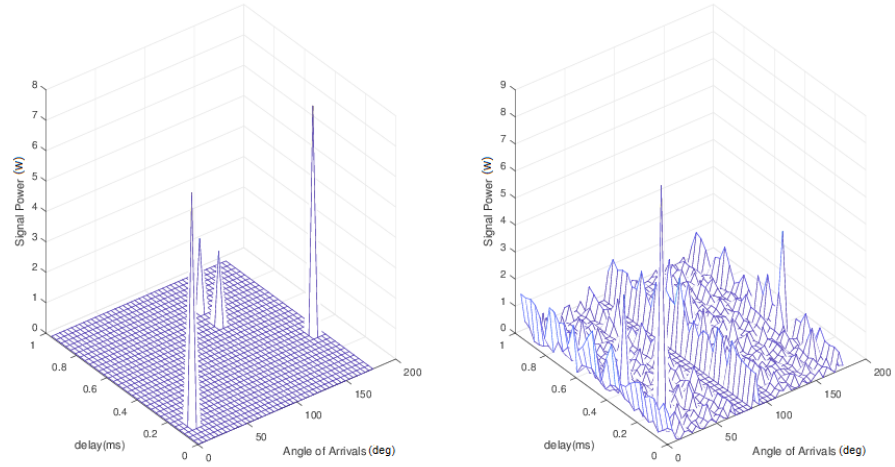

(b) Left:Original Right:Reconstructed

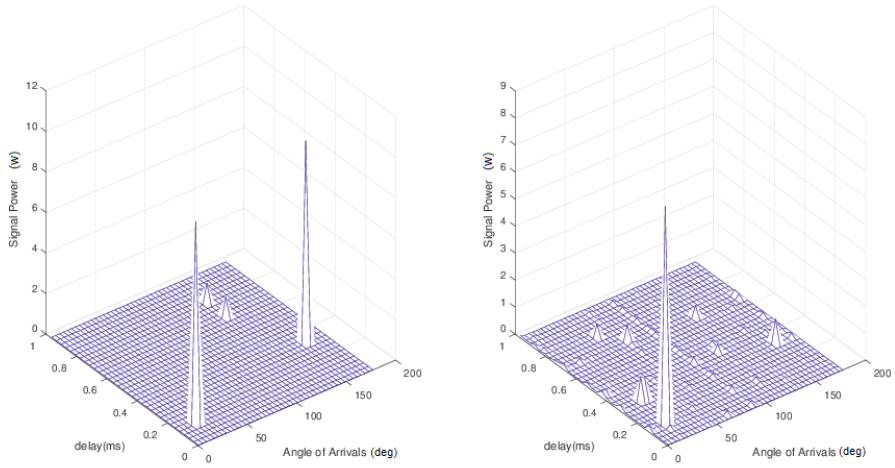

(c) Left:Original Right:Reconstructed

Figure 4.10: Reconstruction signal comparison in Delay-angular domain for target signal SNR = -10dB using: (a) Fast-BesselK; (b) l_1-SVD; and (c) Basis Pursuit.

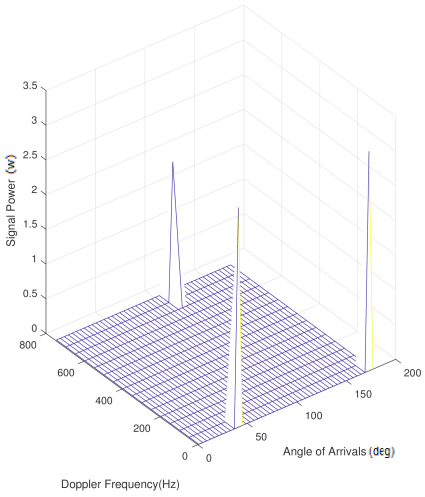

(a) Left:Original

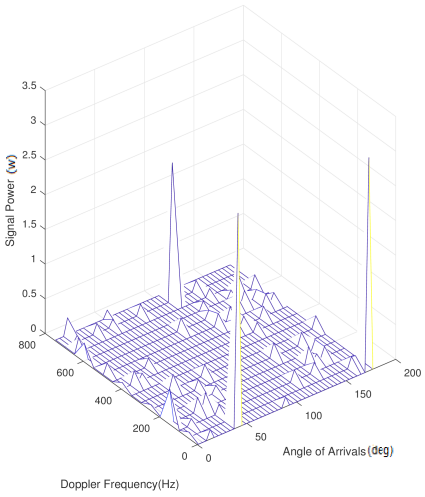

Right:Reconstructed

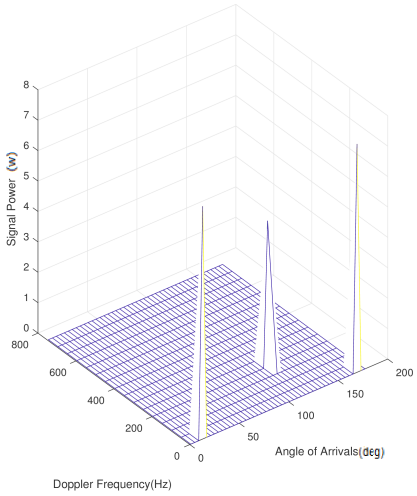

(b) Left:Original

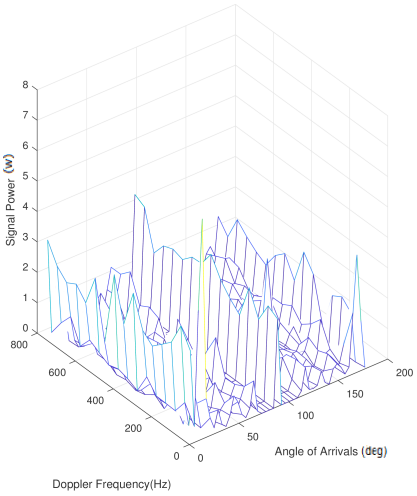

Right:Reconstructed

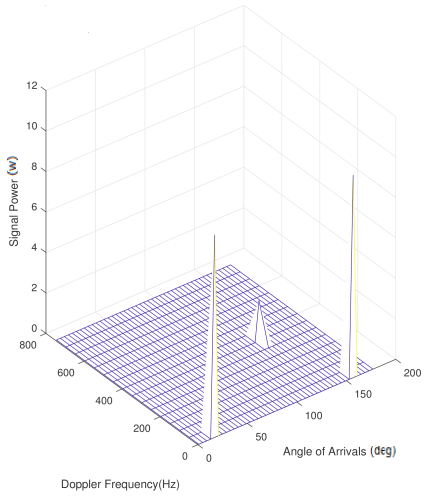

(c) Left:Original

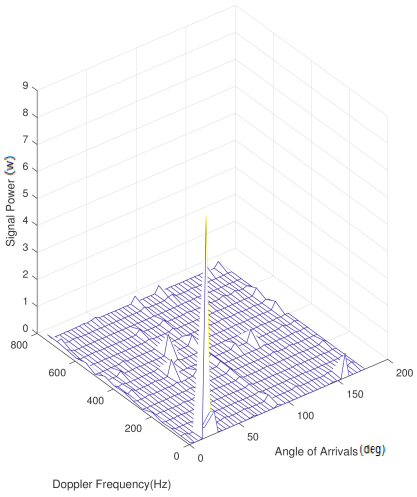

Right:Reconstructed

Figure 4.11: Reconstruction signal comparison in Doppler-angular domain for target signal SNR = -10dB using: (a) Fast-BesselK; (b) l_1-SVD; and (c) Basis Pursuit.

The angle of arrival for the signal emitted from the closer transmitter is 9 degree and 165 degree of the other. The target's AoA in this event is 113 degree. Subsequently, Basis Pursuit scenario, Fig. 4.9c, Fig. 4.10c, Fig. 4.11c, the signal travelling from the closest transmitter provides 0.0938 ms and the other source spends 0.2813 ms. This demonstrates that the farther transmitter is 84.375 km away and the other is 28.125 km away from the receiver array. The time delays corresponding to the target in this scenario are 0.625 ms and 0.75 ms respectively which means the transmitted signals impinge on the target and at the receiver through 187.5 km and 225 km in total. Actual target's Doppler frequency display 300 Hz while travelling at 395.848 m/s. Transmitted signals' AoAs in this BP case are 13 and 153 degree respectively whereas the reflected target signal retains an AoA of 125 degree.

In all domains, the BP algorithm, which consumes the most computation resources, exhibits reasonable reconstruction by comparison with the other two approaches, while l_1-SVD seems to exhibit the highest degree of erroneous reconstruction. It may be concluded that l_1-SVD is not appropriate for this task due to error while BP, although very precise, has an inhibitive degree of complexity. However, the Fast-BesselK approach provides the best performance out of the three with much lower complexity than BP. To further clarify this, in Fig. 4.12 the normalised mean-square error of the reconstructed signals versus the reference signal SNR is plotted. The NMSE in this case is calculated by

$$\text{NMSE} \triangleq \frac{\langle \|\hat{\alpha} - \alpha\|_2^2 \rangle}{\langle \|\alpha\|_2^2 \rangle}. \tag{4.65}$$

As expected, the Fast-BesselK exhibits the minimum error among the three algorithms while BP provides lower error than l_1-SVD but slightly higher than Fast-BesselK especially in the lower SNR area. It is worth to mention that the NMSE for the l_1-SVD is higher than 1 as its results provide non-zero values for most expected zero elements. The norm of error as seen in the above equation may be much higher that the norm of the original signal itself. The total number of channel realisations for fast-BesselK is 20, whereas l_1-SVD and Basis Pursuit can be realised only 2 experiments due to the processing time problem of the workstation. The number of l_1-SVD snapshots is 200.

4.7.4 Comparison of proposed Fast-BesselK method with other Bayesian CS methods.

In order to further exemplify the efficiency of the Fast-BesselK method, it will now be compared with some other BCS-based methods. As mentioned in Section 4.3.3, the two parameters: ε and η, are chosen as: $\varepsilon = 0.5$ and $\eta = 1$, as a means of implementing the

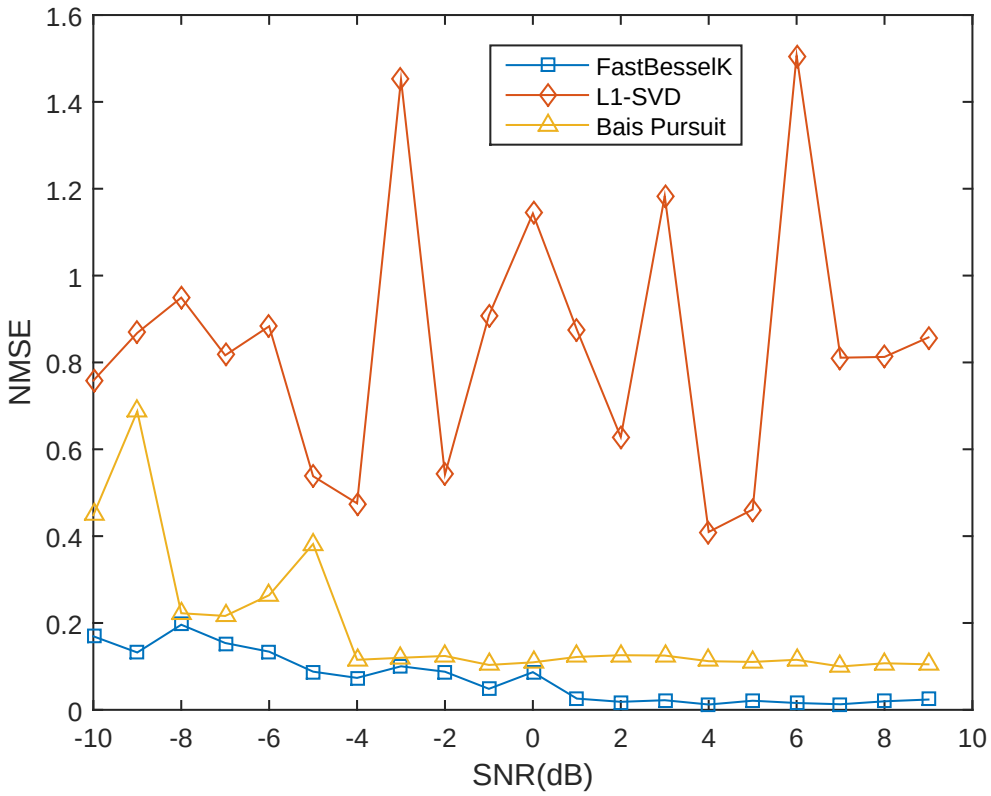

Figure 4.12: Reconstruction Performance in NMSE comparison versus SNR between Bayesian CS and previously applied CS algorithm.

Fast-BesselK algorithm in this work. On the basis of this, the following comparisons are made:

- $\varepsilon = 0.5$ and $\eta = 1$ for the specific Fast-Besselk method used throughout this work;
- $\varepsilon = 0$ and $\eta = 0$ for applying the Jeffreys prior for each γ_i;
- $\varepsilon = 1$ and $\eta = 0$ for applying Fast-RVM;
- $\varepsilon = 1$ and $\eta = 1$ for applying Fast-Laplace.

These approaches are compared under Normalised Mean Square Error (NMSE) in Fig. 4.13a. It can firstly be seen that the Fast-BesselK using Jeffreys prior presents the least amount of errors with respect to the other approaches. Without utilising the prior, the Fast-BesselK has its functioning between Fast-RVM and Fast-Laplace in the low SNR range, however the Fast-BesselK approach proposed here employs the least amount of iterations and computational time with respect to the other three algorithms. Consider the support of a vector α, which is defined as a set of $\{i : \alpha_i \neq 0\}$, it is clear that

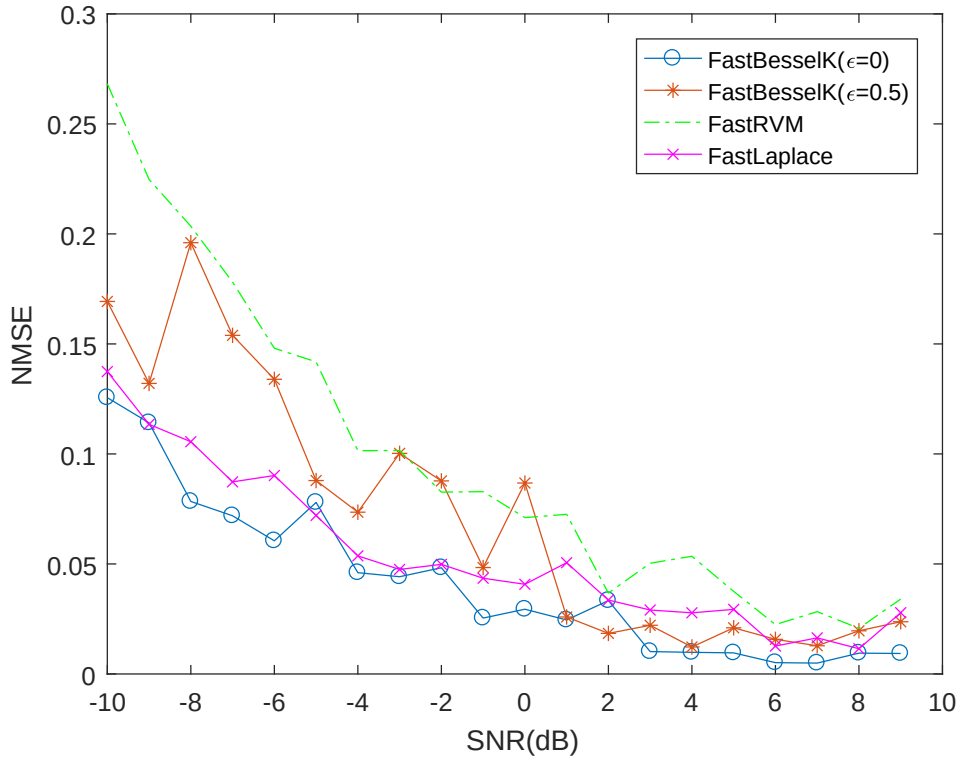

(a)

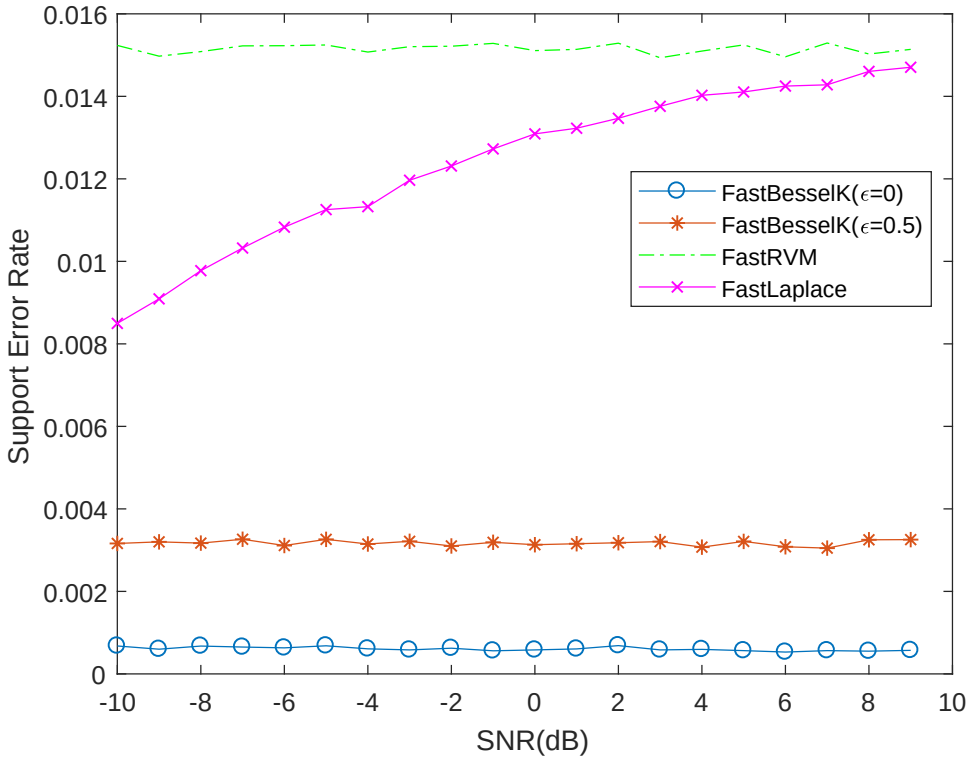

(b)

Figure 4.13: Reconstruction performance comparison versus SNR for Bayesian CS methods by: (a) NMSE; and (b) Support Error Rate. The number of channel realisations is 20.

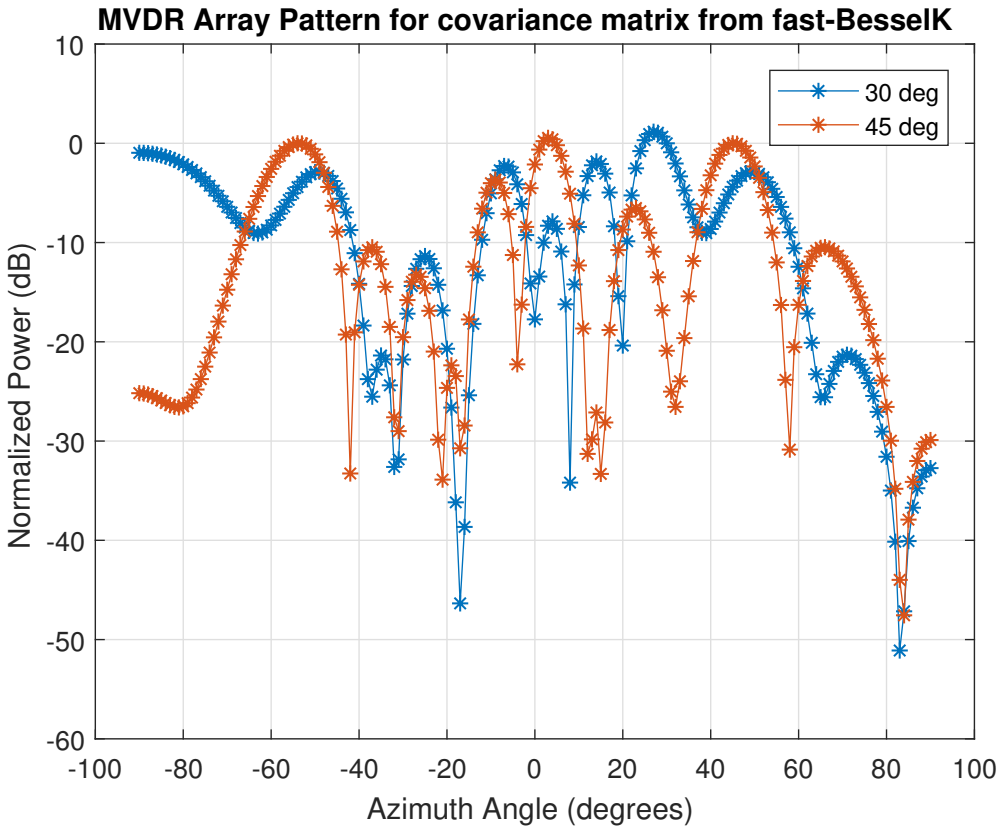

(a)

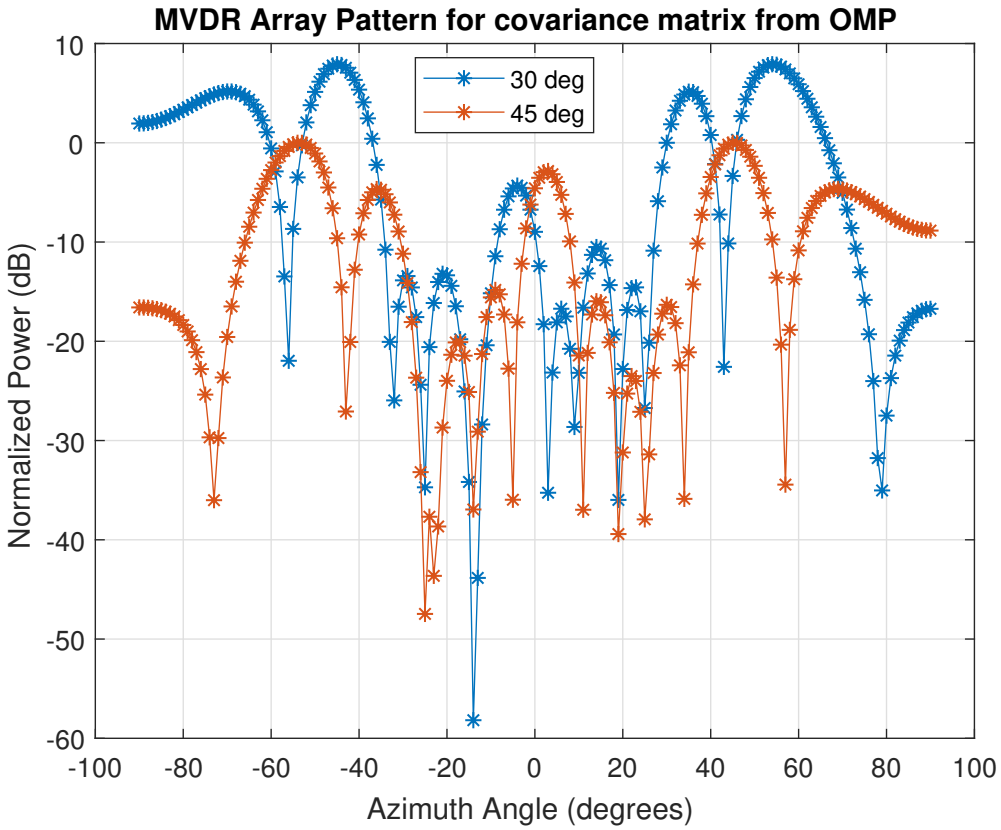

(b)

Figure 4.14: MVDR array pattern when the covariance matrix is incomplete and reconstructed using one channel realisation of: (a) Fast-BesselK; and (b) OMP.

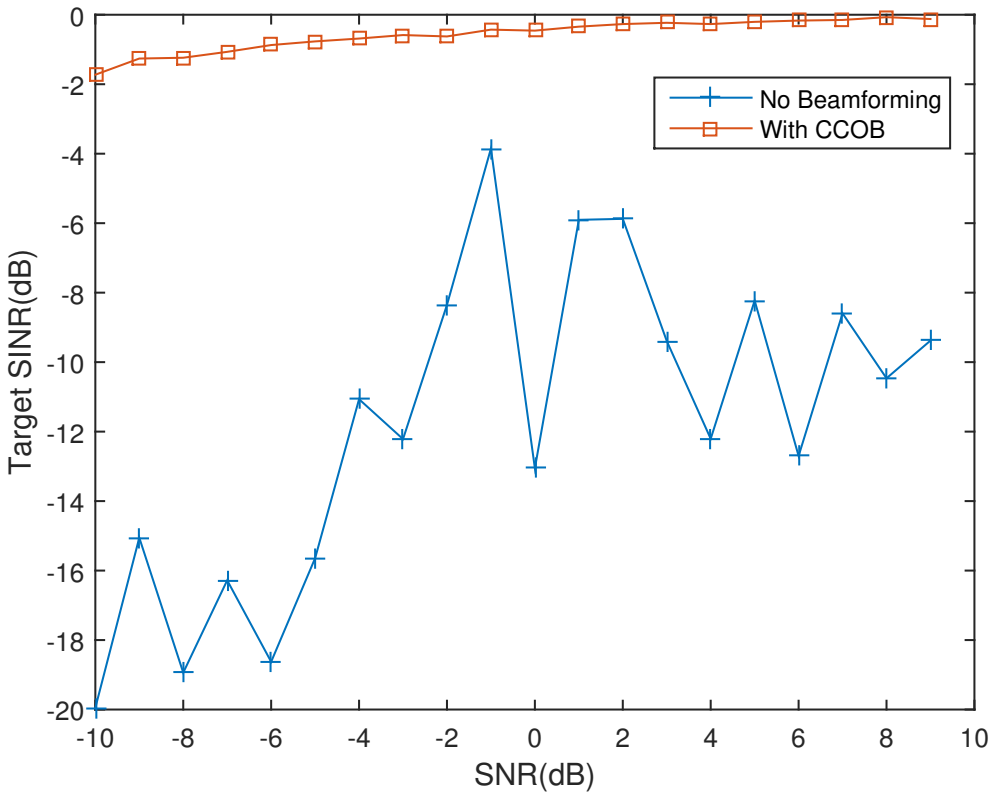

Figure 4.15: Performance in SINR versus input SNR with and without Compressive Domain Beamforming for one channel realisation Fast-BesselK.

the Fast-BesselK provides the smallest error rate, where the support error rate can be calculated as follows:

$$\text{The support error rate} \triangleq \frac{\#\{\{i : \hat{\alpha}_i = 0 \text{ and } \alpha_i \neq 0\} \cup \{i : \hat{\alpha}_i \neq 0 \text{ and } \alpha_i = 0\}\}}{N_\alpha}. \quad (4.66)$$

This further strengthens the appropriateness of the Fast-BesselK approach proposed by this work as an excellent candidate for practical 3D parameter extraction in MIMO passive radar.

4.7.5 Beamforming results

Despite the fact that Fast-BesselK results demonstrate low NMSE and support error rate, there is still the matter of the high powered clean signal, to which the MIMO passive radar listens, to contend. As mentioned, while this signal is useful for the matched filter correlation process, if it is too strong it can have a perturbing effect on the functioning of the Fast-BesselK parameter extraction algorithm. Since beamforming in the compressive domain cannot be achieved by conventional means; this work has proposed a novel CCOB method.

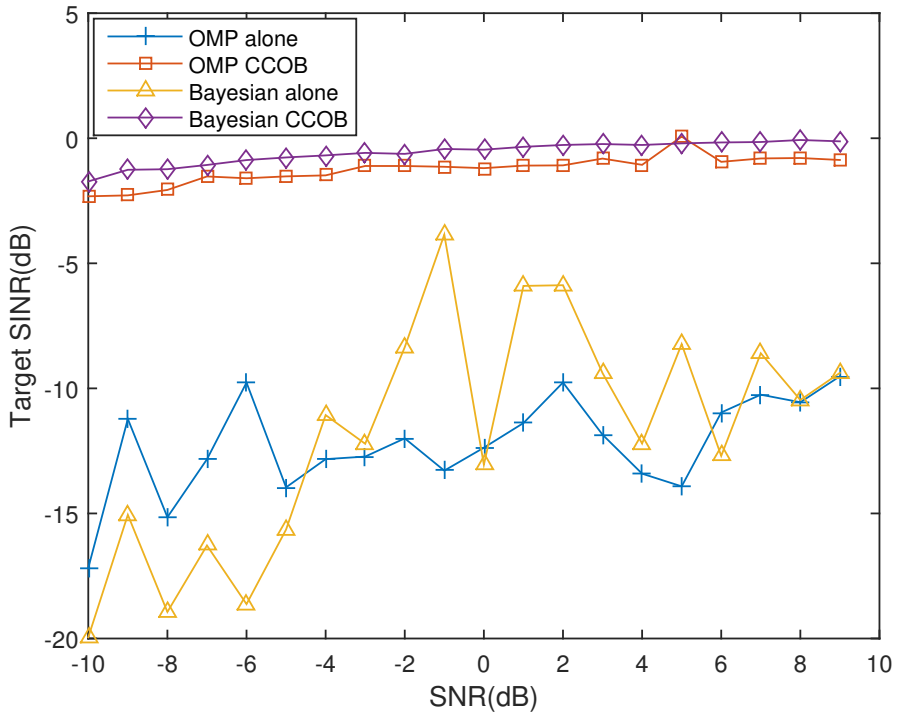

(a)

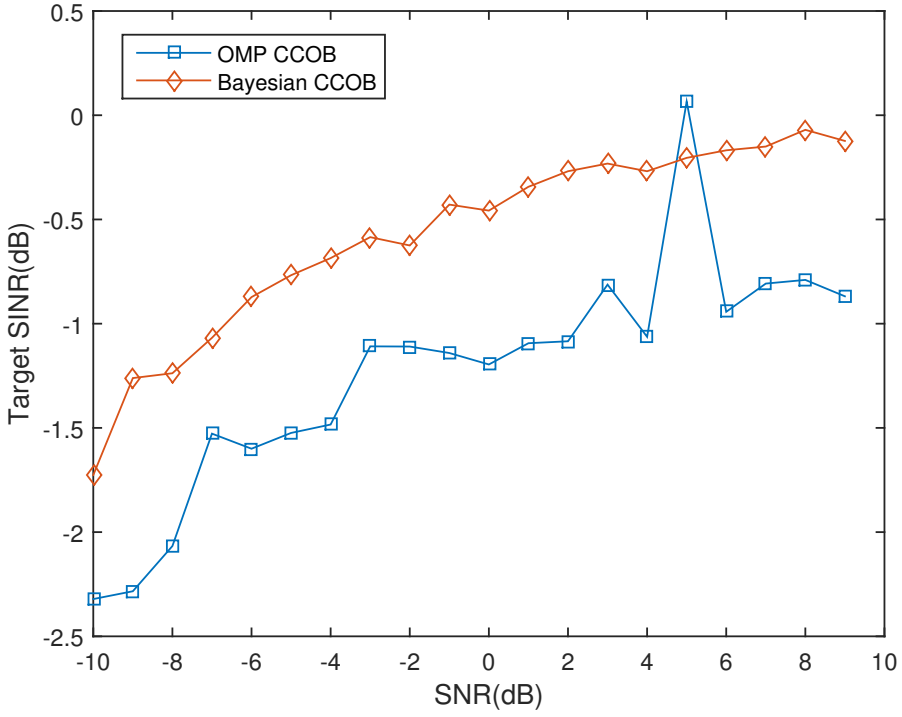

(b)

Figure 4.16: An instance of performance comparison in SINR versus input SNR applying Compressive Domain Beamforming in: (a) full figure; and (b) closer view for weight utilisation. The algorithm has been implemented for one channel realisation and the results demonstrate that most of the OMP outputs are a bit worse than Fast-BesselK.

It is shown that the beamforming for compressive measurements needs to be specific as the covariance matrix may contain incomplete data. Fig. 4.14a displays the result of MVDR beamformer used for the covariance matrix from the fast-BesselK method. The location of the expected beam can be indicated as well as the incorrect beam in other angles, whereas the result in Fig. 4.14b shows that the weight of the receiver antenna cannot be steered in the correct direction. Then, we calculate the target signal to interference plus noise ratio (target SINR) as shown in (4.45) and treat the direct signal as interference. The target SINR of each reconstruction algorithm can inform the target-only detection performance. Without beamforming, the target SINR after Fast-BesselK algorithm in Fig. 4.15 is very low, which means the target parameters may not be extracted as we expected. The beamforming approach achieves an improvement in the same figure. Fig. 4.16 then compares the target SINR of the Fast-BesselK approach with and without CCOB. As it is a useful illustration, we also apply Orthogonal Matching Pursuit (OMP)-CCOB [109] in our work. Both compressive sensing methods provide satisfactory results while incorporating with CCOB, however, a more accurate approximation can be achieved by Bayesian compressive sensing than OMP since OMP continues selecting the possible basis functions without any removal mechanism [101] . It is clear that the CCOB is mitigating the effect of the clean BS signal in an appropriate manner, which would in turn facilitate the correct functioning of the Fast-BesselK algorithm in a manner that would be in line with an expected SNR performance.

4.8 Summary

Drawing from the conclusion in chapter 3, the widely-spread receivers can be replaced by the co-located antennas as the purpose of array processing. Co-located receiver provides the extension from two-dimensional matched filter to three-dimensional version. This chapter discusses the 3D signal model along with the configuration of radar receivers. A number of measurements are also increased while the multiple antennas supply a feasibility of angular domain detection. Matched filter corresponding to three parameters is also considered in order to show the extraction scheme for a full-dimension measurements. To reduce the size of the measurement matrix, compressive sensing methods, which was introduced in the previous work, can also be used. This chapter also presents the design of CS sensing matrix which is suitable for OFDM passive radar. Basis Pursuit outperforms the l_1-SVD when the problem dimension is increased due to the number of

antennas. Concerning the resources consumption, a statistical-based algorithm applying sparse Bayesian learning is proposed. Fast-BesselK utilises probabilistic model and two-layer prior for the expected parameter. It also efficiently employ the fast mechanism from the RVM. The outcomes from the fast-BesselK method display better signal extraction both in illustrations and in mean-square error values. Regarding low-complexity methods, such as other Bayesian-based and OMP, fast-Besselk has a mechanism of better accuracy. The attractive performance is then utilised with the beamforming algorithm, where a complete covariance matrix is not available. Regarding the beamforming, this thesis proposes the convex-optimisation beamformer where the expected target signal is reserved when the unwanted signals are diminished. Fast-BesselK with CCOB also provides satisfactory outcomes compared to OMP-version beamforming. From this chapter, compressive measurements present a dimensionality reduction, along with the signal extraction is impressively achieved by the algorithm mentioned. Beamforming results also allow the system to be operated in the interference-limited scenario provided that the interference characteristics are known at the receiver. This will be discussed in the next chapter.

Chapter 5

Interference modelling for OFDM passive radar networks using stochastic geometry

5.1 Introduction

In the previous chapter, the beamforming in OFDM passive radar that applies the compressive measurements was discussed. It was shown that the beamforming technique provides an advantage in target detection by weighing the antenna probes for the enhancement of the surveillance signal, while the power of the reference signal is reduced. The convex-constrained optimisation beamforming, along with MUSIC algorithm, is able to successfully create the beamforming weights. When the state-of-the-art compressive sensing is utilised, the technique proposed in Section 4.4 supplies a feasible solution to incomplete data. Thus, it is shown that equipping the receiver with multiple antennas can allow the beamforming towards the target of interest without filtering the direct path.

Given the parameter extraction methods and the beamformer previously discussed in this thesis, the system considered is regarded as one multi-antenna receiver. In chapter 3, the separately-located antennas were considered, while the antenna array was introduced in chapter 4. Both passive radar structures can be merged into the group of receivers. This configuration becomes a class of large wireless systems. The passive radar network in which each receiver is equipped with an antenna array will potentially enable a larger area of coverage.

The derivation from [3], where the automotive radar was used, is applied for bistatic passive radar networks modelling and from [68], a cellular networks, is applied for multi-

static radar networks in this chapter. The bistactic radar equation is employed, as well as the target signal to interference (plus noise) ratio are presented. In contrast to communication research, the fading channel considered here is Nakagami-n fading as the channel includes one strong line-of sight and many weak signals. The statistical characteristics for the interference in both systems are then derived by applying stochastic geometry as reviewed in Section 2.5. Specifically, in a multistatic radar networks, the density of radar receivers determine a cell radius and the target signal is emphasised. The approximation of interference is also compared with the simulated scenarios in this work.

5.2 Bistatic passive radar networks using stochastic geometry

In this section, the model of the system that imitates the geometric diagram of passive radar operations is composed. There is a radar receiver established at the origin and this is regarded as the typical receiver. The statistical attitude of the typical receiver is common to all other receivers. As usual, a transitory snapshot of the target movement, which can be acknowledged as immobile, is examined. It should be noted that although the radar scenario statistics are not actually fixed, the phase rotation caused by the Doppler shift is approximately continual over a block duration T'[16] and can be harmlessly considered as static over a justifiable observation period.

5.2.1 Ad-hoc system model

Following on from an automotive radar in [3], this subsection applies a simple paradigm of the passive radar networks scenario. It assumes that a passive radar is operated in bistatic configuration and listens to the closest base station where the reference signal is clear and appropriate to apply the extraction algorithms. For the sake of simplicity, there is one target present for each transceiver pair. To emphasise this, each base station transmits the same OFDM signals, but with different characteristics, such as operational frequency, bandwidth and the number of subcarriers. This means that the passive radar can only utilise the transmitted signal from its pair to perform the matched filter. Hence, the signals from other base stations, as well as the target scattering due to their signals, are considered interference. Considering the signal scattered from the target to the passive radar receiver, the bistatic radar equation [5] can be shown as:

$$P_{xr} = \frac{P_t G_t}{4\pi D_{kx}^{\alpha}} \cdot \frac{\sigma_b}{4\pi D_{xr}^{\alpha}} \cdot \frac{G_r v^2}{4\pi}, \tag{5.1}$$

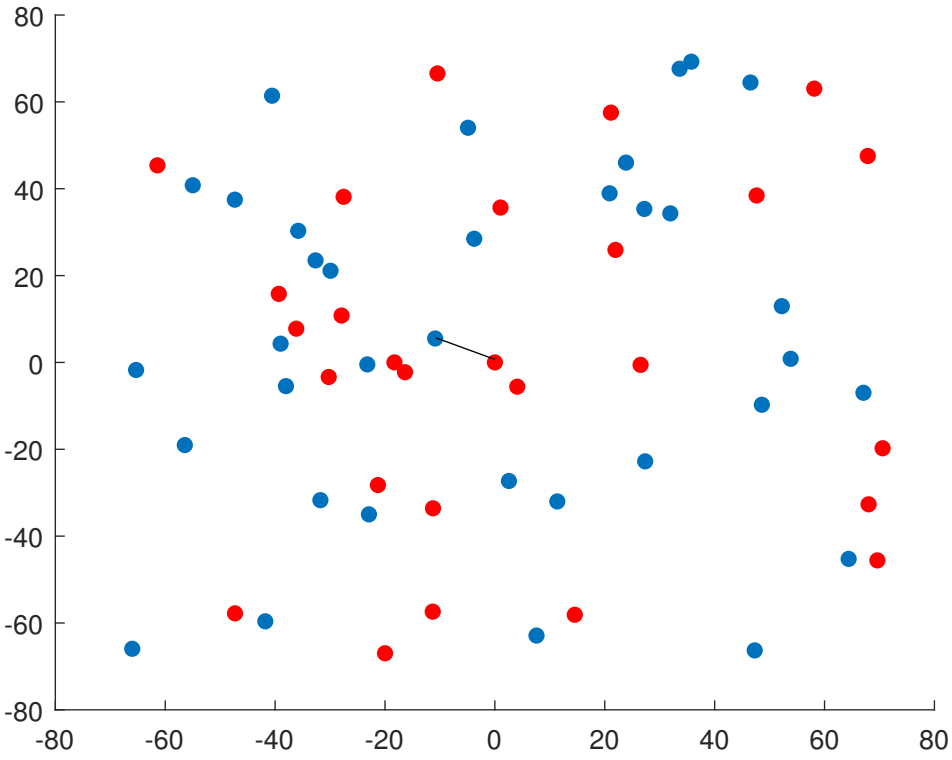

(a)

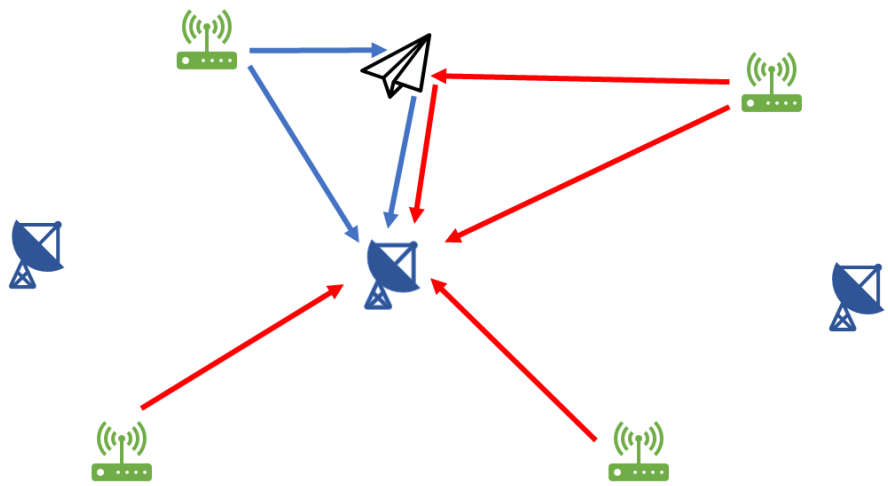

(b)

Figure 5.1: An example of passive radar in ad-hoc networks using stochastic geometry: (a) the OFDM base stations (blue dots) and the passive radar receivers (red dots); (b) the OFDM base stations (green icons), the passive radar receivers (blue icons), the expected signals (blue arrows) and the interfering signals (red arrows).

where the transmitters are assumed to broadcast with the same amount of power P_t and this refers to the transmitted signal sent by the chosen base station. G_t and G_r denote the gain of the transmit antenna and receive radar antenna respectively. σ_b is the bistatic radar cross section corresponding to the kth transmitter, and the operated signal wavelength is denoted by ν. The notation for wavelength in this chapter is altered so the point process density is not replicated. The distances from the k-th transmitter to the target and the target to the radar receiver are respectively expressed by D_{kx} and D_{xr}.

In fitting with the property of a right triangle inside an ellipse, the OFDM station accepted by the receiver is at the Euclidean distance d_0, therefore; $D_{kr} = d_0 = \sqrt{D_{kx}^2 + D_{xr}^2}$. An inverse α-law is introduced instead of an inverse square-law for the flexibility boosting of the radar equation. α is the path loss parameter that can be marginally greater than 2. The volatility in the positions of both OFDM stations and passive radar receivers is occupied by a Poisson Point Process (PPP). Assuming that the passive radars are distributed as a point process $\Phi^{(r)}$ of density $\lambda^{(r)}$, there is a target reflection impinging on each receiver in a random direction. The locations of OFDM stations are also randomised as a part of the process $\Phi^{(t)}$ of density $\lambda^{(t)}$. The example of our ad-hoc networks scenario is displayed in Fig. 5.1a where the blue dots refer to the base stations and red dots show the passive radar. The bistatic configuration is also illustrated in Fig. 5.1b, as well as the distinction between the desired and interference signals. Densities λ are regulated in stations or radars per unit area. The fading for each transmitter-receiver pair is considered independent and identical. PPP admits an evolution of manageable investigation using Campbell's theorem (2.34).

In order to appraise the effectiveness of the passive radar system, the idea of signal-to-interference-plus-noise ratio (SINR) is employed. The interferences provoked by denied base stations, as well as their target-related interferences, can be understood as white noise in the receiver. Referring to the bistatic signal power equation in (5.1), the unwanted signals arising from all interfering OFDM stations are then typified by locating the radar at origin to compute the *typical* link performance, the SINR between the radar and its corresponding target of interest at point x where $\|x\| = D_{xr}$ is

$$\mathrm{TSINR}_{br} = \frac{P_{xr}}{\sigma_N^2 + \mathbf{I}}, \tag{5.2}$$

where $\mathbf{I}$ is the sum of interferences at the passive radar receiver. σ_N^2 is the variance of the additive noise. By using an α-law for the signal deterioration, similar aspects to the desired target channel can be managed. Similar to [3], the interference at the passive radar

induced by an interferer at point y is defined as:

$$\mathbf{I}_y = P_t \mathbf{h}_y \|y\|^{-\alpha} \cdot \frac{G^k G_r v^2}{(4\pi)^2}, \tag{5.3}$$

where the Euclidean distance calculated from the k-transmitter to the origin is denoted by $\|y\|$. In this expression, a statistical fading process in the channel $\mathbf{h}_y$ between the interfering transmitter k and the receiver is involved. This random variable vector is composed of multipath propagation because of echoes from the environment. As a result of this, if all reflections appear within the integration time of the expected signal, this fading model will include the effect of target reflections, as well as clutters. In this simplified case, the interferences caused by the interfering signals that impinge on the target of interest are not separated from the expression above. Due to the homogeneous fading environment, the elements of this random variable vector are i.i.d. The channel statistical process mentioned above can be described as follows [116]:

Fast-fading: As the signals from the base stations to the passive radar are composed of one strong line-of sight and many randomised components, which are weaker. It is then assumed to be Nakagami-n (Rice) fading. The fast-fading can be denoted by h_{yr} or h_y if a typical receiver is being discussed; Hence, the power gain $|h_{yr}|^2$ follows a noncentral chi-square distribution with a mean value of μ, where the PDF can be formulated as follows:

$$f_{|h_{yr}|^2}(\xi) = \frac{(1+n^2)e^{-n^2}}{\mu} \exp\left[-\frac{(1+n^2)\xi}{\mu}\right] B_0\left(2n\sqrt{\frac{(1+n^2)\xi}{\mu}}\right), \tag{5.4}$$

where the Euler's number is denoted by e, $n \in \{0, ..., \infty\}$ is the Nakagami-n fading parameter and $B_0(\cdot)$ represents the zero-order modified Bessel function. In case of shadowing is included in the channel, consider:

Shadowing: denoted by $\mathscr{L}_{yr}$. It is assumed to follow a log-normal distribution [69], where the PDF is as follows:

$$f_{\mathscr{L}_{yr}}(\xi) = \frac{10\log_{10}(e)}{\sqrt{2\pi\sigma^2\xi}} \exp\left[-\frac{\left(10\log_{10}(\xi) - \mu\right)^2}{2\sigma^2}\right], \tag{5.5}$$

where μ and σ are the mean and variance of the random variable $10\log_{10}(\mathscr{L}_{yr})$, respectively. Let us designate β_1 for $\frac{G^k G_r v^2}{(4\pi)^2}$, the sum of the interference observed at a typical passive radar at the origin is shown as:

$$\mathbf{I} = \sum_{y \in \Phi^{(t)} \setminus d_0} P_t \mathbf{h}_y \|y\|^{-\alpha} \beta_1. \tag{5.6}$$

The interference expression for the ad-hoc scenario can be formulated as in the above equation. Regarding the configuration and TSINR_{br} presented in this part, the following

subsection discusses the statistical characteristics of the interfering signals when they are embedded in the passive radar processing.

5.2.2 Interference model in bistatic passive radar networks

To understand the interference characteristic, its mean, variance and distribution are formulated in this section by applying stochastic geometry theory.

Mean of interference

In order to acquire a primary significance on the major parameters that influence the interference, the mean value is realised. Beginning with the expression in (5.6), the sum over a PPP can be considered as follows

$$\mathbb{E}[\mathbf{I}] = \mathbb{E}_{\mathbf{h}}\mathbb{E}_{\Phi^{(t)}}\left[\sum_{y\in\Phi^{(t)}\setminus d_0} \mathbf{h}_y P_t \|y\|^{-\alpha}\beta_1\right], \tag{5.7}$$

where the expectation of the stochastic process of the channel is designated by $\mathbb{E}_{\mathbf{h}}$ and the geometric expectation of all attainable realisations of the points of interferers is denoted by $\mathbb{E}_{\Phi^{(t)}}$. Using Campbell's theorem (2.34), the interference mean can be derived as:

$$\mathbb{E}[\mathbf{I}] = \mathbb{E}_{\mathbf{h}}[\mathbf{h}]\int_{d_0}^{\infty} \lambda^{(t)}\beta_1 P_t u^{-\alpha} du, \tag{5.8}$$

where the interference is limited by the distance from the receiver compared to the paired transmitter. If the interferer locates at point (y_i, y_j), the distance $\|y\|$ can be calculated from $\sqrt{y_i^2 + y_j^2}$. Given that d_0 is the Euclidean distance of the transmitter that provides a signal correlation of the source and the target, the Euclidean distance of interferer $\|y\|$ can be anywhere in a space outside a circle with a radius d_0, so that it can be replaced with u. From (5.7) to (5.8), the acceptance that the geometrical point process has an unrelated distribution from i.i.d propagation channels is adopted. With the assumption that the average channel gain is normalised, $\mathbb{E}[h] = 1$ mean of the interference after performing the integration produces:

$$\mathbb{E}[\mathbf{I}] = \frac{\lambda^{(t)}\beta_1 P_t d_0^{-(\alpha-1)}}{\alpha-1}, \tag{5.9}$$

$$= \frac{\lambda^{(t)}\beta_1 P_t (D_{kx}^2 + D_{xr}^2)^{-(\alpha-1)/2}}{\alpha-1}, \tag{5.10}$$

where, in (5.10), the transmitter distance is substituted with the corresponding distances of the target. Obviously, the mean of interference in bistatic ad-hoc radar networks provides similar expressions as in [3], where the derivation is followed. However, the author

simplifies the system by cancelling the space between the adjacent lanes. In this thesis, the distance d_0 can determine whether the base station is outside the prospect area. Still, the bistatic passive radar configuration is not only concerned with the characteristic of interference; it is also aware of how the target-reflected signal is affected. There should be more consideration of TSINR_{br}, as is discussed in Section 5.2.3.

Variance of interference

Apart from the interference mean, this thesis also presents the variance of the sum of interference, which is not mentioned in the reference. To fulfil the statistical analysis, the variance calculation can start from:

$$\begin{aligned}\text{var}(\mathbf{I}) &= \mathbb{E}\left[(\mathbf{I}-\mathbb{E}[\mathbf{I}])^2\right] \\ &= \mathbb{E}[\mathbf{I}^2]-\mathbb{E}[\mathbf{I}]^2, \end{aligned} \tag{5.11}$$

where

$$\begin{aligned}\mathbb{E}[\mathbf{I}^2] &= \mathbb{E}_{\mathbf{h}}\mathbb{E}_{\Phi^{(t)}}\left[\left(\sum_{y\in\Phi^{(t)}} P_t\mathbf{h}_y\|y\|^{-\alpha}\beta_1\right)^2\right] \\ &= \mathbb{E}_{\mathbf{h}}\mathbb{E}_{\Phi^{(t)}}\left[\left(\sum_{y\in\Phi^{(t)}} P_t\mathbf{h}_y\|y\|^{-\alpha}\beta_1\right)\left(\sum_{z\in\Phi^{(t)}} P_t\mathbf{h}_z\|z\|^{-\alpha}\beta_1\right)\right] \\ &= \mathbb{E}_{\mathbf{h}}\mathbb{E}_{\Phi^{(t)}}\left[\left(\sum_{y\in\Phi^{(t)}} P_t\mathbf{h}_y\|y\|^{-\alpha}\beta_1\right)\left(P_t\mathbf{h}_y\|y\|^{-\alpha}\beta_1+\sum_{z\neq y\in\Phi^{(t)}} P_t\mathbf{h}_z\|z\|^{-\alpha}\beta_1\right)\right] \\ &= \mathbb{E}_{\mathbf{h}}\mathbb{E}_{\Phi^{(t)}}\left[\sum_{y\in\Phi^{(t)}}\left(P_t\mathbf{h}_y\|y\|^{-\alpha}\beta_1\right)^2\right]+\mathbb{E}_{\mathbf{h}}\mathbb{E}_{\Phi^{(t)}}\left[\sum_{y,z\in\Phi^{(t)}}\left(P_t\mathbf{h}_y\|y\|^{-\alpha}\beta_1\right)\left(P_t\mathbf{h}_z\|z\|^{-\alpha}\beta_1\right)\right] \end{aligned} \tag{5.12}$$

$$= \mathbb{E}_{\mathbf{h}}[\mathbf{h}^2]\lambda^{(t)}\int_{d_0}^{\infty}(P_t u^{-\alpha}\beta_1)^2 du+\left(\mathbb{E}_{\mathbf{h}}[\mathbf{h}]\int_{d_0}^{\infty}\lambda^{(t)}\beta_1 P_t u^{-\alpha}du\right)^2. \tag{5.13}$$

From (5.12) to (5.13), the assumption of i.i.d over the fading channels is employed. Referring to (5.8) with the subtraction of the mean square term, the variance can be displayed as

$$\text{var}(\mathbf{I}) = \mathbb{E}_{\mathbf{h}}[\mathbf{h}^2]\lambda^{(t)}\int_{d_0}^{\infty}(P_t u^{-\alpha}\beta_1)^2 du. \tag{5.14}$$

After evaluating the integration, the variance of interference can be derived as:

$$\text{var}(\mathbf{I}) = \mathbb{E}_{\mathbf{h}}[\mathbf{h}^2]\frac{\lambda^{(t)}(P_t)^2\beta_1^2 d_0^{-(2\alpha-1)}}{2\alpha-1}. \tag{5.15}$$

From the equation above, the channel fading still exists. When $\mathbb{E}_{\mathbf{h}}[\mathbf{h}^2]$ becomes known, the result can be explicitly calculated and this is applied to any fading schemes. Moreover, the Gamma variable techniques mentioned in Section 2.5.3 might be useful to approximate the fading of the channel.

Interference distribution

The last part in this subsection in the ad-hoc networks refers to the distribution. The interference characteristic function is acquired, and its cumulative distribution function (CDF) is then developed. Considering the definition of the Characteristic Function (CF) of a random variable, the CF of the interference in the PPP model can be disclosed as:

$$\begin{aligned}\varphi_{\mathbf{I}}(\omega) &= \mathbb{E}[e^{j\omega\mathbf{I}}] \\ &= \mathbb{E}_{\mathbf{h}}\mathbb{E}_{\Phi}\left[\exp\left(j\omega\sum_{y\in\Phi^{(t)}} P_t\mathbf{h}_y\|y\|^{-\alpha}\beta_1\right)\right]. \end{aligned} \tag{5.16}$$

Due to the fact that the geometrical stochastic process and the channel random variable are liberated, the equation above becomes:

$$\varphi_{\mathbf{I}}(\omega) = \mathbb{E}_{\Phi}\left[\prod_{y\in\Phi^{(t)}} \mathbb{E}_{\mathbf{h}}\exp\left(j\omega P_t\mathbf{h}_y\|y\|^{-\alpha}\beta_1\right)\right]. \tag{5.17}$$

Implementing the probability generating functional of the homogeneous PPP [81], as in (2.35). (5.17) can be clarified as:

$$\varphi_{\mathbf{I}}(\omega) = \exp\left(-\mathbb{E}_{\mathbf{h}}\int_{d_0}^{\infty}[1-\exp(j\omega P_t\mathbf{h}u^{-\alpha}\beta_1)]\lambda^{(t)}du\right) \tag{5.18}$$

where the y notation in $\mathbf{h}_y$ is ignored due to an i.i.d random variable. The CDF can be accessed by employing the Gil-Pelaez's inversion theorem in the integral [117]:

$$F_{\mathbf{I}}(\zeta) = \frac{1}{2} - \frac{1}{\pi}\int_0^{\infty}\frac{1}{\omega}\mathrm{Im}\left[\varphi_{\mathbf{I}}(\omega)\exp(-j\omega\zeta)\right]d\omega, \tag{5.19}$$

where the integration in (5.18) is performed with some simplification, whereby $\alpha \approx 2$ is the common case and d_0 is positive. The derivations shown above resemble the expressions in [3]. In this system, however, the CF of interference can be displayed as:

$$\begin{aligned}\varphi_{\mathbf{I}}(\omega) = \exp\Bigg(-\mathbb{E}_{\mathbf{h}}\Bigg[&\lambda^{(t)}d_0\exp\left(\frac{j\omega P_t\mathbf{h}\beta_1}{d_0^2}\right) - \lambda^{(t)}d_0 \\ &- \left(\lambda^{(t)}(j\pi\omega P_t\mathbf{h}\beta_1)^{1/2}\mathrm{erfi}\left(\frac{\sqrt{j\omega P_t\mathbf{h}\beta_1}}{d_0}\right)\right)\Bigg]\Bigg)\end{aligned} \tag{5.20}$$

The equation (5.19) above can be calculated numerically. However, the approximation in [3], as well as the comparable literature with an inverse Gamma distribution, is referred to. Regarding tractability, the distribution can be simplified as:

$$F_{\mathbf{I}}(\zeta) = \text{efrc}\left(\sqrt{\frac{\pi\lambda^2\beta_1 P_t}{4\zeta}}\right), \tag{5.21}$$

where the superscript t is dropped to ensure a readable expression with the understanding that the density of the transmitters is usually discussed.

5.2.3 TSINR probability in ad-hoc Networks

As the interference is included into the system, the performance of the passive radar receiver to detect the target follows the TSINR_{br}, as shown in (5.2). The threshold θ is denoted for an acknowledged detection. The probability of TSINR_{br} achieving the target detection can be calculated as follows:

$$\begin{aligned}\mathbb{P}(\text{TSINR}_{br} > \theta) &= \mathbb{P}\left(\frac{P_{xr}}{\sigma_N^2 + I} \geq \theta\right) \\ &= \mathbb{P}\left(I \leq \frac{P_{xr}}{\theta} - \sigma_N^2\right).\end{aligned} \tag{5.22}$$

From (5.22) above, the distribution derived in Section 5.2.2 can be employed and it can be shown as:

$$\mathbb{P}(\text{TSINR}_{br} > \theta) = F_{\mathbf{I}}\left(\frac{P_{xr}}{\theta} - \sigma_N^2\right), \tag{5.23}$$

with the assumption that the reference and surveillance signal can be completely distinguished, so the reference may not be the disturbance. However, the reference signal is relatively strong so it can interfere with the target signature after correlation. In this case, the reference signal from the paired transmitter can be regarded as the interference. Therefore, the probability becomes:

$$\begin{aligned}\mathbb{P}(\text{TSINR}_{br} > \theta) &= \mathbb{P}(I + I_D \leq \frac{P_{xr}}{\theta} - \sigma_N^2) \\ &= \mathbb{P}(I + P_t \mathbf{h}_D d_0^{-\alpha} \leq \frac{P_{xr}}{\theta} - \sigma_N^2) \\ &= F_{\mathbf{I}}\Big(\frac{P_{xr}}{\theta} - P_t \mathbf{h}_D d_0^{-\alpha} - \sigma_N^2\Big),\end{aligned} \tag{5.24}$$

where $\mathbf{h}_D$ follows the same distribution as $\mathbf{h}_y$, which was discussed in Section 5.2.

In this section, the ad-hoc networks of passive radars that operate in bistatic configuration are modelled. This scenario could be a good beginning for more complex scenes.

Here, the interference statistics are derived using the formulation in [3]. Apart from understanding the interfering signals, passive radar processing requires an acknowledgment of the target detection ability where the differences from the literature become notable. The explanations of the plots regarding the interference statistics discussed in this section are displayed in the last section in this chapter.

5.3 Multistatic passive radar networks using stochastic geometry

In a more complex scheme, a passive radar can integrate many incoming signals in order to increase the chance of detection. This multistatic configuration also provides spatial diversity similar to a MIMO radar, with the assumption that there are many tiers of transmitters that can communicate inside their own group, but not to others. The radar receiver can emulate the cellular networks by locating one receiver in each cell. As the results show, the interference from the neighbouring cells require some understanding. This thesis adopts the interference modelling in cellular networks, as shown in [68]. The passive radar networks, however, can be considered in two different cell association scenarios which are:

1. Downlink communication scenario: this can resemble the system model in [68]. The typical base station can be located at the origin, while the radar receiver is at the point $(d_0, 0)$. The transmitters send the reference signal to the receiver, while the signals impinge on the target and arrive at the receiver, alike the stations transmit their signals to the users in the cell. A technique called *a small ball approximation* can be used as the location of the receiver is non-symmetric with the cell border. Although the uplink scenario can be exploited if the radar receiver works as the base station, the target information is excluded from the analysis. This model is only cencerned with the association between the transmitter and the passive radar, which is considered inappropriate.

2. Target included scenario: the network is then modelled regarding the location of the target. It can be located either at the origin or at the point $(D_{xr}, 0)$ and the radar receiver can be vice versa. In this case, the derivation includes D_{xr} and the target signal is more important than the direct path. Note that the locations of target and the radar receiver in this case do not provide any significant differences. In this thesis, the location of the target is chosen to be at the origin as the small ball approximation is used to provide the upper bound of the interference impact.

Simply, less interference will be involved if the receiver is located at the origin. The density of the target in this work is set to be equal to the density of the radar receiver in order to limit the number of the target to one per cell. Consequently, this cell association is chosen in this work.

5.3.1 Cellular networks system model

Conforming to the configurations in ad-hoc networks, the transmitters and radar receivers are established on the plane $\mathbb{R}^2$ symbolised by two independent stationary point processes, $\Phi^{(t)}$ and $\Phi^{(r)}$. The target distribution also follows $\Phi^{(r)}$. Each passive radar $PR_c \in \Phi^{(r)}$ listens to the stations in a geographical zone that are patterned on its hybrid Voronoi cell $\mathscr{C}_{PR_c}(\Phi^{(r)})$. Note that the system assumes the multistatic passive radar receiver can only correlate the signal of the transmitters BS_c^k from n_t^c closest stations, where $BS_c^k \in \Phi^{(t)}$. A passive radar receiver in the cell c is only able to decode the signals in its own cell as the transmitters in each cell process their own *Single Frequency Network* framework and there should be no more than one randomly-located target in each cell to avoid multiple-target processing. Additionally, the intensities $\lambda^{(t)}$, $\lambda^{(r)}$, regarding the PPP $\Phi^{(t)}$, $\Phi^{(r)}$ respectively, are the parameters applied to the system model. In this case, the density of broadcasting stations is set to be higher than that of the receivers. Assuming that all transmitters transmit at the same power P_t, the target SIR of the typical passive radar received from the x reflector at the origin is

$$\mathrm{TSIR}_{mr} = \frac{\sum_{k=1}^{n_t^c} P_{xr}}{\sum_{y \in \Phi^{(t)} \setminus \mathscr{C}_{PR}} \mathbf{h}_y \|y\|^{-\alpha}}. \tag{5.25}$$

where the passive radar receiver gathers the incoming signals from the transmitters inside a cell, $\sum_{k=1}^{n_t^c} P_{xr}$, to enhance its ability in target detection. $\sum_{y \in \Phi^{(t)}} \mathbf{h}_y \|y\|^{-\alpha}$ refers to the total interferences from the base stations at the point y travelling through the fading channel $\mathbf{h}_y$. In this thesis, the cell configuration employs hybrid Voronoi Tessellations, as discussed below.

Hybrid tessellations

In this thesis, the hybrid tessellations proposed in [68] are applied to the model of the multistatic passive radar networks. The configuration considered here consists of a typical ball engraves a Voronoi cell [82], whose shape and size are fixed and radius is denoted by R_c. The illustrations of the Voronoi cell, as well as an embedded ball, are shown in Fig. 5.2. As some concealed sections at the cell edge fail in the Voronoi cell, its independent functioning is not thoroughly constituted by the ball.

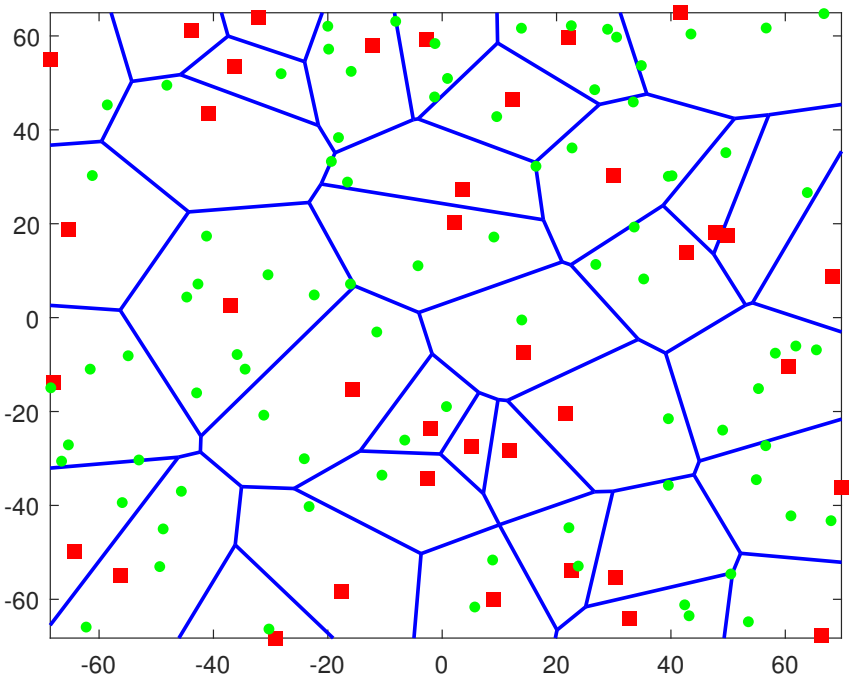

(a)

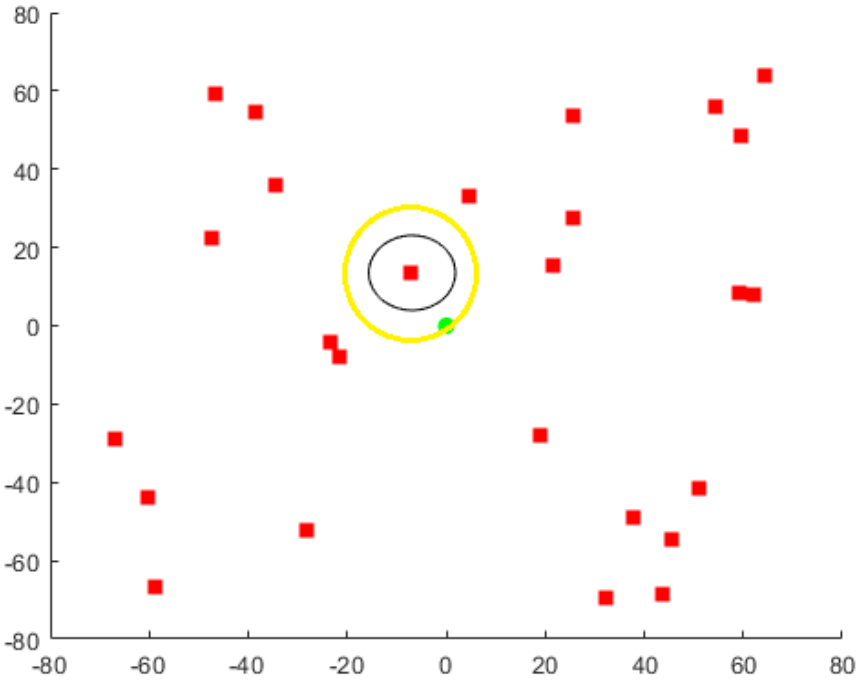

(b)

Figure 5.2: An example of a cellular network of passive radars with: (a) a conventional Voronoi cell where the locations of passive radar in red rectangle and base stations are randomised; and (b) an appearance of the embedded ball with a fixed radius, guard region and one transmitter located on it.

The OFDM stations, where the interference originates, are modelled according to a PPP outside of the fixed ball (cell).

To guarantee that the passive radar receives the most potent signal power from the transmitter, even from the edge of the cell, and it limits the number of radar receivers in the cell to one, a guard region at a distance of R_g from the cell edge is introduced. In conventional stochastic geometry model, in contrast to this network, the size of the inscribing ball of a Voronoi cell is random and the size of the corresponding guard region is verified by the closest neighbouring base station. In a homogeneous network, there is an assumption of a dominant interferer that is uniformly distributed at the edge of the guard region. R_c and R_g could be selected as a function of PPP density, $\lambda^{(r)}$. A target of interest is inhabited at the cell centre and the radar location is secured at $(D_{xr}, 0)$. Note that the cell index c is dropped if the typical cell is referred. Let the distance between the target and the passive radar be proportional to the radius of the cell, $D_{xr} = qR_c$, where $0 < q \leq 1$, the total reference signal power received at the passive radar can be displayed as:

$$S_{tot} = \sum_{k=1}^{n_t} P_t \mathscr{L}_{kr} h_{kr} D_{kr}^{-\alpha} \beta_1. \tag{5.26}$$

While L refers to log-normal shadowing, G is assigned to a fading power. Employing a Gamma-distributed random variable, G can be modelled as $\Gamma[k_g, \theta_g]$ for many types of fading, such as $G = \Gamma[1,1]$ for conventional Rayleigh fading and $G = \Gamma[n_r, 1]$ indicating Rayleigh fading with an n_r-receive antenna along with maximum ratio combining. According to Section 2.5.3, LG can be approximated using another Gamma random variables with the same first- and second-order moments whose distribution is equal to $\Gamma[k_p, \theta_p]$. Statistically, the distribution of reference signal power can also be cast as a Gamma random variable of $\Gamma[k_p, P_t D_{xr}^{-\alpha} \beta_1 \theta_p]$.

Regarding the target signals, (5.1) in bistatic radar networks is straightforwardly derived using a multistatic scenario. This can be shown as:

$$\sum_{k=0}^{n_t} P_{xr} = \sum_{k=0}^{n_t} \frac{P_t G_t}{4\pi D_{kx}^{\alpha}} \cdot \frac{\sigma_{kb}}{4\pi D_{xr}^{\alpha}} \cdot \frac{G_r \nu^2}{4\pi} = \frac{P_t G_t G_r \nu^2}{(4\pi)^3 D_{xr}^{\alpha}} \sum_{k=0}^{n_t} \frac{\sigma_{kb}}{D_{kx}^{\alpha}}, \tag{5.27}$$

where it is assumed that all transmitters carry the same amount of power and antenna gain. The equation above merely displays the target diversity as a consequence of multistatic configuration.

5.3.2 *Interference model in cellular networks*

As the system employs the cellular network model in [68], the derivation discussed below might be similar to the reference paper with the application to the passive radar networks. In contrast to the literature, this system imitates the uplink scenario in the case that the base stations broadcast their signal to the radar receiver, which replaces the serving station in the communication domain. There is only one radar receiver in a cell, along with multiple accepted transmitters. The interference mentioned in the following includes homogeneous and heterogeneous interference.

Homogeneous interference

If a single category of interferer is considered, the interference received at the passive radar is homogeneous. Distinct interferer-receiver channel information can be used in a marked process where each transmitter is marked according to their signal power distribution. Employing Gamma random variables, the log-normal shadowing in (5.5) can be denoted as $\mathscr{L}_\varepsilon$, and the fading distribution (5.4), h_ε can be represented as $\Gamma[\varepsilon_g, \theta_g]$. ε is the interferer index. In a single antenna case, Nagakami fading along with Gamma randomisation can be represented as $\Gamma[\mu, \frac{n_m}{\mu}]$ where $n_m = \frac{(1+n^2)^2}{1+2n^2}$.

The interference power is enumerated at the passive radar receiver where the target of interest is situated at origin; hence the receiver in each cell locates at $(D_{xr}, 0)$, as is shown in Fig. 5.3. Assuming that $D_{kx}, D_{xr} \leq D_{kr} \leq R_c$ and $R_g = R_c = \frac{1}{4\sqrt{\lambda^{(r)}}}$ as the homogeneous interference is considered, and both target and radar receiver should be illuminated by the uniformly transmitted signal. There are two types of interference that can be measured at the receiver: $\mathbf{I}_1$ is the interference from the superior interferer at the border of the guard region, while the interference from all other OFDM stations outside the guard region is donated by $\mathbf{I}_2$. Then, the homogeneous interference is equal to $\mathbf{I}_{ho}(D_{xr}) = \mathbf{I}_1(D_{xr}) + \mathbf{I}_2(D_{xr})$. The dominant interference can be derived as:

$$\mathbf{I}_1(D_{xr}) = \frac{h_1 \mathscr{L}_1 P_t \beta_1}{\|y_1\|^\alpha}. \tag{5.28}$$

Using the law of cosines, the distance between the interference at the guard region edge and the receiver is $\|y_1\| = \sqrt{4 + 4q\cos\eta + q^2} R_c$. η is a uniform random variable over the range $(0, 2\pi]$. To work out $\mathbf{I}_2$, it is shown that the distance to the closest edge of the circle is $R_c + R_g - D_{xr}$, while the distance to the furthest edge is $R_c + R_g + D_{xr}$. As a consequence, the elimination distance to the adjacent interference is asymmetric. To solve this, the interference contribution in a ball of radius $R_c + R_g - D_{xr}$ around the receiver

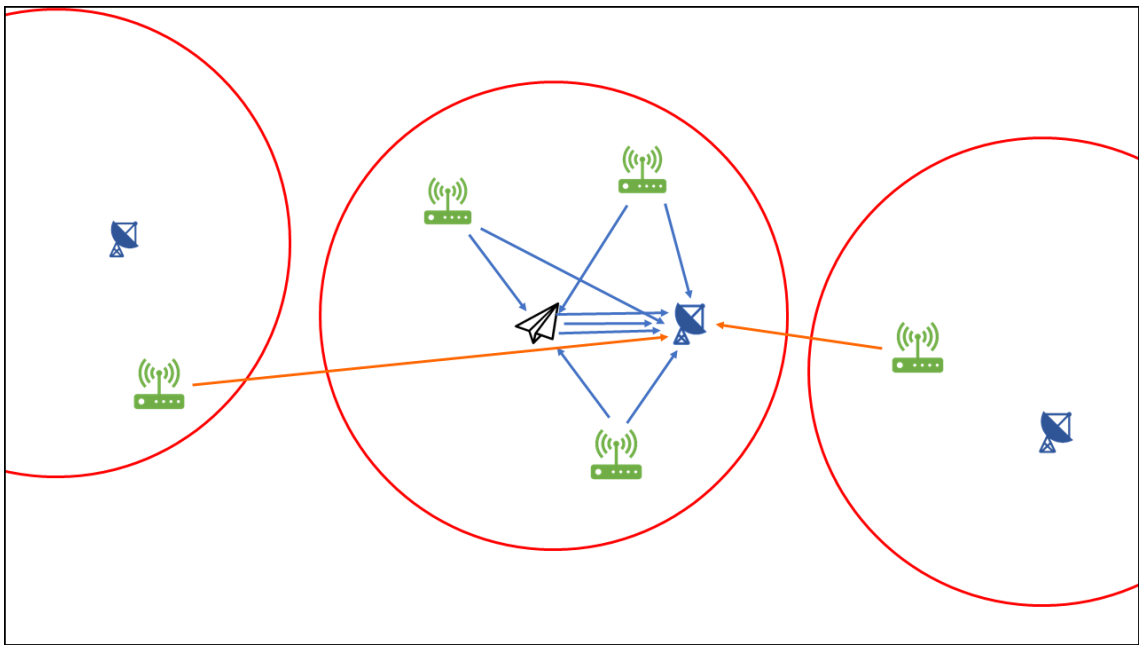

Figure 5.3: An example of a multistatic cellular networks scenario where blue arrows refer to the expected target and reference signals, the orange arrows refer to the interference. Note that there are other interfering signals from the multipath fading, including the target reflection, but they are not shown in this figure due to visibility.

denoted $B(R_c + R_g - D_{xr})$ is calculated to produce an upper bound on the interference power because less space is suspended from the aggregation of the interference. This is known as a small ball approximation where the passive radar is at the centre of the miniaturised interference field. The second type of interference can be shown as:

$$\mathbf{I}_2(D_{xr}) = \sum_{\varepsilon \in \Phi^{(t)} \setminus B(R_c+R_g-D_{xr})} \frac{h_\varepsilon \mathscr{L}_\varepsilon P_t \beta_1}{\|y_\varepsilon\|^\alpha}. \tag{5.29}$$

The small ball approximation can be applied to $\mathbf{I}_1$ to get

$$\mathbf{I}_1(D_{xr}) = \frac{h_1 \mathscr{L}_1 P_t \beta_1}{(R_c + R_g - D_{xr})^\alpha}. \tag{5.30}$$

The distribution of random interference, $\mathbf{I}_{ho}(D_{xr})$, can be characterised by its Laplace transform. Let the interference be marked by $h_\varepsilon \mathscr{L}_\varepsilon$, which follows an arbitrary but identical distribution for all ε, and thus the Laplace transform can be derived as:

$$\mathbb{L}_{\mathbf{I}_{ho}(D_{xr})}(s) = \mathbb{E}_{\mathbf{I}_1(D_{xr})}\left[\exp\left(-s\mathbf{I}_1(D_{xr})\right)\right] \mathbb{E}_{\mathbf{I}_2(D_{xr})}\left[\exp\left(-s\mathbf{I}_2(D_{xr})\right)\right]. \tag{5.31}$$

The first term related to $\mathbf{I}_1(D_{xr})$ can be calculated through the integration given the distribution of $h_1 \mathscr{L}_1$. On the other hand, the Laplace transform of $\mathbf{I}_2(D_{xr})$ can be illustra-

ted as:

$$\mathbb{L}_{\mathbf{I}_2(D_{xr})}(s) = \mathbb{E}_{\mathbf{I}_2(D_{xr})}\left[\exp\left(-s\mathbf{I}_2(D_{xr})\right)\right]$$

$$\approx \mathbb{E}_{\Phi^{(t)},h_\varepsilon,\mathscr{L}_\varepsilon}\left[\exp\left(-s\sum_{\varepsilon\in\Phi^{(t)}\setminus B(R_c+R_g-D_{xr})}\frac{h_\varepsilon\mathscr{L}_\varepsilon P_t\beta_1}{\|y_\varepsilon\|^\alpha}\right)\right]$$

$$= \mathbb{E}_{\Phi^{(t)},h_\varepsilon,\mathscr{L}_\varepsilon}\left[\prod_{\varepsilon\in\Phi^{(t)}\setminus B(R_c+R_g-D_{xr})}\exp\left(-s\frac{h_\varepsilon\mathscr{L}_\varepsilon P_t\beta_1}{\|y_\varepsilon\|^\alpha}\right)\right]. \tag{5.32}$$

Due to the fact that $h_\varepsilon\mathscr{L}_\varepsilon$ holds i.i.d distribution, which is independent of a PPP, the above expression can be shown as:

$$\mathbb{L}_{\mathbf{I}_2(D_{xr})}(s) = \mathbb{E}_{\Phi^{(t)}}\left[\prod_{\varepsilon\in\Phi^{(t)}\setminus B(R_c+R_g-D_{xr})}\mathbb{E}_{h,\mathscr{L}}\left(\exp\left(-s\frac{h\mathscr{L}P_t\beta_1}{\|y_\varepsilon\|^\alpha}\right)\right)\right]$$

$$= \exp\left(-2\pi\lambda^{(t)}\int_{R_c+R_g-D_{xr}}^{\infty}\left(1-\mathbb{E}_{h,\mathscr{L}}\left[\exp(-sh\mathscr{L}P_t\beta_1u^{-\alpha})\right]\right)udu\right), \tag{5.33}$$

where the last expression is derived using PGFL. Similar to [68] with the assumption that the distance $R_c+R_g-D_{xr}$ is greater than the typical target-receiver distance of the system, the above expression is further calculated by denoting $Z = h_\varepsilon\mathscr{L}_\varepsilon P_t$ and introducing

$$F_{\alpha,x,\beta_1}(s) = \mathbb{E}_z z^{\frac{2}{\alpha}}\left[\Gamma\left(-\frac{2}{\alpha},s\beta_1 zx^{-\alpha}\right)-\Gamma\left(-\frac{2}{\alpha}\right)\right]. \tag{5.34}$$

If Z is approximated using a gamma distribution $\Gamma[\varepsilon_g,\theta_g]$, the above function can be shown as:

$$F_{\alpha,x,\beta_1}(s) = \frac{(s\beta_1x^{-\alpha})^{-\frac{2}{\alpha}-\varepsilon_g}\alpha\theta_g^{-\varepsilon_g}}{2+\varepsilon_g\alpha}{}_2F_1\left(\varepsilon_g,\varepsilon_g+\frac{2}{\alpha},1+\varepsilon_g+\frac{2}{\alpha},-\frac{1}{s\beta_1x^{-\alpha}\theta_g}\right)$$

$$-\theta_g^{\frac{2}{\alpha}}\mathbb{B}\left(\varepsilon_g+\frac{2}{\alpha},-\frac{2}{\alpha}\right). \tag{5.35}$$

Finally, the Laplace transform of the total interference apart from the dominant interferer can be displayed as:

$$\mathbb{L}_{\mathbf{I}_2(D_{xr})}(s) = \exp\left(\lambda^{(t)}\pi(R_c+R_g-D_{xr})^2-\frac{2\pi\lambda^{(t)}(sP_t)^{\frac{2}{\alpha}}}{\alpha\beta_1^{2/\alpha}}F_{\alpha,R_c+R_g-D_{xr},\beta_1}(s)\right), \tag{5.36}$$

where ${}_2F_1$ is the Gauss hypergeometric function and $\mathbb{B}(x,y)$ is a Beta Euler function. Note that there is also a choice in that the passive radar receiver can reside at the origin and the small-ball approximation is not needed. This thesis proposes the cellular networks by

setting a typical target of interest at the origin. The reason for this is that the interference discussed here can become an upper bound for other interference modelling in the future.

Heterogeneous interference

In this part, the system considered is composed of the macrocellular networks in combination with a variety of frameworks, such as low-power nodes like small-cells, femtocells, fixed relays, and distributed antennas. There are two scenarios discussed here. First, out-of-cell interference could comprise of the interference from both high power stations and low power distributed antenna. The appearance of a guard region could be inconsistent and the transmission power of different tiers become heterogeneous. The concept of the dominant interferer and the guard region can be developed from the homogeneous network. Second, this kind of heterogeneous interference arises from the second tier of low-power node, like small-cells or femtocells in the form of cross-tier interference. Details of the two types of interference are explained in the following.

Out-of-cell interference: assume the number of dissimilar sorts of framework homogeneously redistributed throughout the network is $\mathscr{K}$. A marked PPP with marks regarding the composite fading distribution, $\Gamma[k_i, \theta_i]$, where $i = 1, \ldots, \mathscr{K}$, can be employed for each interferer. Given that the transmitters are modelled using a PPP with intensity $\lambda_i^{(t)}$ and transmit their power denoted by $P_t^{(i)}$, the radar receiver and the target of interest hold the same density $\lambda_i^{(r)}$; the process is parametrised by $(k_i, \theta_i, P_t^{(i)}, \lambda_i^{(t)}, \lambda_i^{(r)})$. The station connected to the fixed cell is assumed to be in tier 1. With a known R_c, the radius of the guard region for tier i can be denoted as:

$$R_g^{(i)} = (a_i - 1)R_c, \tag{5.37}$$

where $a_i = 1 + (P_t^{(i)}/P_t^1)^{1/\alpha}$. Given $P_t^{(i)}, \lambda_i^{(t)}, \lambda_i^{(r)}$, the average radius of the inscribing ball of the typical Voronoi cell can be figured as:

$$R_c = \frac{1}{2\sqrt{\sum_{i=1}^{\mathscr{K}} a_i^2 \lambda_i^{(r)}}}. \tag{5.38}$$

The total intensity of interference (OFDM base stations), $\lambda^{(t)}$, can be defined as $\sum_{i=1}^{\mathscr{K}} a_i^2 \lambda_i^{(t)}$. With probability $\frac{a_i^2 \lambda_i^{(t)}}{\lambda^{(t)}}$, it establishes a dominant interferer residing in tier i at the edge of tier i's guard region. The overall interference in the $\mathscr{K}$-tier network is counting $\mathscr{K}+1$, where the interference from the dominant interferer is denoted by $\mathbf{I}_1$ and the interference from the stations outside the guard region of the i-th tier is designated as $\mathbf{I}_i, (2 < i \leq \mathscr{K}+1)$. Applying the small ball approximation, the overall interference is

shown as:

$$\mathbf{J}_{ovr} = \sum_{i=2}^{\mathscr{K}+1} \sum_{\kappa \in \Phi_i^{(t)} \setminus (R_c + R_g^{(i)} - D_{xr})} h_\kappa^{(i)} \mathscr{L}_\kappa^{(i)} P_t^{(i)} \beta_1 \|y_\kappa^{(i)}\|^{-\alpha} + \mathbf{I}_1 \tag{5.39}$$

The Laplace transform of the heterogeneous out-of-cell interference regarding an independent $\mathscr{K}$ Poisson Point Processes can be displayed as:

$$\mathbb{L}_{\mathbf{J}}(s) = \prod_{i=1}^{\mathscr{K}+1} \mathbb{L}_{\mathbf{I}_i(D_{xr})}(s), \tag{5.40}$$

where the Laplace transform of $\mathbf{I}_i(D_{xr})$ is donated by $\mathbb{L}_{\mathbf{I}_i(D_{xr})}(s)$.

Cross-tier interference: Cross-tier interference is initiated by some frameworks that are unrelated to the macro base station. Femtocells can assemble another tier of nodes. It is possible to denote an exclusion area around the aimed for radar receiver with radius R_{cr} as B_{cr}. In order to avoid the gathering between the low-power node and the receiver, this area is set to be small. Let the transmitting power of the cross-tier interferer be P_{cr} and the transmitters are drawn from a PPP, Φ_{cr} with the density λ_{cr}; the received interference power is denoted as:

$$\mathbf{I}_{cr} = \sum_{\kappa \in \Phi_{cr} \setminus B_{cr}} h_\kappa \mathscr{L}_\kappa P_{cr} \beta_1 \|y_\kappa\|^{-\alpha}. \tag{5.41}$$

Because of the shifting invariance property of PPP, the above equation displays that the cross-tier interference is invariable and does not depend on the location of the radar receiver.

5.3.3 Interference distribution approximation using the Gamma distribution

Laplace transform is utilised for the characterisation of the interference distribution and unique choices of the parameters and the mark distribution enable further simplification. Two equations from [82], which can be employed for the calculation regarding the moments for interference distribution, are introduced here as shown.

$$\begin{aligned} \mathbb{E}[\mathbf{I}(o)] = \mathbb{E}[\mathbf{I}] &= \mathbb{E}[P]\lambda \int_{\mathbb{R}^2} \frac{1}{l(\|y\|)} dy \\ &= \int_0^\infty (1 - G(s)) ds \cdot 2\pi\lambda \int_0^\infty \frac{r}{l(r)} dr, \end{aligned} \tag{5.42}$$

and

$$\mathbb{E}[\mathbf{I}^2(o)] = (\mathbb{E}[\mathbf{I}])^2 + \mathbb{E}[P^2] \cdot 2\pi\lambda \int_0^\infty \frac{r}{(l(r))^2} dr, \tag{5.43}$$

where the receiver at the origin acquires the interference at point y with the path-loss function $l(r)$ of a distance r. Let $Z = h_\varepsilon \mathscr{L}_\varepsilon P_t$ [68] be the random variable reciprocal to

Table 5.1: Parameters for passive radar networks using stochastic geometry

Symbol	Numerical Value	Explanation
R_{tx}	Variable [m]	Distance from transmitter to target
D_{xr}	Variable [m]	Distance from target to receiver
P_{xr}	Variable [w]	Reflected target power
d_0	Variable [m]	Distance from the closest transmitter to receiver
P_t	10k W	Power of the transmitter
α	2,2.1,2.2	Path-loss exponent
ν	1.3195 m [4]	Carrier wavelength
σ_b	48.58 dBsm	Bistatic radar cross-section
$\lambda^{(t)}$	Variable [unit/m^2]	Density of broadcasting stations
$\lambda^{(r)}$	Variable [unit/m^2]]	Density of passive radar receivers
h	Random variable	Small-scale fading of the channel
$\mathscr{L}$	Random variable	log-normal shadowing of the channel
R_c	Variable [m]	Radius of the cell
R_g	Variable [m]	Distance of the guard region

the mark distribution for the case of a homogeneous interference supply. Applying (5.29) and (5.30), the mean of the homogeneous interference can be shown as

$$\mathbb{E}\left[\mathbf{I}_{ho}(D_{xr})\right] \approx \frac{\mathbb{E}[Z]\beta_1}{(R_c+R_g-D_{xr})^{\alpha}}\left[\frac{2\pi\lambda^{(t)}(R_c+R_g-D_{xr})^2}{\alpha-2}+1\right]. \tag{5.44}$$

The variance of the homogeneous interference can be displayed as:

$$\mathrm{var}\left(\mathbf{I}_{ho}(D_{xr})\right) \approx \frac{\beta_1^2}{(R_c+R_g-D_{xr})^{2\alpha}}\left[\frac{\pi\lambda^{(t)}\mathbb{E}[Z](R_c+R_g-D_{xr})^2}{(\alpha-1)}+\mathrm{var}(Z)\right]. \tag{5.45}$$

The moments of the sum are employed in case of the heterogeneous interference with equivalent mark distribution. The mean of the heterogeneous interference can be illustrated as follows:

$$\mathbb{E}[\mathbf{I}_1(qR_c)] = \frac{\beta_1}{\lambda^{(t)}R_c^4}\sum_{i=1}^{\mathscr{K}}\frac{\lambda_i^{(t)}\mathbb{E}[Z^{(i)}]a_i^2(a_i^2+q^2)}{(a_i^2-q^2)^3} \tag{5.46}$$

$$\mathbb{E}[\mathbf{I}_1^2(qR_c)] = \frac{\beta_1^2}{\lambda R_c^8}\sum_{i=1}^{\mathscr{K}}\lambda_i^{(t)}\mathbb{E}[(Z^{(i)})^2]\frac{a_i^2(a_i^2+q^2)(a_i^4+8a_i^2q^2+q^4)}{(a_i^2-q^2)^7} \tag{5.47}$$

$$\mathbb{E}[\mathbf{I}_i(qR_c)] = \frac{2\pi\lambda_i^{(t)}\mathbb{E}[Z^{(i)}]a_i^2\beta_1}{2R_c(q^2-a_i^2)^2}. \tag{5.48}$$

The variance of the heterogeneous interference can be shown as:

$$\mathrm{var}(\mathbf{I}_i(qR_c)) = \frac{2\pi\lambda_i^{(t)}\mathbb{E}[(Z^{(i)})^2]a_i^2(a_i^4+6a_i^2q^2+3q^4)\beta_1^2}{6R_c^6(a_i^2-q^2)^6}, \tag{5.49}$$

where $Z^{(i)} = h_\varepsilon^{(i)}\mathscr{L}_\varepsilon^{(i)}P_t^{(i)}$. Thus, the cross-tier interference can be considered using the supplementary term by choosing the other appropriate parameters and substitute $R_c + R_g - D_{xr}$ with R_{cr}. Simple or closed-form solutions to the distribution defined by the Laplace transform are often ambitious. It is shown that the approximation of interference can be represented by the random variable $\Gamma[k_\mathbf{I}, \theta_\mathbf{I}]$ with the same mean and variance as $\mathbf{I}(D_{xr})$ where

$$k_\mathbf{I} = \frac{(\mathbb{E}[\mathbf{I}])^2}{\mathrm{var}(\mathbf{I})} \qquad \theta_\mathbf{I} = \frac{\mathrm{var}(\mathbf{I})}{\mathbb{E}[\mathbf{I}]}. \tag{5.50}$$

In this section, a network of passive radars in multistatic configuration has been analysed. The system denotes a passive radar as a node along with a typical base station in a cell. Based on the references followed this section, a small ball approximation has also been applied. An approximation using Gamma distribution reviewed in Chapter 2 has been utilised to estimate the interference. Consequently, the simulations regarding this scenario are displayed in the next section.

5.4 Performance analysis

As has been seen throughout this chapter, stochastic geometry is applied in the passive radar networks in two configurations. First, this chapter discussed bistatic ad-hoc networks, where a simple scenario was examined. Second, a PPP was utilised in cellular-heterogeneous networks, where the systems become more complicated. Stochastic geometry has demonstrated tractable mathematics for interference modelling. In this section, all of the outcomes derived above are illustrated. The results in this section are also shown in [118].

The parameters in Table 5.1 are simulated to produce the results using (5.9) and (5.15) for mean and variance of the interference respectively. By setting the antenna gains of the transmitter and the receiver to be equal and this does not affect the results, Fig. 5.4 provides the plot of interference mean versus the inverse intensity ($1/\lambda^{(t)}$). This graph compares different values of the path-loss exponent (α) and this is also comparable to the outcome from the literature [3]. Regarding the mean figure, the higher path-loss reduces the effect of interference, same as the decrease of base station density.

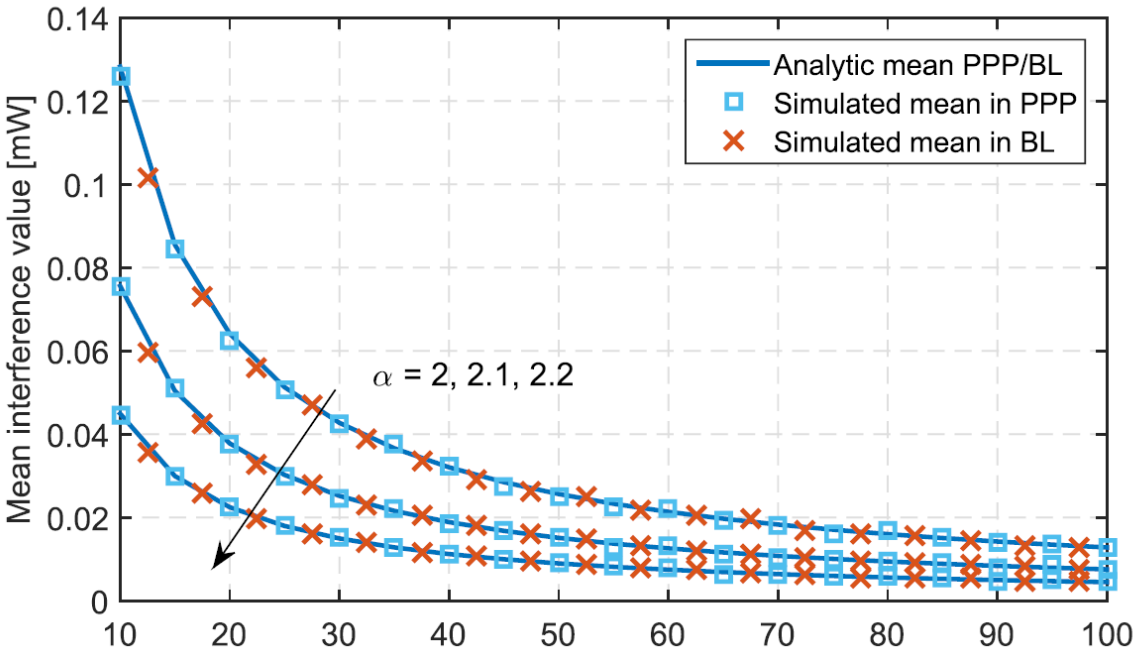

(a)

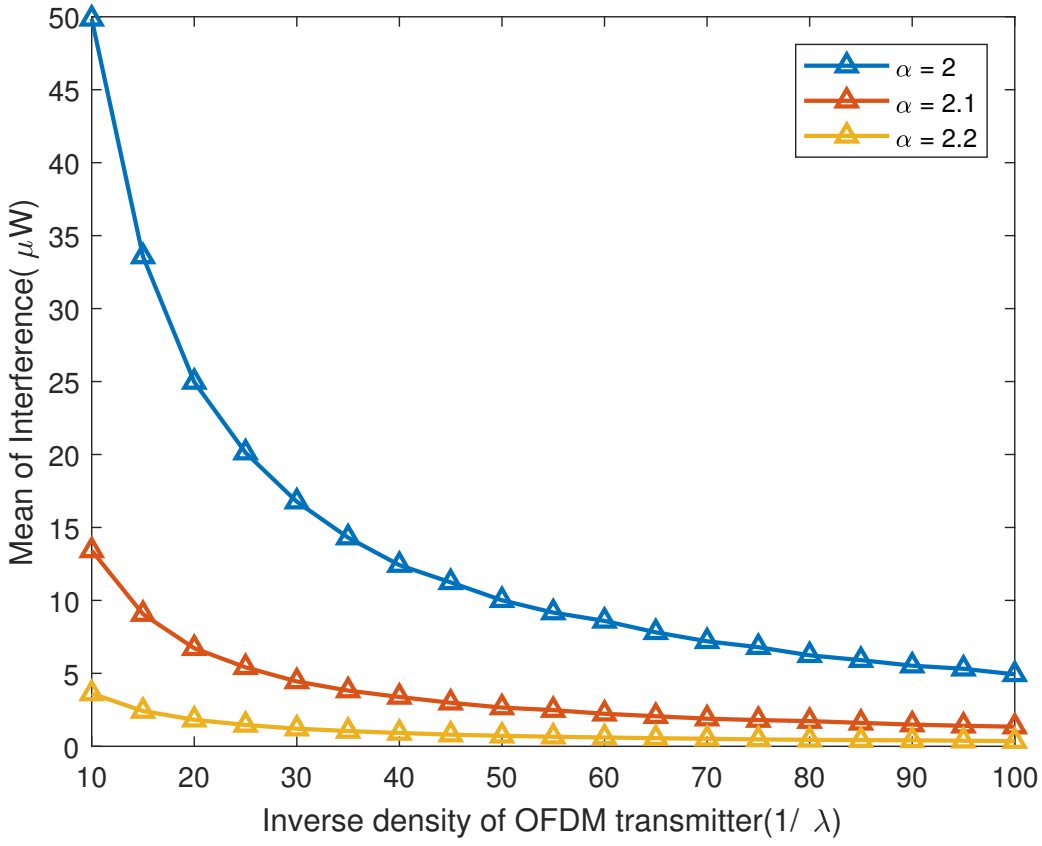

(b)

Figure 5.4: Interference mean comparison between analytical and simulated outputs, along with various α values. (a) from the reference of automotive radar [3] and (b) this thesis OFDM passive radar in ad-hoc networks

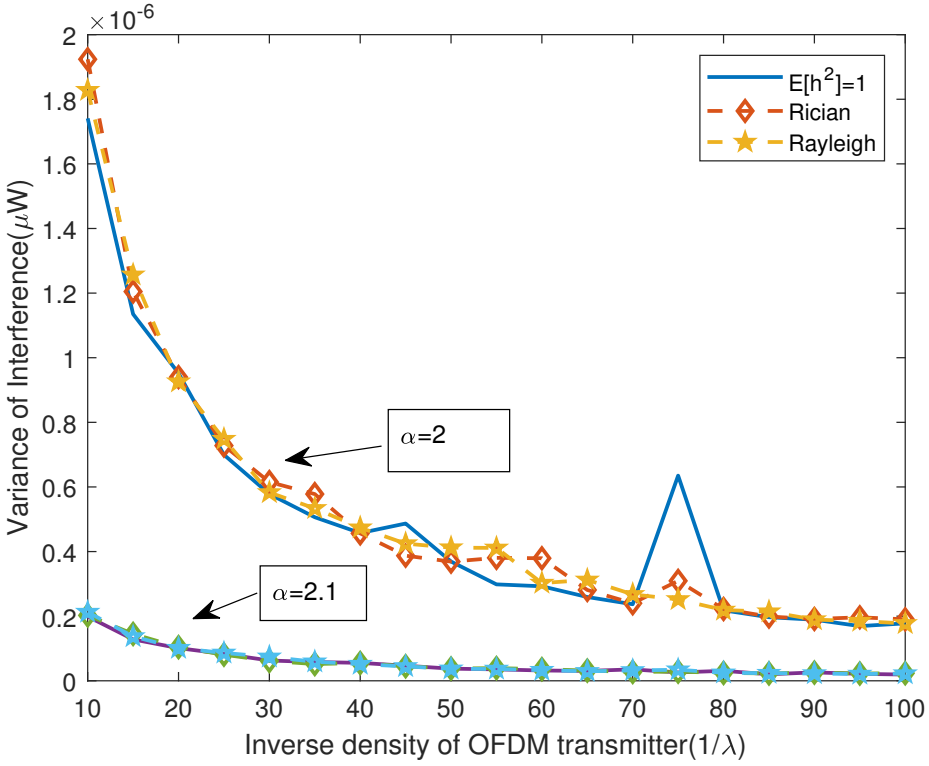

Figure 5.5: Comparison of interference variance of OFDM passive radar with various α values applying Rayleigh and Rician fading channel over a numerical expression where the analytical results employ (5.15) with the approximation $\mathbb{E}(\mathbf{h}^2) = 1$. The results are averaged over 60 simulations.

The order of interference power in the literature is in milliwatts while the results here demonstrate only microwatts. The reason is that the distance of interest in our work is much greater than the automobile spacing in the traffic although the sending power of the automotive radar is much lower. Monte-Carlo simulations for the two types of fading channel, Rayleigh and Rician channel, are also produced. The results are shown in Fig. 5.5, where both of the channels perform equally and are comparable in terms of the analytical expression. The reason for this presentation is that the Rayleigh channel is mostly used in stochastic geometry research, while the channel for passive radar inevitably includes the direct path. The Rician channel is worth considering as part of an interference model.

The distribution of the interference using (5.21) is also demonstrated in Fig. 5.6 by comparing the analytical expression with the approximation using inverse Gamma distribution. The performance of target detection is illustrated in Fig. 5.7 with a very low threshold of -60 dB. The plot also demonstrates the results in different OFDM station densities. The noise level is assumed to be 0 dB compared to the target signature. It is shown from the figure that if the density of the transmitter is closed to 0.1 unit per area,

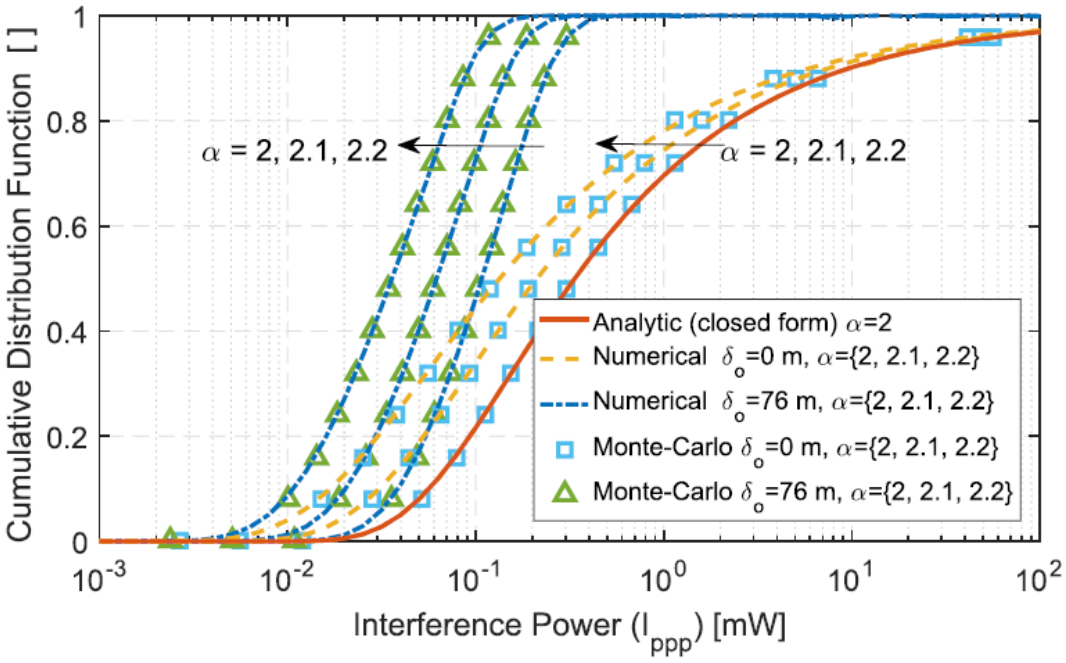

(a)

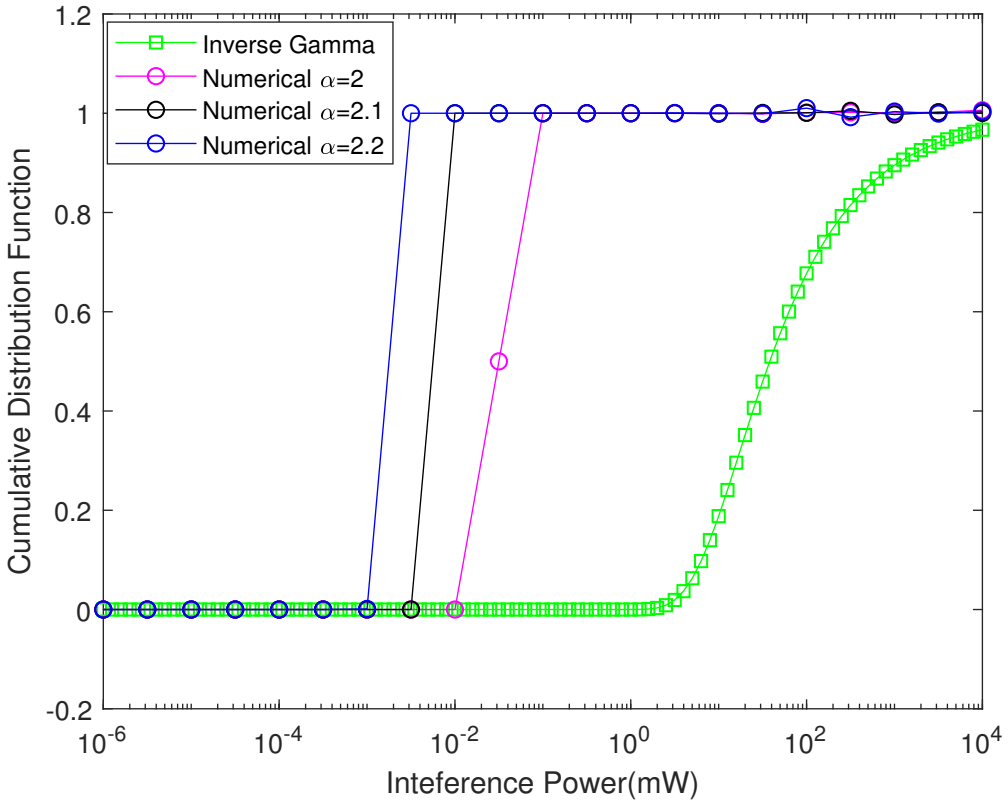

(b)

Figure 5.6: Cumulative Distribution Function of the interference by using inverse Gamma approximation in comparison with numerical integration with various α values. where (a) from the reference of automotive radar [3] and (b) for OFDM passive radar using bistatic ad-hoc networks in this thesis

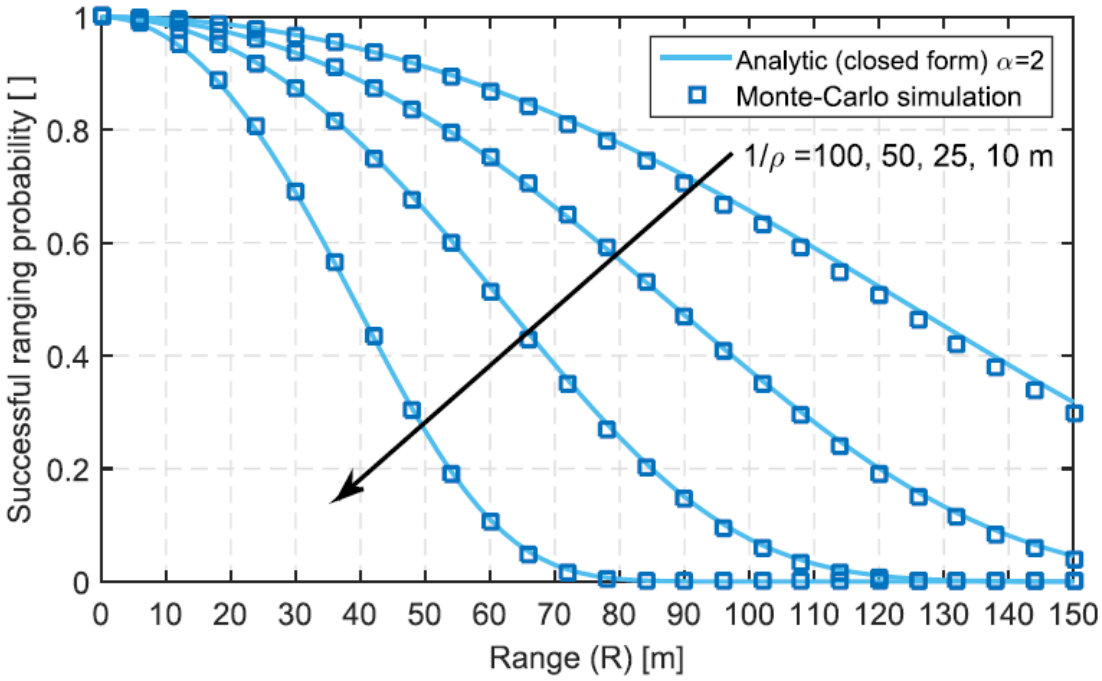

(a)

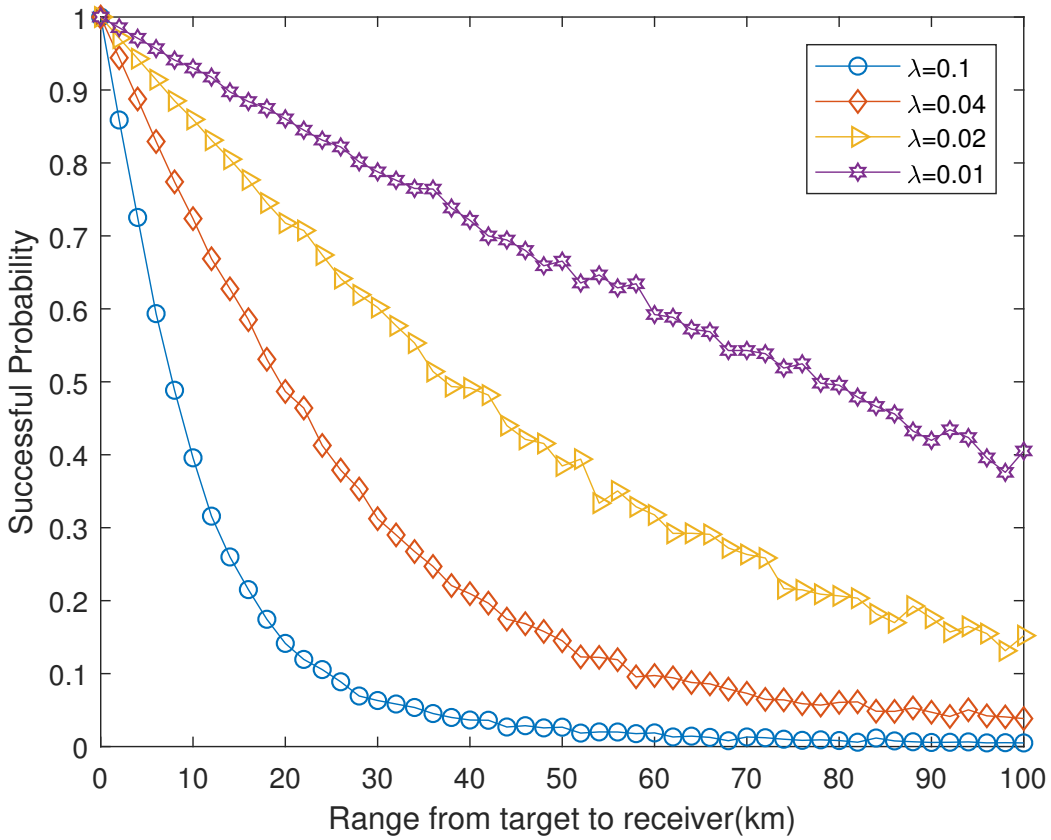

(b)

Figure 5.7: Successful range detection probability in bistatic ad-hoc radar networks comparing various interference intensities. (a) referring to the reference [3] and (b) for the passive radar systems in this thesis

only 50 percent of detection can be achieved for the target distance at 10 km. This performance is not impressive while the target can be detected with probability of 0.5 at about 80 km when the transmitter density is expanded to 0.01 unit per area. However, when the interference caused by the closest transmitter is taken into account, the threshold needs adjusting until the appearance of the target signal is sufficient. With the efficient reference cancellation method, the threshold will be more realistic and not too low.

Regarding the multistatic passive radar systems, the simulations employ (5.44) and (5.45) in order to illustrate the statistical characteristics of the homogeneous interference. Fig. 5.8a displays the mean of the cellular network interference with the passive radar receiver at the location $(D_{xr}, 0)$ in a typical cell. This is plotted versus the inverse density of the OFDM base stations, $1/\lambda^{(t)}$. The mean plot displays the same pattern as in ad-hoc configuration. The interference power, however, is in order of milliwatts. The variance of the cellular network interference is shown in Fig. 5.8b with the same label. Both figures indicate the difference of path-loss exponent (α). Employing the Gamma approximation of small-scale fading allows for the estimation of fading characteristic for multiple-antenna receivers, i.e. $h_\varepsilon \approx \Gamma(n_r, 1)$. Fig. 5.10 displays the mean and variance of the interference versus the number of antenna at the radar receiver. It should be mentioned that the results using Gamma approximation for Rayleigh channel with multiple antennas receiver provide consistency when the number of receive antennas is greater than 10.

As the maximum ratio combiner idea for passive radar networks is excluded from this thesis, the approximation results need to be verified. As the statistical characteristics of the channel, such as fading and shadowing, are included in the system, Fig. 5.11 illustrates the impact of shadowing on the incoming interference by plotting its mean and variance versus the variance of log-normal shadowing. It is shown that the channel with shadowing can have an impact for the system. Not only the interference power decreases, but the capability of target and reference detection is also affected. The density of passive radar receivers determines the radius of the cell in this case. Hence, Fig. 5.12 shows the effect of receiver density where lower density refers to larger cell in the networks. The results determine that the cell radius does not dramatical alter the strenght of the interference but its variance can be highly affected.The homogeneous interference plot concludes with the illustration of the ratio between surveillance signals and reference signals as this determines the necessity of the direct path cancellation process. Fig. 5.13 displays the received signal ratio in a comparison between the effect of log-normal variance and the density of radar receivers. As mentioned, the variance of shadowing provides a significant impact to

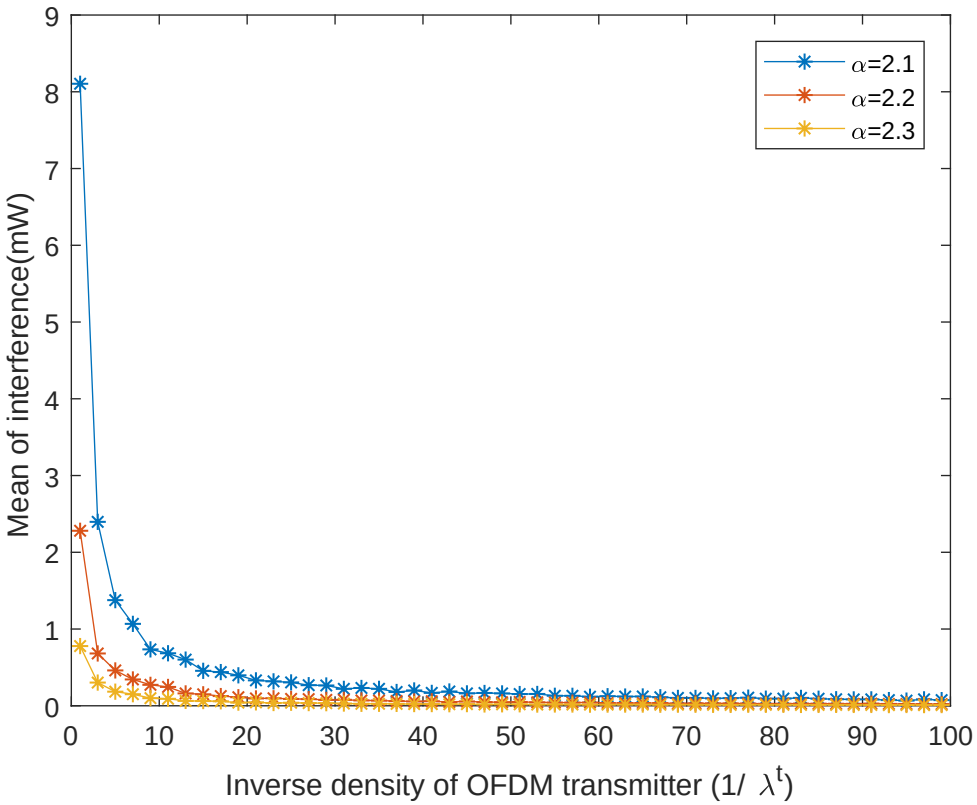

(a)

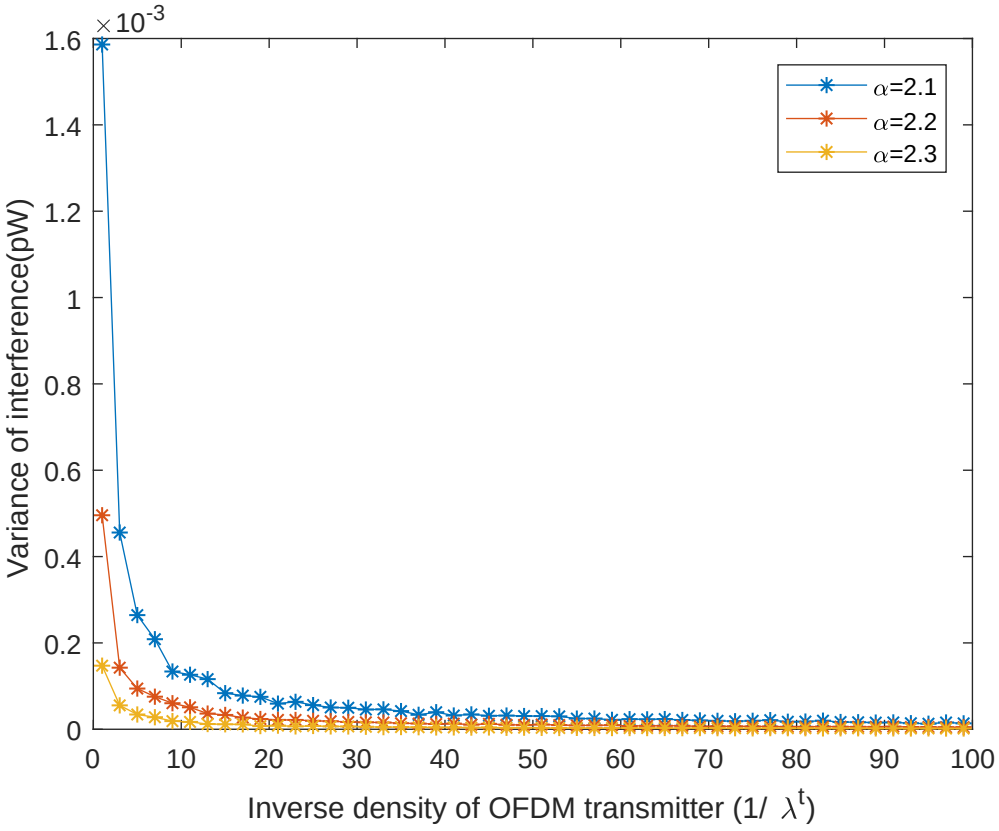

(b)

Figure 5.8: The interference characteristics in multistatic passive radar networks where: (a) mean of interference; and (b) variance of interference, are displayed.

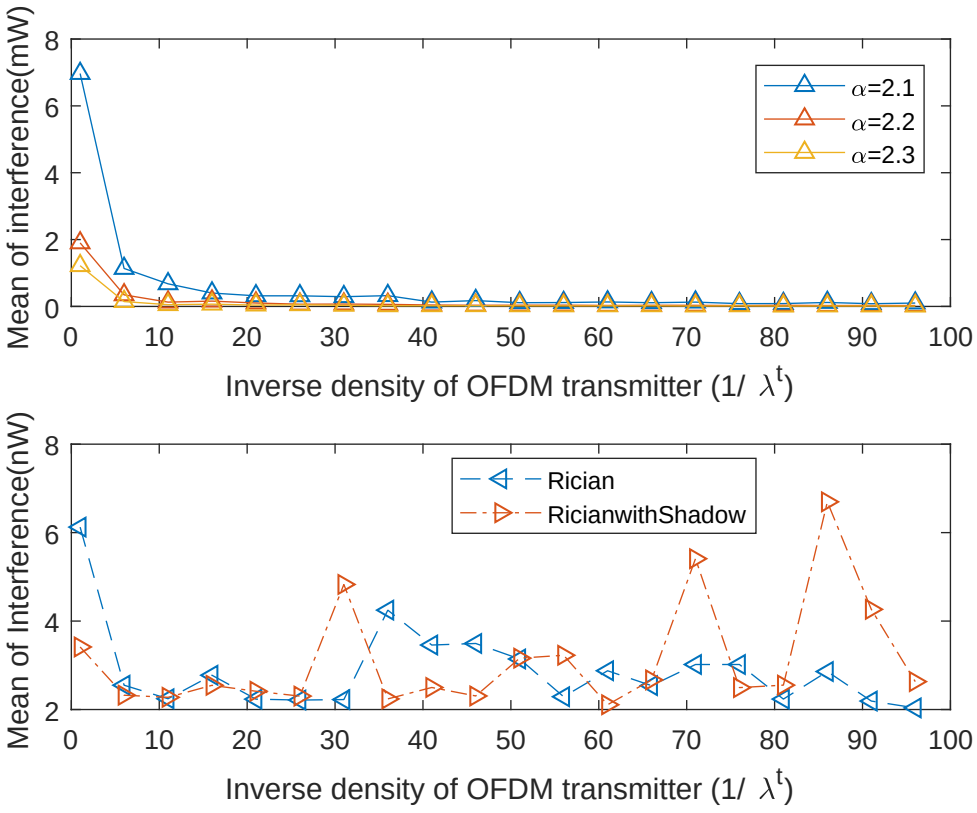

(a)

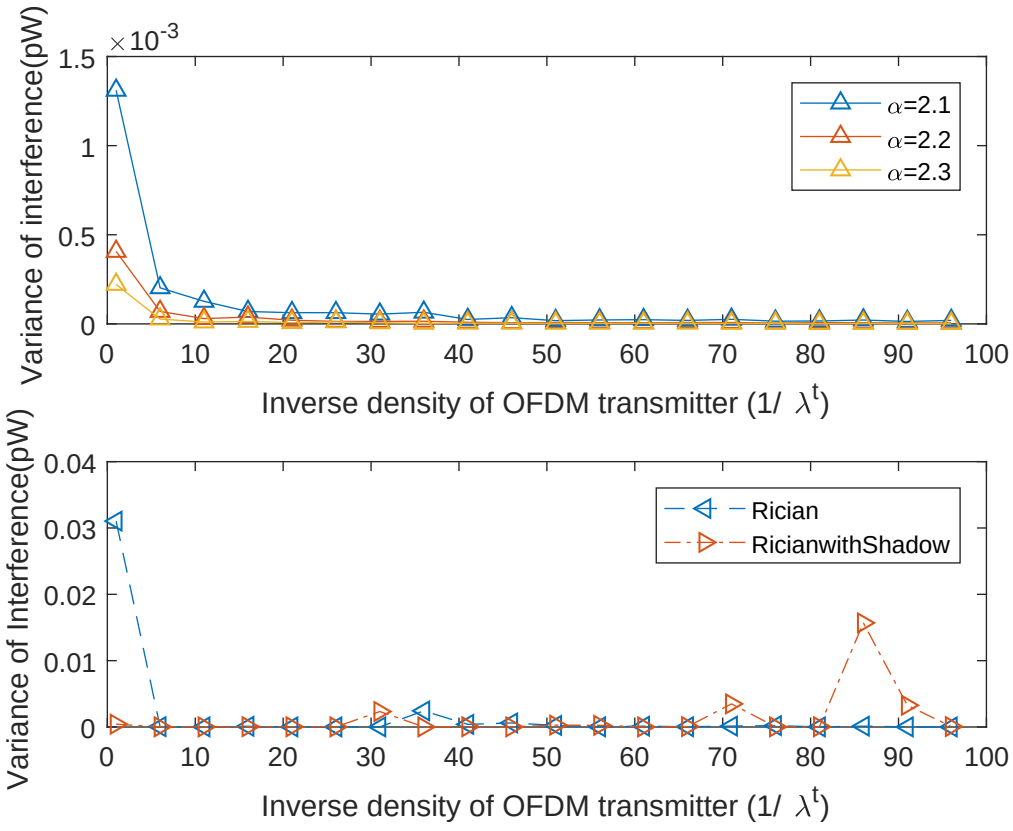

(b)

Figure 5.9: The interference characteristics in multistatic passive radar networks where: (a) mean of interference; and (b) variance of interference, are displayed.

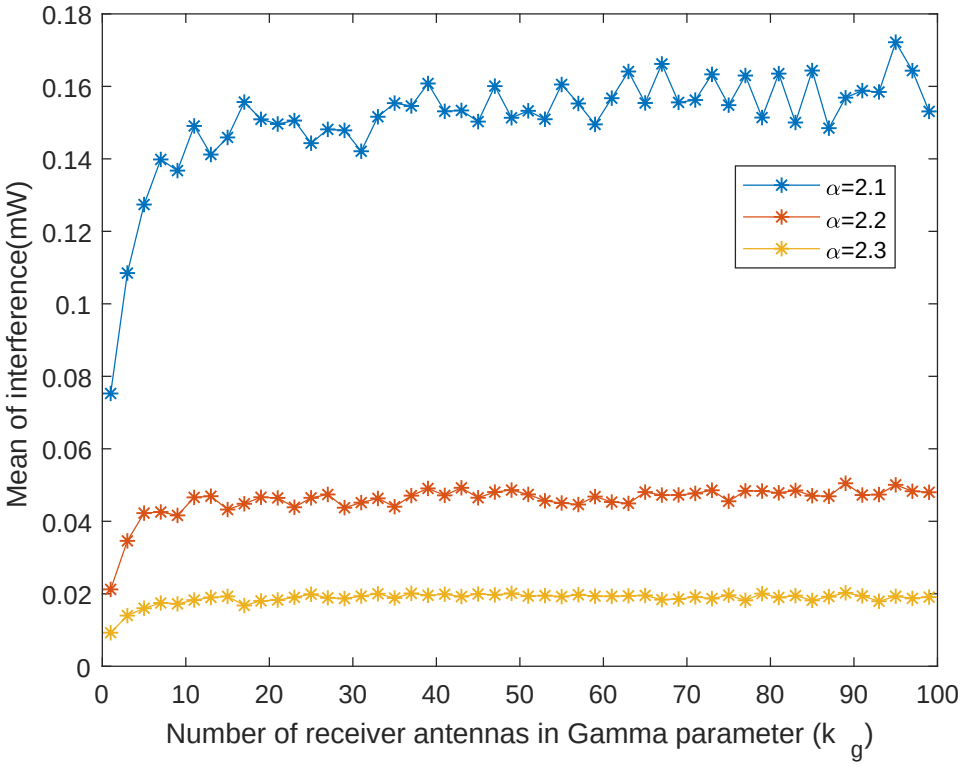

(a)

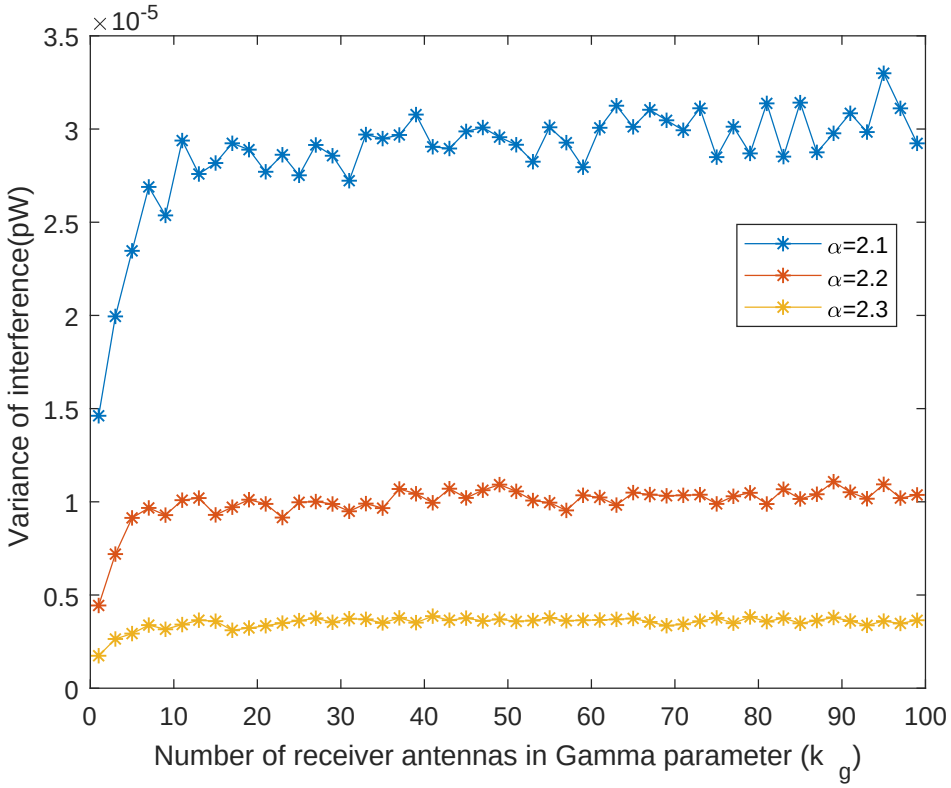

(b)

Figure 5.10: The interference characteristics in multistatic passive radar networks versus the number of receive antennas using the Gamma approximation where: (a) mean of interference; and (b) variance of interference, are displayed.

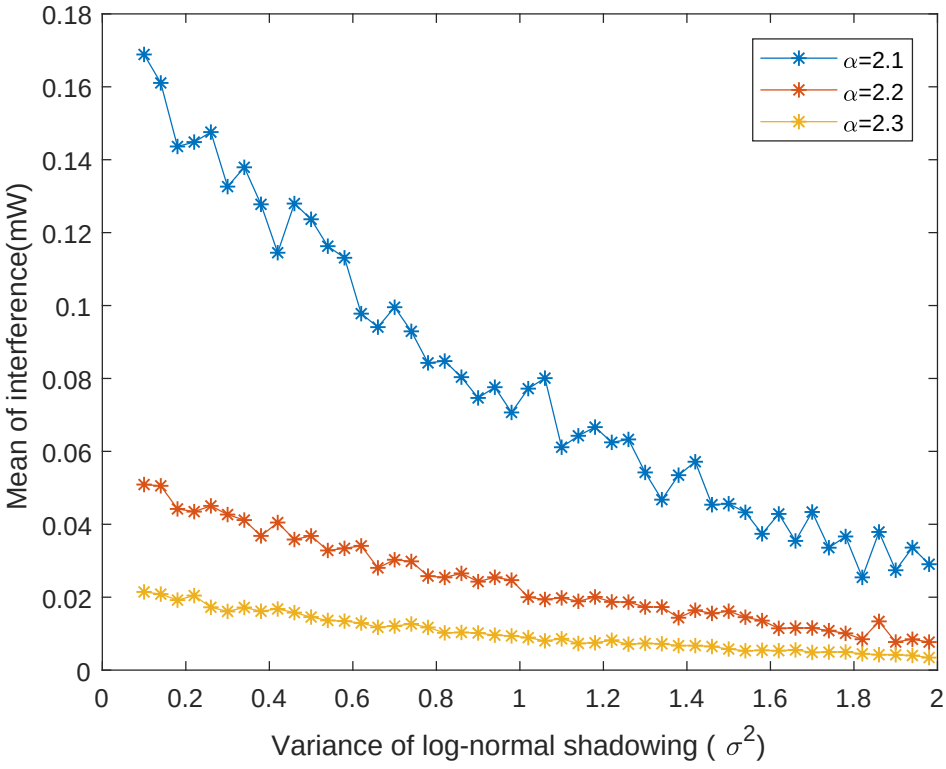

(a)

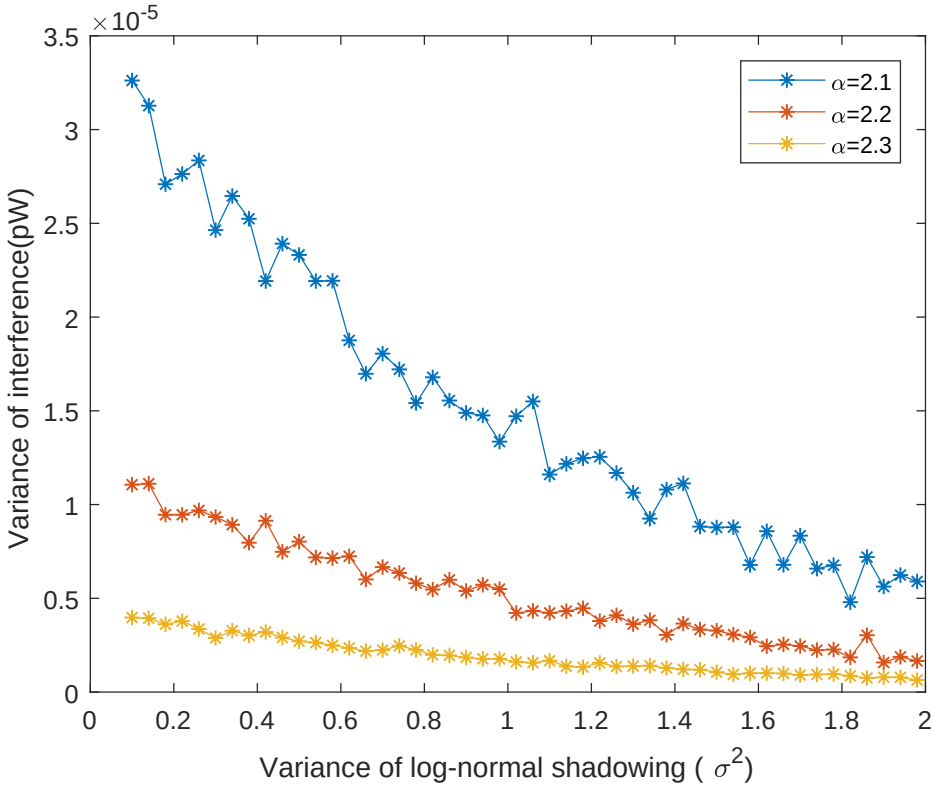

(b)

Figure 5.11: The interference characteristics in multistatic passive radar networks versus the variance of log-normal shadowing where: (a) mean of interference; and (b) variance of interference, are displayed.

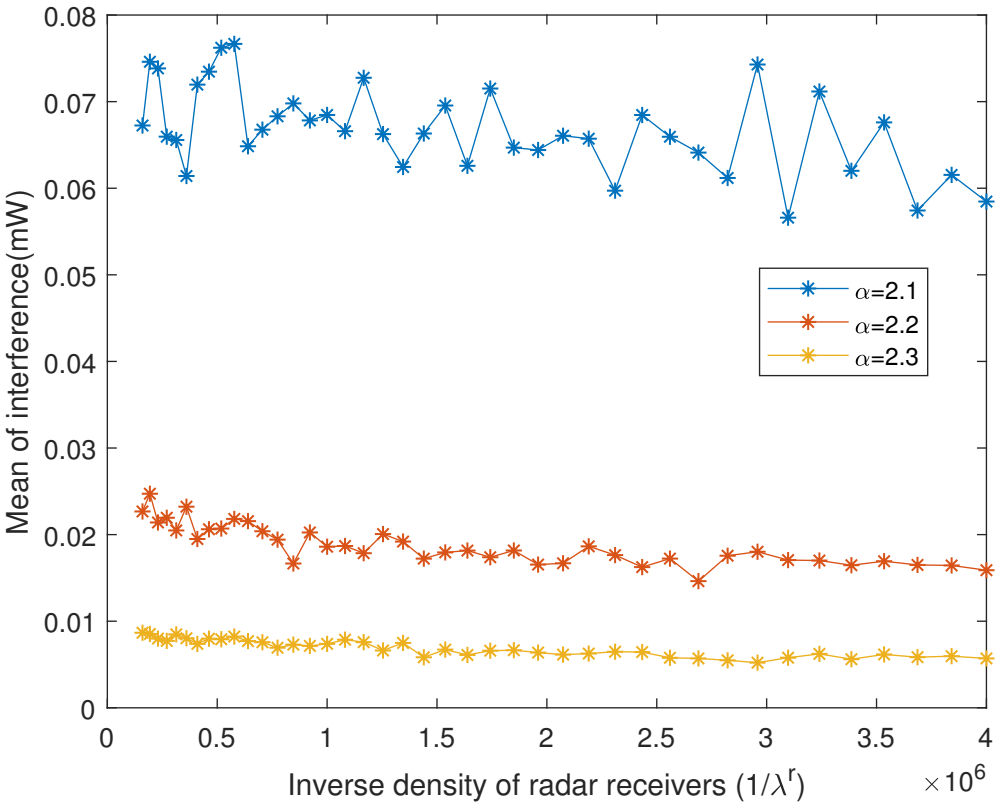

(a)

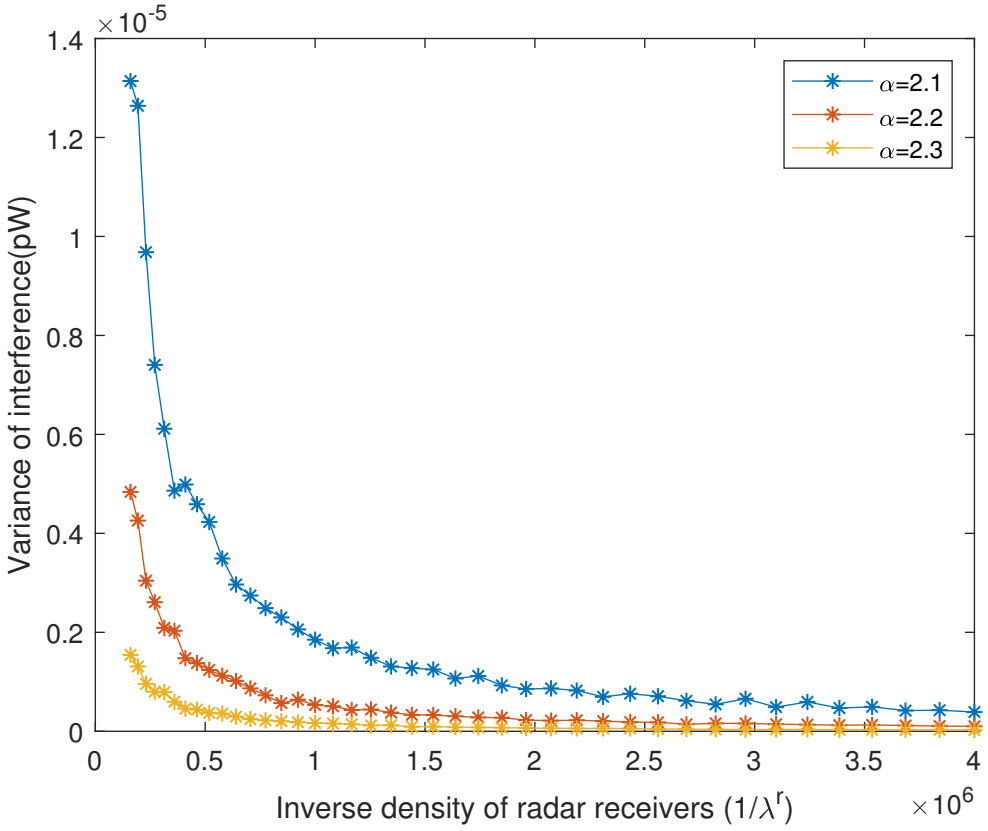

(b)

Figure 5.12: The interference characteristics in multistatic passive radar networks versus the inverse of passive radar density.

the target reflections. On the other hand, the radar density, which provides slow distortion to the interference, also becomes an attenuator for the detection process. To complete the discussion for cellular network interference, a heterogeneous system is simulated. The simulation applies five tiers of communication cells. The interference resulting from each tier is shown in Fig. 5.14 by plotting the statistical characteristics versus the ratio (q) between the distance of radar receiver (D_{xr}) and the cell radius (R_c) corresponding to the target at the origin. Fig. 5.14a displays the mean of interference, whereas the variance is exhibited in Fig. 5.14b. Mean of the dominant interference is the lowest among all tiers and the interference from each tier tends to get stronger when the passive radar moves away from the target. It can also be seen that the variance of dominant interference decreases when the passive radar is closed to the cell border.

Performance of multistatic-cellular passive radar networks is demonstrated in the following figures. In this case, Monte-Carlo simulations for four kinds of channel are employed, i.e., Rayleigh channel, Rayleigh channel with shadowing, Rician channel and Rician channel with shadowing. The results are compared with the channel approximation using Gamma random variables. In Fig. 5.15, it illustrates the surveillance and reference signal to interference ratio and the outcomes from each type of channel are similar though not exactly equal. As frequently mentioned, target reflections are the major problem in passive radar which can be very sensitive to acquire. The reference signal, however, the results show that the receiver is able to collect 5 dB or higher in power. As the results from SIR might not interpret the performance directly, successful probability of detection are then demonstrated. In Fig. 5.16, the simulation performs Monte-Carlo simulations for interference regarding type of channel in comparison with the analytical interference previously shown. It is shown that, with the threshold as low as -20 dB, the target detection can be achieved if the passive radar is less than 15 km from the target of interest, by probability of 0.5. It is important to observe that, using simulated interference, the Gamma approximation performs a lower bound to the other channels and most of the values are matched, whereas the Gamma approximation demonstrates the upper bound when analytical expression is used. This can be interpreted as: (i) the Gamma approximation is a good choice to estimate the Rayleigh coefficients although Rayleigh channel is conceptually not suitable for passive radar channel characteristics; (ii) analytical expressions along with the Gamma approximation provides over-estimate performance of the system, where, in the real scenario, the results may be much worse. To fulfill the discussion in this chapter, the simulation results for reference signal detections are also illustrated in

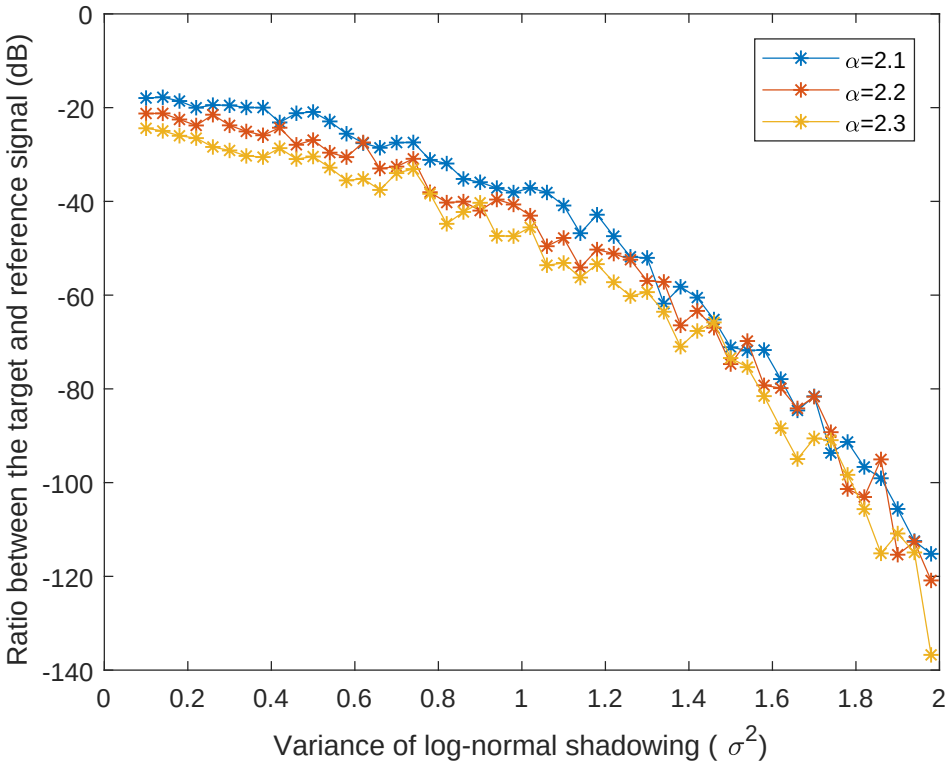

(a)

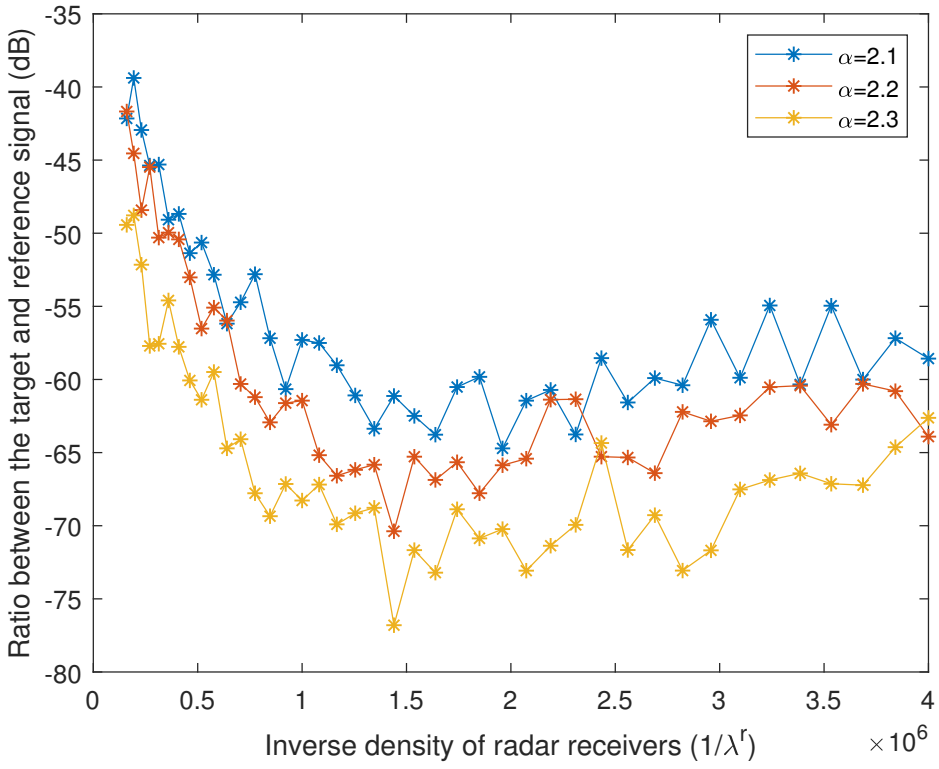

(b)

Figure 5.13: The ratio between the target reflections and the reference signals in multistatic passive radar networks versus: (a) the variance of log-normal shadowing; and (b) the inverse of passive radar density, are displayed.

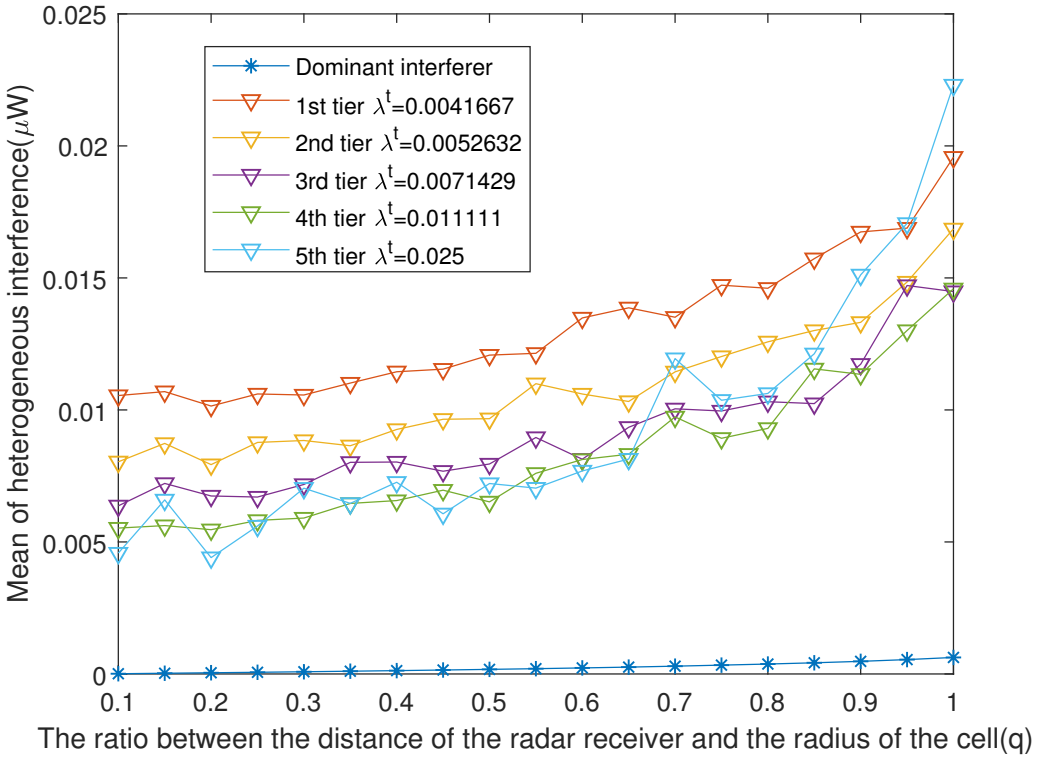

(a)

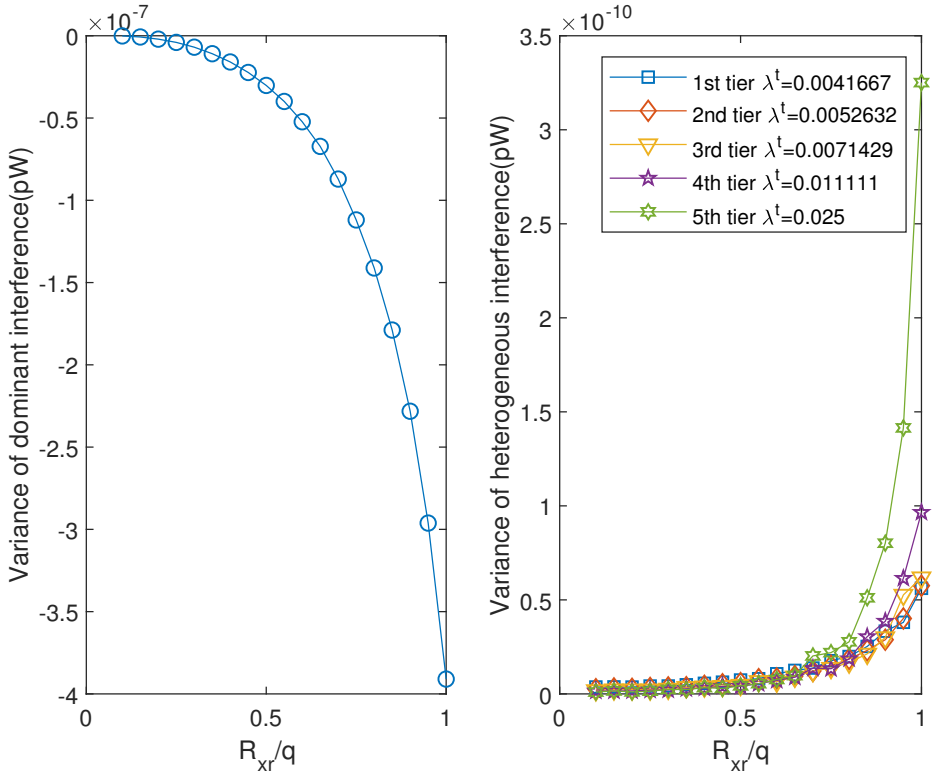

(b)

Figure 5.14: The heterogeneous interference characteristics in multistatic radar networks versus the ratio between the distance of the radar receiver to the target at the origin and the radius of the cell.

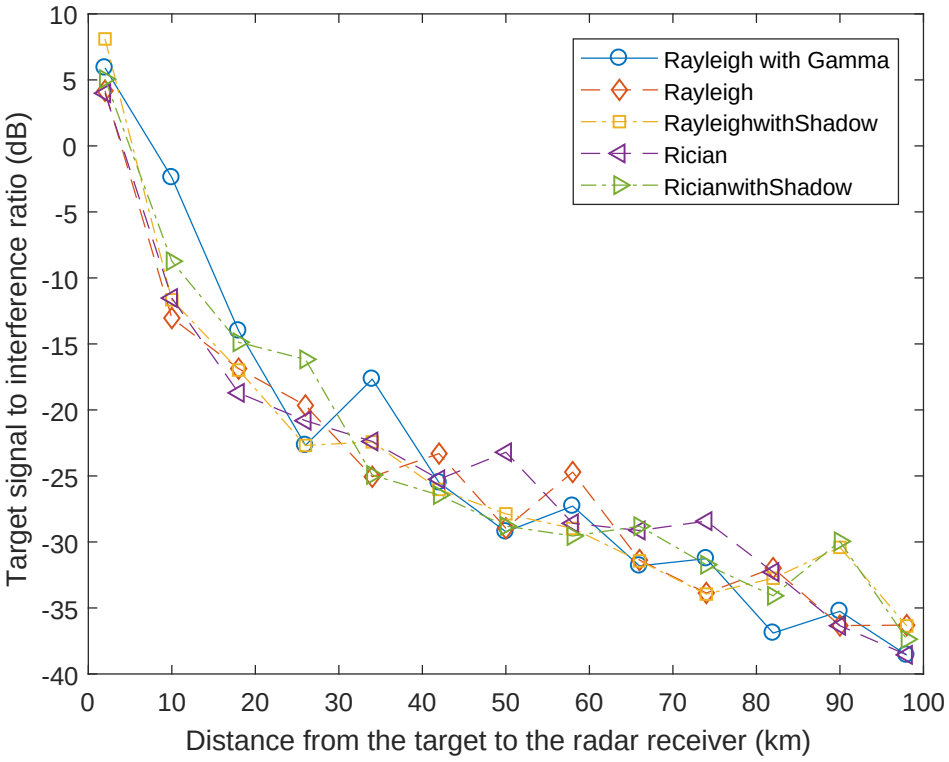

(a)

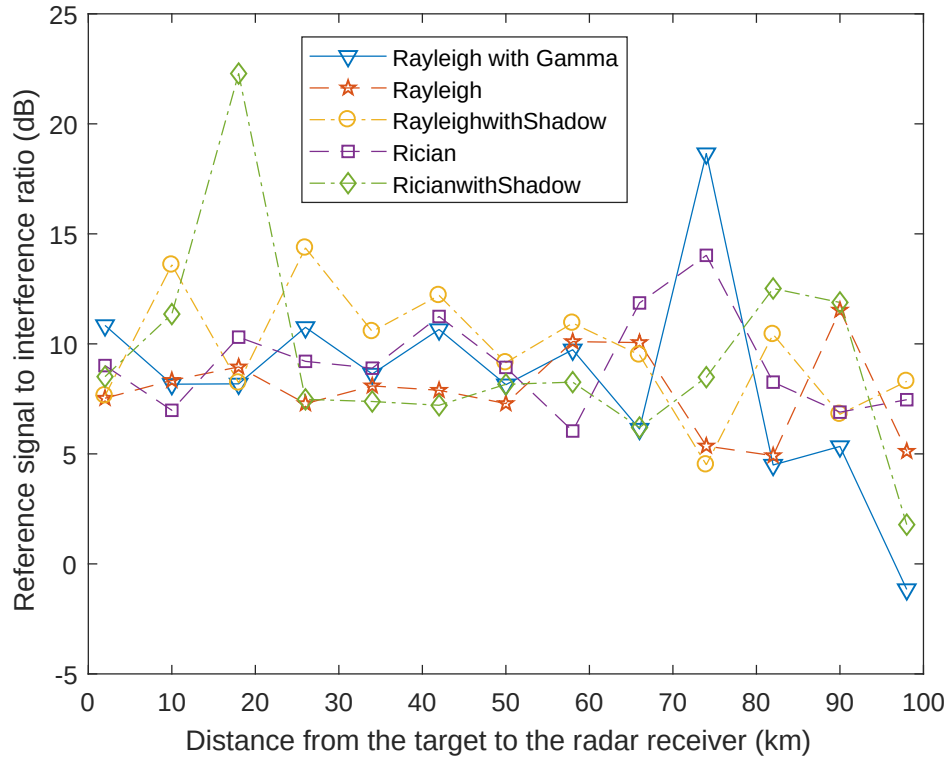

(b)

Figure 5.15: Received signal to interference ratio observed by the passive radar in cellular network where: (a) refer to the target reflections; and (b) refer to the reference signals, using 10 Monte-Carlo experiments

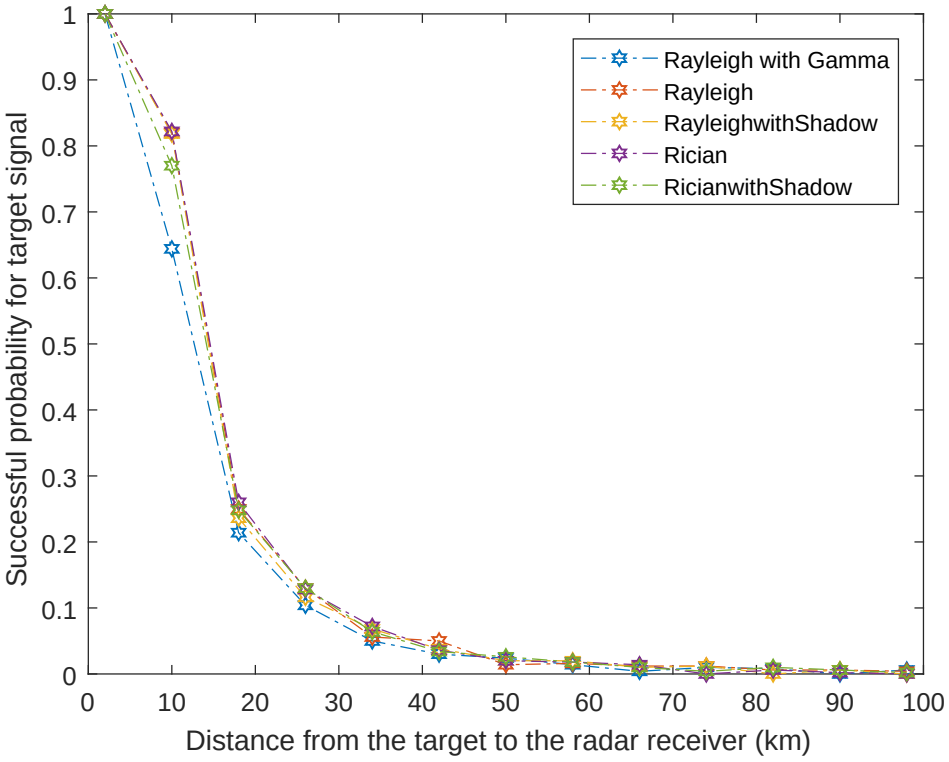

(a)

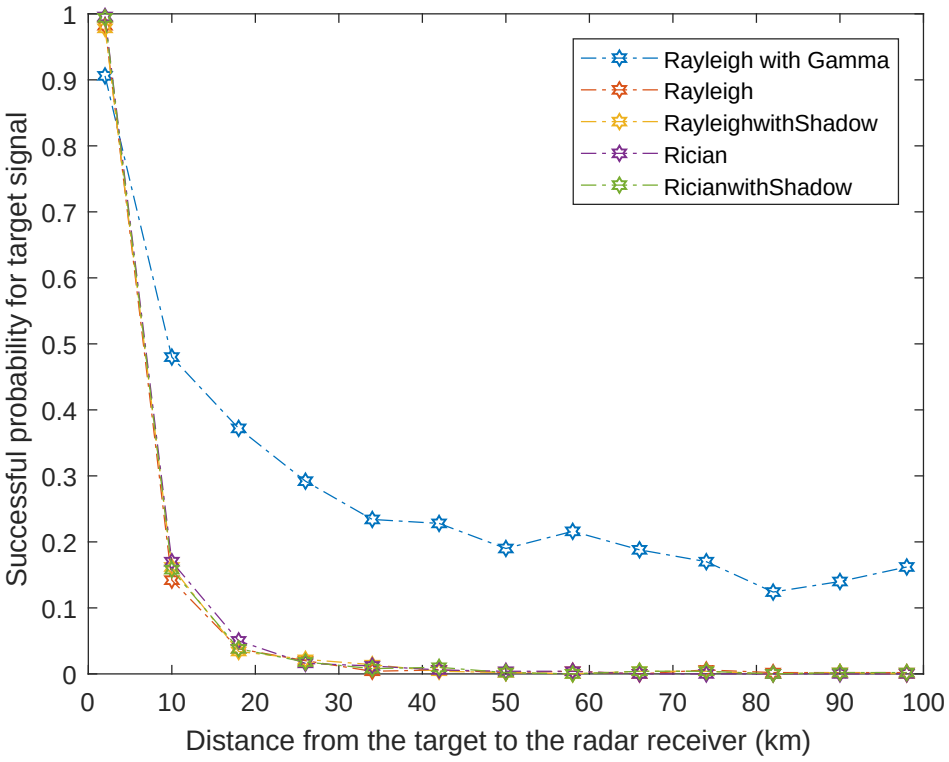

(b)

Figure 5.16: Successful probability of surveillance signals applying (a) Monte-Carlo interference; and (b) analytical interference in this thesis, using 10 Monte-Carlo experiments

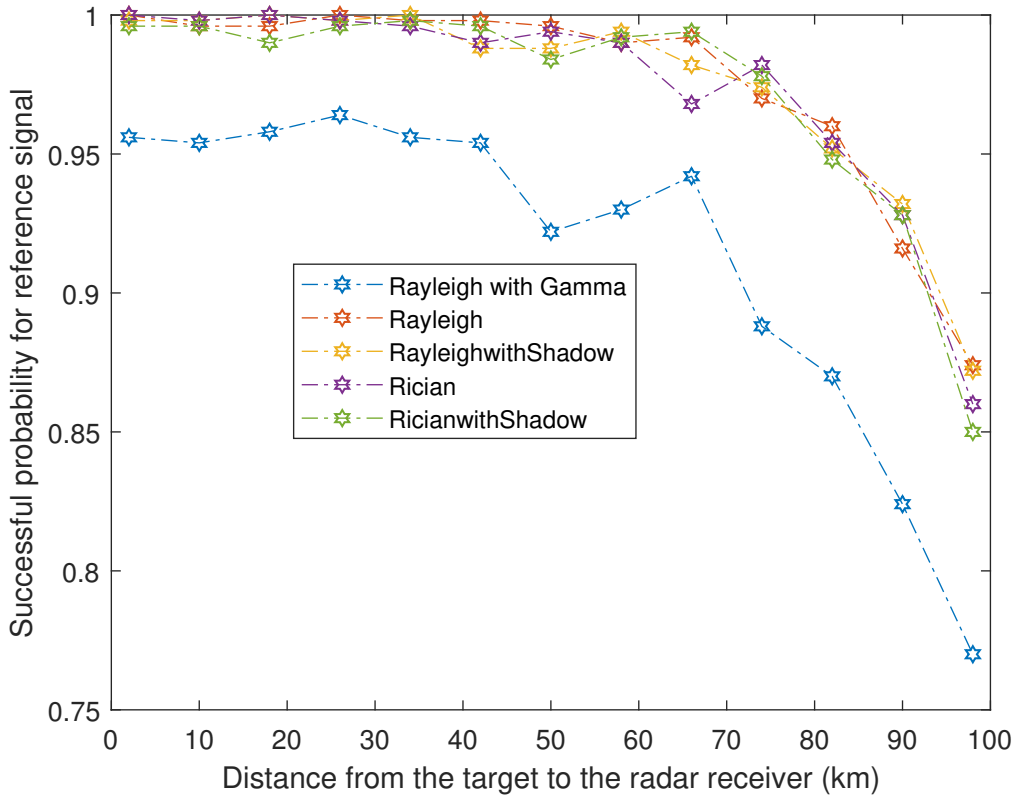

(a)

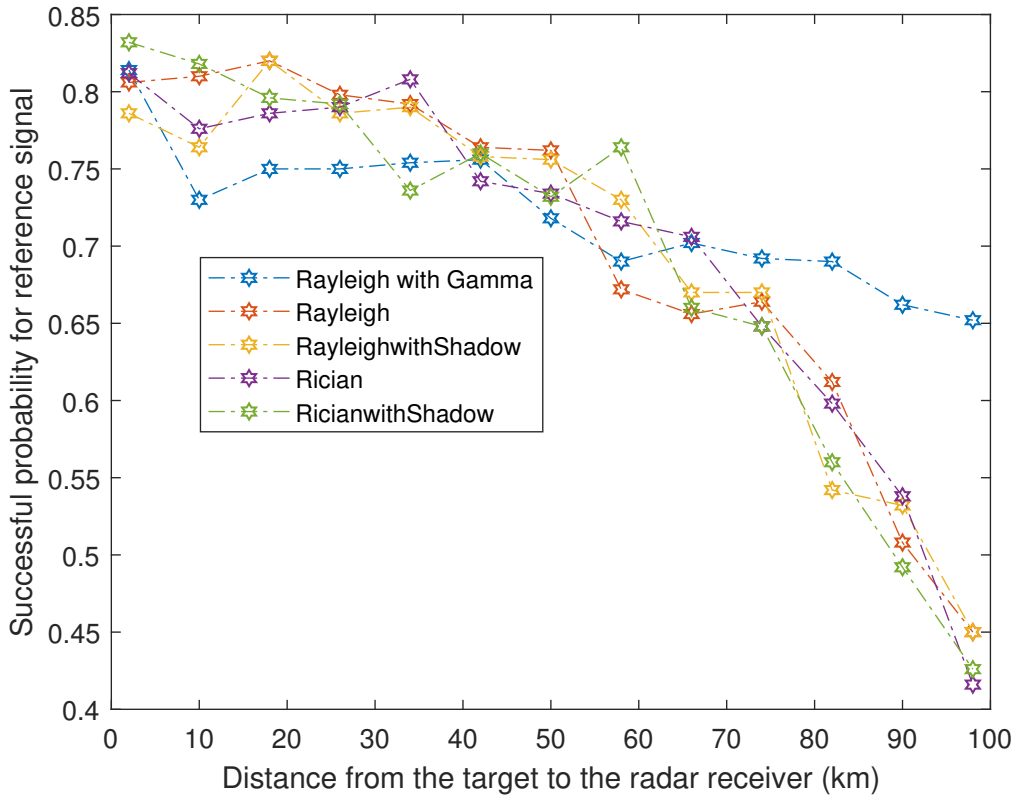

(b)

Figure 5.17: Successful probability of reference signals applying: (a) Monte-Carlo interference; and (b) analytical interference in this thesis, using 10 Monte-Carlo experiments

Fig. 5.17. In contrast to the previous outcomes, Gamma approximation values are quite different from the Monte-Carlo results. From the figure, the system are capable to detect the base station signals in multistatic configuration. It should be concluded that better reference signals can improve the performance of reference reconstruction as the input of the correlator in the matched filter, however, the target signatures are more crucial to be obvious at the end of the process.

5.5 Summary

Since the passive radar can be configured into bistatic and multistatic. Interference from the adjacent passive radar systems requires consideration when multiple receivers are utilised. In this chapter, networks of passive radar receivers are introduced. This thesis employ radar equation to analyse the received power. Without stochastic geometry, the problem of interference modelling becomes mathematical intractable. Two major tools, Campbell's theorem and PGFL, enable the summation and multiplication among the random points. This work assumes the location of passive radar receivers, target of interest and the OFDM base stations are randomised using Poisson point process. The statistical characteristics of interference in bistatic and multistatic passive radar networks are derived. For bistatic configuration, the ad-hoc concept is adapted, whereas the cellular concept is exploited for the multistaic counterpart. Interference derived in this chapter can be employed to calculate the SINR of the receivers. In contrast to communication systems, the target reflection is more crucial at the receivers and is sensitive to the interference. Channel fading in passive radar is also different as this system considers Nakagami-n instead of Rayleigh fading. As a result, the interference integration is limited by the distance between a target and a receiver instead of a transciever pair. The results show that the density of both transmitters and radar receivers produce an impact to the systems, as well as variance of the shadowing and the target-radar distance. To increase detection capability, either reference cancellation processs or target beamforming could be efficient candidates. The algorithms proposed in this thesis can be applied in the high-level system of passive radars.

Chapter 6

Conclusion and future works

6.1 Conclusion

This thesis studies the target detection ability of the OFDM passive radar regarding MIMO configuration using compressive sensing. Previously, the MUSIC algorithm was found to work very well for the signal detection but in passive radar, there is a requirement for a large number of snapshots as well as producing some interference from the direct signals. In order to employ CS, a sparse representation is needed and this thesis has discussed the overcomplete matrix design. A single time sample compressive sensing which consumes high computational resources was applied and satisfaction was not assured. Therefore, this thesis has suggested l_1-SVD, which has an impressive capability of targets detection in the passive radar paradigm. The results shown in this thesis indicate the performance of compressive sensing for MIMO-OFDM passive radar. l_1-SVD, as well as basis pursuit, can detect a target as long as the power of the direct signal is not higher than 20 dB compared to that of the target, whereas it is shown in [16] that the direct signal should be 20 dB to be recovered with error free. The difference between target and direct signal power is set to as low as -50 dB in this reference. The simulation results stated the improvement in passive radar employing the MIMO system, and a diversity gain can be achieved from the data collected from all receivers. Simulation results from the CS algortihms show that it is possible to increase the resolution of the CS detector, while it is unlikely for the MUSIC algorithm. Consequently, incomplete sensing behaviour allows for a fewer number of snapshots and is suitable for moving sensors.

Additionally, a MIMO passive radar system model comprising differently located BS transmitter antennas and collocated array-based receiver antennas is considered with regard to the extraction of 3D target parameter sets using broadcast OFDM signals. With

the co-located antennas receiver, the MIMO scheme is also capable of determining the direction of arrivals of the sources. 3D channel estimates extend the detection capability of the MIMO passive radar using OFDM waveforms for the angular domain. In the case where a Single Frequency Network is used over the Digital Broadcasting base stations, this proposed model can determine the angle of either the reference or surveillance signal. The level of requirement for data association between transmitters and each received signal may be reduced. It has been shown that a novel compressive technique, known as Fast-BesselK, could be used to extract this 3D parameter set in a computationally efficient manner, thus indicating for the first time that a MIMO passive radio employing OFDM signals could perform this task, which was hitherto assumed to be too computationally intractable. Furthermore, the computational efficiency of this approach has been verified by complexity analysis in comparison with other compressive sensing approaches that are used for the less intensive 2D case. Moreover, a novel CCOB-based beamforming technique, which was specifically designed to be compatible with the Fast-BesselK technique, was devised to reduce the effect of the high power of the clean copy of the OFDM signal that was necessary to be received from an assigned nearby BS, thus improving the performance of the MIMO passive radar in the low SNR regime. Concerning the operation scene, the interference which affects the radar system has also been derived using stochastic geometry. This enables a network of passive radars where they can be operated utilising bistatic or multistatic configuration. Stochastic geometry allows the modelling of interference, which is crucial in the target detection of a passive radar system.

6.2 Possible future works

There are some possibilities presented in this section in order to continue exploring the area of passive radar.

- *Association problems*

  This problem is significantly related to the OFDM passive radar with widely-spread receivers, whose association algorithms are replaced by the co-located receivers in this thesis. The three-dimensional matrix, however, may require higher computational resources than a simple association method, provided that the maintenance of the distributed receiver is in control. [11] and [14] proposed an association algorithm which can be straighforwardly applied to the system discussed in this thesis. This is quite interesting in terms of complexity comparison, and the results can be

used for a better localisation scheme than without the effective association.

- *Localisation problems*

  The localisation of an unknown target, as well as the partially known OFDM base stations for the widely-separated receivers, is rather difficult. Doppler and bearing estimation can assist the localisation process [119]. Without the angle of arrivals information, however, the receivers can extract only the time delays, which can be transformed to Euclidean distances. Fortunately, a technique called *Euclidean Distance Matrices* [120] is presented to be impressive. The system does not need to understand complete data matrix in order to perform the algorithm. Equipped with the OFDM passive radar, the method seems to provide a promising result, with efficiency, for widely-spread configuration.

- *Tracking problems*

  After the parameter extraction step is complete, the process of target tracking should be initiated. In chapter 5, the passive radar networks display a challenge in this research area. There are many tracking algorithms applied in the radar, as well as the passive radar scheme. As a suggestion, the probability hypothesis density (PHD) filter [26] has been shown to be attracted to the multiple-sensor multiple-target area of research. There is a conviction that the PHD filter can improve the tracking ability of the OFDM passive radar.

- *Large-scale antennas problems*

  Recently, the concept of Fifth Generation (5G) has extensively been discussed. Not only can the broadcasting stations be equipped with a massive array of antennas, but the radar stations can also exploit the advantage of a massive MIMO paradigm. The receiver where the antennas are located can perform multiple target detection and tracking, as well as simultaneous beamforming. The techniques employed in the large-scale system can be adapted in other areas of research, including passive radar, such as [121] with a full-dimension massive MIMO along with a 3D spatial channel model. A massive MIMO can be configured in distributed arrays and this can lead to an enormous increase in the surveilance area. Although [122] presented a massive MIMO based on communications concept, the sparsity of channel estimates can be exploited. This means compressive sensing can be an interesting method for a large-scale antennas receiver with an appropriate adaptation. Hence, this problem

becomes attractive to future researchers.

- *Extension to chapter 5*

  Due to the fact that the number of base stations is increasing, a dense cellular networks are of interest [70]. The cell association in passive radar networks needs to considered not only the distance of the reference transmitter, but also the receive power from each transmitter. Multiple-antennas at both base stations and radar receivers can be another evolution. Similar to a discussion in [123] and [69], MIMO scenarios are presented with multi-tier heterogeneous cellular network. The system model in chapter 5 also resembles those in the references in case of heterogeneous environment except that Rayleigh fading channel might not be suitable. Maximum Ratio Combining technique can be employed for the receiver with multiple antennas.

- *Stealth target consideration*

  One of the advantages of the passive radar is related to the characteristic of the broadcasting waveforms. As the transmitted signals are aimed to be received by the subscribers, low-altitude aircraft, as well as countermeasure-design stealth platforms, can be detected. Evaluation of RCS referred to a multi-static configuration is considered in [124], along with low flight elevation coverage. As a result, digital broadcasting signals can be employed to detect unmanned aerial vehicles (UAV). It has been shown in [125] that with a multi-static passive radar system, a drone or slow aircraft parameter can be measured. The idea in this thesis can be applied to the available systems, providing the sparsity to increase the detection efficiency. This concept attracts the application of passive radar regarding the present increase in drone usage.

- *Off-grid compressive sensing*

  As seen thoughout this thesis, the value of extracted parameters from the CS method is indicated by the elements of an overcomplete matrix. Since it is arbitrarily designed, the real parameters can demonstrate a value which is within the grid provided. This is a reasonable development of the system in order to improve its precision, and this also allows an adaptive grid to be employed. [126] explained the idea of off-grid compressive sensing applying an atomic norm minimisation with a semi-definite program, and the off-grid CS signal model with the remedy approaches to

radar domain is suggested in [127]. To extend the analysis provided in this thesis, this problem is of interest and its outcome are important to this area of research.

Appendices

Appendix A

Matched Filter Derivation

A.1 Derivation of 2D matched filter

To demonstrate the matched filter from (3.11), the limitation of the integration is first changed and this results in:

$$z_{mf}^{(m)}(\hat{\tau}) = \sum_{k=1}^{n_t} \sum_{i=1}^{\frac{T_i}{T'}} \int_{iT'}^{iT'+T} e^{-j2\pi \hat{a}_{mf} f_c^k (t+iT')} x_k^*(t+iT'-\hat{\tau}) y^{k(m)}(t+iT') dt \tag{A.1}$$

$$= \sum_{k=1}^{n_t} \sum_{i=1}^{\frac{T_i}{T'}} e^{-j2\pi \hat{a}_{mf} f_c^k iT'} \int_0^{T_i} e^{-j2\pi \hat{a}_{mf} f_c^k t} x_k^*(t+iT'-\hat{\tau}) y^{k(m)}(t+iT') dt \tag{A.2}$$

$$= \sum_{k=1}^{n_t} \sum_{i=1}^{\frac{T_i}{T'}} e^{-j2\pi \hat{a}_{mf} f_c^k iT'} z_{mf}^{(i)}(\hat{\tau}), \tag{A.3}$$

where

$$z_{mf}^{(i)}(\hat{\tau}) = \int_0^{T_i} e^{-j2\pi \hat{a}_{mf} f_c^k t} x_k^*(t+iT'-\hat{\tau}) y^{k(m)}(t+iT') dt. \tag{A.4}$$

The next step is to consider only the matched filter output of the ith block (A.4) (for $i \in \{1,\ldots,L\}$). This is feasible due to the occurrence of cyclic prefix. Substituted by (3.4). The result will be shown as:

$$z_{mf}^{(i)}(\hat{\tau}) = \int_0^T e^{-j2\pi \hat{a}_{mf} f_c^k t} \sum_{n=\frac{-N}{2}}^{\frac{N}{2}-1} s_{k(i)}^*[n] e^{-j2\pi n \Delta f (t-\hat{\tau})} y^{k(m)}(t+iT') dt \tag{A.5}$$

$$= \sum_{n=\frac{-N}{2}}^{\frac{N}{2}-1} \left(e^{j2\pi n \Delta f \hat{\tau}} s_{k(i)}^*[n] \int_0^T e^{-j2\pi n \Delta f t} [e^{-j2\pi \hat{a}_{mf} f_c^k t} y^{k(m)}(t+iT')] dt \right). \tag{A.6}$$

Using the approximation in [16], i.e. $e^{-j2\pi \hat{a}_{mf} f_c^k t} \approx e^{-j2\pi \hat{a}_{mf} f_c^k (\frac{T}{2})} \quad \forall t \in [0,T]$, the

above equation can be simplified to:

$$z_{mf}^{(i)}(\hat{\tau}) = e^{-j\pi\hat{a}_{mf}f_c^k T}\sum_{n=\frac{-N}{2}}^{\frac{N}{2}-1} e^{j2\pi n\Delta f\hat{\tau}}s_{k(i)}^*[n]\int_0^T e^{-j2\pi n\Delta f t}y^{k(m)}(t+iT')]dt. \tag{A.7}$$

Focusing on the term $s_{k(i)}^*[n]\int_0^T e^{-j2\pi n\Delta f t}y^{k(m)}(t+iT')]dt$ with an assumption that there is one existing target without noise, the amplitude of the reflected signal is $A_0^{k(m)}$, along with the delay $\tau_0^{k(m)}$ and the Doppler frequency $a_0^{k(m)}f_c^k$. Substitute $y^{k(m)}(t+iT')$ using (3.9), this term can be shown as:

$$= s_{k(i)}^*[n]\int_0^T e^{-j2\pi n\Delta f t}(A_0^{k(m)}x_{k(i)}(t-\tau_0^{k(m)})e^{j2\pi a_0^{k(m)}f_c^k(t+iT')}dt), \tag{A.8}$$

and it is possible to replace $x_{k(i)}(t-\tau_0)$ applying (3.4). The result is:

$$= s_{k(i)}^*[n]\int_0^T e^{-j2\pi n\Delta f t}(A_0^{k(m)}\sum_{m=\frac{-N}{2}}^{\frac{N}{2}-1} s_{k(i)}[m]e^{j2\pi m\Delta f(t-\tau_0^{k(m)})}e^{j2\pi a_0^{k(m)}f_c^k(t+iT')})dt \tag{A.9}$$

$$= A_0^{k(m)}\sum_{m=\frac{-N}{2}}^{\frac{N}{2}-1} s_{k(i)}[m]s_{k(i)}^*[n]e^{-j2\pi m\Delta f\tau_0}\int_0^T e^{-j2\pi(n-m)\Delta f t}e^{j2\pi a_0 f_c(t+iT')}dt \tag{A.10}$$

$$\approx A_0^{k(m)}T|s_{k(i)}[n]|^2 e^{j2\pi(ia_0^{k(m)}f_c^k T'-n\Delta f\tau_0)}. \tag{A.11}$$

(A.11) is approximated employing the phase rotation estimation mentioned above and the orthogonality of all frequencies. This equation is similar to the channel estimation of the uniform rectangular array (URA) receiver, where its elements are identically isolated by T' in Doppler domain and Δf in time domain. Ignoring the constant coefficients, (A.11) *the channel estimates* can be written in the general form as:

$$H_{n(i)}^{k(m)} = \sum_{p=1}^{N_p} A_p^{k(m)}e^{j2\pi(i\hat{a}_p^{k(m)}f_c^k T'-n\Delta f\hat{\tau}_p^{k(m)})}. \tag{A.12}$$

Substituting (A.12) into (A.7) and then into (A.3), the output of the overall matched filter can be derived as:

$$z_{mf}^{(m)}(\hat{\tau}) = \sum_{k=1}^{n_t}\sum_{i=1}^{L}\sum_{n=\frac{-N}{2}}^{\frac{N}{2}-1} e^{-j2\pi(i\hat{a}_{mf}f_c^k T'-n\Delta f\hat{\tau})}H_{n(i)}^{k(m)}. \tag{A.13}$$

A.2 Derivation of 3D matched filter

As seen from (2.1), the matched filter can be implemented as a correlator for the cross-correlation between the transmitted and received signals. For each m-th antenna, the co-th

correlator with a fixed Doppler shift $\hat{a}_{co}f^k$ generates a 2D grid for every $\hat{\tau}$ and $\hat{\phi}$ as:

$$z_{co}^{(m)}(\hat{\tau},\hat{\phi}) = \sum_{k=1}^{n_t} \sum_{\phi=-\frac{\pi}{2}}^{\frac{\pi}{2}} e^{-j2\pi(m-1)\frac{d}{\lambda_k}\sin\hat{\phi}} \int_0^{T_{int}} e^{-j2\pi\hat{a}_{co}f^k t} x_k^*(t-\hat{\tau}) y^{k(m)}(t)dt \tag{A.14}$$

As in (3.5), if an integer, which is a multiple of T', is elected as the integration time, the total output of the correlators will be realised as the summation of the output of the correlator for the ith block and the transmitted signal is divided into the block of time T', where $T' = T + T_{cp}$, the correlator then can be rewritten as:

$$z_{co}^{(m)}(\hat{\tau},\hat{\phi}) = \sum_{k=1}^{n_t} \sum_{\phi=-\frac{\pi}{2}}^{\frac{\pi}{2}} e^{-j2\pi(m-1)\frac{d}{\lambda_k}\sin\hat{\phi}} \sum_{i=1}^{T_{int}/T'} \int_{iT'}^{iT'+T} e^{-j2\pi\hat{a}_{co}f^k t} x_k^*(t-\hat{\tau}) y^{k(m)}(t)dt \tag{A.15}$$

$$= \sum_{k=1}^{n_t} \sum_{\phi=-\frac{\pi}{2}}^{\frac{\pi}{2}} e^{-j2\pi(m-1)\frac{d}{\lambda_k}\sin\hat{\phi}} \sum_{i=1}^{T_{int}/T'} \int_0^{T} e^{-j2\pi\hat{a}_{co}f^k (t+iT')} x_k^*(t+iT'-\hat{\tau}) y^{k(m)}(t+iT')dt \tag{A.16}$$

$$= \sum_{k=1}^{n_t} \sum_{\phi=-\frac{\pi}{2}}^{\frac{\pi}{2}} e^{-j2\pi(m-1)\frac{d}{\lambda_k}\sin\hat{\phi}} \sum_{i=1}^{T_{int}/T'} e^{-j2\pi\hat{a}_{co}f^k iT'} z_{co}^{(i)}(\hat{\tau}). \tag{A.17}$$

From (A.17), it can be shown that:

$$z_{co}^{(i)}(\hat{\tau}) = \int_0^{T} e^{-j2\pi\hat{a}_{co}f^k t} x_k^*(t+iT'-\hat{\tau}) y^{k(m)}(t+iT')dt. \tag{A.18}$$

is the correlator output of the i-th block for each m-th antenna (superscript (m) is temporarily ignored) and has the same form as discussed in [16]. The conjugation of the ith block transmitted signal $x^*(t+iT'-\hat{\tau})$ can be represented as $x_{k(i)}^*(t-\hat{\tau})$. Recall from (3.4) that:

$$x_{k(i)}^*(t-\hat{\tau}) = \sum_{n=-N/2}^{N/2-1} s_{k(i)}^*[n] e^{-j2\pi n\Delta f(t-\hat{\tau})}, \tag{A.19}$$

Utilising the cyclic prefix, the correlation is periodic with the length of T. Then:

$$z_{co}^{(i)}(\hat{\tau},\hat{\phi}) = \int_{-\phi_{max}}^{\phi_{max}} \int_0^T e^{-j2\pi[\hat{a}_{co}f^k t + (m-1)\frac{d}{\lambda_k}\sin\hat{\phi}]} x_{k(i)}^*(t-\hat{\tau}) y^{k(m)}(t+iT')dtd\phi \tag{A.20}$$

$$= \int_{-\phi_{max}}^{\phi_{max}} \int_0^T e^{-j2\pi[\hat{a}_{co}f^k t + (m-1)\frac{d}{\lambda_k}\sin\hat{\phi}]} \sum_{n=-N/2}^{N/2-1} s_{k(i)}^*[n] e^{-j2\pi n\Delta f(t-\hat{\tau})} y^{k(m)}(t+iT')dtd\phi \tag{A.21}$$

$$= \sum_{n=-N/2}^{N/2-1} e^{-j2\pi n\Delta f\hat{\tau}} s_{k(i)}^*[n] \int_{-\phi_{max}}^{\phi_{max}} e^{-j2\pi(m-1)\frac{d}{\lambda_k}\sin\hat{\phi}} \int_0^T e^{-j2\pi[\hat{a}_{co}f^k + n\Delta f]t}$$

$$\times y^{k(m)}(t+iT')dtd\phi.$$

As it will produce very small value when T' is multiplied with the Doppler shift, the phase rotation in one OFDM block, i.e. $e^{-j2\pi\hat{a}_{co}f^k t}$ can be replaced by a constant $e^{-j2\pi\hat{a}_{co}f^k(T/2)}$, same as in [16]:

$$z_{co}^{(i)}(\hat{\tau}) \approx \; e^{-j\pi\hat{a}_{co}f^k T} \sum_{n=-N/2}^{N/2-1} \left(e^{j2\pi n\Delta f\hat{\tau}} s_{k(i)}^*[n] \int_0^T e^{-j2\pi n\Delta f t} y^{k(m)}(t+iT')dt \right). \tag{A.22}$$

Then substitute the result from (A.22) regardless the constant phase rotation out front, (A.17) becomes:

$$z_{co}^{(m)}(\hat{\tau},\hat{\phi}) = \sum_{k=1}^{n_t} \sum_{\phi=-\frac{\pi}{2}}^{\frac{\pi}{2}} e^{-j2\pi(m-1)\frac{d}{\lambda_k}\sin\hat{\phi}} \sum_{i=1}^{T_{int}/T'} e^{-j2\pi\hat{a}_{co}f^k iT'}$$

$$\times \sum_{n=-N/2}^{N/2-1} \left(e^{j2\pi n\Delta f\hat{\tau}} s_{k(i)}^*[n] \int_0^T e^{-j2\pi n\Delta f t} y^{k(m)}(t+iT')dt \right). \tag{A.23}$$

Therefore, the matched filter output can be shown as:

$$z_{co}^{(m)}(\hat{\tau},\hat{\phi}) = \sum_{k=1}^{n_t} \sum_{\phi=-\frac{\pi}{2}}^{\frac{\pi}{2}} \sum_{i=1}^{T_{int}/T'} \sum_{n=-N/2}^{N/2-1} \exp(-j2\pi[r^{k,m}(\hat{\phi}) + \hat{a}_{co}f^k iT' - n\Delta f\hat{\tau}]) H_{n,i}^{k(m)}, \tag{A.24}$$

where $r^{k,m}(\hat{\phi}) = (m-1)\frac{d}{\lambda_k}\sin\hat{\phi}$ and the channel estimates are defined as:

$$H_{n,i}^{k(m)} = s_{k(i)}^*[n] \int_0^T e^{-j2\pi n\Delta f t} y^{k(m)}(t+iT')dt. \tag{A.25}$$

Assume that there is one path impinging on the m-th antenna at angle $\phi_0^{k(m)}$. Its attenuation is equal to $A_0^{k(m)}$ including $\tau_0^{k(m)}$ and $a_0^{k(m)}f^k$ of delay and Doppler frequency respectively. The channel estimates demonstrate:

$$H_{n,i}^{k(m)} = s_{k(i)}^*[n] \int_0^T e^{-j2\pi n\Delta f t} \left(A_0^{k(m)} x^{k(m)}(t-\tau_0^{k(m)}) e^{j2\pi[a_0^{k(m)}f^k(t+iT') + (m-1)\frac{d}{\lambda_k}\sin\phi_0^{k(m)}]} \right) dt. \tag{A.26}$$

Using (A.19), then

$$H_{n,i}^{k(m)} = s_{k(i)}^{*}[n] \int_0^T e^{-j2\pi n\Delta f t} \left(A_0^{k(m)} \sum_{g=N/2}^{N/2-1} s_{k(i)}[g] e^{j2\pi[a_0^{k(m)} f^k (t+iT') + (m-1)\frac{d}{\lambda_k}\sin\phi_0^{k(m)}]} \right.$$

$$\left. \times e^{j2\pi g\Delta f (t-\tau_0^{k(m)})} \right) dt \tag{A.27}$$

$$H_{n,i}^{k(m)} = A_0^{k(m)} \sum_{g=N/2}^{N/2-1} s_{k(i)}[g] s_{k(i)}^{*}[n] e^{-j2\pi g\Delta f \tau_0^{k(m)}} e^{j2\pi[a_0^{k(m)} f^k iT' + (m-1)\frac{d}{\lambda_k}\sin\phi_0^{k(m)}]}$$

$$\times \int_0^T e^{-j2\pi(n-g)\Delta f t} \cdot e^{j2\pi a_0^{k(m)} f^k t} dt. \tag{A.28}$$

As in [16], $e^{j2\pi a_0^{k(m)} f^k t}$ is approximated as $e^{j\pi a_0^{k(m)} f^k T}$ and this has also been used in (A.22). Regardless the constant resulted from the approximation and recall that each frequency is mutually orthogonal, the outcome of the channel estimates after performing the integration is:

$$H_{n,i}^{k(m)} = A_0^{k(m)} [s_{k(i)}[n]]^2 T e^{j2\pi[a_0^{k(m)} f^k iT' + (m-1)\frac{d}{\lambda_k}\sin\phi_0^{k(m)} - n\Delta f \tau_0^{k(m)}]}. \tag{A.29}$$

Finally, the channel estimates can be subtitute into (A.24) and the intepretation of this derivation is the same as shown in proposition 1.

Appendix B

OFDM passive radar Cramer-Rao lower bounds

B.1 Derivation of 2D Cramer-Rao lower bounds

The log-likelihood function can be displayed as:

$$\ln p(\mathbf{h};\theta) = -\ln[2\pi\sigma_w^2]^{\frac{NLn_t n_r}{2}} - \frac{1}{2\sigma_w^2}\sum_m\sum_k\sum_i\sum_n\left(\hat{H}_{n(i)}^{k(m)} - \sum_p A_p^{k(m)} e^{j2\pi[ia_p^{k(m)} f_c^k T' - n\Delta f \tau_p^{k(m)}]}\right)^2, \tag{B.1}$$

Each element of $\mathbf{I}(\theta)$ can be first computed by finding the first-order partial derivative with respect to each parameter as shown:

$$\frac{\partial \ln p(\mathbf{h};\theta)}{\partial \tau} = -\frac{j2\pi\Delta f}{\sigma_w^2}\sum_m\sum_k\sum_i\sum_n n\left(\hat{H}_{n(i)}^{k(m)} H_{n(i)}^{k(m)} - (H_{n(i)}^{k(m)})^2\right),$$

$$\frac{\partial \ln p(\mathbf{h};\theta)}{\partial a} = \frac{j2\pi T'}{\sigma_w^2}\sum_m\sum_k\sum_i\sum_n if^k\left(\hat{H}_{n(i)}^{k(m)} H_{n(i)}^{k(m)} - (H_{n(i)}^{k(m)})^2\right).$$

The second partial derivative can be derived as:

$$\frac{\partial^2 \ln p(\mathbf{h};\theta)}{\partial \tau^2} = -\frac{4\pi^2\Delta f^2}{\sigma_w^2}\sum_m\sum_k\sum_i\sum_n n^2\left(\hat{H}_{n(i)}^{k(m)} H_{n(i)}^{k(m)} - 2(H_{n(i)}^{k(m)})^2\right),$$

$$\frac{\partial^2 \ln p(\mathbf{h};\theta)}{\partial \tau \partial a} = \frac{4\pi^2\Delta f T'}{\sigma_w^2}\sum_m\sum_k\sum_i\sum_n nif^k\left(\hat{H}_{n(i)}^{k(m)} H_{n(i)}^{k(m)} - 2(H_{n(i)}^{k(m)})^2\right),$$

$$\frac{\partial^2 \ln p(\mathbf{h};\theta)}{\partial a^2} = -\frac{4\pi^2 T'^2}{\sigma_w^2}\sum_m\sum_k\sum_i\sum_n (if^k)^2\left(\hat{H}_{n(i)}^{k(m)} H_{n(i)}^{k(m)} - 2(H_{n(i)}^{k(m)})^2\right),$$

where the substitution is performed using (A.12) in order to allow for compactness. The next step is to calculate the negative expectation of the second derivative shown above.

This can be demonstrated as:

$$-E\left[\frac{\partial^2 \ln p(\mathbf{h};\theta)}{\partial \tau^2}\right] = -\frac{4\pi^2\Delta f^2}{\sigma_w^2}\sum_m\sum_k\sum_i\sum_n n^2\left(\sum_p A_p^{k(m)} e^{j2\pi[ia_p^{k(m)} f_c^k T' - n\Delta f \tau_p^{k(m)}]}\right)^2,$$

$$-E\left[\frac{\partial^2 \ln p(\mathbf{h};\theta)}{\partial \tau \partial a}\right] = \frac{4\pi^2\Delta f T'}{\sigma_w^2}\sum_m\sum_k\sum_i\sum_n ni f_c^k\left(\sum_p A_p^{k(m)} e^{j2\pi[ia_p^{k(m)} f_c^k T' - n\Delta f \tau_p^{k(m)}]}\right)^2,$$

$$-E\left[\frac{\partial^2 \ln p(\mathbf{h};\theta)}{\partial a^2}\right] = -\frac{4\pi^2 T'^2}{\sigma_w^2}\sum_m\sum_k\sum_i\sum_n (if^k)^2\left(\sum_p A_p^{k(m)} e^{j2\pi[ia_p^{k(m)} f_c^k T' - n\Delta f \tau_p^{k(m)}]}\right)^2,$$

The results shown above can be substituted into (3.19) with an assumption that no target exists along with summation properties; however, the above expression can be further simplified, as shown in Section 3.4.

B.2 Derivation of 3D Cramer-Rao Lower Bounds

For three-dimensional CRLB, it is to assign:

$$H^* = \sum_{pth=1}^{mpth} A_{pth}^{k(m)} e^{j2\pi[ia_{pth}^{k(m)} f^k T' - n\Delta f \tau_{pth}^{k(m)} + r^{k(m)}(\phi_{pth})]}.$$

Because of the property of partial derivative, the results for τ and a from the 2D CRLB can be used. Considering the first derivative of the other elements in the Fisher information matrix, it can be shown that:

$$\frac{\partial \ln p(\mathbf{h};\theta)}{\partial \phi} = \frac{j2\pi d}{\sigma_w^2}\sum_m\sum_k\sum_i\sum_n \frac{m-1}{\lambda_k}\left(H_{(n,i)}^{k(m)} H_{\cos}^* - H^* H_{\cos}^*\right),$$

where

$$H_{\cos}^* = \sum_{pth=1}^{mpth} A_{pth}^{k(m)} \cos\phi_{pth}^{k(m)} e^{j2\pi[ia_{pth}^{k(m)} f^k T' - n\Delta f \tau_{pth}^{k(m)} + r^{k(m)}(\phi_{pth})]}.$$

For the second derivatives:

$$\frac{\partial^2 \ln p(\mathbf{h};\theta)}{\partial \tau \partial \phi} = \frac{4\pi^2\Delta f d}{\sigma_w^2}\sum_m\sum_k\sum_i\sum_n \frac{n(m-1)}{\lambda_k}\left(H_{(n,i)}^{k(m)} H_{\cos}^* - 2H^* H_{\cos}^*\right),$$

$$\frac{\partial^2 \ln p(\mathbf{h};\theta)}{\partial a \partial \phi} = -\frac{4\pi^2 T' d}{\sigma_w^2}\sum_m\sum_k\sum_i\sum_n \frac{if^k(m-1)}{\lambda_k}\left(H_{(n,i)}^{k(m)} H_{\cos}^* - 2H^* H_{\cos}^*\right),$$

Due to the compactness, let introduce:

$$H_{\sin}^* = \sum_{pth=1}^{mpth} A_{pth}^{k(m)} \sin\phi_{pth}^{k(m)} e^{j2\pi[ia_{pth}^{k(m)} f^k T' - n\Delta f \tau_{pth}^{k(m)} + r^{k(m)}(\phi_{pth})]},$$

and

$$H^*_{\cos^2} = \sum_{pth=1}^{mpth} A_{pth}^{k(m)} \cos^2 \phi_{pth}^{k(m)} e^{j2\pi[ia_{pth}^{k(m)} f^k T' - n\Delta f \tau_{pth}^{k(m)} + r^{k(m)}(\phi_{pth})]}.$$

Therefore:

$$\frac{\partial^2 \ln p(\mathbf{h};\theta)}{\partial \phi^2} = \frac{j2\pi d}{\sigma_w^2} \sum_m \sum_k \sum_i \sum_n \frac{m-1}{\lambda_k} \Bigg[j2\pi(m-1)\frac{d}{\lambda_k} \left(H_{(n,i)}^{k(m)} H^*_{\cos^2} - H^* H^*_{\cos^2} - (H^*_{\cos})^2 \right)$$

$$- \left(H_{(n,i)}^{k(m)} H^*_{\sin} - H^* H^*_{\sin} \right) \Bigg].$$

Then taking the negative expectation of the second derivatives, the outcomes are:

$$[\mathbf{I}(\theta)]_{11} = -E\left[\frac{\partial^2 \ln p(\mathbf{h};\theta)}{\partial \tau^2}\right]$$

$$= -\frac{4\pi^2 \Delta f^2}{\sigma_w^2} \sum_m \sum_k \sum_i \sum_n n^2 \left(\sum_{pth=1}^{mpth} A_{pth}^{k(m)} e^{j2\pi[ia_{pth}^{k(m)} f^k T' - n\Delta f \tau_{pth}^{k(m)} + r^{k(m)}(\phi_{pth})]} \right)^2,$$

$$[\mathbf{I}(\theta)]_{12} = [\mathbf{I}(\theta)]_{21} = -E\left[\frac{\partial^2 \ln p(\mathbf{h};\theta)}{\partial \tau \partial a}\right]$$

$$= \frac{4\pi^2 \Delta f T'}{\sigma_w^2} \sum_m \sum_k \sum_i \sum_n nif^k \left(\sum_{pth=1}^{mpth} A_{pth}^{k(m)} e^{j2\pi[ia_{pth}^{k(m)} f^k T' - n\Delta f \tau_{pth}^{k(m)} + r^{k(m)}(\phi_{pth})]} \right)^2,$$

$$[\mathbf{I}(\theta)]_{13} = [\mathbf{I}(\theta)]_{31} = -E\left[\frac{\partial^2 \ln p(\mathbf{h};\theta)}{\partial \tau \partial \phi}\right]$$

$$= \frac{4\pi^2 \Delta f d}{\sigma_w^2} \sum_m \sum_k \sum_i \sum_n \frac{n(m-1)}{\lambda_k} \left(\sum_{pth=1}^{mpth} A_{pth}^{k(m)} e^{j2\pi[ia_{pth}^{k(m)} f^k T' - n\Delta f \tau_{pth}^{k(m)} + r^{k(m)}(\phi_{pth})]} \right)$$

$$\times \left(\sum_{pth=1}^{mpth} A_{pth}^{k(m)} \cos\phi_{pth}^{k(m)} e^{j2\pi[ia_{pth}^{k(m)} f^k T' - n\Delta f \tau_{pth}^{k(m)} + r^{k(m)}(\phi_{pth})]} \right),$$

$$[\mathbf{I}(\theta)]_{22} = -E\left[\frac{\partial^2 \ln p(\mathbf{h};\theta)}{\partial a^2}\right]$$

$$= -\frac{4\pi^2 T'^2}{\sigma_w^2} \sum_m \sum_k \sum_i \sum_n (if^k)^2 \left(\sum_{pth=1}^{mpth} A_{pth}^{k(m)} e^{j2\pi[ia_{pth}^{k(m)} f^k T' - n\Delta f \tau_{pth}^{k(m)} + r^{k(m)}(\phi_{pth})]} \right)^2,$$

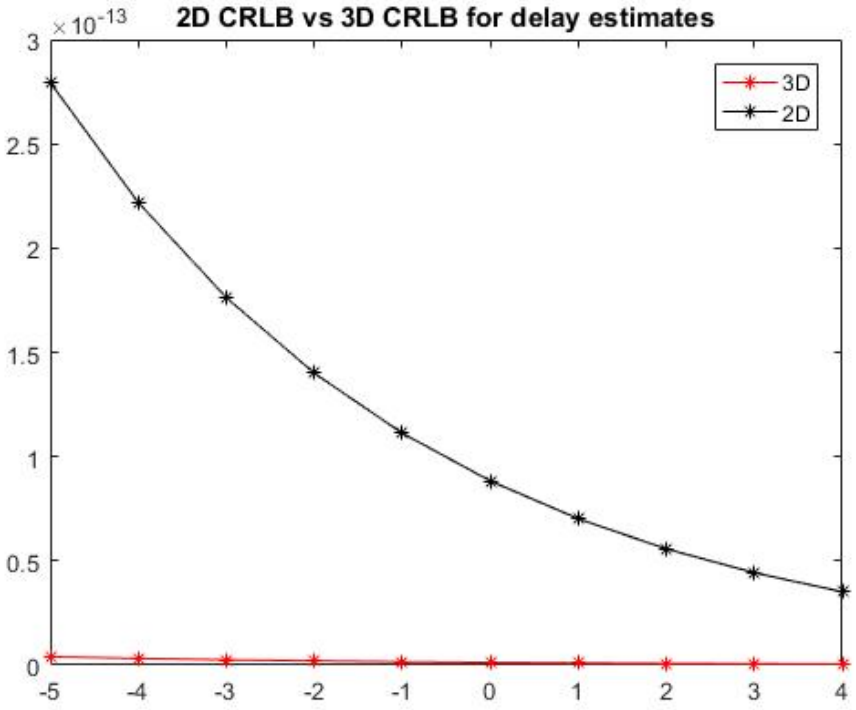

(a)

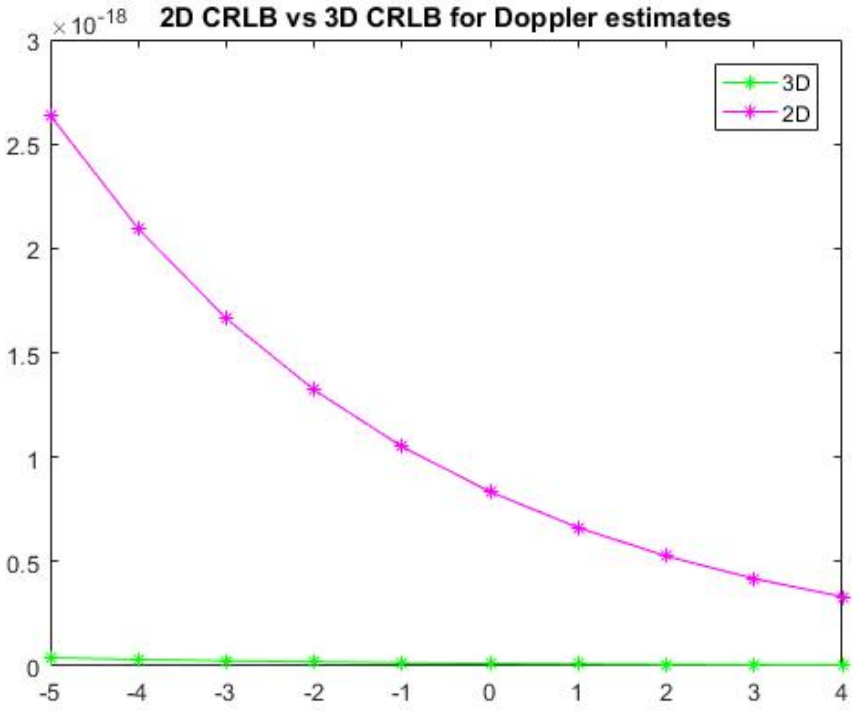

(b)

Figure B.1: Cramer-Rao Lower Bounds for two-dimensional passive radar signal extraction in comparison with three-dimensional version in corresponding domain where: (a) Time delay domain; and (b) Doppler frequency domain (in a form of parameter $a = v/c$).

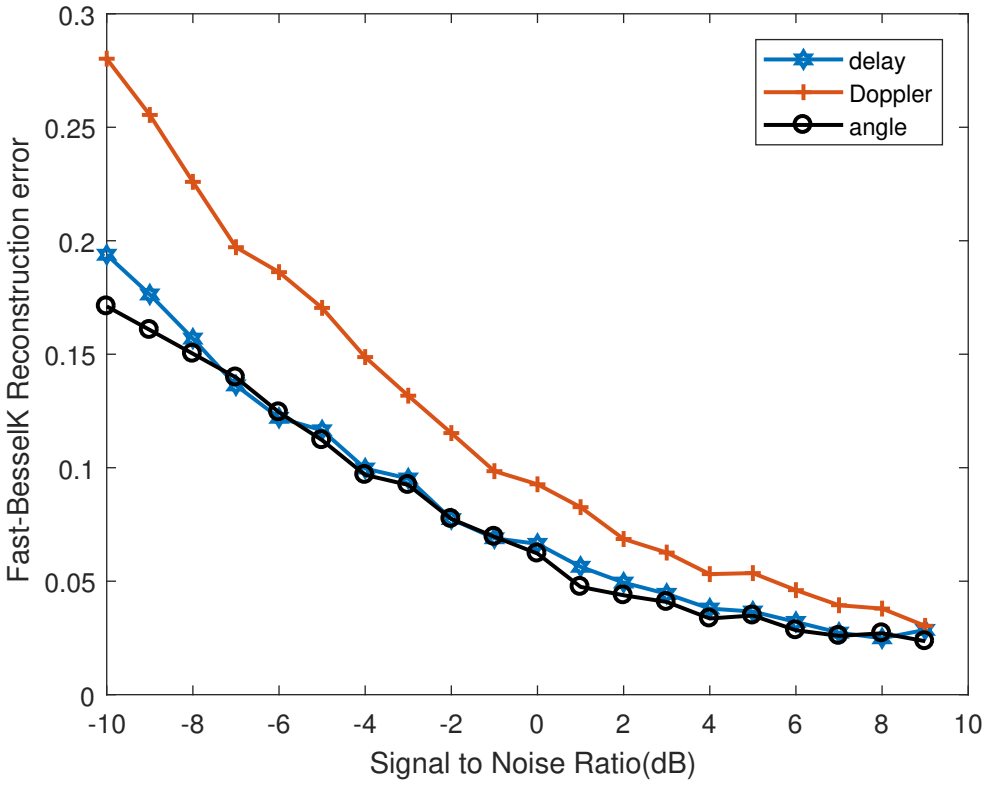

Figure B.2: Reconstruction error after applying Fast-BesselK method for three parameters.

$$[\mathbf{I}(\theta)]_{23} = [\mathbf{I}(\theta)]_{32} = -E\left[\frac{\partial^2 \ln p(\mathbf{h};\theta)}{\partial a \partial \phi}\right]$$

$$= -\frac{4\pi^2 T' d}{\sigma_w^2} \sum_m \sum_k \sum_i \sum_n \frac{i f^k (m-1)}{\lambda_k} \left(\sum_{pth=1}^{mpth} A_{pth}^{k(m)} e^{j2\pi[i a_{pth}^{k(m)} f^k T' - n\Delta f \tau_{pth}^{k(m)} + r^{k(m)}(\phi_{pth})]} \right)$$

$$\times \left(\sum_{pth=1}^{mpth} A_{pth}^{k(m)} \cos\phi_{pth}^{k(m)} e^{j2\pi[i a_{pth}^{k(m)} f^k T' - n\Delta f \tau_{pth}^{k(m)} + r^{k(m)}(\phi_{pth})]} \right),$$

$$[\mathbf{I}(\theta)]_{33} = -E\left[\frac{\partial^2 \ln p(\mathbf{h};\theta)}{\partial \phi^2}\right]$$

$$= -\frac{4\pi^2 d^2}{\sigma_w^2} \sum_m \sum_k \sum_i \sum_n \left(\frac{m-1}{\lambda_k}\right)^2 \left(\sum_{pth=1}^{mpth} A_{pth}^{k(m)} \cos\phi_{pth}^{k(m)} e^{j2\pi[i a_{pth}^{k(m)} f^k T' - n\Delta f \tau_{pth}^{k(m)} + r^{k(m)}(\phi_{pth})]} \right)^2.$$

The above equations can be simplified further, assuming that there is one path per a pair of transmitter and receiver as well as the attenuations between each receive antenna are nearly equal. Using summation and complex exponential properties, the results are eventually displayed as in Section 4.6.

B.3 Illustrations of Cramer-Rao lower bound for the MIMO-OFDM passive radars

Finally, the simulations of 2D and 3D Cramer-Rao Lower Bounds derived in Section 3.4 and 4.6 respectively, are illustrated. Given that the x-axis determine the SNR values, Fig. B.1 displays the comparison between 2D CRLBs and 3D CRLBs in time delay domain and Doppler frequency domain. Specifically in frequency domain, the bound displayed is corresponded to the parameter a, which is the ratio between range-rate and speed of light. It can be seen that 2D version of the bound are higher. Likewise, the 3D CRLBs themselves are shown in Fig. B.3. Obviously from previous figures, the error in variance becomes less if the SNR gets larger. The simulated reconstruction errors resulted from Fast-BesselK are shown in Fig. B.2. In order to demonstrate the capability of the proposed algorithm, the CRLBs between theorical 3D matched filter are compared with the NMSE from selected Fast-BesselK methods in Fig. B.4. It is worth to analyse the extraction performance of the algorithm at the SNR of -5 dB. It is shown that Fast-BesselK, which is demonstrated more accurate than the others in this thesis, still supplies some error and the amount of SNR in the real application might be lessened due to the properties of the target. This can be improved when beamforming is operated or other candidate methods are proposed.

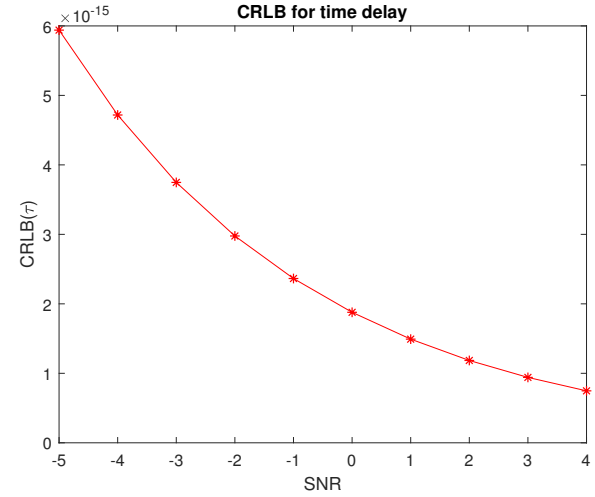

(a)

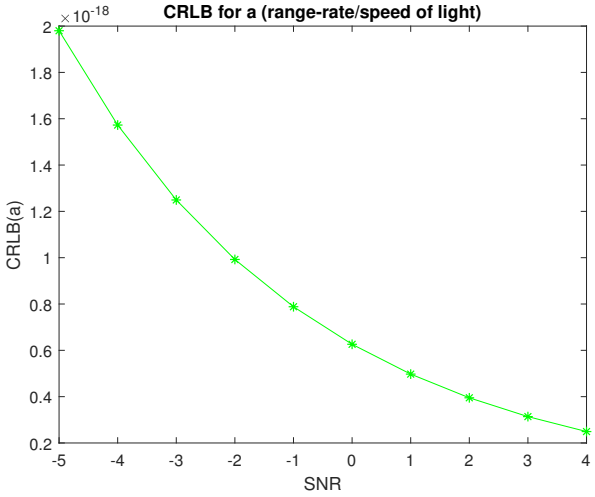

(b)

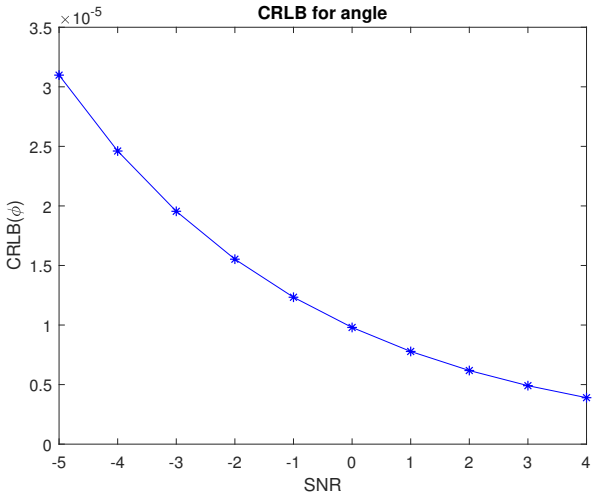

(c)

Figure B.3: Cramer-Rao Lower Bounds for three-dimensional passive radar signal extraction in: (a) Time delay domain; (b) Doppler frequency domain; and (c) angular domain.

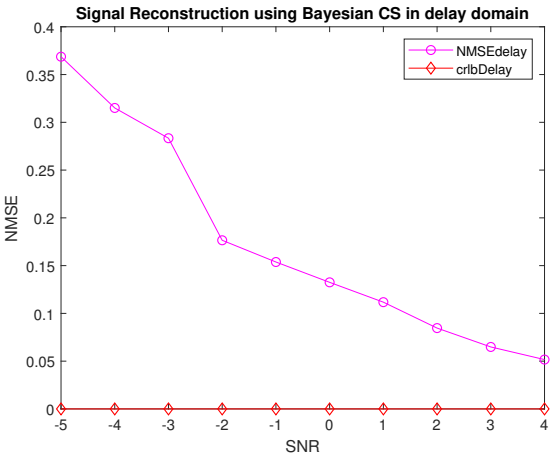

(a)

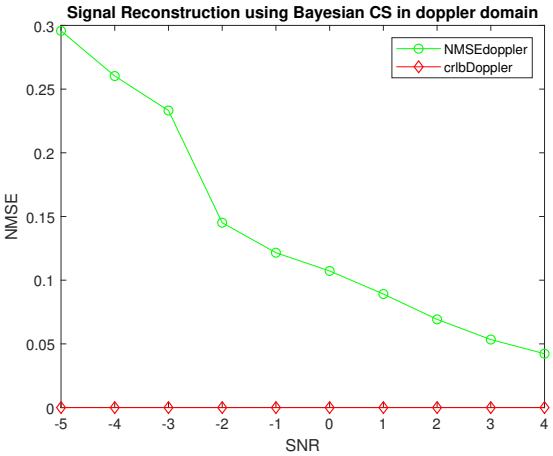

(b)

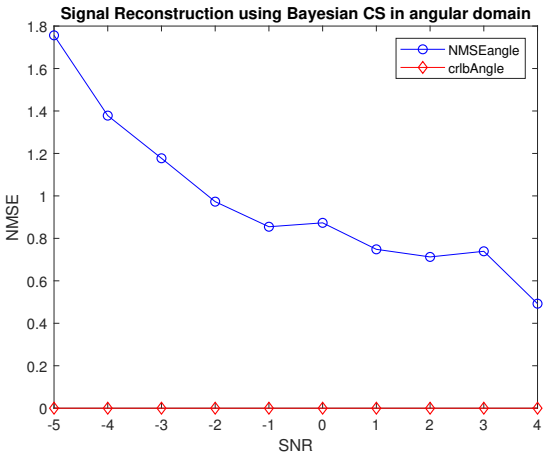

(c)

Figure B.4: The normalised mean square error from the Fast-BesselK algorithm in comparison with 3D CRLB in corresponding domain where: (a) Time delay domain; (b) Doppler frequency domain; and (c) angular domain. The visible lines are the error from the Fast-BesselK while the bounds are much lower and lie on the x-axis.

Bibliography

[1] J. Proakis and M. Salehi, *Digital Communications*, 5th ed. McGraw-Hill, 2008.

[2] D. Malioutov, M. Cetin, and A. Willsky, "A sparse signal reconstruction perspective for source localization with sensor arrays," *IEEE Transactions on Signal Processing*, vol. 53, no. 8, pp. 3010–3022, aug 2005.

[3] A. Al-Hourani, R. J. Evans, S. Kandeepan, B. Moran, and H. Eltom, "Stochastic geometry methods for modeling automotive radar interference," *IEEE Transactions on Intelligent Transportation Systems*, vol. PP, no. 99, pp. 1–12, 2017.

[4] *Digital Audio Broadcasting (DAB) to Mobile, Portable and Fixed Receivers*, European Telecommunications Standards Institute Radio Broadcasting Systems ETS 300 401, 1997.

[5] H. D. Griffiths and C. J. Baker, "Passive coherent location radar systems. part 1: performance prediction," *IEE Proceedings - Radar, Sonar and Navigation*, vol. 152, no. 3, pp. 153–159, June 2005.

[6] M. Cherniakov, *Bistatic radar: emerging technology*. Sussex: John Wiley & Sons, Inc., 2008.

[7] S. Gogineni, M. Rangaswamy, B. D. Rigling, and A. Nehorai, "Cramer-Rao bounds for UMTS-based passive multistatic radar," *IEEE Transactions on Signal Processing*, vol. 62, no. 1, pp. 95–106, Jan 2014.

[8] D. Hack, L. Patton, B. Himed, and M. Saville, "Detection in Passive MIMO Radar Networks," *IEEE Transactions on Signal Processing*, vol. 62, no. 11, pp. 2999–3012, jun 2014.

[9] D. E. Hack, L. K. Patton, B. Himed, and M. A. Saville, "Centralized passive mimo radar detection without direct-path reference signals," *IEEE Transactions on Signal Processing*, vol. 62, no. 11, pp. 3013–3023, June 2014.

[10] Q. Wang, C. Hou, and Y. Lu, "Wimax signal generation based on mimo-ofdm testbed for passive radar application," in *2009 4th IEEE Conference on Industrial Electronics and Applications*, May 2009, pp. 2582–2587.

[11] M. Radmard, S. M. Karbasi, and M. M. Nayebi, "Data Fusion in MIMO DVB-T-Based Passive Coherent Location," *IEEE Transactions on Aerospace and Electronic Systems*, vol. 49, no. 3, pp. 1725–1737, jul 2013.

[12] J. Yi, X. Wan, H. Leung, and F. Cheng, "MIMO Passive Radar Tracking Under a Single Frequency Network," *IEEE Journal of Selected Topics in Signal Processing*, vol. PP, no. 99, pp. 1–1, 2015.

[13] H. Wang, J. Yi, and X. Wan, "A fast direct cartesian localization in single frequency networks-based mimo passive radar," in *2016 CIE International Conference on Radar (RADAR)*, Oct 2016, pp. 1–4.

[14] M. Radmard, S. Karbasi, B. Khalaj, and M. Nayebi, "Data association in multi-input single-output passive coherent location schemes," *IET Radar, Sonar & Navigation*, vol. 6, no. 3, p. 149, 2012.

[15] C. Sturm and W. Wiesbeck, "Waveform design and signal processing aspects for fusion of wireless communications and radar sensing," *Proceedings of the IEEE*, vol. 99, no. 7, pp. 1236–1259, July 2011.

[16] C. R. Berger, B. Demissie, J. Heckenbach, P. Willett, and S. Zhou, "Signal Processing for Passive Radar Using OFDM Waveforms," *IEEE Journal of Selected Topics in Signal Processing*, vol. 4, no. 1, pp. 226–238, feb 2010.

[17] J. L. Garry, C. J. Baker, and G. E. Smith, "Evaluation of direct signal suppression for passive radar," *IEEE Transactions on Geoscience and Remote Sensing*, vol. 55, no. 7, pp. 3786–3799, July 2017.

[18] P. Howland, D. Maksimiuk, and G. Reitsma, "FM radio based bistatic radar," *IEE Proceedings-Radar, Sonar and Navigation*, vol. 152, no. 3, pp. 107–115, 2005.

[Online]. Available: http://digital-library.theiet.org/content/journals/10.1049/ip-rsn_20010473

[19] J. E. Palmer, H. A. Harms, S. Member, S. J. Searle, L. M. Davis, and S. Member, "DVB-T Passive Radar Signal Processing," *IEEE Transactions on Signal Processing*, vol. 61, no. 8, pp. 2116–2126, 2013.

[20] A. Zaimbashi, M. Derakhtian, and A. Sheikhi, "Glrt-based cfar detection in passive bistatic radar," *IEEE Transactions on Aerospace and Electronic Systems*, vol. 49, no. 1, pp. 134–159, Jan 2013.

[21] A. A. Konovalov, "Target tracking algorithm for passive coherent location," *IET Radar, Sonar Navigation*, vol. 10, no. 7, pp. 1228–1233, 2016.

[22] H. W. Li and J. Wang, "Particle filter for manoeuvring target tracking via passive radar measurements with glint noise," *IET Radar, Sonar Navigation*, vol. 6, no. 3, pp. 180–189, March 2012.

[23] D. Pasculli, A. Baruzzi, C. Moscardini, D. Petri, M. Conti, and M. Martorella, "Dvb-t passive radar tracking on real data using extended kalman filter with doa estimation," in *2013 14th International Radar Symposium (IRS)*, vol. 1, June 2013, pp. 184–189.

[24] A. Haimovich, R. Blum, and L. Cimini, "MIMO Radar with Widely Separated Antennas," *IEEE Signal Processing Magazine*, vol. 25, no. 1, pp. 116–129, 2008.

[25] G. Battistelli, L. Chisci, C. Fantacci, A. Farina, and A. Graziano, "Distributed Multitarget Tracking for Passive Multireceiver Radar Systems," in *14th International Radar Sysposium (IRS)*, Dresden, Germany, 2013, pp. 337–342.

[26] R. P. S. Mahler, "Multitarget Bayes Filtering via First-Order Multitarget Moments," *IEEE Transactions on Aerospace and Electronic Systems*, vol. 39, no. 4, pp. 1152–1178, 2003.

[27] S. Bartoletti, A. Conti, and M. Z. Win, "Passive radar via LTE signals of opportunity," in *2014 IEEE International Conference on Communications Workshops (ICC)*. IEEE, jun 2014, pp. 181–185.

[28] B. Dawidowicz, P. Samczynski, M. Malanowski, J. Misiurewicz, and K. S. Kulpa, "Detection of moving targets with multichannel airborne passive radar," *IEEE Aerospace and Electronic Systems Magazine*, vol. 27, no. November, pp. 42–49, 2012.

[29] D. Gromek, P. Samczy, K. Kulpa, J. Misiurewicz, and A. Gromek, "Analysis of Range Migration and Doppler History for an Airborne Passive Bistatic SAR Radar," in *15th International Radar Symposium(IRS)*, 2014, pp. 1–6.

[30] T. Chan, Y. Kuga, and S. Roy, "Combined Use of Various Passive Radar Techniques and Angle of Arrival using MUSIC for the Detection of Ground Moving Objects," in *IEEE International Symposium on Antennas and Propagation (APSURSI)*, 2011, pp. 2561–2564.

[31] MATLAB, *version 8.4.0 (R2014b)*. Natick, Massachusetts: The MathWorks Inc., 2014.

[32] H. Van Trees, *Optimum Array Processing, ser. Detection, Estimation, and Modulation Theory(PartIV)*, 1st ed. Hoboken,NJ: Wiley, 2002.

[33] R. Schmidt, "Multiple emitter location and signal parameter estimation," *IEEE Transactions on Antennas and Propagation*, vol. 34, no. 3, pp. 276–280, 1986.

[34] T. Shan, M. Wax, and T. Kailath, "On Spatial Smoothing for Direction-of-Arrival Estimation of Coherent Signals," *IEEE Transactions on Acoustics, Speech, and Signal Processing*, vol. ASSP-33, no. 4, pp. 806–811, 1985.

[35] G. Lellouch, R. Pribic, and P. van Genderen, "Merging frequency agile ofdm waveforms and compressive sensing into a novel radar concept," in *2009 European Radar Conference (EuRAD)*, Sept 2009, pp. 137–140.

[36] Y. Zhang, G. Wang, and T. Xia, "Compressive orthogonal frequency division multiplexing waveform based ground penetrating radar," in *2015 IEEE Radar Conference (RadarCon)*, May 2015, pp. 0684–0689.

[37] M. Metwally, N. L'Esperance, and T. Xia, "Ground penetrating radar utilizing compressive sampling and ofdm techniques," in *2015 IEEE International Symposium on Circuits and Systems (ISCAS)*, May 2015, pp. 2117–2120.

[38] J. Xiong and W. Q. Wang, "Sparse reconstruction-based beampattern synthesis for multi-carrier frequency diverse array antenna," in *2017 IEEE International Conference on Acoustics, Speech and Signal Processing (ICASSP)*, March 2017, pp. 3395–3398.

[39] D. L. Donoho, "Compressed sensing," *IEEE Transactions on Information Theory*, vol. 52, no. 4, pp. 1289–1306, 2006. [Online]. Available: http://ieeexplore.ieee.org/lpdocs/epic03/wrapper.htm?arnumber=1614066

[40] Y. C. Eldar and G. Kutyniok, *Compressed Sensing: Theory and Applications*. New York: Cambridge University Press, 2012.

[41] Z. Han, H. Li, and W. Yin, *Compressive Sensing for Wireless Networks*. New York: Cambridge University Press, 2013.

[42] M. Weiss, "Compressive sensing for passive surveillance radar using DAB signals," in *2014 International Radar Conference*. IEEE, oct 2014, pp. 1–6.

[43] S. J. Kim, K. Koh, M. Lustig, S. Boyd, and D. Gorinevsky, "An interior-point method for large-scale ℓ_1 -regularized least squares," *IEEE Journal of Selected Topics in Signal Processing*, vol. 1, no. 4, pp. 606–617, Dec 2007.

[44] Q. Wu and K. M. Wong, "Blind adaptive beamforming for cyclostationary signals," *IEEE Transactions on Signal Processing*, vol. 44, no. 11, pp. 2757–2767, Nov 1996.

[45] S. K. Sharma, S. Chatzinotas, and B. Ottersten, "Transmit beamforming for spectral coexistence of satellite and terrestrial networks," in *8th International Conference on Cognitive Radio Oriented Wireless Networks*, July 2013, pp. 275–281.

[46] E. Bjrnson, M. Bengtsson, and B. Ottersten, "Optimal multiuser transmit beamforming: A difficult problem with a simple solution structure [lecture notes]," *IEEE Signal Processing Magazine*, vol. 31, no. 4, pp. 142–148, July 2014.

[47] G. Nauryzbayev, E. Alsusa, and M. Abdallah, "On the feasibility of interference alignment in compounded mimo broadcast channels with antenna correlation and mixed user classes," *IEEE Transactions on Vehicular Technology*, vol. 67, no. 3, pp. 2130–2140, March 2018.

[48] M. Medra and T. N. Davidson, "Robust miso downlink: An efficient algorithm for improved beamforming directions," in *2016 IEEE Sensor Array and Multichannel Signal Processing Workshop (SAM)*, July 2016, pp. 1–5.

[49] N. Sharaga, J. Tabrikian, and H. Messer, "Optimal cognitive beamforming for target tracking in mimo radar/sonar," *IEEE Journal of Selected Topics in Signal Processing*, vol. 9, no. 8, pp. 1440–1450, Dec 2015.

[50] C. Li, J. Benesty, G. Huang, and J. Chen, "Subspace superdirective beamformers based on joint diagonalization," in *2016 IEEE International Conference on Acoustics, Speech and Signal Processing (ICASSP)*, March 2016, pp. 400–404.

[51] H. Lebret and S. Boyd, "Antenna array pattern synthesis via convex optimization," *IEEE Transactions on Signal Processing*, vol. 45, no. 3, pp. 526–532, Mar 1997.

[52] S. A. Haider, Y. Li, K. P. Ho, J. Liu, and I. Ngebani, "2x2 hybrid beamforming mimo system for millimeter wave communication," in *IET International Radar Conference 2015*, Oct 2015, pp. 1–5.

[53] Y. R. Ramadan, A. S. Ibrahim, and M. M. Khairy, "Robust rf beamforming for millimeter wave mimo–ofdm systems," *International Journal of Wireless Information Networks*, vol. 22, no. 4, pp. 327–335, Dec 2015. [Online]. Available: https://doi.org/10.1007/s10776-015-0287-7

[54] M. Malanowski and K. Kulpa, "Digital beamforming for passive coherent location radar," in *2008 IEEE Radar Conference*, May 2008, pp. 1–6.

[55] J.-H. Deng, J.-K. Hwang, C.-Y. Lin, and S.-M. Liao, "Adaptive space-time beamforming technique for passive radar system with ultra low signal to interference ratio," in *2010 IEEE International Conference on Wireless Information Technology and Systems*, Aug 2010, pp. 1–4.

[56] J. Li, P. Stoica, and Z. Wang, "On robust capon beamforming and diagonal loading," *IEEE Transactions on Signal Processing*, vol. 51, no. 7, pp. 1702–1715, July 2003.

[57] H. Cox, R. Zeskind, and M. Owen, "Robust adaptive beamforming," *IEEE Transactions on Acoustics, Speech, and Signal Processing*, vol. 35, no. 10, pp. 1365–1376, Oct 1987.

[58] Q. Wu and K. M. Wong, "Blind adaptive beamforming for cyclostationary signals," *IEEE Transactions on Signal Processing*, vol. 44, no. 11, pp. 2757–2767, Nov 1996.

[59] G. Bournaka, A. Baruzzi, J. Heckenbach, and H. Kuschel, "Experimental validation of beamforming techniques for localization of moving target in passive radar," in *2015 IEEE Radar Conference (RadarCon)*, May 2015, pp. 1710–1713.

[60] C. Berger, S. Zhou, and P. Willett, "Signal Extraction Using Compressed Sensing for Passive Radar with OFDM Signals," in *The 11th International Conference on Information Fusion*, 2008, pp. 422–427.

[61] J. A. Tropp and A. C. Gilbert, "Signal recovery from random measurements via orthogonal matching pursuit," *IEEE Transactions on Information Theory*, vol. 53, no. 12, pp. 4655–4666, Dec 2007.

[62] F. Baccelli, B. Blaszczyszyn, and P. Muhlethaler, "An aloha protocol for multihop mobile wireless networks," *IEEE Transactions on Information Theory*, vol. 52, no. 2, pp. 421–436, Feb 2006.

[63] R. K. Ganti and M. Haenggi, "Interference in ad hoc networks with general motion-invariant node distributions," in *2008 IEEE International Symposium on Information Theory*, July 2008, pp. 1–5.

[64] ——, "Spatial and temporal correlation of the interference in aloha ad hoc networks," *IEEE Communications Letters*, vol. 13, no. 9, pp. 631–633, Sept 2009.

[65] C.-H. Lee, C.-Y. Shih, and Y.-S. Chen, "Stochastic geometry based models for modeling cellular networks in urban areas," *Wireless Networks*, vol. 19, no. 6, pp. 1063–1072, Aug 2013. [Online]. Available: https://doi.org/10.1007/s11276-012-0518-0

[66] A. Ahmed, S. J. Nawaz, N. M. Khan, M. N. Patwary, and M. Abdel-Maguid, "Angular characteristics of a unified 3-d scattering model for emerging cellular networks," in *2015 IEEE International Conference on Communications (ICC)*, June 2015, pp. 2450–2456.

[67] H. D. Nguyen and S. Sun, "Closed-form performance bounds for stochastic geometry-based cellular networks," *IEEE Transactions on Wireless Communications*, vol. 16, no. 2, pp. 683–693, Feb 2017.

[68] R. W. Heath, M. Kountouris, and T. Bai, "Modeling heterogeneous network interference using poisson point processes," *IEEE Transactions on Signal Processing*, vol. 61, no. 16, pp. 4114–4126, Aug 2013.

[69] M. D. Renzo and P. Guan, "Stochastic geometry modeling and system-level analysis of uplink heterogeneous cellular networks with multi-antenna base stations," *IEEE Transactions on Communications*, vol. 64, no. 6, pp. 2453–2476, June 2016.

[70] A. Shojaeifard, K. K. Wong, K. A. Hamdi, E. Alsusa, D. K. C. So, and J. Tang, "Stochastic geometric analysis of energy-efficient dense cellular networks," *IEEE Access*, vol. 5, pp. 455–469, 2017.

[71] A. K. Hassan, M. Moinuddin, and U. M. Al-Saggaf, "Beamforming in massive mu-mimo cellular networks: A stochastic geometry approach," in *2016 6th International Conference on Intelligent and Advanced Systems (ICIAS)*, Aug 2016, pp. 1–5.

[72] S. Biswas, J. Xue, F. A. Khan, and T. Ratnarajah, "Performance analysis of correlated massive mimo systems with spatially distributed users," *IEEE Systems Journal*, vol. PP, no. 99, pp. 1–12, 2017.

[73] M. Haenggi, "On distances in uniformly random networks," *IEEE Transactions on Information Theory*, vol. 51, no. 10, pp. 3584–3586, Oct 2005.

[74] S. A. R. Zaidi, M. Ghogho, D. C. McLernon, and A. Swami, "Achievable spatial throughput in multi-antenna cognitive underlay networks with multi-hop relaying," *IEEE Journal on Selected Areas in Communications*, vol. 31, no. 8, pp. 1543–1558, August 2013.

[75] Y. He, J. Xue, T. Ratnarajah, M. Sellathurai, and F. Khan, "On the performance of cooperative spectrum sensing in random cognitive radio networks," *IEEE Systems Journal*, vol. PP, no. 99, pp. 1–12, 2017.

[76] C. Zhang and W. Zhang, "Spectrum sharing for drone networks," *IEEE Journal on Selected Areas in Communications*, vol. 35, no. 1, pp. 136–144, Jan 2017.

[77] M. Haenggi, J. G. Andrews, F. Baccelli, O. Dousse, and M. Franceschetti, "Stochastic geometry and random graphs for the analysis and design of wireless networks," *IEEE Journal on Selected Areas in Communications*, vol. 27, no. 7, pp. 1029–1046, September 2009.

[78] D. Daley and D. Vere-Jones, *An introduction to the theory of point processes. Vol. 1 : Elementary theory and methods*, 2nd ed. Springer, 2003.

[79] ——, *An introduction to the theory of point processes. Vol 2 : general theory and structure*, 2nd ed. Springer, 2008.

[80] S. N. Chiu, D. Stoyan, W. S. Kendall, and J. Mecke, *Point processes II General theory*. John Wiley and Sons, Ltd, 2013, pp. 108–157. [Online]. Available: http://dx.doi.org/10.1002/9781118658222.ch04

[81] M. Haenggi, *Stochastic Geometry for Wireless Networks*. Cambridge: Cambridge University Press, 2012.

[82] F. Baccelli and B. Blaszczyszyn, *Stochastic Geometry and Wireless Networks, Volume I - Theory*, ser. Foundations and Trends in Networking Vol. 3: No 3-4, pp 249-449, F. Baccelli and B. Blaszczyszyn, Eds. NoW Publishers, 2009, vol. 1, stochastic Geometry and Wireless Networks, Volume II - Applications; see http://hal.inria.fr/inria-00403040. [Online]. Available: https://hal.inria.fr/inria-00403039

[83] R. S. Thomä, C. Andrich, G. Del Galdo, M. Döbereiner, M. A. Hein, M. Käske, G. Schäfer, S. Schieler, C. Schneider, A. Schwind, and P. Wendland, "Cooperative Passive Coherent Location: A Promising Service for Future Mobile Radio Networks," *ArXiv e-prints*, Feb. 2018.

[84] B. K. Chalise, Y. D. Zhang, M. G. Amin, and B. Himed, "Target localization in a multi-static passive radar system through convex optimization," *Signal Processing*, vol. 102, pp. 207–215, sep 2014.

[85] M. Daun, U. Nickel, and W. Koch, "Tracking in multistatic passive radar systems using DAB/DVB-T illumination," *Signal Processing*, vol. 92, no. 6, pp. 1365–1386, jun 2012.

[86] M. Weiss, "Passive wireless local area network radar network using compressive sensing technique," *IET Radar, Sonar & Navigation*, vol. 9, no. 1, pp. 84–91, 2015.

[87] Q. Wu, Y. D. Zhang, M. G. Amin, and B. Himed, "Space-time adaptive processing and motion parameter estimation in multistatic passive radar using sparse Bayesian learning," *IEEE Transactions on Geoscience and Remote Sensing*, vol. 54, no. 2, pp. 944–957, Feb 2016.

[88] M. Skolnik, *Introduction to Radar Systems*, 3rd ed. New York: McGraw-Hill, 2001.

[89] S. M. Kay, *Fundamentals of statistical signal processing: estimation theory*. Prentice-Hall, 1993.

[90] W. Ketpan, S. Phonsri, R. Qian, and M. Sellathurai, "On the Target Detection in OFDM Passive Radar Using MUSIC and Compressive Sensing," in *2015 Sensor Signal Processing for Defence (SSPD)*. IEEE, Sep 2015, pp. 1–5.

[91] M. Grant and S. Boyd, "CVX: Matlab software for disciplined convex programming, version 2.1," http://cvxr.com/cvx, Mar. 2014.

[92] J. Li and P. Stoica, "MIMO Radar with Colocated Antennas," *IEEE Signal Processing Magazine*, vol. 24, no. 5, pp. 106–114, sep 2007.

[93] G. Auer, "3D MIMO-OFDM Channel Estimation," *IEEE Transactions on Communications*, vol. 60, no. 4, pp. 972–985, apr 2012.

[94] L. Tzafri and A. J. Weiss, "High-resolution direct position determination using mvdr," *IEEE Transactions on Wireless Communications*, vol. 15, no. 9, pp. 6449–6461, Sept 2016.

[95] R. Qian, P. Chambers, and M. Sellathurai, "Adaptive bayesian channel estimation for millimeter-wave mimo systems with hybrid architecture," in *2018 52nd Asilomar Conference on Signals, Systems, and Computers*, Oct 2018, p. To appear.

[96] E. Fishler, A. Haimovich, R. S. Blum, L. J. Cimini, D. Chizhik, and R. A. Valenzuela, "Spatial diversity in radars-models and detection performance," *IEEE Transactions on Signal Processing*, vol. 54, no. 3, pp. 823–838, March 2006.

[97] H. Rauhut, "Compressive sensing and structured random matrices," in *Theoretical Foundations and Numerical Methods for Sparse Recovery*, ser. Radon Series on Computational and Applied Mathematics, M. Fornasier, Ed., vol. 9. deGruyter, 2010, pp. 1–94.

[98] W. Ketpan and M. Sellathurai, "Compressive sensing-based 3D signal extraction for MIMO passive radar using OFDM waveforms," in *2016 IEEE International Conference on Communications (ICC)*, May 2016, pp. 1–6.

[99] F. Shu, J. Zhao, X. You, M. Wang, Q. Chen, and B. Stevan, "An efficient sparse channel estimator combining time-domain ls and iterative shrinkage for ofdm systems with iq-imbalances," *Science China Information Sciences*, vol. 55, no. 11, pp. 2604–2610, Nov 2012. [Online]. Available: https://doi.org/10.1007/s11432-012-4691-7

[100] H. Yu, F. Shu, Y. You, J. Wang, T. Liu, X. You, J. Lu, J. Wang, and X. Zhu, "Compressed sensing-based time-domain channel estimator for full-duplex ofdm systems with iq-imbalances," *Science China Information Sciences*, vol. 60, no. 8, p. 082303, Mar 2017. [Online]. Available: https://doi.org/10.1007/s11432-016-0386-x

[101] S. Ji, Y. Xue, and L. Carin, "Bayesian Compressive Sensing," *IEEE Transactions on Signal Processing*, vol. 56, no. 6, pp. 2346–2356, jun 2008.

[102] N. L. Pedersen, C. N. Manchn, M.-A. Badiu, D. Shutin, and B. H. Fleury, "Sparse estimation using Bayesian hierarchical prior modeling for real and complex linear models," *Signal Processing*, vol. 115, pp. 94 – 109, 2015. [Online]. Available: http://www.sciencedirect.com/science/article/pii/S0165168415001140

[103] M. A. T. Figueiredo, "Adaptive sparseness for supervised learning," *IEEE Transactions on Pattern Analysis and Machine Intelligence*, vol. 25, no. 9, pp. 1150–1159, Sept 2003.

[104] D. P. Wipf and B. D. Rao, "Sparse bayesian learning for basis selection," *IEEE Transactions on Signal Processing*, vol. 52, no. 8, pp. 2153–2164, Aug 2004.

[105] M. E. Tipping and A. C. Faul, "Fast Marginal Likelihood Maximisation for Sparse Bayesian Models," *Ninth International Workshop on Aritficial Intelligence and Statistics*, no. x, pp. 1–13, 2003.

[106] D. P. Wipf, B. D. Rao, and S. Nagarajan, "Latent variable Bayesian models for promoting sparsity," *IEEE Transactions on Information Theory*, vol. 57, no. 9, pp. 6236–6255, Sept 2011.

[107] K. L. Bell, Y. Ephraim, and H. L. V. Trees, "A bayesian approach to robust adaptive beamforming," *IEEE Transactions on Signal Processing*, vol. 48, no. 2, pp. 386–398, Feb 2000.

[108] T. Adali and S. Haykin, *Adaptive signal processing:next generation solutions*. Wiley India, 2010.

[109] L. W. Chen, J. S. Zheng, M. K. Su, and S. Huang, "A novel beamforming technique: Introducing a convex constrained optimization and compressed-sensing model," *IEEE Antennas and Propagation Magazine*, vol. 58, no. 4, pp. 48–59, Aug 2016.

[110] P. Stoica and A. Nehorai, "MUSIC, maximum likelihood, and Cramer-Rao bound," *IEEE Transactions on Acoustics, Speech, and Signal Processing*, vol. 37, no. 5, pp. 720–741, May 1989.

[111] S. Kunis and H. Rauhut, "Random sampling of sparse trigonometric polynomials, ii. orthogonal matching pursuit versus basis pursuit," *Foundations of Computational Mathematics*, vol. 8, no. 6, pp. 737–763, Dec 2008. [Online]. Available: https://doi.org/10.1007/s10208-007-9005-x

[112] S. J. Wright, R. D. Nowak, and M. A. T. Figueiredo, "Sparse reconstruction by separable approximation," *IEEE Transactions on Signal Processing*, vol. 57, no. 7, pp. 2479–2493, July 2009.

[113] D. Needell and J. Tropp, "CoSaMP: Iterative signal recovery from incomplete and inaccurate samples," *Applied and Computational Harmonic Analysis*, vol. 26, no. 3, pp. 301 – 321, 2009. [Online]. Available: http://www.sciencedirect.com/science/article/pii/S1063520308000638

[114] W. Ketpan, R. Qian, M. Sellathurai, and P. Chambers, "Ofdm passive radar and compressive domain processing," *IEEE Systems Journal*, p. Submitted, May 2018.

[115] S. D. Babacan, R. Molina, and A. K. Katsaggelos, "Bayesian compressive sensing using laplace priors," *IEEE Transactions on Image Processing*, vol. 19, no. 1, pp. 53–63, Jan 2010.

[116] M. K. Simon and M.-S. Alouini, *Digital Communication over Fading Channels*. John Wiley and Sons, 2000.

[117] J. GIL-PELAEZ, "Note on the inversion theorem," *Biometrika*, vol. 38, no. 3-4, pp. 481–482, 1951. [Online]. Available: + http://dx.doi.org/10.1093/biomet/38.3-4.481

[118] W. Ketpan and M. Sellathurai, "A study of ofdm passive radar networks using stochastic geometry," *IEEE Access*, p. Submitted, July 2018.

[119] P. E. Howland, "Target tracking using television-based bistatic radar," *IEE Proceedings - Radar, Sonar and Navigation*, vol. 146, no. 3, pp. 166–174, Jun 1999.

[120] I. Dokmanic, R. Parhizkar, J. Ranieri, and M. Vetterli, "Euclidean distance matrices: Essential theory, algorithms, and applications," *IEEE Signal Processing Magazine*, vol. 32, no. 6, pp. 12–30, Nov 2015.

[121] Y. H. Nam, B. L. Ng, K. Sayana, Y. Li, J. Zhang, Y. Kim, and J. Lee, "Full-dimension mimo (fd-mimo) for next generation cellular technology," *IEEE Communications Magazine*, vol. 51, no. 6, pp. 172–179, June 2013.

[122] J. C. Shen, J. Zhang, E. Alsusa, and K. B. Letaief, "Compressed csi acquisition in fdd massive mimo: How much training is needed?" *IEEE Transactions on Wireless Communications*, vol. 15, no. 6, pp. 4145–4156, June 2016.

[123] A. Shojaeifard, K. A. Hamdi, E. Alsusa, D. K. C. So, J. Tang, and K. K. Wong, "Design, modeling, and performance analysis of multi-antenna heterogeneous cellular networks," *IEEE Transactions on Communications*, vol. 64, no. 7, pp. 3104–3118, July 2016.

[124] H. Kuschel, J. Heckenbach, S. Mller, and R. Appel, "Countering stealth with passive, multi-static, low frequency radars," *IEEE Aerospace and Electronic Systems Magazine*, vol. 25, no. 9, pp. 11–17, Sept 2010.

[125] G. Fang, J. Yi, X. Wan, Y. Liu, and H. Ke, "Experimental research of multistatic passive radar with a single antenna for drone detection," *IEEE Access*, pp. 1–1, 2018.

[126] G. Tang, B. N. Bhaskar, P. Shah, and B. Recht, "Compressed sensing off the grid," *IEEE Transactions on Information Theory*, vol. 59, no. 11, pp. 7465–7490, Nov 2013.

[127] M. A. Hadi, S. Alshebeili, K. Jamil, and F. E. A. El-Samie, "Compressive sensing applied to radar systems: an overview," *Signal, Image and Video Processing*, vol. 9, no. 1, pp. 25–39, Dec 2015. [Online]. Available: https://doi.org/10.1007/s11760-015-0824-y